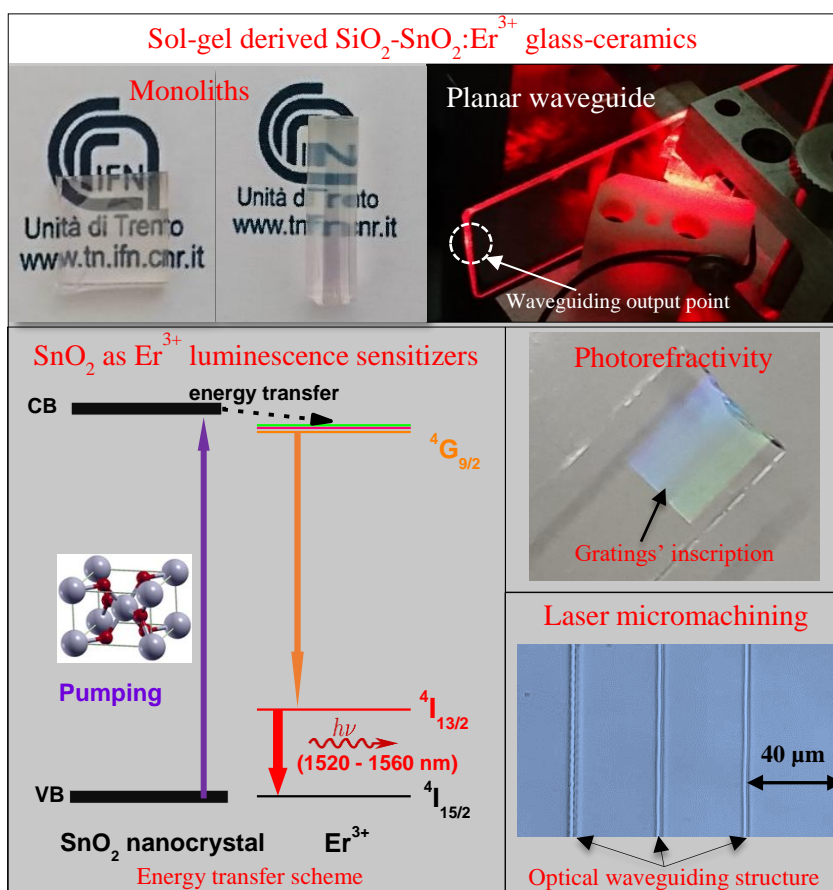


Thi Ngoc Lam Tran

Tin dioxide – based photonic glass-ceramics





Doctoral School in Civil, Environmental and Mechanical Engineering
Topic 3. Modeling and Simulation - 31st cycle 2015/2018

Doctoral Thesis - March 2019

Thi Ngoc Lam Tran

Tin dioxide - based photonic glass-ceramics

Supervisors

Daniele Zonta, DICAM, University of Trento, Italy

Maurizio Ferrari, IFN-CNR Trento, Italy

Lidia Žur, IFN-CNR Trento, Italy

Abstract

Looking at state of the art of optical devices, it is evident that glass-based rare-earth-activated optical structures represent the technological pillar of a huge number of photonic applications covering Health and Biology, Structural Engineering, Environment Monitoring Systems, Lighting, Laser sources and Quantum Technologies. Among different glass-based systems, a strategic place is assigned to transparent glass-ceramics, nanocomposite materials, which offer specific characteristics of capital importance in photonics. Following this strategy, this PhD thesis exploits tin dioxide (SnO_2)-based glass-ceramic activated by erbium ions (Er^{3+}) to put the basis for the fabrication of solid state and integrated lasers. The research discussed in my PhD thesis gives a possible solution to two crucial and decisive points in the development of an optically pumped rare-earth-based laser: (i) the low absorption cross section of the rare-earth ions; (ii) the writing of channels and mirrors in the case of waveguide integrated laser, thanks to the demonstration of two innovative and unique characteristics of SnO_2 -based transparent glass-ceramics, i.e. luminescence sensitizing and photorefractivity. The role of SnO_2 nanocrystals as rare-earth ion luminescence sensitizers allows to overcome the low absorption cross section of the Er^{3+} ion. The photorefractivity in range of 10^{-3} of $\text{SiO}_2\text{-SnO}_2\text{:Er}^{3+}$ glass-ceramics allows applying the robust direct laser photoinscription technique on the systems to fabricate Bragg gratings and channel waveguides for waveguide integrated lasers. Based on an application-oriented approach, a comprehensive study on $\text{SiO}_2\text{-SnO}_2\text{:Er}^{3+}$ glass-ceramic planar waveguides and monoliths, has been carried out. The work covers different research stages and aspects from the material preparation to a complete assessment of systems for the applications employing a rich number and variety of experimental techniques. The energy transfer from SnO_2 to Er^{3+} and the efficient pumping scheme exploiting SnO_2 as Er^{3+} luminescence sensitizers were demonstrated. The relaxation dynamic of the electronic states as well as the location of the dopant and density of states are discussed, and a specific modeling has been developed to the proof of concept realization of the considered devices. The obtained photorefractivity in range of 10^{-3} allowed the inscription of gratings on the fabricated $\text{SiO}_2\text{-SnO}_2\text{:Er}^{3+}$ planar waveguides using UV laser direct writing technique. Exploiting the robust femtosecond laser micromachining, the optical waveguides were inscribed in the fabricated $\text{SiO}_2\text{-SnO}_2\text{:Er}^{3+}$ monolithic squares. Another important outcome of this research is the design of a solid state laser with lateral pumping scheme and of an integrated waveguide laser in two different distributed feedback structures using all the parameters measured during the experimental activity.

Thi Ngoc Lam Tran

Thi Ngoc Lam Tran, born in Tien Giang (Vietnam) on February 5th, 1989, graduated in Physical Electronics in the A.Y. 2013/14 at the University of Science Ho Chi Minh City, Vietnam National University with full marks: Excellent (A).

She enrolled to the 3-year PhD Programme in Civil, Environmental and Mechanical Engineering, in the 31th cycle beginning in the A.Y. 2015/2016. During the 3-year PhD, she has been performing her research activities at the CNR-IFN Trento and CSMFO (Characterization and Development of Materials for Photonics and Optoelectronics) Lab, headed by Maurizio Ferrari.

This book is dedicated to my mom, brother, aunts, uncle and all my beloved family members who always fulfil me with unlimited love and spirit. I want to share my joy with Emanuele Sansone and his family who have made me feel like home in Trento. I wish to thank Renata Wójcik for her warm care and kindness to me. I really appreciate the time spent together with my friend Phan Quoc Tin during our PhD studies at University of Trento.

Declaration

I hereby declare that except where specific reference is made to the work of others, the contents of this dissertation are original and have not been submitted in whole or in part for consideration for any other degree or qualification in this, or any other University. This dissertation is the result of my own work or that where it has been carried out in collaboration with, or supported by others, that this is duly indicated in the acknowledgements. This dissertation contains less than 68000 words including appendices, bibliography, footnotes, tables and equations and has less than 220 figures.

Thi Ngoc Lam Tran
2019

Acknowledgements

First and foremost, I wish to express my thankfulness to my supervisors Maurizio Ferrari, Daniele Zonta and Lidia Žur for their enthusiastic guidance, motivation and support throughout the research. Without their guidance, valuable scientific advices and constant feedbacks, this thesis would not be achieved as it is now.

I would like to thank all the colleagues from IFN-CNR CSMFO Lab. Trento, Italy who have helped and supported me. In particular, I would like to thank Cristina Armellini, Alessandro Chiasera and Andrea Chiappini for their help with the lab activities and measurements. I would like to thank Stefano Varas, Osman Sayginer, Cesare Meroni, Alessandro Carpentiero, Maurizio Mazzola and Tiziana Martinelli for their support.

I would like to thank Damiano Massella and Marcello Meneghetti who joined the tin dioxide based photonic glass-ceramics research during their master thesis at the Department of Physics, University of Trento for their impressive contribution to $\text{SiO}_2\text{-SnO}_2\text{:Er}^{3+}$ glass-ceramics investigation both from experimental and computational point of view. In particular, I thank Damiano for the development of the DFT model for studying the relaxation dynamic of the electronic states of $\text{SnO}_2\text{:Er}^{3+}$ and for the laser designs. I thank Marcello Meneghetti for the numerical study of Er^{3+} location in SnO_2 and the initial DFT model for the study of the electronic structure and density of states of $\text{SnO}_2\text{:Er}^{3+}$. In addition, I would like to thank Alessandro Vaccari, from FBK CMM-ARES Unit, Trento, Italy and Y. G. Boucher from CNRS FOTON (UMR 6082), Lannion, France for the support with the simulations.

Let me thank the colleagues from MiPLab, IFAC - CNR, in Sesto Fiorentino (Florence), Italy for the help with photorefractivity investigation. In particular, many thanks are given to Simone Berneschi for the intensive work on the photorefractivity measurements and to Gualtiero Nunzi Conti for the support and help with the photorefractivity investigation. Let me also thank Stefano Pelli and Cosimo Trono for their valuable experimental support.

I would like to thank James Gates and Pier-John Sazio from ORC, Optoelectronics Research Centre, University of Southampton, UK for the UV laser inscription of gratings on the planar waveguides and their valuable scientific comments.

A particular thank is sent to Anna Lukowiak and Paweł Głuchowski from Institute of Low Temperature and Structure Research, PAS, Wrocław, Poland for the spectroscopic measurements in nanosecond time domain which allow me to see clearer the exciton mediated energy transfer between the nanocrystal and the rare earth ion.

I am indebted with Paola Dentella, Vibhav Bharadwaj, Shane Eaton and Roberta Ramponi for the help and support with the inscription of optical waveguides on the monolithic squares by using femtosecond laser micromachining.

I would like to thank Barbara Rossi from Elettra - Sincrotrone Trieste, Trieste, Italy for the help and support with all the Ceric-Eric and Elettra proposals and the UV-Raman measurements.

I would like to thank Gloria Ischia from DII, University of Trento, Italy for the HR-TEM observations and Erica Iacob from FBK CMM MNF, Trento, Italy for AFM observations.

Victor Micheli and Giorgio Speranza from CMM - FBK, Trento, Italy are acknowledged for the XPS and Auger spectroscopy measurements.

Thanks to Dominik Dorosz from AGH University of Science, Krakow, and to Wojciech Pisarski from University of Silesia, Katowice, Poland, and to Alessandro Martucci from Dipartimento di Ingegneria Industriale Set. Materiali, Università di Padova, the thermal analyses were performed on my samples

Dispersion curves were obtained by ellipsometry measurements thanks to Beata Derkowska-Zielinska from Faculty of Physics, Astronomy and Informatics, Nicolaus Copernicus University, Torun, Poland.

I am glad to thank here my Master Advisor, Van T. T. T. from Faculty of Materials Science and Technology, Ho Chi Minh City University of Science, Vietnam National University who gave me a first chance and encouraged me to work with this innovative tin-dioxide based glass-ceramic.

Finally, I acknowledge the financial support from Vietnamese Ministry of Education and Training for my three-year PhD scholarship and DICAM, University of Trento for the extension grant.

Table of Contents

List of figures.....	xii
List of tables	xxii
List of acronyms	xxv
Chapter 1 Introduction.....	1
1.1 State of the art	1
1.2 Research challenges and objectives	2
1.3 Thesis outline	5
References	7
Chapter 2 Photonic glass-ceramics.....	13
2.1 Introduction	13
2.2 State of the art of photonic glass-ceramics.....	13
2.2.1 General advantages of glass-ceramics	13
2.2.2 Photonic glass-ceramics.....	14
2.3 Tin dioxide-based glass-ceramics	15
2.3.1 Advantages of tin dioxide-based glass-ceramics	15
2.3.2 Brief summary of prior researches.....	16
References	21
Chapter 3 Fabrication	27
3.1 Introduction	27
3.2 Brief summary of SnO ₂ based glasses fabrication	27
3.3 The sol-gel derived fabrication.....	28
3.3.1 General routes.....	28
3.3.2 Chemicals	29
3.3.2.1 Precursor of SiO ₂	29
3.3.2.2 Precursor of SnO ₂	29
3.3.2.3 Precursor of Er ³⁺	30
3.3.2.4 Catalyst	30
3.3.2.5 Solvent.....	31
3.3.3 Reactions.....	31

3.3.3.1	Hydrolysis.....	31
3.3.3.2	Condensation	31
3.3.4	Hydrolysis ratio	32
3.4	Monoliths fabrication	34
3.4.1	Sol formation	34
3.4.1.1	Optimization of reactant ratios	35
3.4.1.1.1	H ₂ O/TEOS (R)	35
3.4.1.1.2	EtOH amount	36
3.4.1.1.3	HCl/TEOS ratio.....	36
3.4.1.2	Final recipe	36
3.4.2	Gelation	37
3.4.3	Aging and drying	38
3.4.4	Heat-treatment	41
3.4.4.1	Thermal analysis.....	41
3.4.5	Obtained monoliths.....	44
3.5	Planar waveguides.....	46
3.5.1	Solution preparation.....	46
3.5.2	Deposition.....	48
3.5.2.1	General dip-coating procedure.....	48
3.5.2.2	Optimization of withdraw speed.....	49
3.5.3	Heat-treatment	52
3.5.3.1	Optimization of annealing temperature	53
3.5.3.2	Optimization of annealing time	54
3.5.4	Obtained planar waveguides.....	56
3.6	Conclusions.....	57
	References	58
Chapter 4	Experimental assessments.....	63
4.1	Introduction	63
4.2	Relevant physical properties of active optical materials	63
4.2.1	Optical loss	64
4.2.1.1	Absorption loss	64

4.2.1.2	Scattering loss.....	64
4.2.2	Spectroscopic properties.....	66
4.2.3	Optical waveguiding properties.....	67
4.3	Assessment techniques and specification.....	67
4.4	Structural, morphological and chemical characterization ..	69
4.4.1	Raman spectroscopy	69
4.4.1.1	Non-resonance micro-Raman ($\lambda_{\text{ex}} = 632 \text{ nm}$)	69
4.4.1.2	Resonance UV macro-Raman ($\lambda_{\text{ex}} = 266 \text{ nm}$)	74
4.4.2	X-ray diffraction (XRD)	75
4.4.3	Scanning transmission electron microscopy (EM)	79
4.4.4	Auger electron spectroscopy (AES)	86
4.4.4.1	Composition.....	87
4.4.4.2	Chemical states	89
4.4.5	Surface roughness.....	92
4.5	Spectroscopic properties	94
4.5.1	Experimental set-ups.....	95
4.5.1.1	Spectrophotometer	95
4.5.1.2	Spectrofluorometer	95
4.5.1.3	Luminescence in waveguiding configuration	95
4.5.1.4	Luminescence in reflection configuration	96
4.5.2	Absorption	98
4.5.2.1	Absorption spectra	98
4.5.2.2	Absorption cross section.....	104
4.5.2.3	An attempt to estimate the absorption cross section of SnO ₂	107
4.5.2.4	McCumber-Miniscalco-Quimby estimated emission cross section	108
4.5.2.5	Internal gain coefficient.....	114
4.5.2.6	Judd-Ofelt analysis	117
4.5.3	Emission	133
4.5.3.1	The planar waveguides	133

4.5.3.2	The monoliths	139
4.5.4	Excitation.....	140
4.5.4.1	The planar waveguides	140
4.5.4.2	The monoliths	143
4.5.5	Time-resolved emission.....	145
4.5.5.1	The planar waveguides	145
4.5.5.2	The monoliths	152
4.5.5.3	A possible scheme for Er^{3+} luminescence sensitization at 1.5 μm	158
4.6	Optical waveguiding characterization.....	160
4.6.1	Refractive index and thickness measurement.....	160
4.6.1.1	M-line spectroscopy.....	160
4.6.1.2	Results of refractive index and thickness	161
4.6.2	Dispersion curves.....	164
4.6.3	Lorentz-Lorenz	164
4.6.3.1	Index profile and confinement.....	166
4.6.4	Propagation losses	168
4.7	Conclusions	171
	References	174
Chapter 5	Numerical calculation on $\text{SnO}_2\text{:Er}^{3+}$	183
5.1	Introduction	183
5.2	Fundamentals	183
5.2.1	Brief overview of location of rare-earth in SnO_2 studies	183
5.2.2	Crystalline structure of pure SnO_2	184
5.2.2.1	Rutile-like structure of SnO_2	184
5.2.2.2	The C_{2h} and D_{2h} symmetry groups.....	185
5.3	Comparison between EXAFS data and a model including C_{2h} symmetry site for RE ions	186
5.4	DFT simulated band-structure and density of states of $\text{SnO}_2\text{:Er}^{3+}$	189
5.4.1	Methodology.....	189

5.4.2	Un-relaxed structure	190
5.4.3	Relaxed structure	192
5.5	Conclusions	195
	References	196
Chapter 6 Photorefractivity investigation		200
6.1	Introduction	200
6.2	Background	200
6.2.1	Refractive index	200
6.2.2	Photorefractivity	201
6.2.3	Short review of photorefractivity of tin dioxide -silica glasses and glass-ceramics	202
6.2.3.1	Photorefractivity of tin-doped silica glasses	202
6.2.3.2	Photorefractivity of tin dioxide-silica glass ceramics 203	
6.3	Photorefractivity measurement.....	204
6.3.1	Experimental setup and characterization techniques .	204
6.3.1.1	Setup schematic	204
6.3.1.2	Characterization techniques.....	206
6.3.2	Results and discussion	207
6.3.2.1	Measured effective index of the planar waveguides 207	
6.3.2.1.1	70SiO ₂ -30SnO ₂ :0.3Er ³⁺ planar waveguide	207
6.3.2.1.2	80SiO ₂ -20SnO ₂ :0.3Er ³⁺ planar waveguide	210
6.3.2.2	Calculated refractive index of the planar waveguides	213
6.3.2.2.1	Method	213
6.3.2.2.2	Results	214
6.3.2.3	Characterization of the irradiated samples.....	215
6.3.2.3.1	AFM	215
6.3.2.3.2	XRD	216
6.3.2.3.3	Absorption.....	218

6.3.2.3.4	Mirco-Raman	220
6.3.2.4	Discussion on photorefractive effect	221
6.4	Inscription of gratings	223
6.5	Conclusions.....	225
	References	226
Chapter 7	Device designs	228
7.1	Introduction.....	228
7.2	Solid state laser design	228
7.2.1	Solid state laser design with a lateral pumping scheme 228	
7.2.2	Estimation of lasing pump power threshold	229
7.2.2.1	Fundamentals.....	229
7.2.2.1.1	General rate equation	230
7.2.2.1.2	Rate equations for a 3-level laser	231
7.2.2.2	Results	234
7.3	Integrated waveguide laser design	235
7.3.1	Brief introduction to Transfer Matrix Formalism.....	235
7.3.2	Used parameters.....	236
7.3.3	Distributed Feedback structures	236
7.3.4	Threshold conditions: numerical calculations	238
7.4	Conclusions.....	239
	References	240
Chapter 8	Optical waveguides fabricated by laser micromachining .	241
8.1	Introduction.....	241
8.2	Advantages of femtosecond laser micromachining.....	241
8.3	Experiments.....	242
8.3.1	Experimental setup and methodology.....	242
8.3.2	Results of femtosecond laser written structures	243
8.3.3	Characterization of femtosecond laser written optical waveguides.....	249
8.3.3.1	Optical waveguiding testing	249

8.3.3.2 Raman spectroscopy of femtosecond laser written optical waveguides	252
8.4 Conclusions	255
References	255
Chapter 9 Conclusions and perspectives	258
Research outcomes	262

List of figures

Figure 3.1 Phase transformation diagram of sol-gel derived monoliths during the synthesis process	34
Figure 3.2 The flow-chart of the solution synthesis used for $(100-x)\text{SiO}_2\text{-}x\text{SnO}_2\text{:Er}^{3+}$ monoliths	35
Figure 3.3 Photos of the final solution of $90\text{SiO}_2\text{-}10\text{SnO}_2\text{:}0.5\text{Er}^{3+}$ monolith synthesis: a) transparent solution under white light and b) Tyndall effect from the colloidal solution	37
Figure 3.4 Photos of fast gelation of the solutions of $(100-x)\text{SiO}_2\text{-}x\text{SnO}_2\text{:}0.5\text{Er}^{3+}$ monolithic samples ($x = 5$ and 10 mol%)	38
Figure 3.5 Photo of $90\text{SiO}_2\text{-}10\text{SnO}_2\text{:}0.5\text{Er}^{3+}$ sols in the sealed molds (monolithic square and cylinder)	38
Figure 3.6 The flow-chart of two different processes of aging and drying the $90\text{SiO}_2\text{-}10\text{SnO}_2\text{:}0.5\text{Er}^{3+}$ gels	39
Figure 3.7 Photos of the as-prepared $(100-x)\text{SiO}_2\text{-}x\text{SnO}_2\text{:}0.5\text{Er}^{3+}$ monolithic square and cylinder xerogels obtained after two aging and drying processes ($x = 5$ and 10 mol%)	40
Figure 3.8 Photos of the as-prepared $90\text{SiO}_2\text{-}10\text{SnO}_2\text{:}0.5\text{Er}^{3+}$ monolithic squares obtained from two aging and drying processes after the heat-treatment trial at 900°C for 10h	41
Figure 3.9 TG-DTA measurements of $95\text{SiO}_2\text{-}5\text{SnO}_2$ monoliths: acquired under the heating rate of $2^\circ\text{C}/\text{min}$	41
Figure 3.10 DSC curves of $(100-x)\text{SiO}_2\text{-}x\text{SnO}_2\text{:}0.5\text{Er}^{3+}$ monoliths with different SnO_2 contents ($x = 5$ and 10 mol%)	42
Figure 3.11 Chart of the heat-treatment process for $(100-x)\text{SiO}_2\text{-}x\text{SnO}_2\text{:}0.5\text{Er}^{3+}$ monoliths ($x = 0, 5$ and 10 mol%)	44
Figure 3.12 Absorption spectra of the $90\text{SiO}_2\text{-}\text{SnO}_2\text{:}0.5\text{Er}^{3+}$ monoliths after different steps of heat-treatment: from dried gel, to thermal treatment at 900°C for 40 h , 67 h and 100 h	44
Figure 3.13 Photos of $90\text{SiO}_2\text{-}10\text{SnO}_2\text{:}0.5\text{Er}^{3+}$ monolithic square ($1\times 1\text{ cm}^2$ cross section and 0.3 cm height) and cylinder (0.5 cm diameter and 1.5 cm height) obtained after heat-treatment at 900°C for 100h	45
Figure 3.14 Photos of $95\text{SiO}_2\text{-}5\text{SnO}_2\text{:}0.5\text{Er}^{3+}$ big pillar with diameter of 1 cm and length of 3.3 cm obtained after heat-treatment at 900°C for 100h	45
Figure 3.15 XRD patterns of $95\text{SiO}_2\text{-}5\text{SnO}_2\text{:}0.5\text{Er}^{3+}$ monoliths obtained after heat-treatment at 900°C for 100h in comparison with SnO_2 rutile crystal phase from cassiterite mineral (JCPDS 41-1445)	46
Figure 3.16 Schematic diagram of the preparation of the $(100-x)\text{SiO}_2\text{-}x\text{SnO}_2\text{:} \% \text{Er}^{3+}$ planar waveguides	48
Figure 3.17 The photo of the withdrawing step of the dip-coating process for a planar waveguide deposition on silicon substrate. One can see the	

entraining of the solution on the substrate and the draining of the excess liquid to form the thin layer in the image on the right side.....	49
Figure 3.18 Thicknesses measured by m-line technique of the planar waveguides deposited at different withdraw speeds after heat-treatment at 1000 °C for 60 mins.....	50
Figure 3.19 Index profiles ($\lambda = 543.5$ nm) of the planar waveguides deposited at different withdraw speeds after heat-treatment at 1000 °C for 60 mins.....	51
Figure 3.20 3D AFM images and the root mean square roughness of the 70SiO ₂ -30SnO ₂ :0.5Er ³⁺ planar waveguides deposited by different withdraw speeds (4.0, 5.6, 7.2 and 8.8 cm/min) after heat-treatment at 1000 °C for 60 mins.....	52
Figure 3.21 The photo of the tubular oven dedicated for the heat-treatment of the planar waveguides	53
Figure 3.22 Visible micro-Raman spectra ($\lambda_{\text{ex}} = 633\text{nm}$) of the 70SiO ₂ -30SnO ₂ :0.5Er ³⁺ planar waveguides after different heat-treatment temperatures (900, 1000 and 1100 °C) for 60 mins. The inset image is the microscope image of the planar waveguide annealed at 1100 °C for 60 mins with a micro-phase separation which reduced the optical quality of the glass-ceramics.....	54
Figure 3.23 XRD patterns of the 70SiO ₂ -30SnO ₂ :0.5Er ³⁺ planar waveguides heat-treated at 1000 °C for 60 mins and 120 mins in comparison with SnO ₂ rutile crystal phase from cassiterite mineral (JCPDS 41-1445).....	55
Figure 3.24 Index profiles ($\lambda = 543.5$ nm) of the 70SiO ₂ -30SnO ₂ :0.5Er ³⁺ planar waveguides heat-treated at 1000 °C for 60 mins and 120 mins.....	55
Figure 3.25 The example of the transparent 70SiO ₂ -30SnO ₂ :0.5Er ³⁺ planar waveguide obtained after the heat-treatment at 1000 °C for 60 mins	56
Figure 3.26 Transmission spectra of the compositional (100-x)SiO ₂ -SnO ₂ :0.5Er ³⁺ planar waveguides (x = 5, 10, 15, 20, 25 and 30 mol%) in comparison with v-SiO ₂ substrate.....	56
Figure 4.1 Visible micro-Raman ($\lambda_{\text{ex}} = 632$ nm) spectra of the (100-x)SiO ₂ -xSnO ₂ :0.5Er ³⁺ planar waveguides (x = 5, 10, 15, 20, 25 and 30 mol%) in comparison with pure SnO ₂ and SiO ₂	70
Figure 4.2 Visible micro-Raman ($\lambda_{\text{ex}} = 632$ nm) spectra of the 70SiO ₂ -30SnO ₂ :0.5Er ³⁺ planar waveguide	72
Figure 4.3 Visible micro-Raman ($\lambda_{\text{ex}} = 632$ nm) spectra of the (100-x)SiO ₂ -xSnO ₂ :0.5Er ³⁺ monoliths (x = 5 and 10 mol%) in comparison with pure SnO ₂ and SiO ₂	74
Figure 4.4 UV macro-Raman ($\lambda_{\text{ex}} = 266$ nm) spectra of the 70SiO ₂ -30SnO ₂ :0.5Er ³⁺ planar waveguide and 90SiO ₂ -10SnO ₂ :0.5Er ³⁺ monolith in comparison with pure SnO ₂	75

Figure 4.5 XRD patterns of the $(100-x)\text{SiO}_2\text{-}x\text{SnO}_2\text{:}0.5\text{Er}^{3+}$ planar waveguides ($x = 5, 10, 15, 20, 25$ and 30 mol%), indexed as SnO_2 Cassiterite (JCPDS 41-1445). Inset shows the XRD patterns in scale of the planar waveguides in range $(10^\circ - 30^\circ)$	77
Figure 4.6 XRD patterns of $(100-x)\text{SiO}_2\text{-}x\text{SnO}_2\text{:}0.5\text{Er}^{3+}$ monoliths ($x = 5$ and 10 mol%), indexed as SnO_2 Cassiterite (JCPDS 41-1445)	78
Figure 4.7 a) TEM image and b) EDXS spectrum of the $70\text{SiO}_2\text{-}30\text{SnO}_2\text{:}0.5\text{Er}^{3+}$ planar waveguide. In the observed grains, the black dots are SnO_2 nanocrystals while the light grey part is SiO_2 matrix	80
Figure 4.8 a) TEM image and b) EDXS spectrum of the $80\text{SiO}_2\text{-}20\text{SnO}_2\text{:}0.5\text{Er}^{3+}$ planar waveguide. In the observed grains, the black dots are SnO_2 nanocrystals while the light grey part is SiO_2 matrix	81
Figure 4.9 HR-STEM images of the cross section of the $(100-x)\text{SiO}_2\text{-}x\text{SnO}_2\text{:}0.3\text{Er}^{3+}$ planar waveguides: a) $x = 10$ mol% and b) $x = 15$ mol%	82
Figure 4.10 High-STEM images and the corresponding EDXS mapping of the Si, Sn and O elements in the $(100-x)\text{SiO}_2\text{-}x\text{SnO}_2\text{:}0.5\text{Er}^{3+}$ planar waveguides: a) $x = 10$ and b) $x = 15$ mol%.	83
Figure 4.11 HR-STEM images of the $(100-x)\text{SiO}_2\text{-}x\text{SnO}_2\text{:}0.3\text{Er}^{3+}$ planar waveguides: a) and c) $x = 10$ mol%; b) and d) $x = 15$ mol%. The red circles are just for visualizing the SnO_2 particles	84
Figure 4.12 a) TEM image, b) EDXS spectrum and c) SAED patterns of the $90\text{SiO}_2\text{-}10\text{SnO}_2\text{:}0.5\text{Er}^{3+}$ monolith. In the TEM image of the observed grains, the black dots are SnO_2 nanocrystals while the light grey part is SiO_2 matrix	85
Figure 4.13 a) TEM image, b) EDXS spectrum and c) SAED patterns of the $95\text{SiO}_2\text{-}5\text{SnO}_2\text{:}0.5\text{Er}^{3+}$ monolith. In the TEM image of the observed grains, the black dots are SnO_2 nanocrystals while the light grey part is SiO_2 matrix	86
Figure 4.14 AES in-depth composition profile vs erosion depth of the top side of the $70\text{SiO}_2\text{-}30\text{SnO}_2\text{:}0.5\text{Er}^{3+}$ planar waveguide	87
Figure 4.15 AES in-depth composition profile vs erosion depth of the top side of the $80\text{SiO}_2\text{-}20\text{SnO}_2\text{:}0.5\text{Er}^{3+}$ planar waveguide	88
Figure 4.16 AES in-depth composition profile vs erosion depth of the top side of the $80\text{SiO}_2\text{-}20\text{SnO}_2\text{:}0.5\text{Er}^{3+}$ planar waveguide	89
Figure 4.17 AES depth profile of tin signal of the first four SnO_x -rich and SiO_y -rich layers on the top side of the $70\text{SiO}_2\text{-}30\text{SnO}_2\text{:}0.5\text{Er}^{3+}$ planar waveguide	90
Figure 4.18 AES spectra acquired at different depth of 268.6, 908.5 nm and at the end of the depth profile of the top side of the $70\text{SiO}_2\text{-}30\text{SnO}_2\text{:}0.5\text{Er}^{3+}$ planar waveguide	90
Figure 4.19 Analysis of LMM line shape of silicon at different depths of the planar waveguide: 23.7 nm (maximum of Sn signal), 55.3 nm (minimum of Sn signal) and 963.8 nm (at the end of the profile)	91

Figure 4.20 Analysis of MNN lineshape of tin at different depths of the planar waveguide: 23.7 nm (maximum of Sn signal), 55.3 nm (minimum of Sn signal) and 963.8 nm (at the end of the profile)	91
Figure 4.21 Analysis of KLL lineshape of oxygen at different depths of the planar waveguide: 23.7 nm (maximum of Sn signal), 55.3 nm (minimum of Sn signal) and 963.8 nm (at the end of the profile)	92
Figure 4.22 AFM images of the surface of the (100-x)SiO ₂ -xSnO ₂ :0.5Er ³⁺ planar waveguides (x = 0, 5, 10, 15, 20, 25 and 30 mol%)	93
Figure 4.23 The setup schematic of luminescence measurement in waveguiding configuration	96
Figure 4.24 The setup schematic of luminescence measurement in reflection configuration	97
Figure 4.25 The original emission spectrum of the Xenon lamp 450W (Edison, NJ, USA)	98
Figure 4.26 Energy-level diagram of SnO ₂ and Er ³⁺ transitions.....	99
Figure 4.27 Room temperature absorption spectra of the (100-x)SiO ₂ -xSnO ₂ :0.5Er ³⁺ monoliths (x = 0, 5 and 10 mol%)	99
Figure 4.28 Room temperature absorption spectra of the 95SiO ₂ -5SnO ₂ :yEr ³⁺ monoliths (x = 0.25, 0.50, 0.75 and 1.00 mol%)	101
Figure 4.29 Room temperature absorption spectra of (of ⁴ I _{15/2} - ⁴ I _{13/2} transition of Er ³⁺ in: a) (100-x)SiO ₂ -xSnO ₂ :0.5Er ³⁺ monoliths containing different SnO ₂ contents (x = 0, 5 and 10 mol%) and b) 95SiO ₂ -5SnO ₂ :yEr ³⁺ monoliths doped with different Er ³⁺ concentrations (y = 0.25, 0.50, 0.75 and 1.00 mol%).....	102
Figure 4.30 Room temperature absorption spectra of (of ⁴ I _{15/2} - ⁴ I _{13/2} transition of Er ³⁺ in: a) (100-x)SiO ₂ -xSnO ₂ :0.5Er ³⁺ monoliths containing different SnO ₂ contents (x = 0, 5 and 10 mol%) and b) 95SiO ₂ -5SnO ₂ :yEr ³⁺ monoliths doped with different Er ³⁺ concentrations (y = 0.25, 0.50, 0.75 and 1.00 mol%).....	105
Figure 4.31 Absorption and calculated emission cross section of Er ³⁺ at 1.5 μm of the monoliths: a) 90SiO ₂ -10SnO ₂ :0.5Er ³⁺ , b) 95SiO ₂ -5SnO ₂ :0.5Er ³⁺ , c) 100SiO ₂ :0.5Er ³⁺ , d) 95SiO ₂ -5SnO ₂ :0.25Er ³⁺ , e) 95SiO ₂ -5SnO ₂ :0.75Er ³⁺ and f) 95SiO ₂ -5SnO ₂ :1.00Er ³⁺	112
Figure 4.32 Calculated internal gain coefficient as a function of the fractional upper-state population N ₂ /N ₀ of the a) 90SiO ₂ -10SnO ₂ :0.5Er ³⁺ , b) 95SiO ₂ -5SnO ₂ :0.5Er ³⁺ , c) 100SiO ₂ :0.5Er ³⁺ , d) 95SiO ₂ -5SnO ₂ :0.25Er ³⁺ , e) 95SiO ₂ -5SnO ₂ :0.75Er ³⁺ and f) 95SiO ₂ -5SnO ₂ :1.00Er ³⁺ . N ₂ /N ₀ =1 is when the full population is achieved and N ₂ /N ₀ =0 when there is no population inversion.....	116
Figure 4.33 Chart illustrating the calculation of Judd-Ofelt parameters, transition probability, radiative lifetime and branching ratios.....	119
Figure 4.34 Emission spectra of the (100-x)SiO ₂ -xSnO ₂ :0.5Er ³⁺ planar waveguides (x = 5, 10, 15, 20, 25 and 30) under indirect excitation λ _{ex} =	

330 nm (using Xenon Lamp source and in reflection configuration) and direct excitation $\lambda_{\text{ex}} = 514.5$ nm (using Ar^+ laser source and in waveguiding configuration).....	134
Figure 4.35 Emission spectra acquired by indirect excitation $\lambda_{\text{ex}} = 330$ nm, using Xenon Lamp in reflection configuration of the $70\text{SiO}_2\text{-}30\text{SnO}_2\text{:yEr}^{3+}$ planar waveguides doped with different y concentration of Er^{3+} (y = 0.5, 1 and 1.5 mol%)	137
Figure 4.36 Emission spectra acquired by indirect excitation $\lambda_{\text{ex}} = 340$ nm, using diode laser and $\lambda_{\text{ex}} = 330$ nm in reflection configuration of the $(100\text{-x})\text{SiO}_2\text{-xSnO}_2\text{:}0.5\text{Er}^{3+}$ planar waveguides (x = 10, 20 and 30) .	138
Figure 4.37 Emission spectra acquired by different indirect excitation $\lambda_{\text{ex}} = 320, 330$ and 350 nm using Xenon Lamp in reflection configuration of the $70\text{SiO}_2\text{-}30\text{SnO}_2\text{:}0.5\text{Er}^{3+}$ planar waveguides	139
Figure 4.38 Emission spectra acquired under indirect excitation $\lambda_{\text{ex}} = 333$ nm, using Edinburgh FLS980 spectrofluorometer of the $(100\text{-x})\text{SiO}_2\text{-xSnO}_2\text{:}0.5\text{Er}^{3+}$ monoliths	140
Figure 4.39 Excitation spectra acquired at emission $\lambda_{\text{em}} = 1530$ nm, using Edinburgh FLS980 spectrofluorometer of the $70\text{SiO}_2\text{-}30\text{SnO}_2\text{:}0.5\text{Er}^{3+}$ planar waveguides	141
Figure 4.40 Excitation spectra of the $(100\text{-x})\text{SiO}_2\text{-xSnO}_2\text{:}0.5\text{Er}^{3+}$ planar waveguides (x = 5, 10, 15, 20, 25 and 30) detected at $\lambda_{\text{em}} = 1535.5$ nm and 1553.5 nm, acquired using Xenon Lamp and in reflection configuration.....	142
Figure 4.41 Excitation spectra of the $70\text{SiO}_2\text{-}30\text{SnO}_2\text{:yEr}^{3+}$ planar waveguides doped with different y concentration of Er^{3+} (y = 0.5, 1 and 1.5 mol%) detected at $\lambda_{\text{em}} = 1535.5$ nm, acquired using Xenon Lamp and in reflection configuration	143
Figure 4.42 Excitation spectra acquired at emission $\lambda_{\text{em}} = 1530$ nm, using Edinburgh FLS980 spectrofluorometer of a) $95\text{SiO}_2\text{-}5\text{SnO}_2\text{:}0.5\text{Er}^{3+}$ monolith and b) $90\text{SiO}_2\text{-}10\text{SnO}_2\text{:}0.5\text{Er}^{3+}$	144
Figure 4.43 Time-resolved luminescence spectra from the $^4\text{I}_{13/2}$ metastable state of Er^{3+} excited indirectly at $\lambda_{\text{ex}} = 306$ nm and excited directly at $\lambda_{\text{ex}} = 522$ nm, acquired using Edinburgh FLS980 spectrofluorometer of the $70\text{SiO}_2\text{-}30\text{SnO}_2\text{:}0.5\text{Er}^{3+}$ planar waveguide. The inset is the rise time curve of the $^4\text{I}_{13/2}$ metastable state of Er^{3+} excited indirectly at $\lambda_{\text{ex}} = 306$ nm.....	146
Figure 4.44 Time-resolved luminescence spectra from the $^4\text{I}_{13/2}$ metastable state of Er^{3+} excited indirectly at $\lambda_{\text{ex}} = 340$ nm, acquired using Thorlabs UV diode laser and in reflection configuration of the $(100\text{-x})\text{SiO}_2\text{-xSnO}_2\text{:}0.5\text{Er}^{3+}$ planar waveguides (x = 5, 10, 15, 20, 25 and 30)	149
Figure 4.45 Time-resolved luminescence spectra from the $^4\text{I}_{13/2}$ metastable state of Er^{3+} excited directly at $\lambda_{\text{ex}} = 514.5$ nm, acquired using	

Ar ⁺ laser source and in waveguiding configuration of the (100-x)SiO ₂ -xSnO ₂ :0.5Er ³⁺ planar waveguides (x = 5, 10, 15, 20, 25 and 30).....	151
Figure 4.46 Time-resolved luminescence spectra from the ⁴ I _{13/2} metastable state of Er ³⁺ excited directly at λ _{ex} = 340 nm, acquired using Xenon lamp source and in reflection configuration of the 70SiO ₂ -30SnO ₂ :yEr ³⁺ planar waveguides doped with different y Er ³⁺ concentration (y = 0.5, 1.0 and 1.5 mol%)	152
Figure 4.47 Time-resolved luminescence spectra from the ⁴ I _{13/2} metastable state of Er ³⁺ excited indirectly at λ _{ex} = 333 nm and excited directly at λ _{ex} = 522 nm, acquired using Edinburg FLS980 spectrofluorometer of the 90SiO ₂ -10SnO ₂ :0.5Er ³⁺ monolith. The inset is the rise time curve of the ⁴ I _{13/2} metastable state of Er ³⁺ excited indirectly at λ _{ex} = 333 nm.....	154
Figure 4.48 Time-resolved luminescence spectra from the ⁴ I _{13/2} metastable state of Er ³⁺ excited indirectly at λ _{ex} = 340 nm, acquired using Thorlabs UV diode laser and in reflection configuration of the (100-x)SiO ₂ -xSnO ₂ :0.5Er ³⁺ monoliths (x = 5 and 10).....	155
Figure 4.49 Time-resolved luminescence spectra from the ⁴ I _{13/2} metastable state of Er ³⁺ excited indirectly at λ _{ex} = 340 nm, acquired using Thorlabs UV diode laser and in reflection configuration of the 95SiO ₂ -5SnO ₂ :yEr ³⁺ monoliths (y = 0.25, 0.50, 0.75 and 1.0).....	157
Figure 4.50 Energy-level diagram of SnO ₂ and Er ³⁺ and a possible Er ³⁺ luminescence sensitization scheme.....	160
Figure 4.51 M-line measurement of the 70SiO ₂ -30SnO ₂ :0.5Er ³⁺ at TE modes of 543.5, 632.8, 1319 and 1542 nm.....	162
Figure 4.52 Sellmeier fitted dispersion curves obtained from the measured refractive indices of the (100-x)SiO ₂ -xSnO ₂ :0.5Er ³⁺ planar waveguides (x = 5, 10, 15, 20, 25 and 30 mol%) and the 100SiO ₂ :0.5Er ³⁺ thin film (x = 0 mol%).	164
Figure 4.53 Lorentz-Lorenz fitting of the refractive indices of the (100-x)SiO ₂ -xSnO ₂ :0.5Er ³⁺ planar waveguides (x = 10, 15, 20, 25 and 30 mol%)	166
Figure 4.54 Index profile of the 70SiO ₂ -30SnO ₂ :0.5Er ³⁺ planar waveguide.....	167
Figure 4.55 Distribution of electric field energy at 1542 nm - TE ₀ mode in the planar waveguide configuration.....	167
Figure 4.56 Propagation losses measurements and the losses fittings using the equation (4.26) of the (100-x)SiO ₂ -xSnO ₂ :0.5Er ³⁺ planar waveguides (x = 5, 10, 15, 20, 25 and 30 mol%)	169
Figure 4.57 The image of the propagation in the red (at 632.5 nm) of the low loss 70SiO ₂ -SnO ₂ :0.5Er ³⁺ planar waveguide. The bright point marked by the blue circle is the indication for the output of the propagating light.....	171

Figure 5.1 Figure of a unit cell of SnO ₂ rutile-like crystalline structure (Sn atoms in grey and O atoms in red), obtained using crysden program [Kokalj 2003].....	185
Figure 5.2 Schematic representation of the C _{2h} and D _{2h} symmetry groups of SnO ₂	185
Figure 5.3 Structure of tin dioxide, viewed along the c axis, obtained by using the VESTA software from JP-minerals [Momma 2011]	186
Figure 5.4 Structure of tin dioxide with interstitial tin, viewed along the c axis, obtained by using the VESTA software from JP-minerals [Momma 2011]	187
Figure 5.5 Figure of the cell of SnO ₂ rutile-like crystalline structure (Sn atoms in grey, O atoms in red and substituting Er ³⁺ in green) used for DFT calculation, obtained using crysden program [Kokalj 2003]. ...	190
Figure 5.6 Band-diagram and Density of States of a single cell calculation of pure SnO ₂ . Energy units are in eV but they are defined up to a constant, so the only relevant quantities are difference in Energies. The line ϵ_f represents the Fermi energy evaluated in this case [Massella 2018].....	191
Figure 5.7 Density of States of a $2 \times 2 \times 2$ cell calculation of a single Er ³⁺ ion doped (~ 6 mol%) shown in Figure 5.5. Energy units are in eV but they are defined up to a constant, so the only relevant quantities are difference in Energies. The line ϵ_f represents the Fermi energy evaluated in this case [Massella 2018].....	192
Figure 5.8 Density of States of a $2 \times 2 \times 2$ relaxed cell calculation of a single Er ³⁺ ion doped (~ 6 mol%) and pure SnO ₂ crystals: a) in a large energy range of band structure; b) only in the band-gap region. Energy units are in eV but they are defined up to a ϵ_f^d is the fermi energy in the doped case and ϵ_f^p is the fermi energy in the pure crystal[Massella 2018].....	193
Figure 5.9 Partial and total DOS adopted from the work [Errico 2007]. The main contribution in the band-gap region is due to O. This explains why the calculation considering only the substitution of Er ³⁺ for Sn ⁴⁺ show a small modification of SnO ₂ band structure.....	194
Figure 6.1 The experimental setup of the UV irradiation for the photorefractivity measurements	204
Figure 6.2 The photos of the masked planar waveguide and the target section for the UV irradiation.....	205
Figure 6.3 The photos of the masked planar waveguide and the target section for the UV irradiation	206
Figure 6.4 The effective index changes for the TE ₀ modes supported by the 70SiO ₂ -30SnO ₂ :0.5Er ³⁺ planar waveguide at the wavelength of 1550 nm as a function of cumulative dose	208

Figure 6.5 The shift to lower values of TE ₀ mode at the wavelength of 1550 nm of the 70SiO ₂ -30SnO ₂ :0.5Er ³⁺ before UV irradiation and after 1 st UV irradiation with cumulative dose of 0.003 kJ/cm ² and after 10 th UV irradiation with cumulative dose of 0.3 kJ/cm ²	208
Figure 6.6 The shift to lower values of the 635 nm TE modes of the 70SiO ₂ -30SnO ₂ :0.5Er ³⁺ planar waveguide before UV irradiation and after 1 st UV irradiation with cumulative dose of 0.003 kJ/cm ² and after 14 th UV irradiation with cumulative dose of 9.0 kJ/cm ²	209
Figure 6.7 The effective index changes for the TE ₀ mode supported by the 80SiO ₂ -20SnO ₂ :0.5Er ³⁺ planar waveguide at the wavelength of 1550 nm as a function of cumulative dose	211
Figure 6.8 The shift to lower values of TE ₀ mode at the wavelength of 1550 nm of the 80SiO ₂ -20SnO ₂ :0.5Er ³⁺ before UV irradiation and after 1 st UV irradiation with cumulative dose of 0.003 kJ/cm ² and after 10 th UV irradiation with cumulative dose of 0.3 kJ/cm ²	211
Figure 6.9 The shift to lower values of the 635 nm TE modes of the 80SiO ₂ -20SnO ₂ :0.5Er ³⁺ planar waveguide before UV irradiation and after 1 st UV irradiation with cumulative dose of 0.003 kJ/cm ² , and after 14 th UV irradiation with cumulative dose of 9.0 kJ/cm ²	212
Figure 6.10 Graphic solution for defining the refractive index of the 70SiO ₂ -30SnO ₂ :0.5Er ³⁺ planar waveguide before and after the final UV irradiation using (6.3)	214
Figure 6.11 3D AFM images of the surface of the 70SiO ₂ -30SnO ₂ :0.5Er ³⁺ planar waveguide before and after UV irradiation ..	216
Figure 6.12 XRD patterns of the 70SiO ₂ -30SnO ₂ :0.5Er ³⁺ planar waveguide before and after UV irradiation, indexed as SnO ₂ Cassiterite (JCPDS 41-1445)	217
Figure 6.13 XRD patterns of the 95SiO ₂ -5SnO ₂ :0.5Er ³⁺ monolith in the front side and back side, indexed as SnO ₂ Cassiterite (JCPDS 41-1445). Front face is the face where the laser beam incidents	218
Figure 6.14 Absorption spectra of the 70SiO ₂ -30SnO ₂ :0.5Er ³⁺ planar waveguide before and after UV irradiation	219
Figure 6.15 Absorption spectra of the 95SiO ₂ -5SnO ₂ :0.5Er ³⁺ monolith before and after UV irradiation	220
Figure 6.16 Raman spectra of the 95SiO ₂ -5SnO ₂ :0.5Er ³⁺ monolith before and after UV irradiation with cumulative dose of 3.264 kJ/cm ²	221
Figure 6.17: The image of the gratings fabricated by CW frequency doubled argon laser: $\lambda = 244$ nm	224
Figure 7.1 A sketch for illustrating the design of a solid state laser with a lateral pumping scheme applied on the obtained 90SiO ₂ -10SnO ₂ :0.5Er ³⁺ cylinders	229

Figure 7.2 Photo of the obtained 90SiO ₂ -10SnO ₂ :0.5Er ³⁺ cylinder used for the laser design: awith the diameter: $r = 0.5$ cm and length of $L = 1.5$ cm	229
Figure 7.3 Demonstration of the three processes with the transition example between the metastable state $^4I_{13/2}$ and $^4I_{15/2}$ of Er ³⁺ [A.E. Siegman 1986].....	230
Figure 7.4 3-level energy diagram applied for SiO ₂ -SnO ₂ :Er ³⁺	231
Figure 7.5 The sketch of a round trip lasing operating of the cavity at the threshold condition	232
Figure 7.6 Basic idea of the transfer matrix formalism [Boucher 2006], the fields on one side of the media are related to the ones on the other side by the matrix	235
Figure 7.7 Two different topologies associated to active zones and inscribed index grating: active Distributed Feedback Structure (DFB) and Quarter-Wave phase Shift DFB (QWS-DFB). The second structure is characterized by a defect layer in the center [Boucher 2019].	237
Figure 7.8 Transmission spectra in the propagation direction of a DFB structure in the pump-off condition. The spectra is obtained with different length of the structure and thus different number of periods. The photorefractivity of 20%SnO ₂ – 80%SiO ₂ planar waveguide was used: $\Delta n_{\text{eff}} = 1.1 \times 10^{-3}$ [Massella 2018].	237
Figure 7.9 Transmission spectra in the propagation direction of a QWS-DFB structure in the pump-off condition. The spectra are obtained with different length of the structure and thus different number of periods. The photorefractivity of 20%SnO ₂ – 80%SiO ₂ planar waveguide was used: $\Delta n_{\text{eff}} = 1.1 \times 10^{-3}$. It is highlighted that the central peak thanks to the defect layer located in the middle of the structure, becomes more pronounced when the length of the structure increases [Massella 2018].	238
Figure 7.10 Behaviour of the $\alpha_{th}L$ vs L for different length of the structure (blue dots). α_{th} is obtained by the solution of boundary condition for each QWF-DFB length. The orange line represents the maximum achievable gain of the 80SiO ₂ -20SnO ₂ :0.5Er ³⁺ planar waveguide [Massella 2018].	239
Figure 8.1 Photo of the polished 90SiO ₂ -10SnO ₂ :0.5Er ³⁺ monolithic square chosen for the fabrication of waveguides (1×1 cm ²).....	243
Figure 8.2 Transmission optical microscope images of the top view and side view of the continuous tracks fabricated by Femtosecond laser as a function of the laser powers of 250, 200 and 150 mW with different scanning speeds (1, 5 and 10 mm/s)	245
Figure 8.3 Transmission optical microscope images of the top view and side view of the continuous tracks fabricated by Femtosecond laser as function of the laser powers of 100 and 50 mW with different scanning speeds (1, 5 and 10 mm/s)	246

Figure 8.4 Transmission optical microscope images of the side view of the continuous tracks fabricated by Femtosecond laser as function of the laser powers of 250, 225, 200, 175, 150, 125, 100, 75 and 50 mW with different scanning speeds (1, 5, 10 and 25 mm/s)	248
Figure 8.5 Transmission optical microscope image of the optical waveguiding structure fabricated with the laser power and writing speed: a) $P = 50$ mW and $v = 1$ mm/s and b) $P = 100$ mW and $v = 10$ mm/s, and the corresponding near field intensity mode-profiles at 635 nm, revealing that the light was guided in the surrounding regions outside the modified zone	250
Figure 8.6 Transmission optical microscope image of the optical waveguiding structure fabricated with the laser power and writing speed: a) $P = 125$ mW and $v = 5$ mm/s and b) $P = 150$ mW and $v = 25$ mm/s, and the corresponding near field intensity mode-profiles at 635 nm, revealing that the light was guided in the surrounding regions outside the modified zone	251
Figure 8.7 Transmission optical microscope images of a) the whole optical waveguiding structure (fabrication conditions: $P = 50$ mW and $v = 1$ mm/s) and b) the characterized region where the Raman spectra were acquired across the modified zone indicated by red line. The blue dots (step = $0.5\ \mu\text{m}$) are the focused areas where the Raman spectra were performed.....	252
Figure 8.8 The representative Raman spectrum obtained for all the focused areas across the modified zones of the fabricated optical waveguide	253
Figure 8.9 a) and b) Transmission optical microscope images of the optical waveguiding structure (fabrication conditions: $P = 50$ mW and $v = 1$ mm/s) and the characterized region respectively; c) the graph of D_2/ω_3 peak intensity ratios along the characterized points indicated by blue dots in the image from Figure 8.7b).....	254

List of tables

Table 2.1 Brief summary of the prior related studies on $\text{SiO}_2\text{-SnO}_2$ glass-ceramics activated by Er^{3+} in monolithic forms	19
Table 2.2 Brief summary of the prior related studies on $\text{SiO}_2\text{-SnO}_2$ glass-ceramics activated by Er^{3+} in planar forms.....	20
Table 3.1 The differences of $90\text{SiO}_2\text{-}10\text{SnO}_2\text{:}0.5\text{Er}^{3+}$ monolithic dried gels prepared by using $\text{SnCl}_2\cdot 2\text{H}_2\text{O}$ and DBTDA in the same synthesis recipe	30
Table 3.2 The effect of $\text{H}_2\text{O}/\text{TEOS}$ molar ratio (R) on the structural network of the resulting gels	32
Table 3.3 The chemicals used for the synthesis of the monoliths and waveguides	33
Table 3.4 Four $\text{H}_2\text{O}/\text{TEOS}$ molar ratio (R) tested for the solution synthesis of 10 mol% SnO_2 monoliths	35
Table 3.5 The final synthesis recipe of $(100\text{-}x)\text{SiO}_2\text{-}x\text{SnO}_2\text{:}\text{Er}^{3+}$ monoliths	36
Table 3.6 The synthesis recipe of $(100\text{-}x)\text{SiO}_2\text{-}x\text{SnO}_2\text{:}y\text{Er}^{3+}$ planar waveguides	47
Table 3.7 The parameters of dipping processes of $70\text{SiO}_2\text{-}30\text{SnO}_2\text{:}0.5\text{Er}^{3+}$ planar waveguides	50
Table 4.1 The calculated average size using Scherrer formula of SnO_2 nanocrystals in $(100\text{-}x)\text{SiO}_2\text{-}x\text{SnO}_2\text{:}0.5\text{Er}^{3+}$ monolith ($x = 5$ and 10 mol%)	78
Table 4.2 The average roughness (Ra) and root mean square roughness (RMS) of the $(100\text{-}x)\text{SiO}_2\text{-}x\text{SnO}_2\text{:}0.5\text{Er}^{3+}$ planar waveguides ($x = 0, 5, 10, 15, 20, 25$ and 30 mol%).....	94
Table 4.3 Table of the absorption bands and the absorption coefficient corresponding to the transitions of Er^{3+} from the ground state $^4\text{I}_{15/2}$ to an excited state of $(100\text{-}x)\text{SiO}_2\text{-}x\text{SnO}_2\text{:}0.5\text{Er}^{3+}$ monoliths containing different SnO_2 contents ($x = 0, 5$ and 10 mol%) and $95\text{SiO}_2\text{-}5\text{SnO}_2\text{:}y\text{Er}^{3+}$ monoliths doped with different Er^{3+} concentrations ($y = 0.25, 0.50, 0.75$ and 1.00 mol%). Notes: GC means glass-ceramics ($x = 5$ and 10 mol%) and G means glass ($x = 0$).	103
Table 4.4 Absorption cross section of the Er^{3+} transitions of from the ground state $^4\text{I}_{15/2}$ to an excited state in $(100\text{-}x)\text{SiO}_2\text{-}x\text{SnO}_2\text{:}0.5\text{Er}^{3+}$ monoliths containing different SnO_2 contents ($x = 0, 5$ and 10 mol%) and $95\text{SiO}_2\text{-}5\text{SnO}_2\text{:}y\text{Er}^{3+}$ monoliths doped with different Er^{3+} concentrations ($y = 0.25, 0.50, 0.75$ and 1.00 mol%). Notes: GC means glass-ceramics ($x = 5$ and 10 mol%) and G means glass ($x = 0$).	106
Table 4.5 Calculated absorption cross section of RE-induced oxygen vacancy in SnO_2 of the 10 and 5 mol% glass-ceramic monoliths	108

Table 4.6 Values σ_a , σ_e and $\Delta\lambda$ of $^4I_{15/2}$ - $^4I_{13/2}$ transition of Er^{3+} in (100-x)SiO ₂ -xSnO ₂ :0.5Er ³⁺ monoliths containing different SnO ₂ contents (x = 0, 5 and 10 mol%) and 95SiO ₂ -5SnO ₂ :yEr ³⁺ monoliths doped with different Er ³⁺ concentrations (y = 0.25, 0.50, 0.75 and 1.00 mol%) in comparison with other host materials in the literature.....	113
Table 4.7 The parameters used to calculate the oscillator strengths in equations (4.12) and (4.10).....	121
Table 4.8 Results of the oscillator strengths of Er ³⁺ transitions from the ground state $^4I_{15/2}$ to an excited state in the compositional (100-x)SiO ₂ -xSnO ₂ :yEr ³⁺ monoliths (x = 0, 5 and 10 mol% and y = 0.25, 0.50, 0.75 and 1.00 mol%). Notes: GC means glass-ceramics (x = 5 and 10 mol%) and G means glass (x = 0).....	122
Table 4.9 The calculated Judd-Ofelt parameters (Ω_2 , Ω_4 , Ω_6) and transition probability from $^4I_{13/2}$ to $^4I_{15/2}$ and lifetime of the metastable state $^4I_{13/2}$	123
Table 4.10 Values of transition probability, branching ratios and radiative lifetimes of Er ³⁺ transitions in 90SiO ₂ -10SnO ₂ :0.5Er ³⁺ glass ceramics obtained using Judd-Ofelt methods.	125
Table 4.11 Table of decay time and rise time of the time-resolved luminescence from the $^4I_{13/2}$ metastable state of Er ³⁺ excited indirectly at λ_{ex} = 306 nm and directly at λ_{ex} = 522 nm, acquired using Edinburgh FLS980 spectrofluorometer of the 70SiO ₂ -30SnO ₂ :0.5Er ³⁺ planar waveguides	147
Table 4.12 Table of the obtained values of A ₁ , τ_1 , A ₂ , τ_1 , and the ratio of $\rho = N_1N_1 + N_2 = A_1\tau_1A_1\tau_1 + A_2\tau_2$ of the decay function of the luminescence from the $^4I_{13/2}$ metastable state of Er ³⁺ under direct excitation at λ_{ex} = 522 nm of the 70SiO ₂ -30SnO ₂ :0.5Er ³⁺ planar waveguide.....	148
Table 4.13 Table of decay time of the luminescence from the $^4I_{13/2}$ metastable state of Er ³⁺ excited indirectly at λ_{ex} = 340 nm, acquired using Xenon Lamp and in reflection configuration of the (100-x)SiO ₂ -xSnO ₂ :0.5Er ³⁺ planar waveguides (x = 5, 10, 15, 20, 25 and 30).....	150
Table 4.14 Table of decay time of the luminescence from the $^4I_{13/2}$ metastable state of Er ³⁺ excited directly at λ_{ex} = 514.5 nm, using Ar ⁺ laser source and in waveguiding configuration of the (100-x)SiO ₂ -xSnO ₂ :0.5Er ³⁺ planar waveguides (x = 5, 10, 15, 20, 25 and 30).....	151
Table 4.15 Table of decay time of the luminescence from the $^4I_{13/2}$ metastable state of Er ³⁺ excited indirectly at λ_{ex} = 340 nm, acquired using diode laser and in reflection configuration of the 70SiO ₂ -30SnO ₂ :yEr ³⁺ planar waveguides (y = 0.5, 1.0 and 1.5 mol%)	152
Table 4.16 Table of decay time and rise time of the 1.5 μ m luminescence from the $^4I_{13/2}$ metastable state of Er ³⁺ excited indirectly at λ_{ex} = 306 nm and directly at λ_{ex} = 522 nm, acquired using Edinburgh FLS980 spectrofluorometer of the 90SiO ₂ -10SnO ₂ :0.5Er ³⁺ monolith and the	

corresponding quantum efficiencies of the $^4I_{13/2}$ metastable state of Er^{3+} under two excitation schemes.....	154
Table 4.17 Table of decay time of the luminescence from the $^4I_{13/2}$ metastable state of Er^{3+} excited indirectly at $\lambda_{ex} = 340$ nm, acquired using diode laser and in reflection configuration of the $(100-x)SiO_2-xSnO_2:0.5Er^{3+}$ planar waveguides ($x = 5$ and 10) and their corresponding quantum efficiencies of the $^4I_{13/2}$ metastable state of Er^{3+}	156
Table 4.18 Table of decay time of the luminescence from the $^4I_{13/2}$ metastable state of Er^{3+} excited indirectly at $\lambda_{ex} = 340$ nm, acquired using Xenon Lamp and in reflection configuration of the $95SiO_2-5SnO_2:yEr^{3+}$ planar waveguides ($y = 0.5, 1.0$ and 1.5 mol%) and their corresponding quantum efficiencies of the $^4I_{13/2}$ metastable state of Er^{3+}	157
Table 4.19 Table of the measured refractive index and average thickness of the $(100-x)SiO_2-xSnO_2:0.5Er^{3+}$ planar waveguides ($x = 10, 15, 20, 25$ and 30 mol%).....	163
Table 4.20 Table of measured propagation losses of the $(100-x)SiO_2-xSnO_2:0.5Er^{3+}$ planar waveguides ($x = 5, 10, 15, 20, 25$ and 30 mol%) at TE_0 modes at $632.8, 1319$ and 1542 nm.....	171
Table 5.1 Character table of the C_{2h} group	185
Table 5.2 Character table of the D_{2h} group.....	186
Table 5.3 The distance of the 1 st shell and the 2 nd shell of the SnO_2 structure at the two sites	188
Table 6.1 The overall effective index change of the $70SiO_2-30SnO_2:0.5Er^{3+}$ planar waveguide after UV irradiation (cumulative dose of 9 kJ/cm ²).....	210
Table 6.2 The overall effective index change of the $80SiO_2-20SnO_2:0.5Er^{3+}$ planar waveguide after UV irradiation (cumulative dose of 17 kJ/cm ²).....	213
Table 6.3 The calculated refractive indices at the wavelengths of 635 and 1550 nm of the $70SiO_2-30SnO_2:0.5Er^{3+}$ and $80SiO_2-20SnO_2:0.5Er^{3+}$ planar waveguides before and after UV irradiation (cumulative dose of 9 kJ/cm ²) and the corresponding refractive index changes.....	215
Table 6.4 The roughness of the $70SiO_2-30SnO_2:0.5Er^{3+}$ planar waveguide before and after UV irradiation	216
Table 6.5 The calculated average size using Scherrer formula of SnO_2 nanocrystals in the front face and back face of the irradiated monolith	218
Table 7.1 The used parameters for the calculation of the threshold pump power for the laser constructed on the $90SiO_2-10SnO_2:0.5Er^{3+}$ cylinders were estimated.....	234
Table 8.1 Writing parameters used for the fabrication of continuous tracks in group A	244
Table 8.2 Writing parameters used for the fabrication of continuous tracks in group B.....	247

List of acronyms

Acronym	Meaning
$\text{SiO}_2\text{-SnO}_2$	Glass-ceramic consisting of tin dioxide (SnO_2) and silica (SiO_2)
$\text{SiO}_2\text{-SnO}_2\text{:Er}^{3+}$	Glass-ceramic consisting of SnO_2 and SiO_2 and activated by Er^{3+}
$(100-x)\text{SiO}_2\text{-xSnO}_2\text{:yEr}^{3+}$	<p>Glass-ceramic consisting of x mol% of SnO_2 and (100-x) mol% of SiO_2 and activated by y mol% of Er^{3+}</p> <p>with $y_{\text{Er}^{3+}} = \frac{n_{\text{Er}^{3+}}}{n_{\text{SnO}_2} + n_{\text{SiO}_2}}$</p> <p>($n_{\text{Er}^{3+}}$, n_{SnO_2} and n_{SiO_2} are molar concentration of Er^{3+}, SnO_2 and SiO_2 respectively)</p>
RE	Rare earth
GC	Glass-ceramic
G	Glass

Chapter 1 Introduction

1.1 State of the art

In the current Age of Light, Photonics is a key enabling technology [Photonics21 2018] for different segments: life science and health, industrial manufacturing and quality, information and communication, emerging light, electronics and displays. And, for the development of optical devices, i.e. the heart elements of photonic applications, glass-based rare-earth-activated optical structures play an essential role. Among different glass-based systems, a strategic place is assigned to transparent glass-ceramics, nanocomposite materials, which offer specific characteristics of capital importance in photonics. Following this strategy, this PhD thesis exploits tin dioxide (SnO_2)-silica glass-ceramic activated by erbium ions (Er^{3+}) to put the basis for the fabrication of solid state and integrated lasers. Based on an application-oriented approach, two forms of $\text{SiO}_2\text{-SnO}_2\text{:Er}^{3+}$ glass-ceramics were chosen to be investigated in this work: monolith for the solid state laser application and planar waveguide for the integrated waveguide laser application. Moreover, the well-known requirements in terms of losses and homogeneity, two crucial points are decisive in the development of an optically pumped rare-earth-based laser: (i) the low absorption cross section of the rare-earth ions; (ii) the writing of channels and mirrors in the case of waveguide integrated laser. The research discussed in my PhD thesis gives a possible solution to these points thanks to the demonstration of two innovative and unique characteristics of SnO_2 -based transparent glass-ceramics, i.e. luminescence sensitizing and photosensitivity. The role of SnO_2 nanocrystals as rare-earth ion luminescence sensitizers allows to overcome the low absorption cross section of the Er^{3+} ion. The photorefractivity of SnO_2 allows applying the robust direct laser photoinscription technique on the systems to fabricate Bragg gratings and channel waveguides for waveguide integrated laser. Last but not least, the developed transparent glass-ceramics prevent luminescence quenching effect due to rare-earth clustering, effectively optimizing the photoluminescence quantum yield of the system. This effect, together with the Er^{3+} luminescence sensitizers of SnO_2 nanocrystals are beneficial for obtaining miniaturized and efficient integrated photonic devices. Moreover, Er^{3+}

is employed as the rare-earth activator of $\text{SiO}_2\text{-SnO}_2$ glass-ceramics for the desired lasing operating wavelength at $1.5\ \mu\text{m}$ which finds huge practical engineering applications in structural sensing and monitoring in civil engineering, aerospace, marine, smart structures, communication, health diagnosis [Méndez 2007][Rodriguez-Cobo 2018]. For instance, in case of civil infrastructural sensing and monitoring, [Majumder 2008] [Rao 1999] the $\text{SiO}_2\text{-SnO}_2\text{:Er}^{3+}$ solid state laser can be employed as a generation source of the signal and the integrated waveguide laser can find its role in the signal amplifier for being embedded in the structures. The Er^{3+} luminescence sensitizing role of SnO_2 can help improving both the miniaturization and efficiency. Moreover, the engagement of the photorefractivity [Dong 1995][Brambilla 2000] and luminescence sensitizing at a time in $\text{SiO}_2\text{-SnO}_2\text{:0.5Er}^{3+}$ glass-ceramic fibers can offer better performance in comparison with the currently used Fiber Bragg gratings made from Ge-doped silica optical fibers [Majumder 2008].

1.2 Research challenges and objectives

In general, the potentials of tin-silicate glasses in terms of photorefractivity was first realized in tin-codoped germanosilicate [Dong 1995b] and phosphosilicate [Dong 1995a], [Laurence 1997] optical fibers. Some of the first studies of the photorefractivity were the works on single tin-doped silicate fibers [Brambilla et al. 2000], [Brambilla 2002]. The results showed a comparable photorefractivity in with less consumed SnO_2 based glass compared to GeO_2 based glasses, a well-known strong photorefractive class of material used for Fiber Bragg gratings [Majumder 2008] and integrated optics. Moreover, tin-doping helped avoiding hydrogen loading, which is time-consuming and high induced-losses at $1.5\ \mu\text{m}$ region. In addition, $\text{SnO}_2\text{-SiO}_2$ fibers potentially provide a lower numerical aperture and higher thermal stability. However, due to the SnO_2 volatilization during the high temperature preparation of MCVD, the content of SnO_2 in SiO_2 matrix was limited to 0.15 mol% [Brambilla 2000]. The issues of low SnO_2 contents or $\alpha\text{-Sn}$ nanoclusters and nonstoichiometric SnO_x nanoparticles was encountered also in some other fabrication techniques such as melt quenching [Yu 2011] and ion-implantation method [Zatsepin 2012] which may be a limitation to obtain high photorefractivity and luminescence sensitizing. On the other hand, sol-gel has been a profitable alternative fabrication method to produce photonic glasses

with higher SnO_2 content [Zur 2017c] [Van Tran 2010] [Bhaktha 2009a] thanks to its low temperature and melt-free synthesis and ease of multicomponent fabrication [Zur 2017c]. In fact, compared to the other mentioned methods, sol-gel derived SiO_2 - SnO_2 glasses and glass-ceramics made up much higher number of publications. The sol-gel derived SiO_2 - SnO_2 glass-ceramics were studied both in forms of monoliths [Paleari 2006],[Yanes 2010],[Van 2014] and thin films [Van 2015],[Zur 2017c],[Van 2015],[Quang 2015],[Van 2010],[Bhaktha 2009a]. Most of the studies of the photorefractivity of this glass-ceramic was focused on the monolithic forms [Chiodini 2002][Chiodini 2003][Buso 2009] and only two publications on the SiO_2 - SnO_2 planar waveguides [Berneschi 2010], [Lukowiak 2017] but activated by Eu^{3+} . Therefore, in this work, for the aim of using the robust direct laser photoinscription technique exploiting the photorefractivity of tin dioxide based glass-ceramics, it is necessary to carry out the photorefractivity investigation of both fabricated SiO_2 - SnO_2 : Er^{3+} planar waveguides and monoliths. A particular attention is paid on the impact of SnO_2 content on the photorefractivity especially in the compositional planar waveguides for the integrated waveguide laser.

Concerning the role of SnO_2 as rare-earth luminescence sensitizers in the SiO_2 - SnO_2 glass-ceramics, evidences of energy transfer from SnO_2 to different rare-earth ions have been realized such as Eu^{3+} [Hayakawa 2006][Bhaktha 2009b][Yanes 2004][Tran 2017], Sm^{3+} [Yanes 2010][Mu 2007] and Er^{3+} [Zur 2017c][Van 2014][Brovelli 2006][Del-Castillo 2008]. In case of Er^{3+} activation, small size SnO_2 - SiO_2 monoliths were fabricated and characterized by several research groups [Paleari 2006], [Van 2014]. On the other hand, in case of the planar form of SiO_2 - SnO_2 : Er^{3+} glass-ceramics, there were only few publications [Van 2015] [Zur 2017c][Lin 2014][Chiodini 2005] but in thin films without a test of waveguiding properties. There was only one work on SiO_2 - SnO_2 : Er^{3+} planar waveguides [Guddala 2015] but the studied luminescence was in the visible range without exploiting the energy transfer from SnO_2 to Er^{3+} . Moreover, most of the reported spectroscopic properties of SiO_2 - SnO_2 : Er^{3+} glass-ceramics were focused on the spectral emission characteristics of Er^{3+} in this two-phase nanocomposite material. In fact, considering the desired lasing operating at $1.5\ \mu\text{m}$, the lifetime of the upper-state of the lasing radiation, i.e. $^4\text{I}_{13/2}$ metastable state of Er^{3+} is also an important factor. One reported $^4\text{I}_{13/2}$ decay time of Er^{3+} in this SiO_2 - SnO_2 glass-ceramic was found in the

work [Van 2014] on the monolithic form but only under directly excited Er^{3+} to its $^2\text{H}_{11/2}$ electronic state. Moreover, for the lasing validity of $\text{SiO}_2\text{-SnO}_2\text{:Er}^{3+}$ glass-ceramics exploiting the role of SnO_2 as Er^{3+} luminescence sensitizers, not only the spectral characteristics and the lifetime of the $^4\text{I}_{13/2}$ upper-state of the lasing radiation of Er^{3+} but also energy transfer features from SnO_2 to Er^{3+} are decisive spectroscopic properties. Besides these spectroscopic properties, the optical losses arising from the material structure, chemical contamination and residual, geometrical imperfection should be inspected. For this reason, the elaboration of spectroscopic, structural, morphological and chemical properties is mandatory to valid and define the necessary experimental parameters for the laser designs on the fabricated $\text{SiO}_2\text{-SnO}_2\text{:Er}^{3+}$ glass-ceramic planar waveguides and monoliths. In the particular case of the planar waveguides, the optical waveguiding properties should be also evaluated.

Furthermore, to achieve as high as possible the photorefractivity and luminescence sensitization, the high content of SnO_2 is necessary. Therefore, among the mentioned fabrication methods, sol-gel was chosen for the fabrication of $\text{SiO}_2\text{-SnO}_2\text{:Er}^{3+}$ glass-ceramic planar waveguides and monoliths. Even though the systems have been investigated for several years as mentioned above but there has been ongoing quest of developing reliable fabrication protocols and controlling the ion-ion interaction [Cascales 2018], [Zur 2017a], [Zur 2017b]. Both the problems are highly detrimental for the efficiency of active devices [De Pablos-Martin 2015], [Dymshits 2017], [Gonçalves 2002a], [Gorni 2018]. Therefore, to obtain homogeneous and transparent glass-ceramics, the first and foremost demand is the development of sol-gel synthesis protocols with defined thermal treatment. Moreover, the proposed fabrication processes must allow not only introducing high contents of SnO_2 in the systems, but also controlling the very small sizes of SnO_2 nanocrystals (at least less than 10 nm) in the planar waveguides and monoliths.

These addressed issues and the aim of putting the basis for the fabrication of solid state and integrated lasers of this PhD research lead to the demands for reliable sol-gel synthesis protocols development, photonic assessments and device designs for $\text{SiO}_2\text{-SnO}_2\text{:Er}^{3+}$ glass-ceramic planar waveguides and monoliths. Therefore, to fulfil these demands and achieve the research aim, this PhD thesis study must cover different research stages and aspects from the material preparation to a

complete assessment of the fabricated $\text{SiO}_2\text{-SnO}_2\text{:Er}^{3+}$ glass-ceramic systems for the applications and device designs. The research objectives can be summarized as follows:

- (i) developing a reliable sol-gel synthesis protocols with defined thermal processes which allow not only introducing high contents of SnO_2 in the systems but also controlling the very small sizes of SnO_2 nanocrystals (at least less than 10 nm);
- (ii) a complete photonic experimental assessment of the $\text{SiO}_2\text{-SnO}_2\text{:Er}^{3+}$ glass-ceramic systems focusing on the key considered characteristics including the structural, morphological, chemical and spectroscopic properties, and optical waveguiding properties in case of the planar waveguides;
- (iii) developing a model for understanding $\text{SnO}_2\text{:Er}^{3+}$ nanostructure and the relaxation dynamic of the electronic states supporting for the proof of concept realization of the considered devices;
- (iv) investigating the photorefractivity of $\text{SiO}_2\text{-SnO}_2$ glass-ceramics with the particular attention on the influential role of SnO_2 contents;
- (v) designing a solid state laser and an integrated waveguide laser using all the experimentally measured parameters;
- (vi) checking applicability of another robust direct laser inscription technique: femtosecond micromachining technique for fabricating optical channel waveguides on $\text{SiO}_2\text{-SnO}_2\text{:Er}^{3+}$ glass-ceramics for integrated photonic applications.

1.3 Thesis outline

This thesis is structured into nine chapters. The first two chapters: Chapter 1 Introduction and Chapter 2 Photonic glass-ceramics are dedicated to the overview and fundamental concepts of the work and the related field of glass-ceramics applied for photonics respectively. The next six chapters are ordered in the manner of providing solutions to six objectives of the research stated above.

Chapter 3 Fabrication describes the fabrication of $\text{SiO}_2\text{-SnO}_2\text{:Er}^{3+}$ planar waveguides and monoliths using sol-gel method. The detailed

optimization of the fabrication factors such as synthesis protocols, deposition parameters, thermal analyses and heat-treatment strategies is elaborated to obtain transparent glass-ceramics with high content and homogeneous dispersion of small nanosized SnO₂.

Chapter 4 Experimental assessments is dedicated to the experimental assessments of the fabricated SiO₂-SnO₂:Er³⁺ planar waveguides and monoliths. Diverse characterization techniques have been employed to provide fundamental data for the validation of these two systems. The key considered characteristics includes the structural, morphological, chemical and spectroscopic properties. In particular, the optical waveguiding characterization of the planar waveguides have been carried out.

Chapter 5 Numerical calculation on SnO₂:Er³⁺ shows the simulation studies on the location of Er³⁺ in SnO₂ and the corresponding SnO₂:Er³⁺ nanostructure using Density Functional Theory (DFT). The relaxation dynamic of the electronic states plays a supporting role for the proof of concept realization of the considered devices.

Chapter 6 Photorefractivity investigation demonstrates the photorefractive effect under the UV pulsed KrF excimer laser ($\lambda = 248$ nm) of SiO₂-SnO₂:Er³⁺ glass-ceramics. The first fabricated gratings through direct UV writing technique will be shown as a proof of concept for exploiting this special property for the writing of the channel waveguides and mirrors.

Chapter 7 Device designs is dedicated to the designs of a solid state laser with lateral pumping scheme and of an integrated waveguide laser in two different distributed feedback structures using all the parameters measured during the experimental assessments.

Chapter 8 Optical waveguides fabricated by laser micromachining demonstrates the fabrication of optical waveguiding structures on the SiO₂-SnO₂:Er³⁺ monolithic squares exploiting the femtosecond laser micromachining, another approach of tailoring the refractive index of the glass-ceramics.

Chapter 9 Conclusions and perspectives gives an overview of the achieved outcomes of the thesis and future work of the topic.

Last but not least, the research outcomes show all the publications and communications obtained during this PhD thesis research as validation of the work.

References

- [Berneschi 2010] Berneschi, S., Bhaktha, B. N. S., Chiappini, A., ... Righini, G. C., “Highly photorefractive Eu^{3+} activated sol-gel $\text{SiO}_2\text{-SnO}_2$ thin film waveguides”. Proceedings of SPIE 7604, pp. 76040Z(1–6) (2010), doi: 10.1117/12.843210.
- [Bhaktha 2009a] Bhaktha B N Shivakiran, Kinowski Christophe, Bouazaoui Mohamed, Capoen Bruno, Robbe-cristini Odile, Beclin Franck, Roussel Pascal, Ferrari Maurizio & Turrell Sylvia, “Controlled Growth of SnO_2 Nanocrystals in Eu^{3+} -Doped SiO_2 - SnO_2 Planar Waveguides : A Spectroscopic Investigation”, Physical Chemistry C, 113(52), pp. 21555–21559 (2009), doi: 10.1021/jp907764p.
- [Bhaktha 2009b] S. N. B. Bhaktha, C. Armellini, F. Beclin, M. Bouazaoui, B. Capoen, A. Chiappini, A. Chiasera, M. Ferrari, Y. Jestin, C. Kinowski, E. Moser, D. N. Rao, G. C. Righini & S. Turrell, “ $\text{SiO}_2\text{-SnO}_2$ glass-ceramic planar waveguides activated by rare earth ions”, Proceedings of SPIE Volume 7212, Optical Components and Materials VI, 721207(2–9) (2009), doi: 10.1117/12.808277.
- [Brambilla 2000] Brambilla G., Pruneri V., & Reekie L, “Photorefractive index gratings in $\text{SnO}_2\text{:SiO}_2$ optical fibers”, Applied Physics Letters, 76(7), pp. 807-809 (2000), doi:10.1063/1.125591.
- [Brambilla 2002] Brambilla, G., & Rutt, H. (2002). “Fiber Bragg gratings with enhanced thermal stability”. Applied Physics Letters, 80(18), pp. 3259–3261 (2002), doi: 10.1063/1.1475366.
- [Brovelli 2006] Brovelli S., Chiodini N., Lauria A., Meinardi F., & Paleari A., “Kinetics of luminescence of interface defects and resonant Er^{3+} ions in nanostructured $\text{SnO}_2\text{:SiO}_2$ ”, Solid State Communications, 138(12), pp. 574–576 (2006), doi: 10.1016/j.ssc.2006.04.035.
- [Buso 2009] Buso Dario, Giustina Gioia Della, Brusatin Giovanna, Guglielmi Massimo, Martucci Alessandro, Chiasera Alessandro, Ferrari Maurizio & Romanato Filippo, “Patterning of sol-gel hybrid organic-inorganic film doped with luminescent semiconductor quantum dots”,

Journal of Nanoscience and Nanotechnology, 9(3), pp. 1858–1864 (2009), doi: 10.1166/jnn.2009.373.

[Cascales 2018] Cascales, C., Balda, R., Lezama, L., & Fernández, J. (2018), “Site symmetry and host sensitization-dependence of Eu^{3+} real time luminescence in tin dioxide nanoparticles”, *Optic Express*, 26(13), pp. 16155–16170, doi: 10.1364/OE.26.016155.

[Chiodini 2002] Chiodini N., Paleari A., Brambilla G., & Taylor, E. R., “Erbium doped nanostructured tin-silicate glass-ceramic composites”, *Applied Physics Letters*, 80(23), pp. 4449–4451 (2002), doi: 10.1063/1.1485105.

[Chiodini 2003] Chiodini, N., Paleari, A., Spinolo, G., & Crespi, P., “Photorefractivity in $\text{SiO}_2\text{:SnO}_2$ glass-ceramics by visible light”. *Journal of Non-Crystalline Solids*, 322(1–3), pp. 266–271(2003), doi: 10.1016/S0022-3093(03)00213-8.

[Chiodini 2005] Chiodini N., Paleari A., & Romagnoli M., “Nanostructured $\text{SnO}_2\text{-SiO}_2$ glass ceramic: a competitor for Si nanodots in silica”, *Proceedings of SPIE Vol. 5925 -Nanophotonic Materials and Systems II*, Vol. 5925, pp. 59250J(1–10) (2005), doi: 10.1117/12.616537.

[De Pablos-Martin 2015] De Pablos-Martin A., Ferrari M., Pascual M. J. & Righini G. C., “Glass-ceramics: A class of nanostructured materials for photonics. *Rivista Del Nuovo Cimento*”, 38(7–8), pp. 311–369(2015), doi: 10.1393/ncr/i2015-10114-0.

[Del-Castillo 2008] Del-Castillo J., Rodríguez V. D., Yanes A. C., & Ramos J., “Energy transfer from the host to Er^{3+} dopants in semiconductor SnO_2 nanocrystals segregated in sol – gel silica glasses”, *Journal of Nanoparticle Research*, 10, pp. 499–506(2008), doi: 10.1007/s11051-007-9283-x.

[Dong 1995a] Dong L., Cruz J. L., Tucknott J. A., Reekie L., & Payne, D. N., “Strong photosensitive gratings in tin-doped phosphosilicate optical fibers”. *Optics Letters*, 20(19), pp. 1982–1984 (1995), doi: 10.1364/OL.20.001982.

[Dong 1995b] Dong L., Reekie L., Xu M. G., Payne D. N., & Cruz J. L., “Enhanced Photosensitivity in Tin-Codoped Germanosilicate Optical Fibers”, *IEEE Photonics Technology Letters*, 7(9), pp. 1048–1050 (1995), doi: 10.1364/OL.20.001982.

[Dymshits 2017] Dymshits O., Shepilov M., & Zhilin A., “Transparent glass-ceramics for optical applications”, *MRS Bulletin*, 42(3), pp. 200–205(2017), doi: 10.1557/mrs.2017.29.

[Gonçalves2002] Gonçalves M. C., Santos, L. F., & Almeida, R. M., “Rare-earth-doped transparent glass ceramics”, *Comptes Rendus Chimie*, 5(12), pp. 845–854(2002), doi: 10.1016/S1631-0748(02)01457-1.

[Gorni 2018] Gorni G., Velázquez J. J., Mosa J., Rolindes B., Joaquin F., Alicia D., Castro Y., “Transparent glass-ceramics produced by Sol-Gel: A suitable alternative for photonic materials”, *Materials*, 11(212), pp. 1–30(2018), doi: 10.3390/ma11020212.

[Guddala 2015] Guddala S., Chiappini A., Armellini C., Turell S., Righini G. C., Ferrari M., Rao D. N., “Fabrication and characterization of Er^{3+} doped $\text{SiO}_2/\text{SnO}_2$ glass-ceramic thin films for planar waveguide applications”, *IOP Conference Series: Materials Science and Engineering*, 73, pp.012102(1-4) (2015), doi: 10.1088/1757-899X/73/1/012102.

[Hayakawa 2006] Hayakawa T. & Nogami M., “High-Efficient Eu^{3+} Red Emission due to Excitation Energy Transfer from Nano-Sized SnO_2 Crystals”, *Advanced Materials Research*, 11–12, pp. 579–582(2006), doi: 10.4028/www.scientific.net/AMR.11-12.579.

[Laurence 1997] Laurence R. & Liang D., “Material considerations for Bragg fiber gratings”, *Proceedings Volume 2998, Photosensitive Optical Materials and Devices*, pp. 2–10(1997), doi: 10.1117/12.264168.

[Lin 2014] Lin T., Zhang X., Lin T., Zhang P., Xu J., Lin S., Xu L. & Chen, K., “Highly efficient near-infrared emission in Er^{3+} doped silica films containing size-tunable SnO_2 nanocrystals”, *Optics Express*, 22(1), pp. 369-376(2014), doi:10.1364/OE.22.000369.

[Lukowiak 2017] Lukowiak, A., Zur, L., Tran, T. N. L., Meneghetti M., Berneschi S., Conti G. N., Pelli S., Trono C., Bhaktha B.N. S., Zonta D., Taccheo S., Righini G. C., Ferrari M., “Sol–Gel-Derived Glass-Ceramic Photorefractive Films for Photonic Structures”, *Crystals*, 7(61), pp. 1-7 (2017), doi: 10.3390/cryst7020061.

[Majumder 2008] Majumder M., Gangopadhyay T. K., Chakraborty A. K., Dasgupta K. & Bhattacharya, D. K., “Fibre Bragg gratings in structural health monitoring-Present status and applications”, *Sensors and Actuators A: Physical*, 147(1), pp.150–164(2008), doi: 10.1016/j.sna.2008.04.008.

[Méndez 2007] Méndez A., “Fiber Bragg grating sensors: a market overview”, *Proceedings of SPIE Volume 6619, Optical Fibre Sensors*, Vol. 6619, p. 661905(1-6) (2007), doi: 10.1117/12.738334.

- [Mu 2007] Mu J., Liu L., & Kang S. Z., “Enhancement of Sm^{3+} emission by SnO_2 nanocrystals in the silica matrix”, *Nano Express*, 2(2), pp.100–103(2007), doi: 10.1007/s11671-006-9037-1.
- [Paleari 2006] Paleari A., Franchina E., Chiodini N., & Lauria A. “ SnO_2 nanoparticles in silica: Nanosized tools for femtosecond-laser machining of refractive index patterns”, *Applied Physics B: Lasers and Optics*, 88, pp. 131912(1-3) (2006), doi: 10.1063/1.2192579.
- [Photonics21 2018], Photonics21 Secretariat “Photonics - A critical Key Enabling Technology for Europe”, Düsseldorf, Germany (2018), <https://www.photonics21.org/download/ppp-services/photonics-downloads/Photonics-in-Horizon-2020-finaldigital-C1.pdf>
- [Quang 2015] Quang B., Ngoc N., Ngoc T., & Duc N., “Correlation between SnO_2 nanocrystals and optical properties of Eu^{3+} ions in SiO_2 matrix : Relation of crystallinity, composition, and photoluminescence”, *Journal of Luminescence*, 163, 28–31(2015), doi: 10.1016/j.jlumin.2015.03.002.
- [Rao 1999] Rao Y. J., “Recent progress in applications of in-fibre Bragg grating sensors”. *Optics and Lasers in Engineering*, 31(4), pp. 297–324(1999), doi: 10.1016/S0143-8166(99)00025-1.
- [Rodriguez-Cobo 2018] Rodriguez-Cobo L., Perez-Herrera R. A., Quintela M. A., Ruiz-Lombera R., Lopez-Amo M. & Lopez-Higuera J. M., “Virtual FBGs using saturable absorbers for sensing with fiber lasers”, *Sensors*, 18(11), pp. 3593(1-10) (2018). doi:10.3390/s18113593.
- [Tran 2017] Tran T. T. V., Cao T. M. D., Lam Q. V., & Le V. H., “Emission of Eu^{3+} in SiO_2 -ZnO glass and SiO_2 - SnO_2 glass-ceramic: Correlation between structure and optical properties of Eu^{3+} ions”, *Journal of Non-Crystalline Solids*, 459, pp. 57–62(2017), doi: 10.1016/j.jnoncrysol.2016.12.040.
- [Van 2010] Van T. T., Turrell S., Eddafi M., Capoen B., Bouazaoui M., Roussel P., Berneschi S., Righini G., Ferrari M., Bhaktha S. N. B., Cristini O., Kinowski C., “Investigations of the effects of the growth of SnO_2 nanoparticles on the structural properties of glass-ceramic planar waveguides using Raman and FTIR spectroscopies”, *Journal of Molecular Structure*, 976(1–3), pp. 314–319(2010), doi: 10.1016/j.molstruc.2010.04.010.
- [Van 2014] Tran T. T. Van, S. Turrell, B. Capoen, Le V. H., M. Ferrari, Davor R., Boussekey L., Kinowski C., “Environment segregation of Er^{3+} emission in bulk sol-gel-derived SiO_2 - SnO_2 glass ceramics”, *Journal of*

Materials Science, 49(24), 8226–8233(2014), doi: 10.1007/s10853-014-8531-6.

[Van 2015] Van T. T. T., Turrell S., Capoen B., Vinh L. Q., Cristini-Robbe O., Bouazaoui M., D’Acapito F., Ferrari M., Ristic D., Lukowiak A., Almeida R., Santos L., Kinowski C., “Erbium-Doped Tin-Silicate Sol–Gel-Derived Glass-Ceramic Thin Films: Effect of Environment Segregation on the Er^{3+} Emission”, *Science of Advanced Materials*, 7(2), pp. 301–308(2015), doi: 10.1166/sam.2015.2022.

[Yanes 2004] Yanes A. C., Del Castillo J., Torres M., Peraza J., Rodríguez V. D., & Méndez-Ramos J., “Nanocrystal-size selective spectroscopy in $\text{SnO}_2\text{:Eu}^{3+}$ semiconductor quantum dots”, *Applied Physics Letters*, 85(12), pp. 2343–2345(2014), doi: 10.1063/1.1790039.

[Yanes 2010] Yanes A. C., Méndez-Ramos J., Del-Castillo J., Velázquez J. J., & Rodríguez V. D., “Size-dependent luminescence of Sm^{3+} doped SnO_2 nano-particles dispersed in sol-gel silica glass”. *Applied Physics B: Lasers and Optics*, 101(4), pp. 849–854(2010), doi: 10.1007/s00340-010-4331-0.

[Yu 2011] Yu Y., Chen D., Huang P., Lin H., Yang A., & Wang Y.. “Distribution-related luminescence of Eu^{3+} sensitized by SnO_2 nanocrystals embedding in oxide glassy matrix”, *Journal of Solid State Chemistry*, 184(2), pp. 236–240(2011), doi: 10.1016/j.jssc.2010.11.021.

[Zatsepin 2012] Zatsepin A. F., Buntov E. A., Kortov V. S., Pustovarov V. A., Fitting H.-J., Schmidt B., Gavrilov N. V., “Low-temperature photoluminescence of ion-implanted $\text{SiO}_2\text{:Sn}^+$ films and glasses”. *Journal of Surface Investigation*, 6(4), pp. 668–672(2012), doi: 10.1134/S1027451012080198.

[Zur 2017a] Zur L., L. Tran T. N., Meneghetti M & Ferrari M., “Sol-gel derived SnO_2 -based photonic systems”, *Handbook of Sol-Gel Science and Technology*, Eds. Lisa Klein, Mario Aparicio, Andrei Jitianu, Springer International Publishing AG, pp. 1-19((2017), doi:10.1007/978-3-319-19454-7

[Zur 2017b] Zur, L., L. T. N. Tran, Meneghetti M., Varas S., Armellini C., Ristic D., Chiasera A., Scotognella F., Pelli S., Nunzi C. G., Boulard B., Zonta D., Dorosz D., Lukowiak A., Righini G. C., Ramponi R., Ferrari M., “Glass and glass-ceramic photonic systems”, In *Proceeding of SPIE 10106, Integrated Optics: Devices, Materials, and Technologies XXI*, Vol. 10106, p. 1010603(1-12) (2017), doi: 10.1117/12.2254965.

[Zur 2017c] Zur, L., Tran, L. T. N., Meneghetti, M., Tran V. T. T., Lukowiak A., Chiasera A., Zonta D., Ferrari M., Righini, G. C. “Tin-

dioxide nanocrystals as Er^{3+} luminescence sensitizers: Formation of glass-ceramic thin films and their characterization”, *Optical Materials*, 63, pp. 95–100(2017), doi: 10.1016/j.optmat.2016.08.041.

Chapter 2 Photonic glass-ceramics

2.1 Introduction

This chapter introduces briefly some fundamentals and current states of photonic glass-ceramics, including their advantages in term of spectral and luminescent properties tailoring in rare-earth-activated photonic structures. The advantages of $\text{SiO}_2\text{-SnO}_2$ glass-ceramics are also addressed with a brief summary of the prior works on this topic.

2.2 State of the art of photonic glass-ceramics

2.2.1 General advantages of glass-ceramics

Glass-ceramics can be defined as a class of composite materials containing one or more crystalline phases evenly distributed within a glass phase [Ferrari 2015]. In general, the crystalline phases can have the sizes ranging from nanometers to micrometers. Different microstructure and nanostructure configurations of glass-ceramics can be obtained by just changing the chemical composition and fabrication processes. As a result, diverse properties can be achieved and controlled, and this is the key advantage of glass-ceramics [Höland 2012]. Several relevant advantages of glass-ceramics and some corresponding applications can be summarized as follows:

- (i) Thermal and mechanical properties: thanks to the combination of the almost zero shrinkage, i.e. thermal shock resistance and achievable flexural strengths, specific glass-ceramics are produced on a large scale for industrial, technological, and domestic applications [Höland 2012] and they are among commercially successful glass-ceramics [Zanotto 2010].
- (ii) Biological and chemical properties: the biocompatibility, bioactivity, chemical durability of glass-ceramics have been exploited for the applications in implantology and dentistry [Saint-Jean 2014].
- (iii) Electrical and magnetic properties: special electrical or magnetic properties of glass-ceramics can also be exploited and applied for the electronics or micro - electronics industries [Zanotto 2010].
- (iv) Optical and spectroscopic properties: translucent, opaque, opalescent, fluorescent, and colored and photo-induction nucleations are of attractive optical properties of glass-ceramics [Zanotto 2010]. Moreover, the low thermal expansion coefficients

and high hardness of glass-ceramics make them viable for precise optical equipment applications [Höland 2012].

2.2.2 Photonic glass-ceramics

In field of glass photonics, the innovation of photonic glass-ceramics comes from the fact that they combine the optical and glass-manufacturing processing properties of the amorphous phase and the single-crystal-like optical and spectroscopic properties of the crystalline phases, which is important in luminescent materials activated species, e.g. rare-earths. And, this is an exciting advantage of glass-ceramics over glasses, single crystals and sintered transparent ceramics for photonic applications [Zanotto 2010], [Dymshits 2017].

For photonic applications, applicable glass-ceramics must possess crystalline phases in nanometer sizes much smaller than the desired working wavelength to avoid optical scattering and obtain high transparency [Ferrari 2015]. There are two models which can be applied for achieving high transparency in glass-ceramics:

- (i) Based on Rayleigh-Gans [Milton 1969], [Bohren 2007], if the scattering centers are independent and widely separated [Beall 1999], the decisive factors of low scattering are: crystals sizes much smaller than the wavelength of the incident light (less than 15 nm for the visible), a narrow size distribution and a refractive index contrast of less than 0.1 between the two phases.
- (ii) According to a quasi-continuum model proposed by Hopper [Hopper 1985] and Andreev [Andreev 1978], if the spacing of nanocrystals is 6 times less than their average size, the maximum allowed values of nanocrystal size and refractive index are 30 nm and 0.3 respectively [Beall 1999].

The correlation between structure and scattering is quite complex [Champagnon 2000], [Tick 2000] and still under investigation. In fact, the experimental results have shown that high transparency is still achievable in glass-ceramics with higher grain sizes up to few microns and high volume fraction of the crystalline phases [Beall 1999], [De Pablos-Martin 2015]. Although scattering is unavoidable in glass-ceramics due to the presence of nanocrystals as summarized in the work [De Pablos-Martin 2015], its effect is not an absolute limitation inhibiting the photonic applications of glass-ceramics. Furthermore, a compromise between the

volume fraction and size of the crystalline phases and the advantages in terms of spectroscopic, manufacturing and extra mechanical properties can make glass-ceramics become more competitive in field of optics and photonics.

Therefore, more and more intensive studies have been carried out to exploit the glass-ceramics for photonic and optic applications and devices [Boulard 2015]. In case of luminescent glass-ceramics activated by rare-earths, the crystalline environment around the rare earth ions leads to high absorption and emission cross sections, tailoring of the ion-ion interaction by the control of the rare earth ion partition [Dymshits 2017], [Boulard 2015]. Moreover, crystalline phases usually have a lower cut-off phonon energy when compared to glasses and this helps reducing non-radiative relaxation [Zur 2017a]. However, the nature of amorphous environment of glass matrices has also impacts on the properties of rare-earth ions embedded in nanocrystals. Therefore, an impressive variety of photonic glass-ceramics have been developed with an attempt of tailoring specifically the spectroscopic properties of rare-earth ion for desired purposes. One can find how diverse and innovative properties of the rare-earths can be tailored and achieved in different photonic glass-ceramics depending on their compositions and nature as addressed in the recent review papers [Łukowiak 2014], [Boulard 2015], [De Pablos-Martin 2015], [Ferrari 2015], [Gorni 2018], [Teng 2012], [Zur 2017a].

2.3 Tin dioxide-based glass-ceramics

2.3.1 Advantages of tin dioxide-based glass-ceramics

Although tin dioxide has been a well-known material for widespread technological applications in gas sensors [Chen 2014], oxidation catalyst and transparent electrodes [Batzill 2005], it also presents several interesting characteristics for photonic applications. Therefore, in this work, tin dioxide (SnO_2) is employed as nanocrystals to be embedded into silica for the formation of photonic glass-ceramics. The advantages of tin dioxide-based glass-ceramics can be briefly summarized as follows:

- (i) Tin dioxide is a wideband-gap semiconductor ($E_g = 3.6$ eV at 300 K) exhibiting a broad window of transparency from visible to infrared covering significant emission range of rare earth ions [Saadeddin 2007]. Therefore, it is a suitable material for optical and photonic applications.

- (ii) Tin dioxide can be used as a rare-earth luminescence sensitizer with high absorption cross section [Zur 2017b]. For this reason, rare-earth-activated SnO_2 -based glass-ceramics have been extensively studied for improving luminescence efficiencies of several rare-earth ions exploiting exciton mediated energy transfer from SnO_2 nanocrystals to the rare-earth ions, e.g. Eu^{3+} [Hayakawa 2006], [Bhaktha 2009], [Yanes 2004], [Tran 2017], Sm^{3+} [Yanes 2010], [Mu 2007] and Er^{3+} [Zur 2017b], [Van 2014], [Brovelli 2006], [Del-Castillo 2008].
- (iii) The presence of tin dioxide nanocrystals in SiO_2 matrix allows an increase in both solubility and luminescence efficiencies of RE ions [Zur 2017b], [Lukowiak 2017].
- (iv) In addition, tin dioxide has a maximum phonon energy of 630 cm^{-1} , which is approximately two times lower than the one of the fused silica (1100 cm^{-1}) [Tran 2018], [Zur 2017b]. Therefore, considering the multiphonon relaxation process of the rare-earth ions in a material, the number of phonons needed for bridging the electronic energy gap in the specific case of the $1.5 \text{ }\mu\text{m}$ ($\sim 6667 \text{ cm}^{-1}$) emission of Er^{3+} is 11 phonons for SnO_2 and 6 phonons for SiO_2 . The higher number of phonons, the lower multiphonon non-radiative decay rate to prevent the Er^{3+} luminescence [Layne 1977], [Reisfeld 1985], [Tanabe 1992]. This is an advantage in term of reducing the non-radiative multiphonon losses of Er^{3+} luminescence [Seddon 2010] for the laser action.
- (v) Last but not least, the photorefractivity of SiO_2 - SnO_2 [Berneschi 2010], [Lukowiak et al. 2017] even makes the photonic glass-ceramics more promising since this property allows applying the robust direct UV laser photoinscription technique for many applications in integrated optics.

2.3.2 Brief summary of prior researches

Based on the mentioned advantages, several studies were carried out for the realization and demonstration of the photorefractivity of SiO_2 - SnO_2 glass-ceramics and the role of SnO_2 nanocrystals as rare-earth luminescence sensitizers as already discussed in the Chapter 1 Introduction. Concerning the research interest of this work: SiO_2 - SnO_2 glass-ceramics activated by

Er^{3+} , several related studies in the literature are summarized in Table 2.1 and Table 2.2 for the monolithic forms and the planar forms respectively. The highlights taken from these works are referring to three aspects beneficial for the research interest of this thesis: (i) sol-gel derived fabrication; (ii) energy transfer from SiO_2 to Er^{3+} and (iii) photorefractivity of the $\text{SiO}_2\text{-SnO}_2\text{:Er}^{3+}$ glass-ceramics.

(i) *Sol-gel derived fabrication*

Looking at the researches on the monolithic forms listed Table 2.1, several studies such as [Chiodini 1999], [Van Tran 2012] were dedicated to find and optimize the sol-gel derived synthesis protocols and other related fabrication parameters such as tin content and heat-treatment. Comparing the two different synthesis protocols from these two works, the inorganic precursor of tin in the work [Van 2012] is preferable for the preparation of photonic materials due to the demand for good optical quality of the obtained systems. Considering the typical issues of sol-gel derived bulk fabrication: the fracture during the processes [Shuo 2010] and high reactivity of tin observed in [Chiodini 1999], the strategies to avoid fracture and to achieve densification of the sol-gel bulk materials need to be elaborated. These factors are important to obtain homogeneous and transparent glass-ceramics for photonic applications, but they have not been reported in these works. Concerning the planar forms, the investigation of the influence of SnO_2 contents and heat-treatment on the structural properties of the $\text{SiO}_2\text{-SnO}_2$ glass-ceramic thin films fabricated using sol-gel method and dip-coating technique was carried out in the work [Van 2010]. However, the work did not explore the influential factors related to the dip-coating processes which govern the homogeneity and uniformity of the thin films being crucial for optical waveguiding purposes. The other two works [Lin 2014], [Chiodini 2005] on $\text{SiO}_2\text{-SnO}_2\text{:Er}^{3+}$ thin films employed the spin-coating technique, but this technique has limitation on the homogeneity and the size of the thin films. Therefore, they are not suitable for the fabrication of the planar waveguides.

(ii) *Energy transfer from SiO_2 to Er^{3+}*

In the prior works, the spectroscopic measurements were also carried out and the energy transfer from SnO_2 to Er^{3+} was evidenced in both bulks [Van 2014], [Chiodini 2002a] and thin films [Chiodini 2005], [Guddala 2015]. An estimation of the energy transfer efficiency from SnO_2 to Er^{3+} (63.4 %) was given in the work [Lin 2014] on a very thin $\text{SiO}_2\text{-SnO}_2\text{:Er}^{3+}$ film (thickness of 110 nm). However, for the amplification and lasing applications, it is important to know the information of absorption cross

sections, emission cross sections, gain, etc. The information of these parameters of $\text{SiO}_2\text{-SnO}_2\text{:Er}^{3+}$ glass-ceramics has not been well-reported.

(iii) Photorefractivity of $\text{SiO}_2\text{-SnO}_2$ glass-ceramics

Several works were also dedicated to the investigation of the photorefractivity of the $\text{SiO}_2\text{-SnO}_2$ glass-ceramics. Concerning the monoliths, the works [Chiodini 2002a], [Chiodini 2001a], [Chiodini 2002b], [Chiodini 2003a], [Chiodini 2003c] put the first bricks for the photorefractive response investigation in this binary system: positive refractive index change for the substitutional tin-doped silica glasses and negative refractive index change for the $\text{SiO}_2\text{-SnO}_2$ glass-ceramics. In these works, the refractive index change was reported to be in the order of 10^{-4} in the $\text{SiO}_2\text{-SnO}_2$ glass-ceramic monoliths containing 5 mol% SnO_2 . The photorefractivity of the $\text{SiO}_2\text{-SnO}_2$ glass-ceramic planar waveguides was investigated in the works [Bhaktha 2010], [Berneschi 2010], [Lukowiak 2017] with 25 mol% SnO_2 content and the planar waveguides in these cases were doped with Eu^{3+} . The obtained negative effective index change was -1.5×10^{-3} . This is an indication for the high photorefractivity which are expected to obtain in $\text{SiO}_2\text{-SnO}_2\text{:Er}^{3+}$ glass-ceramics.

Overall, these prior works have put the fundamental information and motivate the investigation and development of the innovative $\text{SiO}_2\text{-SnO}_2\text{:Er}^{3+}$ glass-ceramics doped with Er^{3+} aiming to the desired lasing applications.

Chapter 2 Photonic glass-ceramics

Table 2.1 Brief summary of the prior related studies on SiO₂-SnO₂ glass-ceramics activated by Er³⁺ in monolithic forms

Works	Samples	Highlights
[Chiodini 1999], [Chiodini 2001c], [Clementi 2004]	Undoped SiO ₂ -SnO ₂ monolithic disks	<ul style="list-style-type: none"> - Investigation and optimization of sol-gel synthesis for the pure SiO₂-SnO₂ monolithic samples with the usage of organic precursors of SnO₂; - Structural and composition investigation of a segregation of SnO₂ nanocrystals in SiO₂;
[Chiodini 2001b], [Chiodini 2002a] [Chiodini 2001a], [Chiodini 2002c], [Chiodini 2003a], [Chiodini 2003c]	SiO ₂ -SnO ₂ :Er ³⁺ monolithic disks	<ul style="list-style-type: none"> -Investigation of the photosensitive response of the substitutional tin-doped silica glasses under UV exposure; - A small positive refractive index change (10⁻⁴) in the glasses containing small SnO₂ content of 0.5 mol%;
[Chiodini 2002b]	SiO ₂ -SnO ₂ monolithic disks	<ul style="list-style-type: none"> - Investigation of the photosensitive response of the SiO₂-SnO₂ glass-ceramics to different laser beams from UV to visible (266, 458 and 532nm); - SiO₂-SnO₂ glass-ceramic containing 5 mol% SnO₂ with negative refractive index change of 6×10⁻⁴;
[Van 2012]	Undoped SiO ₂ -SnO ₂	<ul style="list-style-type: none"> - Investigation of the influence of SnO₂ contents and heat-treatment on the structural properties of the SiO₂-SnO₂ glass-ceramic monoliths fabricated using sol-gel synthesis with the usage of inorganic precursors (SnCl₂) of SnO₂;
[Van 2014], [Chiodini 2002b] [Chiodini 2003b], [Brovelli 2006]	SiO ₂ -SnO ₂ :Er ³⁺ monoliths	<ul style="list-style-type: none"> - Putting evidences of energy transfer from SnO₂ to Er³⁺ based on spectroscopic characterization such as absorption, emission and time-resolved emission spectra;

Table 2.2 Brief summary of the prior related studies on SiO₂-SnO₂ glass-ceramics activated by Er³⁺ in planar forms

Works	Samples	Highlights
[Van 2010]	Undoped SiO ₂ -SnO ₂ thin films	- Investigation of the influence of SnO ₂ contents and heat-treatment on the structural properties of the SiO ₂ -SnO ₂ glass-ceramic thin films fabricated using sol-gel method and dip-coating technique;
[Lin 2014]	SiO ₂ -SnO ₂ :Er ³⁺ thin films	- Demonstration of the efficient energy transfer from SnO ₂ to Er ³⁺ in very thin films of 110 nm and estimation of the energy transfer efficiency of 63.4 %;
[Chiodini 2005]	SiO ₂ -SnO ₂ :Er ³⁺ thin films	- Demonstration of the efficient energy transfer from SnO ₂ to Er ³⁺ in the thin films with small SnO ₂ content of 3.2 mol%;
[Guddala 2015]	SiO ₂ -SnO ₂ :Er ³⁺ planar waveguides	- Putting evidences of the energy transfer from SnO ₂ to Er ³⁺ in the visible range emission of Er ³⁺ ;
[Bhaktha 2010], [Berneschi 2010], [Lukowiak 2017]	SiO ₂ -SnO ₂ :Eu ³⁺ planar waveguides	- Investigation of the photorefractivity of the SiO ₂ -SnO ₂ glass-ceramic planar waveguides containing 25 mol% SnO ₂ with the obtained negative refractive index change of 1.5×10^{-3} ;

References

- [Batzill 2005] Batzill M. & Diebold U., “The surface and materials science of tin oxide”, *Progress in Surface Science*, 79(2–4), pp. 47–154(2005), doi: 10.1016/j.progsurf.2005.09.002.
- [Bhaktha 2010] B. N. Shivakiran Bhaktha, Berneschi S. Conti G. N., Righini G. C., Chiappini A., Chiasera A., Ferrari M., Turrell S., (2010). “Spatially localized UV-induced crystallization of SnO_2 in photorefractive SiO_2 - SnO_2 thin film”, *Proceeding of SPIE Volume 7719, Silicon Photonics and Photonic Integrated Circuits II*, pp. 77191B–(2010), doi: 10.1117/12.854894(1-5).
- [Beall 1999] Beall G. H., & Pinckney L. R., “Nanophase Glass-Ceramics”, *Journal of American Ceramic Society*, 82(1), pp. 5–16(1999), doi: 10.1111/j.1151-2916.1999.tb01716.x.
- [Berneschi 2010] Berneschi, S., Bhaktha, B. N. S., Chiappini, A., ... Righini, G. C., “Highly photorefractive Eu^{3+} activated sol-gel SiO_2 - SnO_2 thin film waveguides”. *Proceedings of SPIE 7604*, pp. 76040Z(1–6) (2010), doi: 10.1117/12.843210.
- [Bhaktha 2009] S. N. B. Bhaktha, C. Armellini, F. Beclin, M. Bouazaoui, B. Capoen, A. Chiappini, A. Chiasera, M. Ferrari, Y. Jestin, C. Kinowski, E. Moser, D. N. Rao, G. C. Righini & S. Turrell, “ SiO_2 - SnO_2 glass-ceramic planar waveguides activated by rare earth ions”, *Proceedings of SPIE Volume 7212, Optical Components and Materials VI*, 721207(2–9) (2009), doi: 10.1117/12.808277.
- [Bohren 2007] Bohren C. F. & Huffman D. R. (1983). “Absorption and Scattering of light by small particles”, John Wiley & Sons (2007), doi: 10.1002/9783527618156.
- [Boulard 2015] Boulard, B., Van, T. T. T., Łukowiak, A., Łukowiak A., Bouajaj A., Gonçalves R. R., Chiappini A., Chiasera A., Blanc W., Duran A., Turrell S., Prudenzano F., Scotognella F., Ramponi R., Marciniak M., Giancarlo C. R., Ferrari M., “Photonic glass-ceramics: consolidated outcomes and prospects”, *Proceedings of SPIE Volume 9364*, pp. 93640Z(1-2) (2015), doi: 10.1117/12.2078263.
- [Brovelli2006] Brovelli S., Chiodini N., Lauria A., Meinardi F., & Paleari A., “Kinetics of luminescence of interface defects and resonant Er^{3+} ions in nanostructured SnO_2 : SiO_2 ”, *Solid State Communications*, 138(12), pp. 574–576 (2006), doi: 10.1016/j.ssc.2006.04.035.

- [Champagnon 2000] Champagnon B., Chemarin C., Duval E. & Parc R. Le., “Glass structure and light scattering”, *Journal of Non-Crystalline Solids*, 274, pp. 81–86(2000), doi: 10.1016/S0022-3093(00)00207-6.
- [Chen 2014] Chen, Z., Pan, D., Li, Z., Jiao Z., Wu M., Shek C. H., Wu C. M. L., Lai J. K. L. (2014). “Recent advances in tin dioxide materials: Some developments in thin films, nanowires, and nanorods”, *Chemical Reviews*, 114(15), pp. 7442–7486, doi: 10.1021/cr4007335.
- [Chiodini 2001a] Chiodini N., Ghidini S. & Paleari A., “Mechanisms responsible for the ultraviolet photosensitivity of SnO₂ -doped silica” *Physical Review B*, 64(7), pp. 073102(1-3) (2001), doi: 10.1103/PhysRevB.64.073102.
- [Chiodini 2001b] Chiodini N., Meinardi F., Morazzoni F., Padovani J., Paleari A., Scotti R., Spinolo G., “Thermally induced segregation of SnO₂ nanoclusters in Sn-doped silica glasses from oversaturated Sn-doped silica xerogels”, *Journal of Materials Chemistry*, 11, pp. 926-929(2001), doi: 10.1039/b006999j.
- [Chiodini 1999] Chiodini N., Morazzoni F., Paleari A., Scotti R., & Spinolo G., “Sol-gel synthesis of monolithic tin-doped silica glass”, *Materials Chemistry*, 9, pp. 2653–2658(1999), doi: 10.1039/A904415I.
- [Chiodini 2002a] Chiodini N., Paleari A., Brambilla G., & Taylor, E. R., “Erbium doped nanostructured tin-silicate glass-ceramic composites”, *Applied Physics Letters*, 80(23), pp. 4449–4451 (2002), doi: 10.1063/1.1485105.
- [Chiodini 2002b] Chiodini, N., Paleari, A., Spinolo, G., Chiasera A., Ferrari M., Brambilla G., Taylor, E. R. (2002c), “Photosensitive erbium doped tin-silicate glass”, *Journal of Non-Crystalline Solids*, 311(3)1–6(2002), doi: /10.1016/S0022-3093(02)01419-9.
- [Chiodini 2003a] Chiodini N., Paleari A., & Spinolo G., “Photorefractivity in Nanostructured Tin-Silicate Glass Ceramics : A Radiation-Induced Nanocluster Size Effect”, *Physical Review Letters*, 90(5), pp. 055507 (1-4) (2003), doi: 10.1103/PhysRevLett.90.055507.
- [Chiodini 2003b] Chiodini, N., Paleari, A., & Spinolo, G. (2003b). “Synthesis and applications in photonics of SiO₂ : SnO₂ nanostructured glass-ceramics”, *Proceedings Volume 4987, Integrated Optics: Devices, Materials, and Technologies VII*, pp. 60–68(2003), doi: 10.1117/12.474352.
- [Chiodini 2003c] Chiodini, N., Paleari, A., Spinolo, G., & Crespi, P., “Photorefractivity in SiO₂:SnO₂ glass-ceramics by visible light”. *Journal*

of Non-Crystalline Solids, 322(1–3), pp. 266–271(2003), doi: 10.1016/S0022-3093(03)00213-8.

[Chiodini 2005] Chiodini N., Paleari A., & Romagnoli M., “Nanostructured SnO₂-SiO₂ glass ceramic: a competitor for Si nanodots in silica”, Proceedings of SPIE Vol. 5925 -Nanophotonic Materials and Systems II, Vol. 5925, pp. 59250J(1–10) (2005), doi: 10.1117/12.616537.

[Clementi 2004] Clementi. A., Chiodini N., & Paleari A. , “Cubic optical nonlinearity in nanostructured SnO₂:SiO₂”. Applied Physics Letters, 84(6), pp.960-962(2004), doi: 10.1063/1.1645664.

[De Pablos-Martin 2015] De Pablos-Martin A., Ferrari M., Pascual M. J. & Righini G. C., “Glass-ceramics: A class of nanostructured materials for photonics. Rivista Del Nuovo Cimento”, 38(7–8), pp. 311–369(2015), doi: 10.1393/ncr/i2015-10114-0.

[Del-Castillo 2008] Del-Castillo J., Rodri’guez V. D., Yanes A. C., & Ramos J., “Energy transfer from the host to Er³⁺ dopants in semiconductor SnO₂ nanocrystals segregated in sol – gel silica glasses”, Journal of Nanoparticle Research, 10, pp. 499–506(2008), doi: 10.1007/s11051-007-9283-x.

[Dymshits 2017] Dymshits O., Shepilov M., & Zhilin A., “Transparent glass-ceramics for optical applications”, MRS Bulletin, 42(3), pp. 200–205(2017), doi: 10.1557/mrs.2017.29.

[Ferrari 2015] Ferrari M. & Righini G. C. “Glass-Ceramic Materials for Guided-Wave Optics”, International Journal of Applied Glass Science, 6(3), 240–248(2015), doi: 10.1111/ijag.12129.

[Gorni 2018] Gorni G., Velázquez J. J., Mosa J., Rolindes B., Joaquin F., Alicia D., Castro Y., “Transparent glass-ceramics produced by Sol-Gel: A suitable alternative for photonic materials”, Materials, 11(212), pp. 1–30(2018), doi: 10.3390/ma11020212.

[Guddala 2015] Guddala S., Chiappini A., Armellini C., Turell S., Righini G. C., Ferrari M., Rao D. N., “Fabrication and characterization of Er³⁺ doped SiO₂/SnO₂ glass-ceramic thin films for planar waveguide applications”, IOP Conference Series: Materials Science and Engineering, 73, pp.012102(1-4) (2015), doi: 10.1088/1757-899X/73/1/012102.

[Hayakawa 2006] Hayakawa T. & Nogami M., “High-Efficient Eu³⁺ Red Emission due to Excitation Energy Transfer from Nano-Sized SnO₂ Crystals”, Advanced Materials Research, 11–12, pp. 579–582(2006), doi: 10.4028/www.scientific.net/AMR.11-12.579.

- [Höland 2012] Höland W., & Beall G. H. “Chapter 1- Principles of designing glass-ceramic formation”, Glass-ceramic technology, 2nd Edition, John Wiley & Sons, pp. 1–72(2012), doi: 10.1002/9781118265987.ch1.
- [Hopper 1985] Hopper R. W. “Stochastic theory of scattering from idealized spinodal structures”, Journal of Non-Crystalline Solids, 70(1), pp. 111–142(1985), doi: 10.1016/0022-3093(82)90124-7.
- [Layne 1977] Layne C. B., Lowdermilk W. H. & M. J. Weber. “Multiphonon relaxation of rare earth ions in oxide glasses” Physics Review B, 16(1), pp. 10–20(1977), doi: 10.1103/PhysRevB.16.10.
- [Lin 2014] Lin T., Zhang X., Lin T., Zhang P., Xu J., Lin S., Xu L. & Chen, K., “Highly efficient near-infrared emission in Er³⁺ doped silica films containing size-tunable SnO₂ nanocrystals”, Optics Express, 22(1), pp. 369-376(2014), doi:10.1364/OE.22.000369.
- [Łukowiak 2014] Łukowiak, A., Vasilchenko, I., Normani, S., Chiappini A., Chiasera A., Armellini C., Duverger C. A., Boulard B., Wiglusz R. J., Pelli S., Inas K., Prudenzeno F., Righini G. C., Marciniak M., Ferrari, M., “Glass-Ceramics for Photonics: Advances and Perspectives”, Proceeding of 16th International Conference on Transparent Optical Networks (ICTON) -IEEE, pp. 1–4(2014), doi: 10.1109/ICTON.2014.6876584.
- [Lukowiak 2017] Lukowiak, A., Zur, L., Tran, T. N. L., Meneghetti M., Berneschi S., Conti G. N., Pelli S., Trono C., Bhaktha B.N. S., Zonta D., Taccheo S., Righini G. C., Ferrari M., “Sol–Gel-Derived Glass-Ceramic Photorefractive Films for Photonic Structures”, Crystals, 7(61), pp. 1-7 (2017), doi: 10.3390/cryst7020061.
- [Milton 1969] Milton K “Chapter 8 Rayleigh-Debye Scattering”, The Scattering of Light and Other Electromagnetic Radiation, Academic Press, (1969).
- [Mu 2007] Mu J., Liu L., & Kang S. Z., “Enhancement of Sm³⁺ emission by SnO₂ nanocrystals in the silica matrix”, Nano Express, 2(2), pp.100–103(2007), doi: 10.1007/s11671-006-9037-1.
- [Andreev 1978] Andreev N. S., “Scattering of visible light by glasses undergoing phase separation and homogenization”, Journal of Non-Crystalline Solids, 30(2), pp. 99–126(1978), doi: 10.1016/0022-3093(78)90060-1.
- [P.A.Tick 2000] Tick P. A., Borrelli N. F., & Reaney I. M. .. “The relationship between structure and transparency in glass-ceramic materials”, Optical Materials, 15, pp.81–91(2000), doi: 10.1016/S0925-3467(00)00017-3 .

- [Reisfeld 1985] Reisfeld R., & Eyal M., “Possible ways of relaxation of excited states of rare earth ions in amorphous media”, *Le Journal de Physique Colloques*, 46(C7), pp. C7(349-355) (1985), doi: 10.1051/jphyscol:1985763.
- [Saadeddin 2007] Saadeddin I., Pecquenard B., Manaud J. P., Decourt R., Labrugère C., Buffeteau T. & Campet, G. Synthesis and characterization of single-and co-doped SnO_2 thin films for optoelectronic applications, 253(12), pp. 5240-5249 (2007). doi:10.1016/j.apsusc.2006.11.049.
- [Saint-Jean 2014] Saint-Jean, S. J., “Chapter 12-Dental glasses and glass-ceramics”, *Advanced Ceramics for Dentistry*, Elsevier Inc., pp. 255–277(2014), doi: 10.1016/B978-0-12-394619-5.00012-2.
- [Seddon 2010] Seddon A. B., Tang Z., Furniss D., Sujecki S., & Benson T. M., “Progress in rare-earth-doped mid-infrared fiber lasers”, *Optics Express*, 18(25), 26704(2010), doi: 10.1364/OE.18.026704.
- [Shuo 2010] Shuo W., Qingnan Z., Dengkui M., & Yuhong D., “Synthesis and characterization of Sb-doped SnO_2 -(CeO_2 - TiO_2) composite thin films deposited on glass substrates for antistatic electricity and UV-shielding”, *Journal of Rare Earths*, 28, pp. 189–193(2010), doi: 10.1016/S1002-0721(10)60377-8.
- [Tanabe 1992] Tanabe S., Yoshii S., Hirao K., & Soga N., “Upconversion properties, multiphonon relaxation, and local environment of rare-earth ions in fluorophosphate glasses”, *Physical Review B*, 45(9), pp. 4620–4625(1992), doi: 10.1103/PhysRevB.45.4620.
- [Teng 2012] Teng Y., Sharafudeen K., Zhou S., & Qiu J., “Glass-ceramics for photonic devices”, *Journal of the Ceramic Society of Japan*, 120(11), pp. 458–466(2012), doi: doi.org/10.2109/jcersj2.120.458.
- [Tran 2018] Tran T.N. L., Massella D., Zur L., Chiasera A., Varas S., Armellini C., Righini C. G., Lukowiak A., Zonta D., Ferrari M., “ SiO_2 - SnO_2 : Er^{3+} glass-ceramic monoliths”. *Applied Sciences*, 8(8), pp. 1335(1-8) (2018), doi: 10.3390/app8081335.
- [Tran 2017] Tran T. T. V., Cao T. M. D., Lam Q. V., & Le V. H., “Emission of Eu^{3+} in SiO_2 - ZnO glass and SiO_2 - SnO_2 glass-ceramic: Correlation between structure and optical properties of Eu^{3+} ions”, *Journal of Non-Crystalline Solids*, 459, pp. 57–62(2017), doi: 10.1016/j.jnoncrysol.2016.12.040.
- [Van 2014] Tran T. T. Van, S. Turrell, B. Capoen, Le V. H., M. Ferrari, Davor R., Boussekey L., Kinowski C., “Environment segregation of Er^{3+}

emission in bulk sol-gel-derived $\text{SiO}_2\text{-SnO}_2$ glass ceramics”, *Journal of Materials Science*, 49(24), 8226–8233(2014), doi: 10.1007/s10853-014-8531-6.

[Van 2012] Van T. T. T., Si B., Turrell S., Capoen B., Roussel P., Bouazaoui M., Ferrari M., Cristini O., Kinowski C., “Controlled SnO_2 nanocrystal growth in $\text{SiO}_2\text{-SnO}_2$ glass-ceramic monoliths”, *Journal of Raman Spectroscopy*, 43(7), 869–875(2012), doi: 10.1002/jrs.3099.

[Van 2010] Van T. T., Turrell S., Eddafi M., Capoen B., Bouazaoui M., Roussel P., Berneschi S., Righini G., Ferrari M., Bhaktha S. N. B., Cristini O., Kinowski C., “Investigations of the effects of the growth of SnO_2 nanoparticles on the structural properties of glass-ceramic planar waveguides using Raman and FTIR spectroscopies”, *Journal of Molecular Structure*, 976(1–3), pp. 314–319(2010), doi: 10.1016/j.molstruc.2010.04.010.

[Yanes 2004] Yanes A. C., Del Castillo J., Torres M., Peraza J., Rodríguez V. D., & Méndez-Ramos J., “Nanocrystal-size selective spectroscopy in $\text{SnO}_2\text{:Eu}^{3+}$ semiconductor quantum dots”, *Applied Physics Letters*, 85(12), pp. 2343–2345(2014), doi: 10.1063/1.1790039.

[Yanes 2010] Yanes A. C., Méndez-Ramos J., Del-Castillo J., Velázquez J. J., & Rodríguez V. D., “Size-dependent luminescence of Sm^{3+} doped SnO_2 nano-particles dispersed in sol-gel silica glass”. *Applied Physics B: Lasers and Optics*, 101(4), pp. 849–854(2010), doi: 10.1007/s00340-010-4331-0.

[Zanotto 2010], Zanotto, E. D. (2010). “A bright future for glass-ceramics”, *American Ceramic Society Bulletin*, 89(8), pp. 19–27.

[Zur 2017a] Zur, L., L. T. N. Tran, Meneghetti M., Varas S., Armellini C., Ristic D., Chiasera A., Scotognella F., Pelli S., Nunzi C. G., Boulard B., Zonta D., Dorosz D., Lukowiak A., Righini G. C., Ramponi R., Ferrari M., “Glass and glass-ceramic photonic systems”. In *Proceeding of SPIE 10106, Integrated Optics: Devices, Materials, and Technologies XXI*, Vol. 10106, p. 1010603(1-12) (2017), doi: 10.1117/12.2254965.

[Zur 2017b] Zur, L., Tran, L. T. N., Meneghetti, M., Tran V. T. T., Lukowiak A., Chiasera A., Zonta D., Ferrari M., Righini, G. C. “Tin-dioxide nanocrystals as Er^{3+} luminescence sensitizers: Formation of glass-ceramic thin films and their characterization”, *Optical Materials*, 63, pp. 95–100(2017), doi: 10.1016/j.optmat.2016.08.041].

Chapter 3 Fabrication

3.1 Introduction

In this chapter, the fabrication of $\text{SiO}_2\text{-SnO}_2\text{:Er}^{3+}$ planar waveguides and monoliths using sol-gel method, a wet-chemical route, will be described. A brief summary of tin dioxide based glasses fabrication will show specific advantages of sol-gel over other reported methods in preparing such materials. Optimized synthesis protocols for monoliths will be given with details in terms of overcoming fast gelation issue. Thanks to thermal analyses, heat-treatment strategies have been defined to avoid fracture during drying and phase transformation, a typical problem of sol-gel derived bulk fabrication. Concerning the planar waveguides, to maintain the solution homogeneity and dilution for dip-coating process, the synthesis recipe has been adjusted to obtain the compositional samples. Effect of deposition speed and thermal treatment on the properties of the planar waveguides has been also explored.

3.2 Brief summary of SnO_2 based glasses fabrication

Several methods have been employed to produce $\text{SnO}_2\text{-SiO}_2$ materials but generally, they have a limitation of low SnO_2 content or the presence of nonstoichiometric SnO_x . In [Brambilla 2001], modified chemical vapor deposition (MCVD) was employed to produce $\text{SnO}_2\text{-SiO}_2$ preforms and consequent drawn fibers. However, the problem of SnO_2 volatility due to high fabrication temperature of this method leads to a limited SnO_2 concentration of around 0.15 mol% [Brambilla 2000]. Coupons of 1 cm^2 silica-based multicomponent glass-ceramics, containing 3 mol% of SnO_2 nanocrystals were prepared in [Yu 2011] using melt-quenching method. Ion-implantation method was also used to embed tin ions into SiO_2 bulks and films in [Zatsepin 2012]. The obtained materials contained only $\alpha\text{-Sn}$ nanoclusters and nonstoichiometric SnO_x nanoparticles. The “inverse-dip coating” and the “powder in tube” were applied to obtain nanostructured optical fibers in [Granger 2014] but the evaporation of SnO_2 during the drawing steps led to the loss of SnO_2 concentration in the cores.

Considering above mentioned issues, sol-gel has been a profitable alternative to produce photonic glasses with higher SnO_2 content thanks

to its low temperature and melt-free synthesis [Gorni 2018], [Zur 2017a]. Sol-gel provides versatility of fabricating multicomponent materials with controlled composition, shape, morphological and textual properties of final products. In case of monoliths, small size $\text{SnO}_2\text{-SiO}_2$ samples were fabricated and characterized by several research groups [Hayakawa 2002], [Paleari 2006], [Yanes 2010], [Van 2014]. In the case of $\text{SnO}_2\text{-SiO}_2$ thin films, high SnO_2 contents have been reached (30 mol% [Zur 2017c]) via sol-gel and dip-coating technique. Several structural, morphological and optical properties of the thin films have been characterized [Zur et al. 2017c], [Van 2015], [Quang 2015], [Van Tran 2010] and they have shown good waveguide properties with low losses [Bhaktha 2009]. Even though the systems have been investigated for several years but there has been ongoing quest of developing reliable fabrication protocols and controlling the ion-ion interaction [Cascales 2018], [Zur 2017b], [Zur 2017a]. Both the problems are highly detrimental for the efficiency of active devices [De Pablos-Martin 2015], [Dymshits 2017], [Gonçalves 2002a], [Gorni et al. 2018]. Therefore, to obtain homogeneous and transparent glass-ceramics, the first demand is the development of sol-gel synthesis protocols with defined thermal treatment. Moreover, the proposed fabrication processes must allow not only introducing high contents of SnO_2 in the systems, but also controlling the very small sizes of SnO_2 nanocrystals (at least less than 10 nm) in the planar waveguides and monoliths.

3.3 The sol-gel derived fabrication

3.3.1 General routes

Both sol-gel routes used for the planar waveguides and monoliths fabrication start from the solution synthesis in which all hydrolysis and polycondensation reactions could occur. Afterwards, depending on the structural geometry of each system, the viscosity, reactant ratios and treatment for the solutions are established specifically. In monoliths, to obtain 3D structure xerogel, the synthesized solutions are transferred into molds and left to finish aging, being dried and eventually heat-treated. In planar waveguides, i.e. 2D structures, for the dip-coating deposition, low viscosity of the solutions for the waveguides is required [Brinker 2013] which is much lower than the ones for the monoliths and thus, the aging time is also limited in several hours. The solutions then

are used for dip-coating to deposit the planar waveguides. The chemicals and synthesized solutions play principal role in defining texture and consequent properties of the final sol-gel derived products.

3.3.2 Chemicals

For the solution synthesis of tin dioxide based glass-ceramics, the basic chemicals are the precursors of SiO_2 , SnO_2 and Er^{3+} , the catalyst, distilled water and the solvent.

3.3.2.1 Precursor of SiO_2


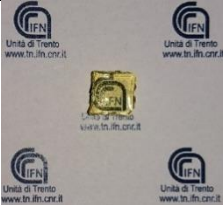
In the resulting $x\text{SnO}_2-(100-x)\text{SiO}_2-y\text{Er}^{3+}$ (x, y : mol%) systems, silica (SiO_2) accounted for dominant molar proportions and it mostly decided the fundamental texture of the systems. There are two most commonly used silicon-based alkoxide precursors: tetraethyl orthosilicate (TEOS) and tetramethoxy orthosilicate (TMOS). Due to the steric effect, the larger size of the alkoxy group of TEOS facilitates the slower reaction rate of hydrolysis than the one of TMOS [Bernards 1991]. As a result, the synthesis is more controllable in case of TEOS, which is a substantial factor to compensate the high reactivity of the other two reactive metals Sn and Er precursors. Based on all addressed issues, TEOS was chosen for the syntheses of the systems.

3.3.2.2 Precursor of SnO_2

According to the initial researches on SiO_2 - SnO_2 systems in the literature [Zur et al. 2017c], [Van 2014], [Yanes 2010], [Palaeri et al. 2006], [Nogami 2003], there were two kinds of precursors used for SnO_2 : the inorganic salt- tin(II) chloride ($\text{SnCl}_2 \cdot 2\text{H}_2\text{O}$) and organic compound dibutyltin diacetate (DBTDA: $(\text{CH}_3\text{CH}_2\text{CH}_2\text{CH}_2)_2\text{Sn}(\text{OCOCH}_3)_2$). Several testing syntheses have been done using both precursors DBTDA and $\text{SnCl}_2 \cdot 2\text{H}_2\text{O}$ for the monolith fabrication. Although DBTDA led to a slower gelation time than $\text{SnCl}_2 \cdot 2\text{H}_2\text{O}$, it easily induced cracking during the drying processes. An example of this feature is shown in Table 3.1. Moreover, due to the demand for good optical quality of the obtained systems, the organic dibutyltin diacetate (DBTDA) was eliminated. Therefore, $\text{SnCl}_2 \cdot 2\text{H}_2\text{O}$

was chosen to be the precursor for SnO_2 in the syntheses of the monoliths and also of the planar waveguides.

Table 3.1 The differences of $90\text{SiO}_2\text{-}10\text{SnO}_2\text{:}0.5\text{Er}^{3+}$ monolithic dried gels prepared by using $\text{SnCl}_2\cdot 2\text{H}_2\text{O}$ and DBTDA in the same synthesis recipe

Precursor of SnO_2	$\text{H}_2\text{O}/\text{HCl}/\text{EtOH}/\text{TE}$ OS ratios	Gelation time	Samples after drying at 65°C
DBTDA	10/0.009/4/1	2 days	
$\text{SnCl}_2\cdot 2\text{H}_2\text{O}$		1 days	

3.3.2.3 Precursor of Er^{3+}

Concerning the precursor of Er^{3+} , the commonly used inorganic salt Erbium(III) nitrate pentahydrate ($\text{Er}(\text{NO}_3)_3\cdot 5\text{H}_2\text{O}$) was employed like in the previous work reported elsewhere [Zur 2017c].

3.3.2.4 Catalyst

As studied in [Pope 1986], the kind of acidic or basic catalyst and their concentration in the solution affect dramatically the gelation time, porosity, bulk and apparent density, and volume shrinkage during drying. These factors are crucial for the fabrication, especially of the monoliths. In [Brinker 1988] and [Nogami 1980], acid HCl is demonstrated to promote slow hydrolysis reaction relative to the condensation one with the small pores and high bulk density in the final product while the contrary trend is obtained with base NH_3OH . Hydrochloride acid (HCl) was chosen to be the catalyst for hydrolysis and condensation reactions during the syntheses. HCl leads to the

electrophilic reaction in hydrolysis process and it provides glass with higher optical and densified quality [Kajihara 2013]. In addition, the combination of the two chemicals, TEOS and HCl has been well-studied [Zur 2017c], [Van 2014] and shown its success in sol-gel fabrication of optical silica-based glasses.

3.3.2.5 Solvent

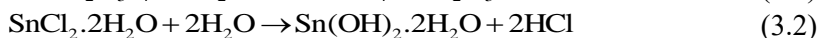
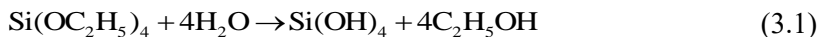
To obtain the miscible homogeneous solutions, it is necessary to dissolve all the precursors in a solvent before they carry out the reactions with water. This aspect was much more important in case of TEOS since it is not miscible in water [Jeffrey 2013]. To avoid any extra effect from alcohol exchange reactions, EtOH, the parent alcohol of TEOS, was selected.

3.3.3 Reactions

3.3.3.1 Hydrolysis

In sol-gel, after being dissolved in a solvent, the constituent metal cations M in precursor molecules are solvated. These cations then react with the surrounding water molecules in the first solvated shell by deprotonation of one or more protons [Barnum 1983]. This reaction is called hydrolysis and it results in the formation of mononuclear complexes of M, called sol particles.

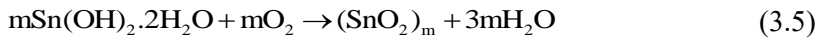
Here is the complete hydrolysis of all the used precursors for the syntheses of the final products in this work:



3.3.3.2 Condensation

Another reaction happens in sol-gel is condensation. This reaction starts when mononuclear complexes of metal M react one with another to build polynuclear complexes. These polynuclear complexes in their turns react again with each other to construct bigger species. When all

the condensation reactions finish, gels are formed. During the sol-gel synthesis, the hydrolysis and polycondensation always occur parallelly and compete each other. The complete reactions of the polycondensation for the formation of SiO₂ network and SnO₂ nanocrystals are described as follows:



3.3.4 Hydrolysis ratio

The hydrolysis ratio defined by the molar ratio $R = \text{H}_2\text{O}/\text{TEOS}$ is also one of the main factors which define the general skeleton of sol-gel derived SiO₂ - based materials. The principal effect of R on the structural network of the resulting gels can be summarized in Table 3.2.

Table 3.2 The effect of H₂O/TEOS molar ratio (R) on the structural network of the resulting gels

H₂O/TEOS molar ratio (R)	Favored structural network of the gels	Application
$R \leq 2$	linear chain formation due to lack of H ₂ O	Micro- or nano-fiber fabrication
$2 < R < 4$	two-dimensional network	thin film fabrication
$4 \leq R \leq 10$	three-dimensional network	monolith fabrication
$10 < R$	three-dimensional network with low density	aerogel monolith fabrication

Table 3.3 below summarizes all the chemicals used for the syntheses of the final tin dioxide-based monoliths and planar waveguides. The details of specific reactant ratios and synthesis protocols the monoliths and planar waveguides will be discussed in sections 3.4 and 3.5 respectively.

Chapter 3 Fabrication

Table 3.3 The chemicals used for the synthesis of the monoliths and waveguides

Reactants	Precursor of SiO ₂	Precursor of SnO ₂	Precursor of Er ³⁺	Water	Solvent	Catalyst
Chemical name	Tetraethyl orthosilicate (TEOS)	Tin (II) chloride dehydrate	Erbium (III) nitrate pentahydrate	Distilled water	Ethanol	Hydrochloric acid 37%
Molecular formula	Si(OC ₂ H ₅) ₄	SnCl ₂ ·2H ₂ O	Er(NO ₃) ₃ ·5H ₂ O	H ₂ O	C ₂ H ₅ OH	HCl
Origin	Aldrich Chemistry	Aldrich Chemistry	Aldrich Chemistry	Distilled in the lab	VWR Chemicals	Carlo-Erre Reagents
Purity	≥ 99.0 %	≥ 98.0%	≥ 99.9%	≥99.9%	≥ 99.9%	≥ 99.0 %
Molecular weight (g/mol)	208.33	225.63	443.35	18.00	46.07	36.46

3.4 Monoliths fabrication

In general, the preparation of sol-gel derived monoliths consists of five stages: sol formation, gelation, aging, drying and heat-treatment. Figure 3.1 describes the synthesis process during which the material carried out its transformation from sol-particles to gels and finally to glass or glass-ceramic.

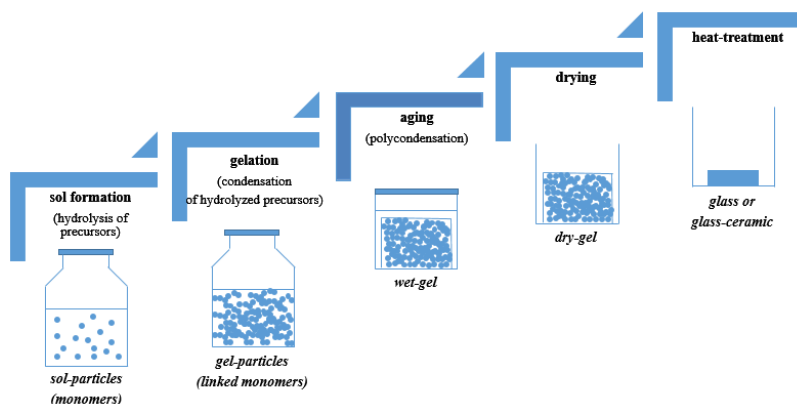


Figure 3.1 Phase transformation diagram of sol-gel derived monoliths during the synthesis process

3.4.1 Sol formation

Sol formation are the first step of the fabrication of the monoliths, as described in Figure 3.1 above. The synthesis started by dissolving TEOS, $\text{SnCl}_2 \cdot 2\text{H}_2\text{O}$ and $\text{Er}(\text{NO}_3)_3 \cdot 5\text{H}_2\text{O}$ in ethanol separately and these solutions were then mixed together. The hydrochloric acid solution was poured drop by drop to the mixture. While the sol particles were created by hydrolysis of solvated precursors, the gel-particles were formed based on condensation of hydrolyzed precursors. In fact, the condensation can start even when all the hydrolysis reactions of the precursors have not completed. In other words, these two reactions happened parallelly and competed each other until precursors are hydrolyzed completely. In fact, the sols are colloidal dispersion of the sol-particles and their continual linked clusters, i.e. “gel-particles”.

The flowchart in Figure 3.2 described the detailed synthesis process of $(100-x)\text{SiO}_2-x\text{SnO}_2:\text{Er}^{3+}$ monoliths.

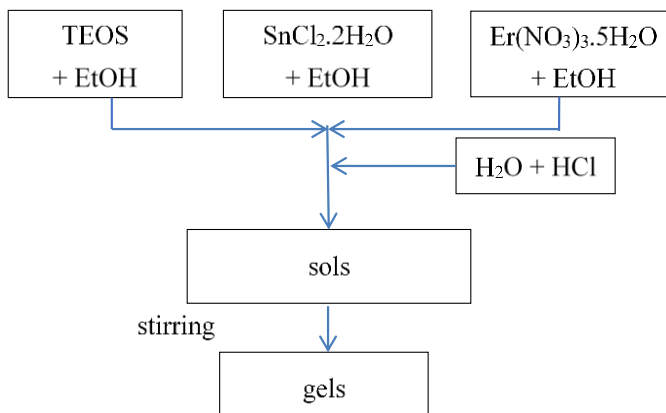


Figure 3.2 The flow-chart of the solution synthesis used for (100-x)SiO₂-xSnO₂:Er³⁺ monoliths

The details of the synthesis recipes and optimization of all the influential factors of the synthesis kinetics, the thermal treatment and the qualities of the final products are described in the following subsections.

3.4.1.1 Optimization of reactant ratios

3.4.1.1.1 H₂O/TEOS (R)

The effect of H₂O/TEOS (R) ratio in range $4 \leq R \leq 10$, which supports the 3D network structure as discussed in 3.3.4., on the gelation time and the dried-gel texture was explored for the solution synthesis of 10 mol% SnO₂ monoliths as listed in Table 3.4.

Table 3.4 Four H₂O/TEOS molar ratio (R) tested for the solution synthesis of 10 mol% SnO₂ monoliths

H ₂ O/TEOS R	HCl/EtOH/TEOS	Gelation time @RT	Obtained gels dried@65 °C
10	0.009/4/1	1 day	Transparent and less sensitive to crack
8		3 days	
6		2 weeks	Transparent and sensitive to crack
4		4 weeks	Cracked after dried

3.4.1.1.2 EtOH amount

Although EtOH plays an important role in forming the miscible homogeneous solutions, its evaporation is one of the factors inducing cracking especially in monolithic fabrication. Therefore, the ratio of EtOH/TEOS was limited to 4 which is just enough for solvating the four (C₂H₅O-) ligands of TEOS.

3.4.1.1.3 HCl/TEOS ratio

When SnCl₂.2H₂O and Er(NO₃)₃.5H₂O are dissolved into EtOH, their solvated complexes are strongly acidic [Barnum 1983], [Chiodini 1999]. Therefore, they catalysed the hydrolysis of Si and led to the fast gelation. To avoid such problem, different molar ratios of HCl/TEOS were tested. The results showed that the optimal HCl/TEOS ratio for the monolithic syntheses reduced dramatically from 0.5 in the solutions containing only Si⁴⁺ [Brinker 1988] and Er³⁺ down to 0.009 with the presence of Sn⁴⁺ in the solutions.

3.4.1.2 Final recipe

Based on the optimized reactant ratios, the final synthesis recipe was defined and summarized in Table 3.5.

Table 3.5 The final synthesis recipe of (100-x)SiO₂-xSnO₂:Er³⁺ monoliths

(100-x)SiO ₂ - xSnO ₂ :y Er ³⁺ monoliths (x, y: mol%)	H ₂ O/TEOS (R) (molar ratio)	HCl/TEOS (molar ratio)	EtOH/TEOS (molar ratio)
x = 0; y = 0.5	10	0.5	4
x = 5, 7.5 and 10 y = 0.25, 0.5, 1 and 1.5	10	0.009	4

Apart from the amount of EtOH listed in Table 3.5 mainly for the solvation of TEOS, a small extra EtOH amount was added to the solutions to dissolve SnCl₂.2H₂O and Er(NO₃)₃.5H₂O with the defined ratios as follows: 6.684 ml EtOH/1.064g SnCl₂.2H₂O and 1.671 ml

EtOH/ 0.209g $\text{Er}(\text{NO}_3)_3 \cdot 5\text{H}_2\text{O}$. Figure 3.3 shows the illustration for the formation of the colloidal particles in the final solution. The light scattering line passing through the solution is due to Tyndall effect and this is used to confirm and check the homogeneous formation of sol particles.

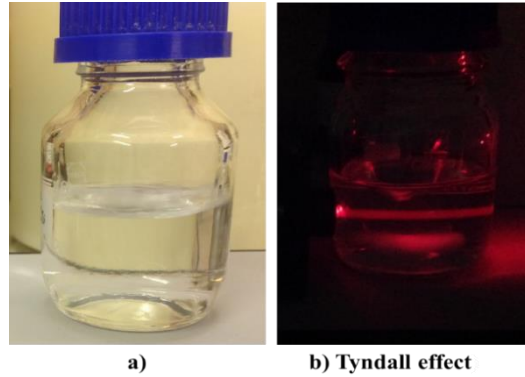


Figure 3.3 Photos of the final solution of $90\text{SiO}_2\text{-}10\text{SnO}_2\text{:}0.5\text{Er}^{3+}$ monolith synthesis: a) transparent solution under white light and b) Tyndall effect from the colloidal solution

3.4.2 Gelation

The fast gelation problem was observed when $\text{SnCl}_2 \cdot 2\text{H}_2\text{O}$ and $\text{Er}(\text{NO}_3)_3 \cdot 5\text{H}_2\text{O}$ were mixed together. They accelerate the gelation and lead to uncontrollable process as shown in Figure 3.4. Therefore, it is necessary to separate the solvated $\text{SnCl}_2 \cdot 2\text{H}_2\text{O}$ and $\text{Er}(\text{NO}_3)_3 \cdot 5\text{H}_2\text{O}$ when mixing. In addition, pouring the solution of H_2O and HCl slowly to the mixture help dropping the reaction rate. As a result, it was possible to control the viscosity of the solution. After last drop of H_2O and HCl , the solutions were stirred for 60 mins before transferred to the molds. Three different molds were used to obtain samples of monolithic squares, cylinders and big pillars for writing channel waveguides, solid state lasers and fiber preforms.

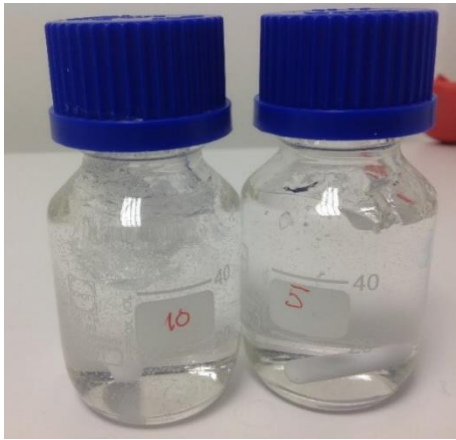


Figure 3.4 Photos of fast gelation of the solutions of $(100-x)\text{SiO}_2-x\text{SnO}_2:0.5\text{Er}^{3+}$ monolithic samples ($x = 5$ and $10 \text{ mol}\%$)

3.4.3 Aging and drying

After molding, the sols were kept sealed to proceed aging as shown in Figure 3.5.



Figure 3.5 Photo of $90\text{SiO}_2-10\text{SnO}_2:0.5\text{Er}^{3+}$ sols in the sealed molds (monolithic square and cylinder)

Aging is a continuous polycondensation process to construct the 3D structure of the monolithic samples. When all the polycondensation finished, the gel skeletal is formed and swelled inside the liquid phase, called wet-gels. To eliminate part of the residual liquid, the drying step was applied after aging.

Two different processes were applied to transform the gels to wet-gels and then dry-gels (see Figure 3.6). Adopted from [Armellini 1999], in process A, the sealed liquid-gels were put into the oven at 65°C for 7

days and then cooled down to room temperature. The covers of the molds were then perforated, and the samples were left at 35 °C to allow the gradual evaporation of the residual solvent. The drying process finished when there was no change in the weight of the samples. On the contrary, in process B, the sealed liquid gels were left aging at room temperature until the wet-gels were formed. Then, the covers of the molds were also perforated, and the samples were dried gradually up to 80 °C.

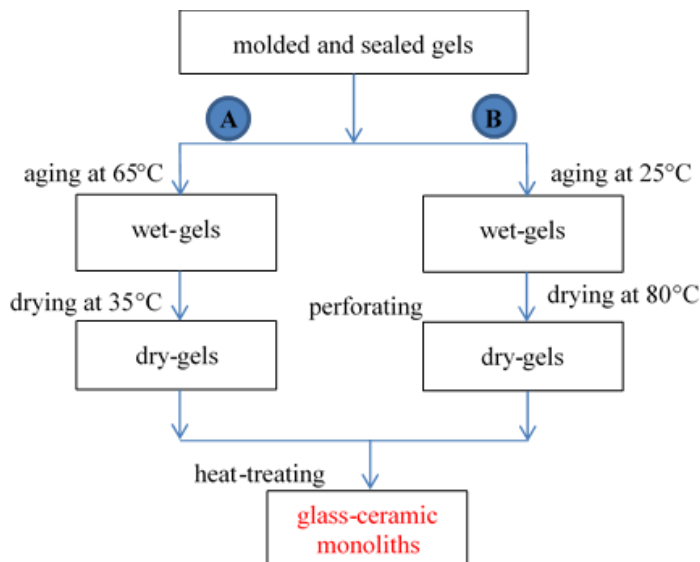


Figure 3.6 The flow-chart of two different processes of aging and drying the $90\text{SiO}_2\text{-}10\text{SnO}_2\text{:}0.5\text{Er}^{3+}$ gels

Figure 3.7 shows the photos of the xerogels obtained after the two aging and drying processes. One can see that the samples obtained from process A were more homogeneous. This is properly because in process A, the aging at 65 °C leads to more complete hydrolysis and condensation reactions inside the gels in comparison with process B.

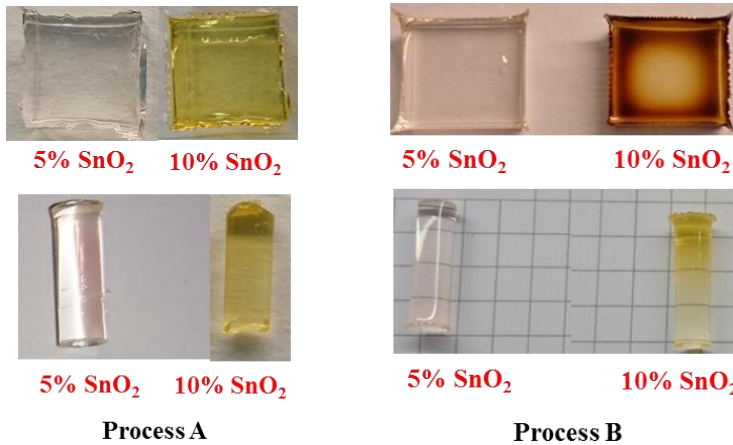


Figure 3.7 Photos of the as-prepared $(100-x)\text{SiO}_2\text{-}x\text{SnO}_2\text{:}0.5\text{Er}^{3+}$ monolithic square and cylinder xerogels obtained after two aging and drying processes ($x = 5$ and 10 mol%)

To check the viability for monoliths preparation of two aging and drying processes, several heat-treatment trials were applied on the two series of the obtained xerogels. The samples obtained from processes B usually had phase separation while the samples from process A showed good optical properties. This aspect is demonstrated in the photos of the $90\text{SiO}_2\text{-}10\text{SnO}_2\text{:}0.5\text{Er}^{3+}$ samples heat-treated at 900°C for 10h in Figure 3.8 below. Based on this, process A was eventually chosen to prepare the monoliths. Moreover, also from Figure 3.8, one can see the fracture problem occurred during the heat-treatment. Therefore, it was necessary to optimize the heat-treatment for the monolith preparation, which is discussed in detail in the following section.

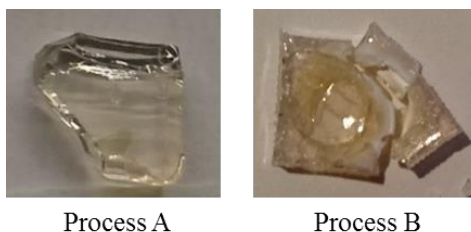


Figure 3.8 Photos of the as-prepared $90\text{SiO}_2\text{-}10\text{SnO}_2\text{:}0.5\text{Er}^{3+}$ monolithic squares obtained from two aging and drying processes after the heat-treatment trial at 900°C for 10h

3.4.4 Heat-treatment

3.4.4.1 Thermal analysis

Fracture problem during the synthesis processes has been one of the typical issues of sol-gel derived bulk fabrication [Shuo 2010]. To avoid such problem, the heat-treatment strategies for the monoliths were explored based on the thermal analyses. Figure 3.9 below shows the TG-DTA measurements of the undoped $95\text{SiO}_2\text{-}5\text{SnO}_2$ monoliths under the heating rate of $2^\circ\text{C}/\text{min}$ [Tran 2018b].

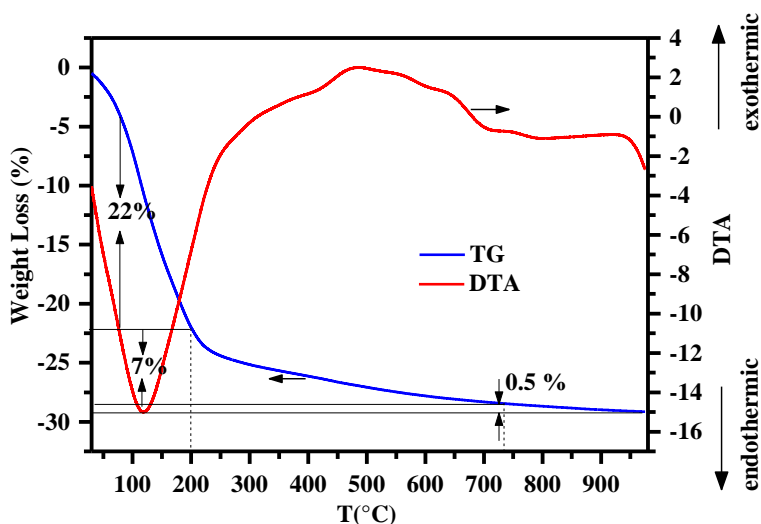


Figure 3.9 TG-DTA measurements of $95\text{SiO}_2\text{-}5\text{SnO}_2$ monoliths: acquired under the heating rate of $2^\circ\text{C}/\text{min}$

According to the work [Maziar 2015], the DTA curves in Figure 3.9 show endothermic features associated to two large weight losses observed well by TG. The first mass loss is 22%, from room temperature to 200 °C, whereas the second weight loss is 6%, from 200 °C to nearly 750 °C. Above 750 °C, the weight has a very small change 0.5%, which indicates that the gel was converted into a glass. Similar thermal characteristics were also observed in doped samples with different SnO₂ contents (5 and 10%).

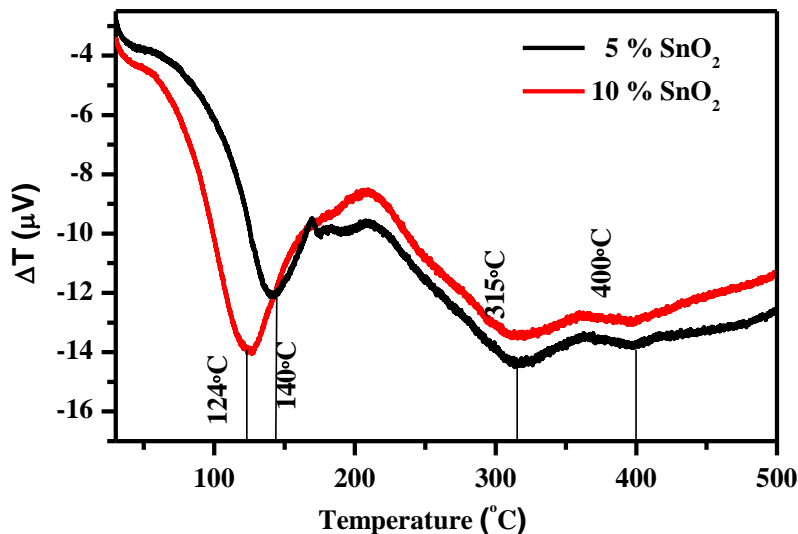


Figure 3.10 DSC curves of (100-x)SiO₂-xSnO₂:0.5Er³⁺ monoliths with different SnO₂ contents (x = 5 and 10 mol%)

To observe more clearly the transformation processes occurring at the first step of the heat-treatment, when the fracture easily happens, the detailed DSC curves shown in Figure 3.10 above were acquired under the same heating rate at intermediate temperature of the thermal treatment processes (35-500 °C). The first large endothermic feature changes slightly from 120 °C to 140 °C depending on SnO₂ contents. The first mass loss is related to the endothermic process of desorption of physically adsorbed water. Also, two endothermic features at about 310 °C and 400 °C corresponding to the decomposition of organics and chemisorbed hydroxy groups [Chiodini 2008] are quite well observed. The results are similar to those obtained for bioactive silica-zirconia based glasses using sol-gel route in [Ebendorff 1998] and it was suggested that the next mass loss stages can be attributed to the evolution

of the resulting sub-products from incomplete condensation of the precursors, mostly elimination of the nitrate ions as well as the nitrate decomposition in the studied samples.

3.4.4.1.1 Defined sintering process

Based on the discussed thermal analyses, the heat-treatment strategy for the $\text{SiO}_2\text{-SnO}_2\text{:Er}^{3+}$ monoliths was established. Different steps of slow sintering at moderate temperatures (25 °C - 400 °C) associated with the range in Figure 3.10 above were needed to avoid cracking. While the swelling at 130 °C was accounted for the elimination of physisorbed water, the ones at 300 °C and 400 °C was to remove the chemisorbed OH groups and burning of organic entities inside the xerogels groups [Chiodini 2008]. The next swelling step at 750 °C for 10 h was carried out to stabilize the samples before the last sintering at 900 °C. The sintering process at 900 °C were applied for different swelling time such as 40 h [Tran 2018a], 67 h and 100 h on the monoliths.

Eventually, the sintering at 900 °C for 100 h shown in Figure 3.11 gives the better performance on removal of water and densification of the monoliths. Figure 3.12 shows the absorption spectra of the $90\text{SiO}_2\text{-}10\text{SnO}_2\text{:}0.5\text{Er}^{3+}$ monoliths after different steps of heat-treatment from dried gel, to thermal treatment at 900 °C for 40 h, 67 h and 100 h. As one can see from Figure 3.12, the heat-treatment at 900 °C for 100 h induced a significant removal of residual organic groups and water from the sol-gel synthesis as indicated by the disappearance of their broad absorption bands in the NIR region. Although the absorption band centered at 2656 nm assigned to the fundamental –OH asymmetric stretching vibration ν_3 band (3675cm^{-1}) still presents, the band centered at 1386 nm assigned to two –OH stretching vibrations [Grzechnik 1998], which directly competes Er^{3+} luminescence at 1.5 μm [Righini 2005] was reduced significantly when the monoliths were heat-treated at 900 °C for 100 h.

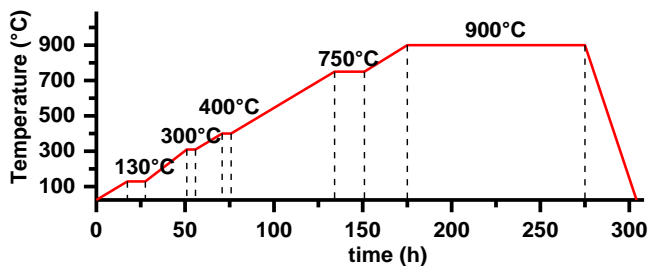


Figure 3.11 Chart of the heat-treatment process for $(100-x)\text{SiO}_2-x\text{SnO}_2:0.5\text{Er}^{3+}$ monoliths ($x = 0, 5$ and 10 mol%)

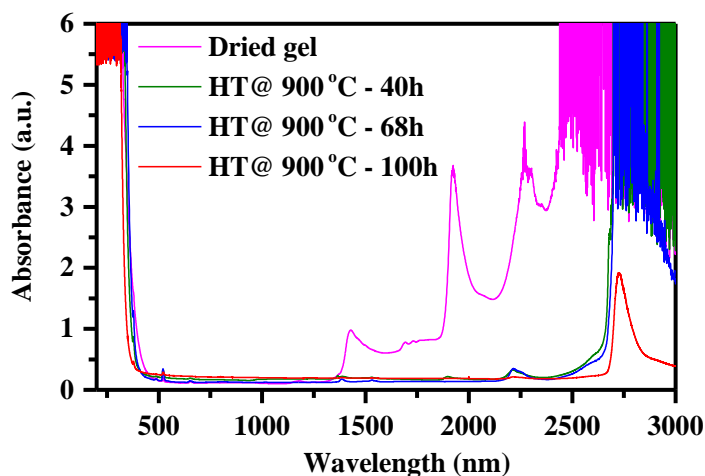


Figure 3.12 Absorption spectra of the $90\text{SiO}_2\text{-SnO}_2:0.5\text{Er}^{3+}$ monoliths after different steps of heat-treatment: from dried gel, to thermal treatment at 900°C for 40 h, 67 h and 100 h.

3.4.5 Obtained monoliths

With the optimized synthesis protocol and heat-treatment process, the monoliths containing up to 10 mol% SnO_2 were obtained. Photos in Figure 3.13 shows some examples of the monolithic square and cylinder obtained after heat-treatment at 900°C for 100 h.



Figure 3.13 Photos of $90\text{SiO}_2\text{-}10\text{SnO}_2\text{:}0.5\text{Er}^{3+}$ monolithic square ($1\times 1\text{ cm}^2$ cross section and 0.3 cm height) and cylinder (0.5 cm diameter and 1.5 cm height) obtained after heat-treatment at $900\text{ }^\circ\text{C}$ for 100h

This synthesis protocol also allows preparing the big pillar shown in Figure 3.14, which can be used as fiber preform.



Figure 3.14 Photos of $95\text{SiO}_2\text{-}5\text{SnO}_2\text{:}0.5\text{Er}^{3+}$ big pillar with diameter of 1 cm and length of 3.3 cm obtained after heat-treatment at $900\text{ }^\circ\text{C}$ for 100h

All the $(100-x)\text{SiO}_2\text{-}x\text{SnO}_2$ monoliths ($x = 5, 7.5$ and $10\text{ mol}\%$) are glass-ceramics containing small SnO_2 nanocrystals. From Figure 3.15, one can see the presence of SnO_2 nanocrystals in the $95\text{SiO}_2\text{-}5\text{SnO}_2\text{:}0.5\text{Er}^{3+}$ monolith based on XRD patterns, which are comparable to SnO_2 rutile crystal phase from cassiterite mineral (JCPDS 41-1445). The small nanosizes of SnO_2 will be assessed and discussed in the section 4.4 in the next chapter.

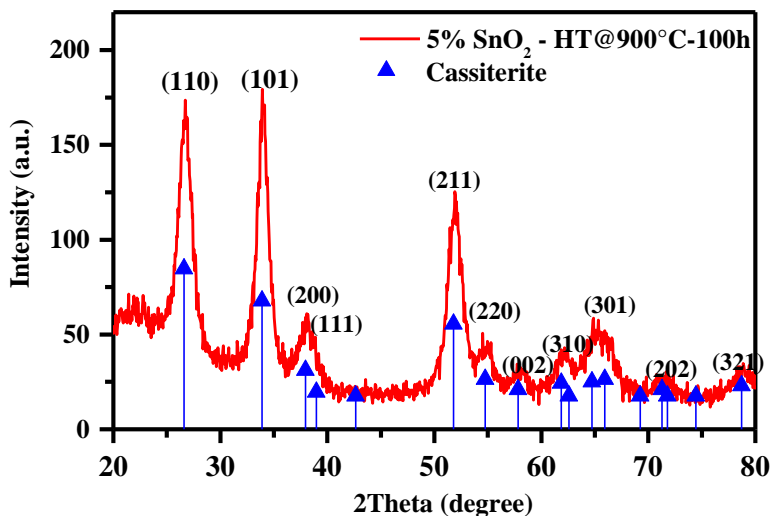


Figure 3.15 XRD patterns of 95SiO₂-5SnO₂:0.5Er³⁺ monoliths obtained after heat-treatment at 900 °C for 100h in comparison with SnO₂ rutile crystal phase from cassiterite mineral (JCPDS 41-1445)

3.5 Planar waveguides

3.5.1 Solution preparation

For the planar waveguides, the goal was to build the 2D structure. Therefore, the viscosity of the solutions for the planar waveguides was maintained much lower than the ones for the monoliths. To obtain such solutions, the small reactant ratios of 2 and 0.0037 were chosen for H₂O/TEOS and HCl/TEOS respectively. In addition, it was necessary to use very high EtOH amounts. For the pure SiO₂ planar waveguides doped with 0.5 mol% Er³⁺, the EtOH/TEOS ratio was only 33.8. However, the addition of SnCl₂·2H₂O led to faster reaction and consequently higher viscosity of the solutions. Therefore, an extra EtOH amount with molar ratio to TEOS varying from 2.0 to 16.4 was needed to dilute the solutions, with increasing SnO₂ contents from 5 to 30 mol%. In case of the 70SiO₂-30SnO₂ planar waveguides, different concentrations of Er³⁺ (0, 0.5, 1 and 1.5 mol%) were used. However, since Er³⁺ concentrations were very small, it was not necessary to add any extra EtOH accounting for it. The details of the synthesis recipe of

(100-x)SiO₂-xSnO₂:yEr³⁺ planar waveguides were described in Table 3.6.

Table 3.6 The synthesis recipe of (100-x)SiO ₂ -xSnO ₂ :yEr ³⁺ planar waveguides			
Composition (100-x)SiO ₂ - xSnO ₂ :yEr ³⁺	H ₂ O/TEOS (R) (molar ratio)	HCl/TEOS (molar ratio)	EtOH/TEOS (molar ratio)
x = 0; y = 0.5	2	0.0037	33.8
x = 5; y = 0.5	2	0.0037	35.8
x = 10; y = 0.5	2	0.0037	38.1
x = 15; y = 0.5	2	0.0037	40.6
x = 20; y = 0.5	2	0.0037	43.4
x = 25; y = 0.5	2	0.0037	46.6
x = 30; y = 0.5	2	0.0037	50.2
x = 30; y = 0	2	0.0037	
x = 30; y = 1	2	0.0037	
x = 30; y = 1.5	2	0.0037	

The synthesis process can be described as follows:

To obtain 60 ml of the final solutions, the two halves of the volume were separated for the two solutions, one containing TEOS and the other containing SnCl₂.2H₂O and Er(NO₃)₃.5H₂O. Tetraethyl orthosilicate (TEOS), de-ionized water, and hydrochloric acid with the molar ratios of 1:2:0.0037 were mixed together into a certain amount of ethanol to reach 30 ml of solution 1. In solution 2, the two precursors, SnCl₂.2H₂O and Er(NO₃)₃.5H₂O, were dissolved in 30 ml of ethanol. After 60 mins of stirring, the two solutions were mixed together, and the final mixture was stirred for 16 h at room temperature. The final solutions were filtered with 200 nm Millipore filters and then used for the planar waveguide deposition. The preparation steps of the planar waveguides can be briefly illustrated in Figure 3.16.

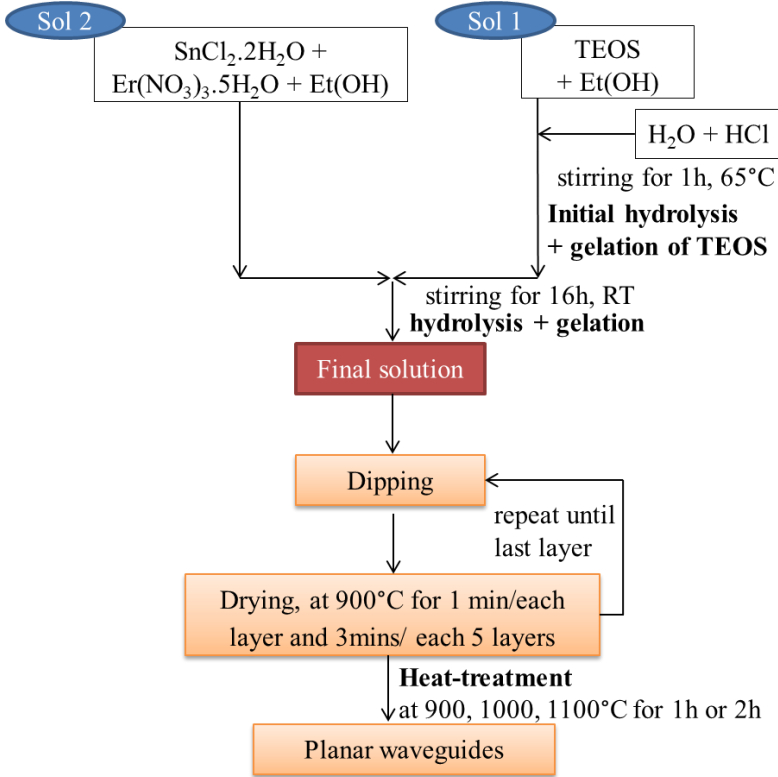


Figure 3.16 Schematic diagram of the preparation of the (100-x)SiO₂-xSnO₂: %Er³⁺ planar waveguides

3.5.2 Deposition

3.5.2.1 General dip-coating procedure

The deposition of the planar waveguides was carried out by employing dip-coating technique. According to [Brinker 2013], general dip-coating processes include three consecutive stages: (i) immersion and dwell time, (ii) deposition and drainage, and (iii) evaporation. In case of (100-x)SiO₂-xSnO₂:yEr³⁺ planar waveguides, the deposition process can be specified as follows:

- Before starting the first stage, i.e. immersion and dwell time, the prepared solutions were transferred into a Teflon container, which played important role in keeping the solution stable during the deposition. Then, the substrate made of vitreous silica or silicon was immersed into the solution. The immersion speed

and dwelling time in this stage were not the most critical factors and they were chosen to allow the substrate to interact and completely covered by the solution. In this work, the constant immersion speed of 7.2 cm/min and the dwell time of 0.5 min were sufficient for such purposes.

- The withdraw speed was the more important factor since it governs the entraining of the solution on the substrate and the draining of the excess liquid to form the thin layer. An example of the withdrawing step in the planar waveguide deposition is illustrated in Figure 3.17.

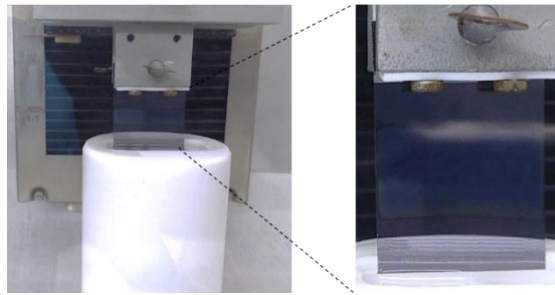


Figure 3.17 The photo of the withdrawing step of the dip-coating process for a planar waveguide deposition on silicon substrate. One can see the entraining of the solution on the substrate and the draining of the excess liquid to form the thin layer in the image on the right side.

- To promote the evaporation of the solvent, a temporary annealing at 900 °C for 1 min was needed before the next dip-coating turn. In addition, after every 5 layers, the drying time at 900 °C was prolonged up to 3 minutes.

3.5.2.2 Optimization of withdraw speed

Since the target is to achieve as high as possible the SnO_2 content, the optimization has been applied on the planar waveguide with 30 mol% SnO_2 , i.e. the highest one. In the dip-coating procedure, withdraw speed is one crucial factor since it defines the textural properties of the deposited layer. Therefore, among the working range of the dip-coater, four different withdraw speeds (4, 5.6, 7.2 and 8.8 cm/min) were chosen. The detailed parameters used for optimizing the dip-coating deposition of $(100-x)\text{SiO}_2-x\text{SnO}_2:y\text{Er}^{3+}$ planar waveguides were listed in Table 3.7.

Table 3.7 The parameters of dipping processes of 70SiO₂-30SnO₂:0.5Er³⁺ planar waveguides

Stage 1: Immersion & dwell time		Stage 2: Deposition & drainage	Stage 3: Evaporation	
constant immersion speed (cm/min)	dwell time (min)	constant withdraw speeds (cm/min)	T (°C)	t (min)
7.2	0.5	4.0	900	1 min/ each layer 3 mins/ each 5 layers
		5.6		
		7.2		
		8.8		

There was no significant change of the thickness between the planar waveguides deposited at different withdraw speeds as shown in Figure 3.18.

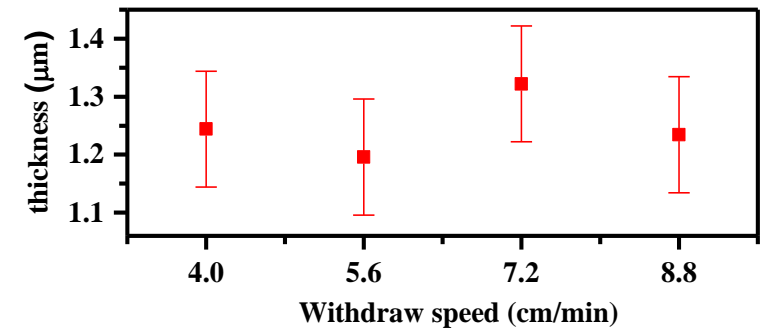


Figure 3.18 Thicknesses measured by m-line technique of the planar waveguides deposited at different withdraw speeds after heat-treatment at 1000 °C for 60 mins

From the Figure 3.19, except the planar waveguide deposited at withdraw speed of 4.0 cm/min, the others exhibit a step-index profile, which is an important factor for confining propagating light in the planar waveguides.

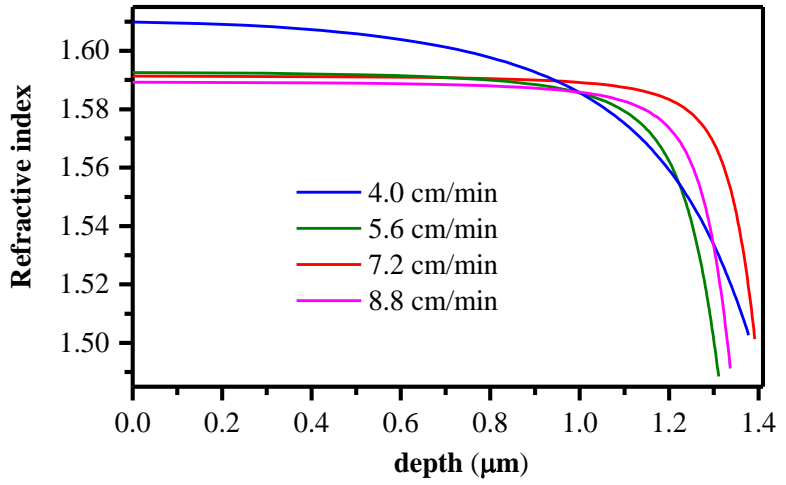


Figure 3.19 Index profiles ($\lambda = 543.5$ nm) of the planar waveguides deposited at different withdraw speeds after heat-treatment at 1000 °C for 60 mins

However, the planar waveguide deposited at the withdraw speed of 7.2 cm/min yields the lowest roughness of 1.8 nm in comparison with the others as shown in Figure 3.20. This helps reducing the propagation losses due to the surface scattering, which is an important requirement for applications in integrated optics. Therefore, based on the criteria of the step-index profile and low roughness, the withdraw speed of 7.2 cm/min was chosen to deposit all the final products of the compositional planar waveguides.

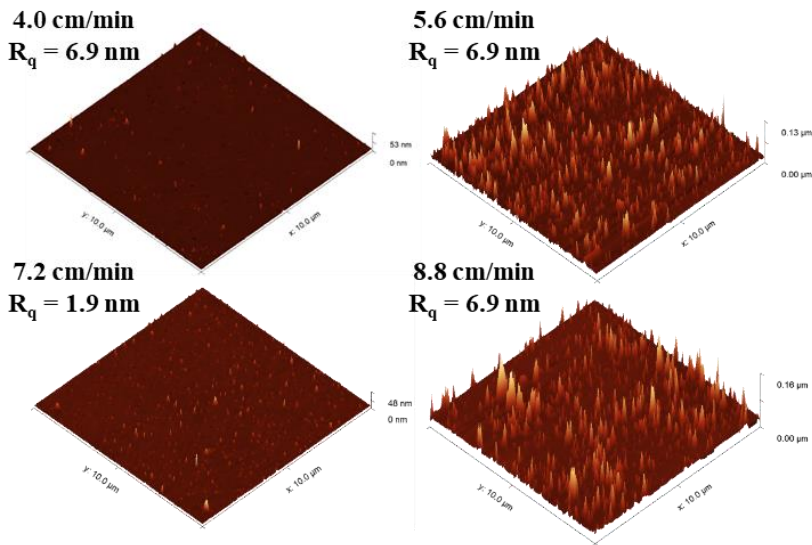


Figure 3.20 3D AFM images and the root mean square roughness of the 70SiO₂-30SnO₂:0.5Er³⁺ planar waveguides deposited by different withdraw speeds (4.0, 5.6, 7.2 and 8.8 cm/min) after heat-treatment at 1000 °C for 60 mins

3.5.3 Heat-treatment

To eliminate all the residual components of the final 25-layer planar waveguides, a further heat-treatment is necessary. In case of the (100-x)SiO₂-xSnO₂:yEr³⁺ planar waveguides, the heat-treatment is even more essential to induce the crystallization of SnO₂. All the drying steps and heat-treatment were carried out in a tubular oven as shown in Figure 3.21. The optimization of the annealing temperature and time has been also carried out on the highest SnO₂ content planar waveguide, i.e. 70SiO₂-30SnO₂:0.5Er³⁺.



Figure 3.21 The photo of the tubular oven dedicated for the heat-treatment of the planar waveguides

3.5.3.1 Optimization of annealing temperature

Different annealing temperature 900, 1000 and 1100 °C were tested to find the optimal condition for the preparation of the glass-ceramic planar waveguides. Figure 3.22 shows micro-Raman spectra of the planar waveguides after different annealing temperature for 60 mins. The Raman spectrum of the 900 °C annealed planar waveguide reveals a non-constructed SiO_2 network accompanied by a broad band centered at 2500 cm^{-1} Raman shift due to defects. At higher annealing temperatures, this band disappears, and no observable characteristic bands centered at 3670 and 3750 cm^{-1} indicates the removal of OH groups which is one of the causal factors of Er^{3+} luminescence quenching [Righini 2005], [Gonçalves 2002]. However, the heat-treatment at 1100 °C leads to the disruption of silica network indicated by appearance of the band centered at 330 cm^{-1} . This effect leads to localized micro phase separation, which reduced the optical quality of the planar waveguide as one can see from the dots ($20 \mu\text{m}$ size) in the inset microscope image of the 1100 °C annealed planar waveguide in Figure 3.22. On the other hand, the Raman spectrum of the 1000 °C annealed planar waveguide reveals a typical Raman feature of densified silicate glasses. Therefore, the annealing temperature at 1000 °C is sufficient to achieve the complete densification of all planar waveguides.

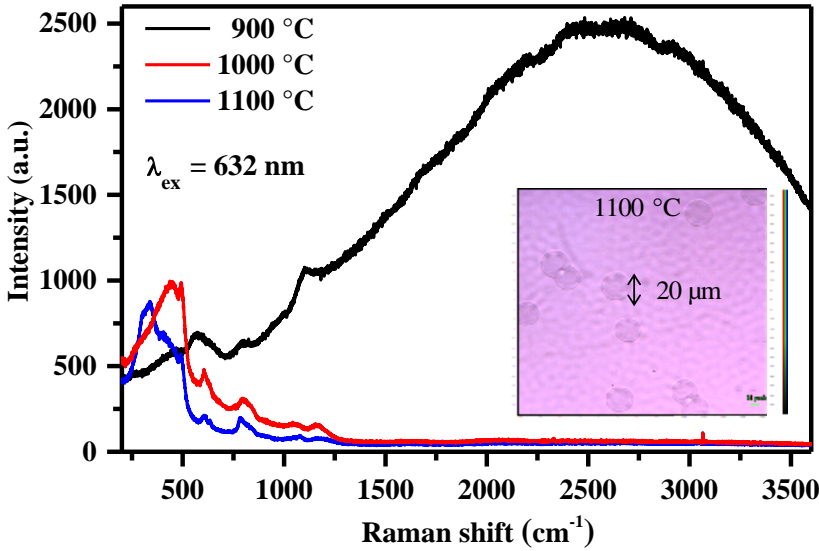


Figure 3.22 Visible micro-Raman spectra ($\lambda_{ex} = 633\text{nm}$) of the $70\text{SiO}_2\text{-}30\text{SnO}_2\text{:}0.5\text{Er}^{3+}$ planar waveguides after different heat-treatment temperatures (900, 1000 and 1100 °C) for 60 mins. The inset image is the microscope image of the planar waveguide annealed at 1100 °C for 60 mins with a micro-phase separation which reduced the optical quality of the glass-ceramics

3.5.3.2 Optimization of annealing time

The heat-treatment at 1000 °C for two annealing time of 60 mins and 120 mins were applied on $70\text{SiO}_2\text{-}30\text{SnO}_2\text{:}0.5\text{Er}^{3+}$ planar waveguides. However, no significant changes in spectroscopic, structural and optical properties were observed in the two planar waveguides. XRD patterns in Figure 3.23 and index profiles in Figure 3.24 are some of the indications for this. Therefore, the heat-treatment at 1000 °C for 60 mins was sufficient to obtain the densified planar waveguides with good optical quality and it was chosen for the fabrication of all the $\text{SiO}_2\text{-SnO}_2\text{:Er}^{3+}$ glass ceramic planar waveguides.

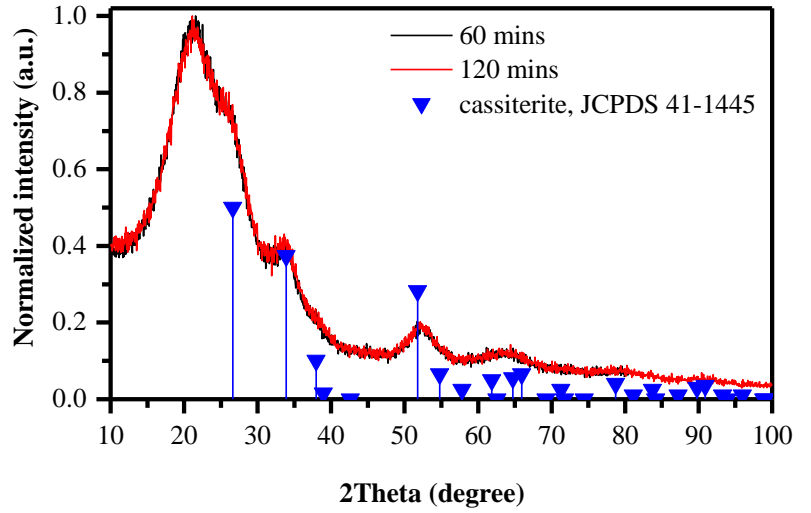


Figure 3.23 XRD patterns of the $70\text{SiO}_2\text{-}30\text{SnO}_2\text{:}0.5\text{Er}^{3+}$ planar waveguides heat-treated at $1000\text{ }^\circ\text{C}$ for 60 mins and 120 mins in comparison with SnO_2 rutile crystal phase from cassiterite mineral (JCPDS 41-1445)

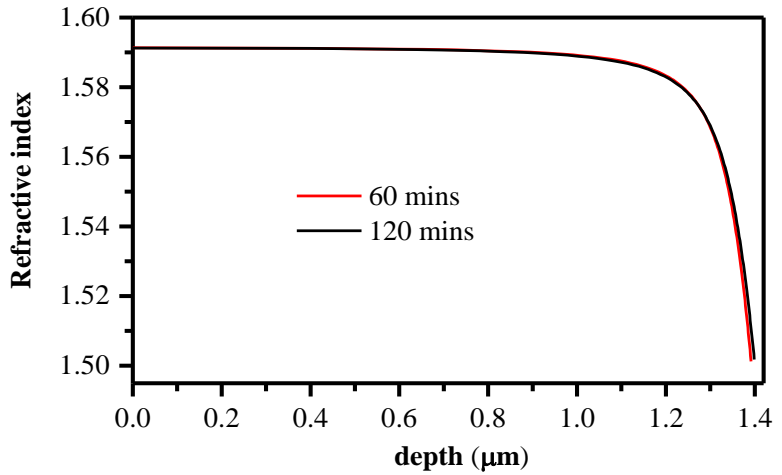


Figure 3.24 Index profiles ($\lambda = 543.5\text{ nm}$) of the $70\text{SiO}_2\text{-}30\text{SnO}_2\text{:}0.5\text{Er}^{3+}$ planar waveguides heat-treated at $1000\text{ }^\circ\text{C}$ for 60 mins and 120 mins

3.5.4 Obtained planar waveguides

All the obtained planar waveguides are glass-ceramics with the presence of SnO₂ nanocrystals which exhibit XRD patterns of SnO₂ rutile crystal phase from cassiterite like in case of the 70SiO₂-30SnO₂:0.5Er³⁺ planar waveguide shown in Figure 3.23 . One can see the photo of a transparent 70SiO₂-30SnO₂:0.5Er³⁺ planar waveguide in Figure 3.25.



Figure 3.25 The example of the transparent 70SiO₂-30SnO₂:0.5Er³⁺ planar waveguide obtained after the heat-treatment at 1000 °C for 60 mins

All the compositional (100-x)SiO₂-SnO₂:0.5Er³⁺ planar waveguides (x = 5, 10, 15, 20, 25 and 30 mol%) exhibit high transparency as one can see from Figure 3.26. The absorption band centered at 2656 nm assigned to the fundamental –OH asymmetric stretching vibration ν_3 band (3675cm⁻¹) is attributed mainly from v-SiO₂ substrate [Schleife 2011].

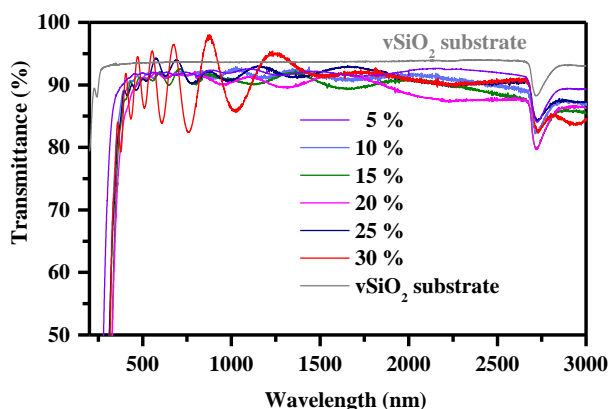


Figure 3.26 Transmission spectra of the compositional (100-x)SiO₂-SnO₂:0.5Er³⁺ planar waveguides (x = 5, 10, 15, 20, 25 and 30 mol%) in comparison with v-SiO₂ substrate

One unexpected feature of the planar waveguides was figured out. After different characterization techniques such as AES, XRD and AFM, the two sides of the coatings appeared to be inequivalent. Surprisingly, there is no evidence of the presence of tin on the bottom-side of the coating. Therefore, all the photonic assessments and processing were carried out on the top-side coating of the planar waveguides.

3.6 Conclusions

By optimizing the involved fabrication parameters, the reliable sol-gel synthesis protocols with defined thermal processes have been defined for the preparation of compositional planar waveguides and monoliths. Concerning the monoliths fabrication, the fast gelation issue is controllable, and this allows introducing up to 10 mol% SnO₂ nanocrystals in SiO₂ matrix. The thermal analyses help defining the proper heat-treatment strategy to avoid the typical fracture problem of sol-gel derived bulk fabrication. After the heat-treatment at 900 °C for 100 h, the homogeneous and transparent glass-ceramic monoliths are obtained. The monolithic squares (cross section of 1×1 cm² and height of 0.3 cm) are produced for writing channel waveguides. The cylinders (diameter of 0.5 cm and height of 1.5 cm) are fabricated aiming to solid state laser construction. In addition, the versatility of this method allows the fabrication of big pillars with diameter of 1 cm and length of 3.3 cm which can be used as fiber preforms. Referring to the planar waveguide fabrication, the adjustment of the synthesis protocol was carried out to embed up to 30 mol% SnO₂ nanocrystals in the SiO₂ matrix but still maintain the low solution viscosity to obtain homogeneous deposition. The withdraw speed of the dip-coating process was optimized to deposit the planar waveguides with low roughness and step-index profile which are crucial factors for the integrated waveguide laser application. The proper thermal treatment was also defined to obtain densified glass-ceramic planar waveguides with high optical quality.

To assess the applicability of the obtained systems for the solid state and integrated laser fabrication, a rich number and variety of experimental characterization techniques were employed. Therefore, in next chapter, Chapter 4 Experimental assessments, a comprehensive characterization of the compositional, structural, morphological, and spectroscopic properties of the glass-ceramic planar waveguides and monoliths will be discussed.

References

- [Armellini 1999] Armellini C., Ferrari M., Montagna M., Pucker G., Bernard C., & Monteil A., “Terbium (III) doped silica-xerogels : effect of aluminium (III)”, *Journal of Non-Crystalline Solids*, 245(1-3), pp. 115–121(1999), doi: 10.1016/S0022-3093(98)00856-4.
- [Barnum 1983] Barnum D. W., “Hydrolysis of Cations. Formation Constants and Standard Free Energies of Formation of Hydroxy Complexes”, *Inorganic Chemistry*, 22(16), pp. 2297–2305(1983), doi: 10.1021/ic00158a016.
- [Bernards 1991] Bernards T. N. M., Bommel M. J. Van, & Boonstra A. H., “Hydrolysis-condensation processes of the tetra-alkoxysilanes TPOS, TEOS and TMOS in some alcoholic solvents”, *Journal of Non-Crystalline Solids*, 134, pp. 1–13(1991), doi: 10.1016/0022-3093(91)90005-Q.
- [Bhaktha 2009] Bhaktha B N Shivakiran, Kinowski Christophe, Bouazaoui Mohamed, Capoen Bruno, Robbe-cristini Odile, Beclin Franck, Roussel Pascal, Ferrari Maurizio & Turrell Sylvia, “Controlled Growth of SnO₂ Nanocrystals in Eu³⁺ -Doped SiO₂ - SnO₂ Planar Waveguides : A Spectroscopic Investigation”, *Physical Chemistry C*, 113(52), pp. 21555–21559 (2009), doi: 10.1021/jp907764p.
- [Brambilla 2000] Brambilla G., Pruneri V., & Reekie L., “Photorefractive index gratings in SnO₂:SiO₂ optical fibers”, *Applied Physics Letters*, 76(7), pp. 807-809 (2000), doi:10.1063/1.125591.
- [Brambilla 2001] Brambilla G., Pruneri V., Reekie L., Paleari A., Chiodini N., Booth H., “High Photosensitivity in SnO₂:SiO₂ Optical Fibers”, *Fiber & Integrated Optics*, 20(6), pp. 553–564(2001), doi: 10.1080/014680301317080990.
- [Brinker 1988] Brinker, C. J., “Hydrolysis and condensation of silicates: effects on structure”, *Journal of Non-Crystalline Solids*, 100(1–3), pp. 31–50(1988), doi: 10.1016/0022-3093(88)90005-1.
- [Brinker 2013] Brinker, C. J., “Chapter 10 Dip coating”, *Chemical Solution Deposition of Functional Oxide Thin Films*, pp. 233–261(2013), doi: 10.1007/978-3-211-99311-8.
- [Cascales 2018] Cascales, C., Balda, R., Lezama, L., & Fernández, J. (2018), “Site symmetry and host sensitization-dependence of Eu³⁺ real time luminescence in tin dioxide nanoparticles”, *Optic Express*, 26(13), pp. 16155–16170, doi: 10.1364/OE.26.016155.

- [Chiodini 1999] Chiodini N., Morazzoni F., Paleari A., Scotti R., & Spinolo G., “Sol-gel synthesis of monolithic tin-doped silica glass”, *Materials Chemistry*, 9, pp. 2653–2658(1999), doi: 10.1039/A904415I.
- [Chiodini 2008] Chiodini, N., Morazzoni, F., & Scotti, R., “Monolithic Tin-doped Silica Glass”, *Materials Syntheses: A Practical Guide*, pp. 169–177(2008), doi: 10.1007/978-3-211-75125-1.
- [De Pablos-Martin 2015] De Pablos-Martin A., Ferrari M., Pascual M. J. & Righini G. C., “Glass-ceramics: A class of nanostructured materials for photonics. *Rivista Del Nuovo Cimento*”, 38(7–8), pp. 311–369(2015), doi: 10.1393/ncr/i2015-10114-0.
- [Dymshits 2017] Dymshits O., Shepilov M., & Zhilin A., “Transparent glass-ceramics for optical applications”, *MRS Bulletin*, 42(3), pp. 200–205(2017), doi: 10.1557/mrs.2017.29.
- [Ebendorff-Heidepriem 1998] Ebendorff-Heidepriem H. & Ehrt D. (1998), “Optical spectroscopy of rare earth ions in glasses”, *Glass Science and Technology*, 71(10), pp. 289–300(1998).
- [Gonçalves 2002a] Gonçalves M. C., Santos, L. F., & Almeida, R. M., “Rare-earth-doped transparent glass ceramics”, *Comptes Rendus Chimie*, 5(12), pp. 845–854(2002), doi: 10.1016/S1631-0748(02)01457-1.
- [Gonçalves 2002b] Gonçalves R. R., Carturan G., Zampedri L., Ferrari M., Montagna M., Chiasera A., Righini G.C., Pelli S., Ribeiro S. J. L. & Messaddeq, Y., “Sol-gel Er-doped SiO₂-HfO₂ planar waveguides: A viable system for 1.5 μ m application”, *Applied Physics Letters*, 81(1), pp. 28–30(2002), doi: 10.1063/1.1489477.
- [Gorni 2018] Gorni G., Velázquez J. J., Mosa J., Rolindes B., Joaquin F., Alicia D., Castro Y., “Transparent glass-ceramics produced by Sol-Gel: A suitable alternative for photonic materials”, *Materials*, 11(212), pp. 1–30(2018), doi: 10.3390/ma11020212.
- [Granger 2014] Granger G., Restoin C., Roy P., Jamier R., Rougier S., Lecomte A., Blondy J. M., “Nanostructured optical fibers in the SiO₂/SnO₂ system by the sol-gel method”, *Materials Letters*, 120, pp. 292–294(2014), doi: 10.1016/j.matlet.2014.01.104.
- [Hayakawa 2002] Hayakawa T., Enomoto T., & Nogami M., “Nanocrystalline SnO₂ particles and twofold-coordinated Sn defect centers in sol-gel-derived SnO₂ – SiO₂ glasses”, *Journal of Materials Research*, 17(6), pp. 1305–1311(2002), doi: 10.1557/JMR.2002.0195.

- [Jeffrey 2013] Jeffrey Brinker C., & Scherer G. W., “Sol-gel science: the physics and chemistry of sol-gel processing”, Academic press(2013), doi: 10.1002/adma.19910031025.
- [Kajihara 2013] Kajihara K., “Recent advances in sol–gel synthesis of monolithic silica and silica-based glasses”, *Journal of Asian Ceramic Societies*, 1(2), pp. 121–133(2013), doi: 10.1016/j.jascer.2013.04.002.
- [Maziar 2015] Maziar M., Schneider J. F., Yekta B. E., Marghussian V. K., Rodrigues A. M. & Zannotto E. D., “Sol–gel, synthesis, structure, sintering and properties of bioactive and inert nano-apatite–zirconia glass–ceramics”, *Ceramics International*, 41, pp. 11024–11045(2015), doi: 10.1016/j.ceramint.2015.05.047.
- [Nogami 1980] Nogami M., & Moriya Y. “Glass formation through hydrolysis of $\text{Si}(\text{OC}_2\text{H}_5)_4$ with NH_4OH and HCl solution”, *Journal of Non-Crystalline Solids*, 37(2), pp. 191–201(1980), doi: 10.1016/0022-3093(80)90150-7.
- [Nogami 2003] Nogami, M., Ohno, A., & You, H. (2003). “Laser-induced SnO_2 crystallization and fluorescence properties in Eu^{3+} -doped SnO_2 - SiO_2 glasses”, *Physical Review B*, 68(10), pp. 104204(1-7), doi: 10.1103/PhysRevB.68.104204.
- [Palaeri 2006] Palaeri A., Franchina E., Chiodini N., & Lauria A. “ SnO_2 nanoparticles in silica: Nanosized tools for femtosecond-laser machining of refractive index patterns”, *Applied Physics B: Lasers and Optics*, 88, pp. 131912(1-3) (2006), doi: 10.1063/1.2192579.
- [Pope 1986] Pope E. J. & Mackenzie J. D., “Sol-gel processing of silica: II. The role of the catalyst”, *Journal of Non-Crystalline Solids*, 87(1–2), pp.185–198(1986), doi: 10.1016/S0022-3093(86)80078-3.
- [Quang 2015] Quang B., Ngoc N., Ngoc T., & Duc N., “Correlation between SnO_2 nanocrystals and optical properties of Eu^{3+} ions in SiO_2 matrix : Relation of crystallinity, composition, and photoluminescence”, *Journal of Luminescence*, 163, 28–31(2015), doi: 10.1016/j.jlumin.2015.03.002.
- [Righini 2005] Righini G. C., & Ferrari M, “Photoluminescence of rare-earth-doped glasses”, *Rivista Del Nuovo Cimento*, 28(12), pp. 1–53(2005), doi: 10.1393/ncr/i2006-10010-8.
- [Shuo 2010] Shuo W., Qingnan Z., Dengkui M., & Yuhong D., “Synthesis and characterization of Sb-doped SnO_2 -(CeO_2 - TiO_2) composite thin films deposited on glass substrates for antistatic electricity and UV-shielding”, *Journal of Rare Earths*, 28, pp. 189–193(2010), doi: 10.1016/S1002-0721(10)60377-8.

[Tran 2018a] Tran T.N. L., Massella D., Zur L., Chiasera A., Varas S., Armellini C., Righini C. G., Lukowiak A., Zonta D., Ferrari M., “SiO₂-SnO₂:Er³⁺ glass-ceramic monoliths”. *Applied Sciences*, 8(8), pp. 1335(1-8) (2018), doi: 10.3390/app8081335.

[Tran 2018b] L. T. N. Tran, L. Zur, D. Massella, B. Derkowska-Zielinska, A. Chiasera, S. Varas, C. Armellini, A. Martucci, D. Zonta, T. T. V. Tran, A. Lukowiak, S. Taccheo, D. Dorosz, G. C. Righini, Y. G. Boucher, M. Ferrari, “SiO₂-SnO₂:Er³⁺ transparent glass-ceramics: fabrication and photonic assessment”, *Proceeding of SPIE. 10683, Fiber Lasers and Glass Photonics: Materials through Applications*, 10638, pp. 106832C(1-10), doi: 10.1117/12.2306767.

[Van 2010] Van T. T., Turrell S., Eddafi M., Capoen B., Bouazaoui M., Roussel P., Berneschi S., Righini G., Ferrari M., Bhaktha S. N. B., Cristini O., Kinowski C., “Investigations of the effects of the growth of SnO₂ nanoparticles on the structural properties of glass-ceramic planar waveguides using Raman and FTIR spectroscopies”, *Journal of Molecular Structure*, 976(1–3), pp. 314–319(2010), doi: 10.1016/j.molstruc.2010.04.010.

[Van 2014] Tran T. T. Van, S. Turrell, B. Capoen, Le V. H., M. Ferrari, Davor R., Boussekey L., Kinowski C., “Environment segregation of Er³⁺ emission in bulk sol-gel-derived SiO₂-SnO₂ glass ceramics”, *Journal of Materials Science*, 49(24), 8226–8233(2014), doi: 10.1007/s10853-014-8531-6.

[Van 2015] Van T. T. T., Turrell S., Capoen B., Vinh L. Q., Cristini-Robbe O., Bouazaoui M., D’Acapito F., Ferrari M., Ristic D., Lukowiak A., Almeida R., Santos L., Kinowski C., “Erbium-Doped Tin-Silicate Sol–Gel-Derived Glass-Ceramic Thin Films: Effect of Environment Segregation on the Er³⁺ Emission”, *Science of Advanced Materials*, 7(2), pp. 301–308(2015), doi: 10.1166/sam.2015.2022.

[Yanes 2010] Yanes A. C., Méndez-Ramos J., Del-Castillo J., Velázquez J. J., & Rodríguez V. D., “Size-dependent luminescence of Sm³⁺ doped SnO₂ nano-particles dispersed in sol-gel silica glass”. *Applied Physics B: Lasers and Optics*, 101(4), pp. 849–854(2010), doi: 10.1007/s00340-010-4331-0.

[Yu 2011] Yu Y., Chen D., Huang P., Lin H., Yang A., & Wang Y.. “Distribution-related luminescence of Eu³⁺ sensitized by SnO₂ nano-crystals embedding in oxide glassy matrix”, *Journal of Solid State Chemistry*, 184(2), pp. 236–240(2011), doi: 10.1016/j.jssc.2010.11.021.

[Zatsepin 2012] Zatsepin A. F., Buntov E. A., Kortov V. S., Pustovarov V. A., Fitting H.-J., Schmidt B., Gavrilov N. V., “Low-temperature photoluminescence of ion-implanted $\text{SiO}_2\text{:Sn}^+$ films and glasses”. *Journal of Surface Investigation*, 6(4), pp. 668–672(2012), doi: 10.1134/S1027451012080198.

[Zur 2017a] Zur L., L. Tran T. N., Meneghetti M & Ferrari M., “Sol-gel derived SnO_2 -based photonic systems”, *Handbook of Sol-Gel Science and Technology*, Eds. Lisa Klein, Mario Aparicio, Andrei Jitianu, Springer International Publishing AG, pp. 1-19((2017), doi:10.1007/978-3-319-19454-7

[Zur 2017b] Zur, L., L. T. N. Tran, Meneghetti M., Varas S., Armellini C., Ristic D., Chiasera A., Scotognella F., Pelli S., Nunzi C. G., Boulard B., Zonta D., Dorosz D., Lukowiak A., Righini G. C., Ramponi R., Ferrari M., “Glass and glass-ceramic photonic systems”. In *Proceeding of SPIE 10106, Integrated Optics: Devices, Materials, and Technologies XXI*, Vol. 10106, p. 1010603(1-12) (2017), doi: 10.1117/12.2254965.

[Zur 2017c] Zur, L., Tran, L. T. N., Meneghetti, M., Tran V. T. T., Lukowiak A., Chiasera A., Zonta D., Ferrari M., Righini, G. C. “Tin-dioxide nanocrystals as Er^{3+} luminescence sensitizers: Formation of glass-ceramic thin films and their characterization”, *Optical Materials*, 63, pp. 95–100(2017), doi: 10.1016/j.optmat.2016.08.041.

Chapter 4 Experimental assessments

4.1 Introduction

In general, for any device design and fabrication process, the characterization of investigated photonic systems is a mandatory step. Therefore, this chapter is dedicated to the experimental assessments of the fabricated $\text{SiO}_2\text{-SnO}_2\text{:Er}^{3+}$ planar waveguides and monoliths. Based on the aim of putting the basis for the fabrication of solid state and integrated lasers, several relevant physical properties of active optical materials are recalled as standards for the assessment specification. Diverse characterization techniques have been employed to provide fundamental data for the validation of the two systems. The key considered characteristics includes the structural, morphological, chemical and spectroscopic properties. In particular, the optical waveguiding characterization of the planar waveguides have been also carried out.

4.2 Relevant physical properties of active optical materials

To validate the obtained $\text{SiO}_2\text{-SnO}_2\text{:Er}^{3+}$ planar waveguides and monoliths for the development of optically pumped lasers, it is necessary to refer to several relevant physical properties of active optical materials. The first desirable property is the low optical loss, which in fact is a combination of all possible kinds of losses from the material structure, chemical contamination and residual, geometrical imperfection. The next considered properties for active optical materials to be applied as laser gain media is their spectroscopic properties including the absorption, emission, excitation scheme features and the upper-state lifetime of the photoluminescence at the target wavelength. Referring to the planar waveguides, the characterization is also focused on the optical waveguiding properties. All the evaluated factors, which decide the waveguide performance are refractive index, thickness, surface flatness, index profile, confinement and propagation losses.

4.2.1 Optical loss

When light travels in a medium, it suffers attenuation and losses due to many factors. Therefore, to apply any material into any functional optical device, the first requirement is low loss at least in the working spectral region. Understanding each kind of loss factors helps to avoid or reduce them and consequently, improve the optical performance of the investigated material.

4.2.1.1 Absorption loss

Absorption loss is the destruction of photons due to the interaction between them and a matter in which the electromagnetic energy is transferred into undesirable absorptive centers or converted into another form, usually heat [Tong 2014]. Absorption loss can be called material loss and sorted into two kinds: intrinsic and extrinsic ones. The intrinsic absorption is caused due to phonon creation, a non-radiative relaxation process in which the absorbed light is converted into form of heat of the constituent atoms of the material. The presence of any absorptive structural disorder or defect also contributes to this intrinsic material absorption. The material inter-band and carrier absorption can account for this kind of loss. On the other hand, the extrinsic absorption occurs when there are impurities in the material [Bohren 2007]. This absorption coming from impurities can be either contaminants, dopants or residuals (e.g. OH groups, organic ligands). Therefore, the structural characterization especially at the molecular structure and elemental analysis are essential to evaluate the contribution of the absorption loss of the material.

4.2.1.2 Scattering loss

Scattering is the interaction between light and a matter in which the light is redirected or diffused causing a loss. The scattering can be elastic or inelastic process. Brillouin and Raman scatterings belong to the inelastic ones and of the nature of any matter. While Brillouin is the inelastic interaction of the light with the thermally generated acoustic waves of the material lattice, Raman is with the vibrational and rotational of the constituent bonds of the material [Righini 2005]. On the contrary,

Rayleigh scattering is the elastic interaction when light wave encounters any microscopic imperfection of the material morphology (defect size \ll light wavelength). The scattering loss can be sorted due to the surface or the volume imperfection. The surface scatter comes from material roughness. In case of optical waveguides, the surface imperfection can induce losses due to mode conversion [Dietrich 1969]. For optics, the limit of rough mean square (rms) surface roughness can be defined based on the Rayleigh smooth-surface criterion [Jonh 2012]:

$$\frac{1}{2} \left(\frac{4\pi h_{\text{roughness}} \cos \theta_i}{\lambda} \right)^2 \ll 1 \quad (4.1)$$

where λ is the wavelength of the light;

$h_{\text{roughness}}$ is the height amplitude of the surface roughness;

and θ_i is the angle between the incident light and the scattered direction.

Applying the restriction of less than 0.01 from UV to mid-IR, the maximum amplitude allowed for the surface roughness is about 10 nm. In practical, this kind of scatter loss can be suppressed by polishing the material surface lower than the mentioned limit. On the other hand, the volume scatter is less avoidable since the scattering centers come from the microstructure of the sample which depends strongly on the material nature and fabrication process. The imperfections arising from material fabrication are pores, density inhomogeneity, cracks and contaminant particles and so on. In case of glass-ceramics, which are nanocomposite materials, the boundaries and the density fluctuation between the two phases are also contributed to the volume scatter loss. Moreover, to reduce the Rayleigh scattering loss coming from the nanoparticles, their sizes should be also reduced following the equation [Bohren 2007], [Jonh 2012]:

$$\frac{I_s}{I_0} = \frac{8\pi^4 a^6}{\lambda^4 R^2} \left(\frac{n^2 - 1}{n^2 + 2} \right)^2 (1 + \cos^2 \theta_i) \quad (4.2)$$

where I_s and I_0 are scattering and unpolarized source beam intensities respectively;

λ is the wavelength of the light;

a is the radius of the particles;

n is the effective refractive index of the particle material in compared with surrounding environment;

θ is the angle between the incident light and the scattered direction;

and R is the distance between the particles and the scattering detect.

To exploit the role of Er^{3+} luminescence sensitizer and the photorefractivity of SnO_2 in SiO_2 , the crystallization of SnO_2 is necessary. However, the size of SnO_2 nanocrystals should be controlled as small as possible to reduce both the surface and bulk scattering loss due to Rayleigh scattering. In addition, to avoid the loss due to Mie scattering [Mundy 1974], [Wiscombe 1980], the presence of defects with larger size (from the same order of magnitude of light wavelength) should be avoided during the fabrication process.

Therefore, it is beneficial to predict the existing losses which in fact decide the gain and the lasing action design by characterization:

- Molecular structure of the $\text{SiO}_2\text{-SnO}_2\text{:Er}^{3+}$ glass-ceramics
- Crystallization and nanosize of SnO_2
- Chemical and compositional analyses
- Surface morphology of the planar waveguides

4.2.2 Spectroscopic properties

Besides the losses, other features deciding the lasing validity of an active material are its spectroscopic properties. In general, some of the main spectroscopic characteristics of laser materials are: sharp luminescence lines, strong absorption bands and reasonably high quantum efficiency of the desired luminescence transition [Walter 2006]. For the laser design and operation, the decisive radiation parameters needed to be determined are upper-state lifetime (τ_{lasing}), emission cross section (σ_{em}) which in fact relates to absorption cross section of the pump (σ_{pump}) and energy transfer efficiency in case of using sensitizer (η_{trans}) and gain bandwidth ($\Delta\nu$). In fact, the pump power threshold of a continuous wave

(cw) lasing operation is proportional to $\frac{1}{\sigma_{\text{pump}} \tau_{\text{lasing}}}$ which will be

described with details in section 7.2 of Chapter 7. Therefore, concerning the $1.5 \mu\text{m}$ lasing validity of $\text{SiO}_2\text{-SnO}_2\text{:Er}^{3+}$ glass-ceramics, it is mandatory to characterize:

- Spectral characteristics of Er^{3+} luminescence in the $\text{SiO}_2\text{-SnO}_2$;
- Absorption and emission cross sections and the internal gain coefficient of Er^{3+} in $\text{SiO}_2\text{-SnO}_2$ glass-ceramics;

- Properties of energy transfer from SnO_2 to Er^{3+} and absorption cross section of SnO_2 ;
- Lifetime and quantum efficiency of upper-state of the lasing radiation, i.e. $^4\text{I}_{13/2}$ metastable state of Er^{3+} ;

4.2.3 Optical waveguiding properties

Concerning the $\text{SiO}_2\text{-SnO}_2\text{:Er}^{3+}$ planar waveguides, besides the above-mentioned features, their optical waveguiding properties need to be inspected. For integrated waveguide laser construction, a high confinement and low propagation loss of the desired light wavelength is mandatory. Therefore, all the parameters which decide the light confinement and waveguiding performance must be characterized such as:

- Geometrical features including thickness and surface morphology
- Mode structure
- Refractive index distribution
- Propagation loss

4.3 Assessment techniques and specification

As discussed above, the characterization of structural, chemical and morphological properties of the $\text{SiO}_2\text{-SnO}_2\text{:Er}^{3+}$ glass-ceramics play a crucial role in predicting the contribution of optical losses existing in the systems. This helps to minimize the avoidable optical losses and evaluate the unavoidable ones which, in fact, affect the optical gain of the active materials. Furthermore, the investigation of the spectroscopic properties provides the fundamental data to reveal the possible lasing operation of the active glass-ceramics. All the characterization of mentioned properties was applied on both the planar waveguides and monoliths. However, in the case of planar waveguides, based on the validation interest of the light confinement and propagation loss, other specific characterizations for the optical waveguiding properties were also carried out such as: the surface roughness measurements, compositional distribution along the depth and optical waveguiding

properties. The assessment specification and characterization techniques can be briefly summarized as follows:

- For the structural characterization of the $\text{SiO}_2\text{-SnO}_2\text{:Er}^{3+}$ glass-ceramics, the non-destructive Raman spectroscopy was employed. Two Raman spectroscopy techniques: non-resonance micro-Raman ($\lambda_{\text{ex}} = 632 \text{ nm}$) and resonance UV macro-Raman ($\lambda_{\text{ex}} = 266 \text{ nm}$) were applied on both the planar waveguides and monoliths. The two techniques play complementary role in investigating molecular structure of the $\text{SiO}_2\text{-SnO}_2$ binary system as discussed in the next concepts. The crystallization and more important the sizes of SnO_2 nanocrystals in SiO_2 matrix are investigated by using X-ray Diffraction and Electron Microscopies. The Energy-dispersive X-ray spectroscopy allows the chemical analysis of the glass-ceramics. In addition, the Selected Area Electron Diffraction also provides the crystallization information of the observed area. Concerning the optical waveguiding properties, the Auger electron spectroscopy provides not only the quantitative composition, the chemical states of the elements but also their distribution along the depth of the planar waveguides. To evaluate the scattering loss from the surface of the planar waveguides, the surface roughness is checked using Atomic force microscope.
- The spectroscopic properties of the $\text{SiO}_2\text{-SnO}_2$ glass-ceramics are studied based on absorption and photoluminescence spectroscopies. The emission and excitation spectra are used to reveal the efficient role of SnO_2 as Er^{3+} luminescence sensitizers. The time-resolved photoluminescence spectra at microsecond and picosecond time domains provide the energy transfer from SnO_2 to Er^{3+} and relaxation mechanism from the $^4\text{I}_{13/2}$ metastable state of Er^{3+} in the compositional $\text{SiO}_2\text{-SnO}_2$ glass-ceramics.
- The m-line spectroscopy is employed to measure the thickness, refractive index, and index profile of the planar waveguides. The propagation loss was measured by scanning a fiber optic probe and photodetector along the propagating streaks.

All results of the three characterization aspects are discussed with details in the next sections.

4.4 Structural, morphological and chemical characterization

4.4.1 Raman spectroscopy

The Raman spectroscopy is a versatile and non-destructive technique to study the structure of multicomponent glasses [Righini 2005] at both micro and macro-scale [Smith 2013]. Fundamentals of Raman spectroscopy can be easily found in the literature [Demtröder 2015]. Briefly, the working principle of Raman spectroscopy is to use a coherent light source to excite the sample and detect the optical frequency difference, called Raman shift, in comparison with the excitation source. Exploiting the inelastic scattering effect due to molecular vibration, Raman spectroscopy provides information of molecular structure of the investigated material.

Using two different excitation schemes: resonance and non-resonance Raman spectroscopy, complementary results of the molecular structure of the $\text{SiO}_2\text{-SnO}_2$ binary material were gained. In case of resonance Raman spectroscopy, the excitation frequency needs to be higher or close to the electronic transition frequency of the investigated materials. Concerning silica-based glasses and glass-ceramics, UV light at 266 nm is sufficient for resonance Raman spectra acquisition. Thanks to the UV resonance effect, there is an improvement of the sensitivity and especially selective enhancement of some vibration modes associated to specific chemical groups [Rossi 2018]. These scattering signals may be silent or extremely weak in the conventional non-resonance Raman spectra which has sensitivity of the order of 1 over 10 million photons [Woodward 1967]. Nevertheless, the conventional Raman spectroscopy which has been a powerful tool for intensive studies on glasses [Duverger 1999], [Armellini 1999], [Van Tran 2010], [Zampedri 2003], was also employed for the structural characterization of $\text{SiO}_2\text{-SnO}_2\text{:Er}^{3+}$.

4.4.1.1 Non-resonance micro-Raman ($\lambda_{\text{ex}} = 632 \text{ nm}$)

The non-resonance micro-Raman spectra were acquired using a Labram Aramis (Horiba Jobin-Yvon) equipped with an optical microscope and a 100 \times objective. A He-Ne laser source of 632 nm has been used for the excitation of the Raman measurements.

Figure 4.1 shows the visible micro-Raman spectra of the $(100-x)\text{SiO}_2-x\text{SnO}_2:0.5\text{Er}^{3+}$ planar waveguides ($x = 5, 10, 15, 20, 25$ and 30 mol%) in comparison with pure SnO_2 pellet and sol-gel derived pure SiO_2 thin film.

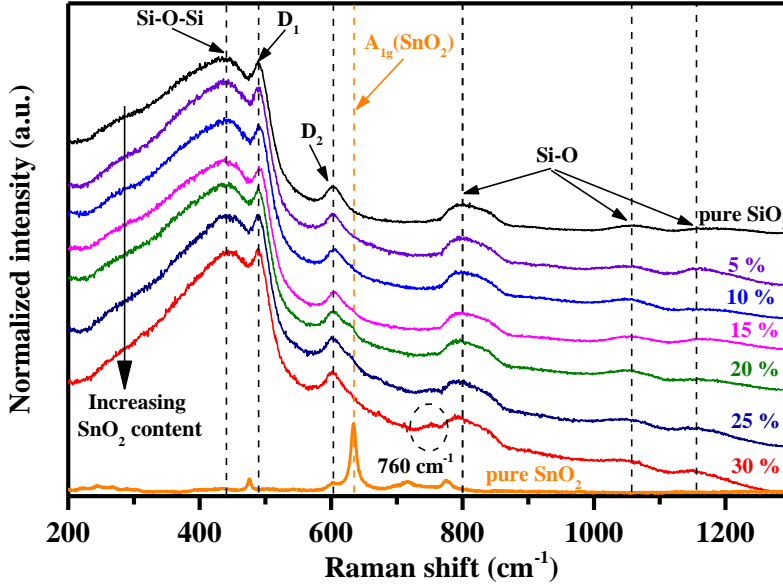


Figure 4.1 Visible micro-Raman ($\lambda_{\text{ex}} = 632$ nm) spectra of the $(100-x)\text{SiO}_2-x\text{SnO}_2:0.5\text{Er}^{3+}$ planar waveguides ($x = 5, 10, 15, 20, 25$ and 30 mol%) in comparison with pure SnO_2 and SiO_2

All the typical Raman features of pure SiO_2 have been observed in the compositional $\text{SiO}_2\text{-SnO}_2$ planar waveguides:

- (i) the intense broad band at about 440 cm^{-1} which was assigned to SiO_4 tetrahedra deformation vibrations in silica network [Armellini 1999], [Galeener 1985] and in fact this band was specified in [Henderson 1985] as symmetric stretching of Si-O-Si bonds predominantly with 6-membered rings of SiO_4 tetrahedra with a minor contribution from 5-membered and higher than 6-membered rings;
- (ii) the two D_1 and D_2 defect bands centered at 489 and 600 cm^{-1} which are attributed to the presence of local defects of four-fold and three-membered rings in the normal six-membered rings of SiO_2 network [Galeener 1985], [Bouajaj 1997], [Kinowski 2001];

- (iii) the ω_3 band at 800 cm^{-1} is assigned to a complex motion of Si atoms against the bridging oxygen atoms in O-Si-O in silica network [Armellini 1999], [Okuno 2005];
- (iv) the bands at 1063 and 1170 cm^{-1} , attributed respectively to symmetric and anti-symmetric Si-O stretching vibrations [Montagna 2004];

However, several observable changes of the Raman features of $(100-x)\text{SiO}_2\text{-}x\text{SnO}_2\text{:}0.5\text{Er}^{3+}$ in comparison with the pure SiO_2 thin films can be summarized as follows:

- (i) Small luminescence background as already observed in sol-gel derived SiO_2 xerogels by [Armellini 1999] is present in the Raman spectra of $(100-x)\text{SiO}_2\text{-}x\text{SnO}_2\text{:}0.5\text{Er}^{3+}$. Increasing the SnO_2 contents lead to increasing contribution of the luminescence background.
- (ii) The presence of SnO_2 in the glass-ceramics leads to the narrowing of the broad band at 440 cm^{-1} as already observed in [Van Tran 2010]. The higher is the SnO_2 content, the narrower is the bandwidth. As suggested in the work [Montagna 2004], the width of this band is related to the disorder-induced distribution of angles in the Si-O-Si units connecting the SiO_4 tetrahedra. On the other hand, as suggested by Henderson in the work [Henderson 1985], this band is attributed to the symmetric stretching of Si-O-Si bonds predominantly in with 6-membered rings of SiO_4 tetrahedra with a minor contribution from 5-membered rings. The higher membered rings lead to the pronounced low-frequency tail of this band. On the other hand, McMillan in the work [McMillan 1986] suggested that the narrowing and the shift to higher frequency of this band is due to the narrower of average Si-O-Si angle in more compact SiO_2 structure. Therefore, this band narrowing can be explained as follows: the introduction of SnO_2 in SiO_2 matrix may prevent the formation of higher-membered rings or induce a narrower Si-O-Si angle of SiO_4 tetrahedra.
- (iii) No band at about 965 cm^{-1} , assigned to Si-(OH) stretching is observed as indicated in the work [Armellini 1999].
- (iv) Compared with the Raman features of the pure SnO_2 pellet with around 50 nm grain size, a very small contribution of A_{1g} crystal-mode SnO_2 at 630 cm^{-1} is revealed as also

observed in the work [Van 2012]. However, this band is very weak and covered by the defect band D₂ which is due to the high distortion of SnO₂ nanocrystals as suggested by Diéguez in [Diéguez 2001].

- (v) A new weak band centered at 770 cm⁻¹ was observed, assigned to B_{2g}, one of the non-degenerate vibration modes of the plane vibration perpendicular to the c axis of the 6-atom unit cell of tetragonal rutile crystalline structure of SnO₂ [Diéguez 2001], [Percy 1973], [Fazio 2012].

To check the presence of O-H in the glass-ceramic planar waveguides, a representative non-resonance Raman spectrum of the 70SiO₂-30SnO₂:0.5Er³⁺ is shown in Figure 4.2 with a larger Raman shift range from 200 to 3800 cm⁻¹. As one can see, there is no observable asymmetric band near 3670 cm⁻¹ assigned to the O-H stretching vibration of hydroxyl groups [McMillan 1986]. This indicates low concentration of O-H groups in the planar waveguides. To further extent, together with the well-defined Raman features as discussed in Figure 4.1, this aspect is typically observed in densified silicate glasses which indicates the densification of the glass-ceramic planar waveguides.

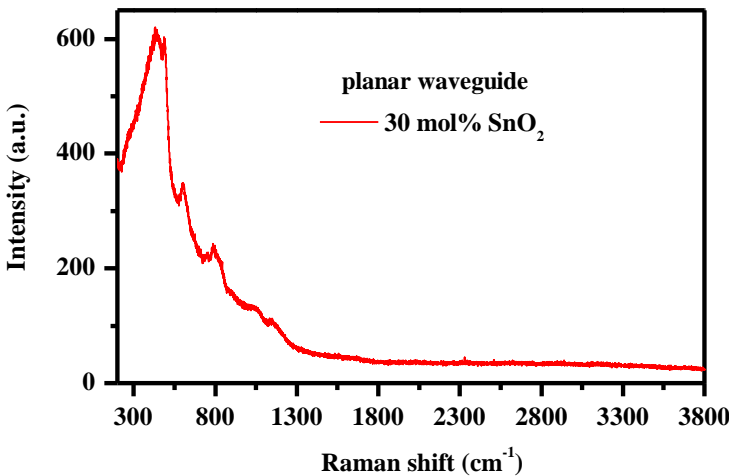


Figure 4.2 Visible micro-Raman ($\lambda_{\text{ex}} = 632 \text{ nm}$) spectra of the 70SiO₂-30SnO₂:0.5Er³⁺ planar waveguide

Figure 4.3 shows the non-resonance Raman spectra of the $(100-x)\text{SiO}_2$ - $x\text{SnO}_2:0.5\text{Er}^{3+}$ monoliths ($x = 0, 5$ and 10 mol%). Some observed Raman features are similar to the planar waveguides shown in Figure 4.1 such as: small luminescence background and the presence of all the typical SiO_2 Raman modes at $440, 489, 600$ and 800 cm^{-1} with the assignments as indicated above. However, several differences of Raman features can be revealed in the monoliths compared to the planar waveguides such as:

- (i) Compared to the planar waveguide, the A_{1g} crystal-mode at 630 cm^{-1} of SnO_2 appears clearer in the monoliths, especially in the 90SiO_2 - $10\text{SnO}_2:0.5\text{Er}^{3+}$. This aspect can be explained due to the more ordered SnO_2 nanocrystals in the monoliths. However, compared to pure SnO_2 pellet, the broadening of this A_{1g} band reveals the small size of SnO_2 nanocrystals [Diéguez 2001].
- (ii) The narrowing behavior of the broad band at 440 cm^{-1} was also observed in the compositional monoliths (with 5 and 10 mol% SnO_2). Similar to the planar waveguides, the higher is the SnO_2 content in the monoliths, the narrower is the bandwidth of the band centered at 440 cm^{-1} .
- (iii) The Raman features of 90SiO_2 - $10\text{SnO}_2:0.5\text{Er}^{3+}$ monolith exhibit further differences and there is small contribution of B_{2g} mode at 760 cm^{-1} integrated with the S_3 (or Au_2) mode which appears as a consequence of disorder activation [Diéguez 2001]. The intensity of D_1 defect band centered at 489 cm^{-1} assigned to the four-fold rings present in SiO_2 network [Galeener 1985], [Bouajaj 1997], [Kinowski 2001] is much higher than the 5 mol% SnO_2 and pure SiO_2 . Together with the narrower bandwidth at 440 cm^{-1} , this high D_1 defect intensity indicates that the introduction of 10 mol% SnO_2 in the monolithic systems induces higher modification of SiO_2 matrix.
- (iv) The band at about 965 cm^{-1} , assigned to $\text{Si}(\text{OH})$ stretching reveals the presence of residual $\text{Si}(\text{OH})$ groups in the monoliths excepting the one containing 5 mol% of SnO_2 .

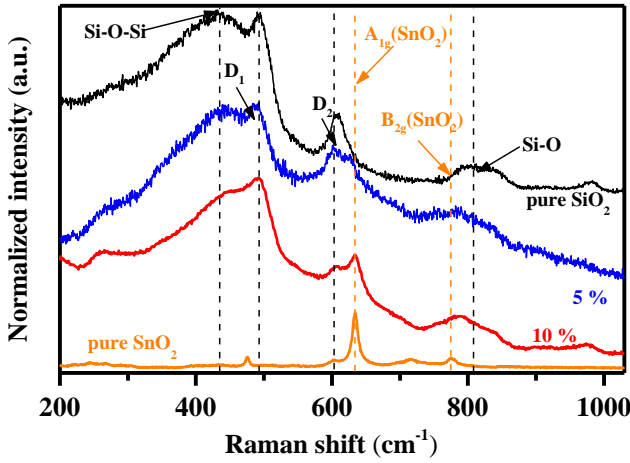


Figure 4.3 Visible micro-Raman ($\lambda_{\text{ex}} = 632 \text{ nm}$) spectra of the $(100-x)\text{SiO}_2\text{-}x\text{SnO}_2\text{:}0.5\text{Er}^{3+}$ monoliths ($x = 5$ and 10 mol\%) in comparison with pure SnO_2 and SiO_2

4.4.1.2 Resonance UV macro-Raman ($\lambda_{\text{ex}} = 266 \text{ nm}$)

Although the non-resonance Raman spectra provide the structural characteristics of both phases of the $\text{SiO}_2\text{-SnO}_2$ glass-ceramics as discussed in subsection 4.4.1.1, most of Raman features are predominantly of the amorphous SiO_2 and minor information of the crystalline SnO_2 nanocrystals is obtained. Therefore, the resonance Raman spectroscopy with $\lambda_{\text{ex}} = 266 \text{ nm}$ higher than the band gap of SnO_2 is beneficial for the Raman characterization of SnO_2 [Rossi 2018]. Figure 4.4 shows the resonance macro Raman spectra of the $70\text{SiO}_2\text{-}30\text{SnO}_2\text{:}0.5\text{Er}^{3+}$ planar waveguide and $90\text{SiO}_2\text{-}10\text{SnO}_2\text{:}0.5\text{Er}^{3+}$ monolith in comparison with the pure SnO_2 pellet. Thanks to the resonance enhancement, the Raman features of SnO_2 , which are weak in non-resonance Raman regime become more apparently in Figure 4.4. As one can see, besides the two typical modes A_{1g} (630 cm^{-1}) and E_g (480 cm^{-1}) of pure SnO_2 [Diéguez 2001], [Fazio 2012], [Percy 1973], the glass-ceramic monolith exhibits the more enhance surface mode at 380 cm^{-1} [Van 2014] and the S_3 disorder activation mode of SnO_2 [Diéguez 2001]. This reveals the disorder and surface aspect coming from the SnO_2 nanocrystals. All these features can be observed also in the planar waveguides. However, due to the strong fluorescence from the vitreous

SiO₂ substrate, the resonance Raman feature of the planar waveguide is less apparent than the monolith.

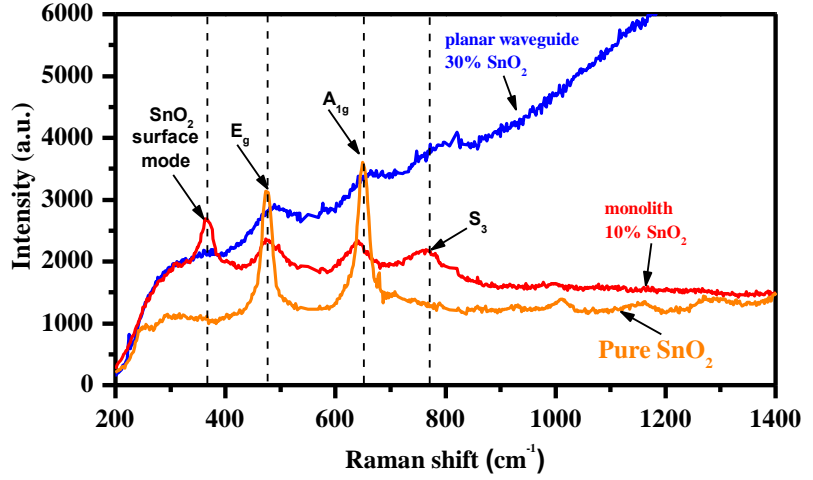


Figure 4.4 UV macro-Raman ($\lambda_{\text{ex}} = 266 \text{ nm}$) spectra of the 70SiO₂-30SnO₂:0.5Er³⁺ planar waveguide and 90SiO₂-10SnO₂:0.5Er³⁺ monolith in comparison with pure SnO₂

4.4.2 X-ray diffraction (XRD)

X-ray diffraction was employed to scope the crystallization of SnO₂ in the glass-ceramics. Figure 4.5 shows the XRD patterns of the (100-x)SiO₂-xSnO₂:0.5Er³⁺ planar waveguides ($x = 5, 10, 15, 20, 25$ and 30 mol\%) acquired using X'PERT PRO diffractometer equipped with a Cu X-ray tube. All the samples exhibit a broad band at 22° of amorphous SiO₂ which comes from the v-SiO₂ substrate and (100-x) mol% of SiO₂ glass in the planar waveguides (x : from 5 to 30 mol%). Except the 5 mol% SnO₂ planar waveguide showing only amorphous phase, XRD peaks at 26, 34, 52° indexed as the planes (110), (101) and (211) of SnO₂ Cassiterite (JCPDS 41-1445) are present in the other samples. The inset shows in scale XRD patterns of the samples in range of 10° - 30°. Concerning the broad band at 22°, increasing SnO₂ content leads to an intensity decrease of this band due to the reduction of SiO₂ content in the planar waveguides. Due to the high domination of SiO₂ XRD patterns at diffracted angles from 10 to 40°, it is not possible to obtain Scherrer-defined size of SnO₂. Nevertheless, with respect to the

background signal, the broad SnO₂ rutile XRD peaks, especially from the plane (211), can be used to interpret its crystallization and estimated average sizes (less than 10 nm). When the SnO₂ content increases from 10 to 20 mol%, the SnO₂-rutile XRD peaks increase their intensity. However, their intensity starts to decrease when the SnO₂ content increases from 25 to 30 mol%. These aspects reveal higher contribution of larger-sized SnO₂ nanocrystals in the planar waveguides containing from 10 to 20 mol % SnO₂ and smaller-sized SnO₂ in the 25 and 30 mol% ones. There are two factors coming from the fabrication technique which influences the size of SnO₂ nanocrystals: the chemical kinetics of SiO₂-SnO₂ binary system and the different time of applied thermal treatment. Concerning the chemical kinetics of SiO₂-SnO₂ binary system, SiO₂ matrix was demonstrated as a crystal growth inhibitor of SnO₂ [Leonhardt 2013], [Tricoli 2012], [Zhu 2014]. Therefore, different SnO₂/SiO₂ content ratio can lead to different inhibiting behavior of SiO₂ on SnO₂ crystal growth and it rules the size of SnO₂ in each glass-ceramic composition. On the other hand, referring to one composition, there is still the different size of SnO₂ nanocrystals along the thickness, i.e. the size-distribution of SnO₂ due to the different applied time of thermal effect on different layers. Since after each deposition of a single layer, a drying step was applied on the sample, the time that the inner layers are under thermal effect are longer than the outer ones. Consequently, the crystallinity of the SnO₂ in the inner part of the planar waveguides can be higher than the outer part. In any case, the decreasing contribution of larger-sized SnO₂ nanocrystals in the 70SiO₂-30SnO₂ planar waveguides is beneficial for achieving both the scattering losses reduction and the high light confinement and high photorefractivity at a time.

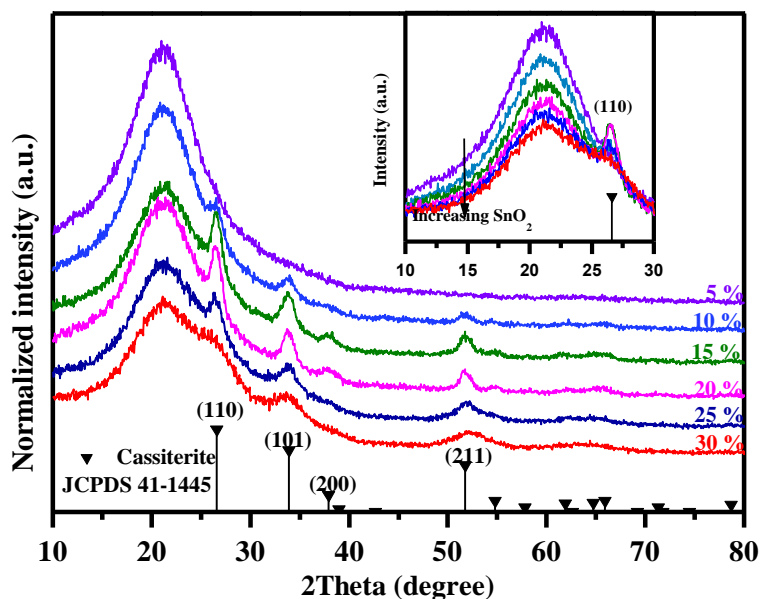


Figure 4.5 XRD patterns of the $(100-x)\text{SiO}_2-x\text{SnO}_2:0.5\text{Er}^{3+}$ planar waveguides ($x = 5, 10, 15, 20, 25$ and 30 mol%), indexed as SnO_2 Cassiterite (JCPDS 41-1445). Inset shows the XRD patterns in scale of the planar waveguides in range ($10^\circ - 30^\circ$)

Concerning the glass-ceramic monoliths, the XRD patterns of $(100-x)\text{SiO}_2-x\text{SnO}_2:0.5\text{Er}^{3+}$ ($x = 5$ and 10 mol%) in comparison with the pure SnO_2 pellets are shown in Figure 4.6. All the XRD peaks of SnO_2 -rutile phase become more apparent for the monoliths than for the planar waveguides which can be due to the higher crystallinity and less disorder of SnO_2 nanocrystals as discussed from the Raman spectroscopy in 4.4.1. In addition, there is still a small contribution of the broad band at 22° corresponding to the amorphous phase of SiO_2 .

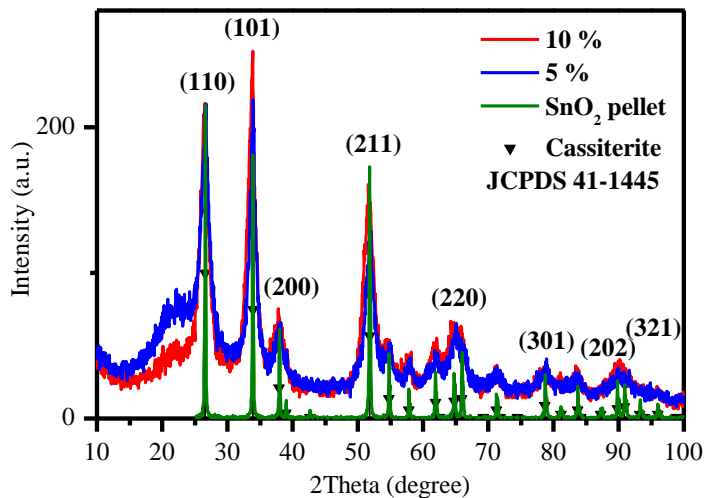


Figure 4.6 XRD patterns of $(100-x)\text{SiO}_2\text{-}x\text{SnO}_2\text{:}0.5\text{Er}^{3+}$ monoliths ($x = 5$ and 10 mol\%), indexed as SnO_2 Cassiterite (JCPDS 41-1445)

Much broader bandwidth of these diffraction peaks in comparison with the pure SnO_2 pellet (50 nm) indicates much smaller size of SnO_2 nanocrystals in the glass-ceramic monoliths. In fact, using Scherrer formula, the estimated average size of SnO_2 nanocrystals was obtained as listed in Table 4.1. Both compositional monoliths exhibit small SnO_2 nanocrystals with size from 7 to 8 nm.

Table 4.1 The calculated average size using Scherrer formula of SnO_2 nanocrystals in $(100-x)\text{SiO}_2\text{-}x\text{SnO}_2\text{:}0.5\text{Er}^{3+}$ monolith ($x = 5$ and 10 mol\%)				
Plane (hkl)	$90\text{SiO}_2\text{-}10\text{SnO}_2\text{:}0.5\text{Er}^{3+}$		$95\text{SiO}_2\text{-}5\text{SnO}_2\text{:}0.5\text{Er}^{3+}$	
	FWHM (degree)	d_{hkl} (nm)	FWHM (degree)	d_{hkl} (nm)
(110)	1.46663	5.59	1.51711	5.79
(101)	1.21708	7.76	1.04465	9.06
(211)	1.95541	6.48	1.60549	7.92
Average size (nm)	6.6 ± 0.8		7.6 ± 1.2	

4.4.3 Scanning transmission electron microscopy (EM)

Scanning transmission electron microscopy (STEM) was used to observe the nanoscale structure of the glass-ceramic planar waveguides and monoliths. This is an important information to check the losses from bulk scattering. Several representative samples were chosen from the compositional glass-ceramics for the STEM observations. There were two different STEM instrumentations applied:

- (i) Conventional TEM images were performed by TEM Philips CM12 microscope equipped with EDXS detector. The analyzed samples are $70\text{SiO}_2\text{-}30\text{SnO}_2\text{:}0.5\text{Er}^{3+}$ and $80\text{SiO}_2\text{-}20\text{SnO}_2\text{:}0.5\text{Er}^{3+}$ planar waveguides and $90\text{SiO}_2\text{-}10\text{SnO}_2\text{:}0.5\text{Er}^{3+}$ and $95\text{SiO}_2\text{-}5\text{SnO}_2\text{:}0.5\text{Er}^{3+}$ monoliths. For these observations, all the chosen samples were grounded into powders and the Transmission Electron Microscopy (TEM) images and Energy-dispersive X-ray spectroscopy (EDXS) were acquired on obtained powders.
- (ii) High resolution STEM (HR-STEM) images of the $(100\text{-}x)\text{SiO}_2\text{-}x\text{SnO}_2\text{:}0.5\text{Er}^{3+}$ planar waveguides ($x = 10$ and 15 mol%) with images were acquired on TALOS F200S STEM instrumentation-ThermoFisher Scientific.

Figure 4.7 and Figure 4.8 show the conventional TEM images with the corresponding EDXS analyses of the $70\text{SiO}_2\text{-}30\text{SnO}_2\text{:}0.5\text{Er}^{3+}$ and $80\text{SiO}_2\text{-}20\text{SnO}_2\text{:}0.5\text{Er}^{3+}$ planar waveguides respectively.

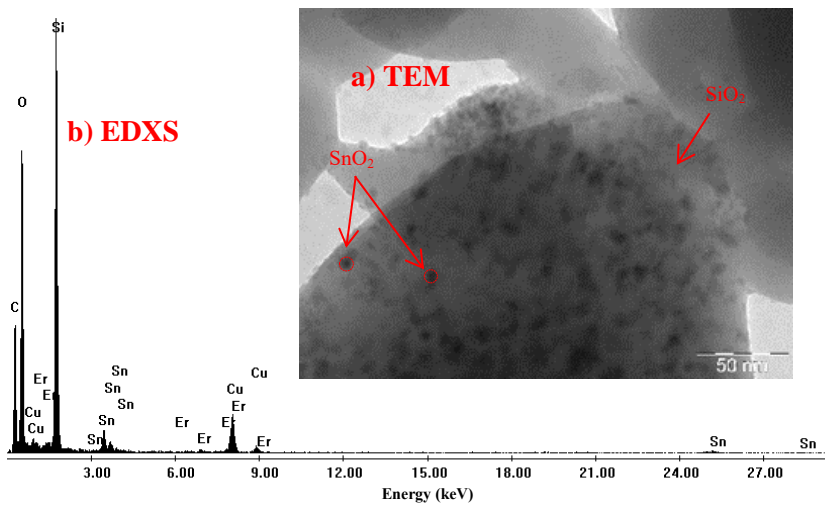


Figure 4.7 a) TEM image and b) EDXS spectrum of the 70SiO₂-30SnO₂:0.5Er³⁺ planar waveguide. In the observed grains, the black dots are SnO₂ nanocrystals while the light grey part is SiO₂ matrix

The dark dots in TEM images of the observed grains are referring to the SnO₂ nanocrystals dispersing in the SiO₂ matrix revealed in light grey color. These grains show the presence of small particles homogenously distributed. The dimension of these SnO₂ nanocrystals is less than 10 nanometers. The grains with nanoparticles are composed of Si, O and Sn as principal elements, Er is also present. The presence of Cu comes from the TEM Grids used for powder observations. The SAED of this area was not collected since no evidence of diffraction was present. This may be due to the small volume of crystalline material leading to an extremely low signal.

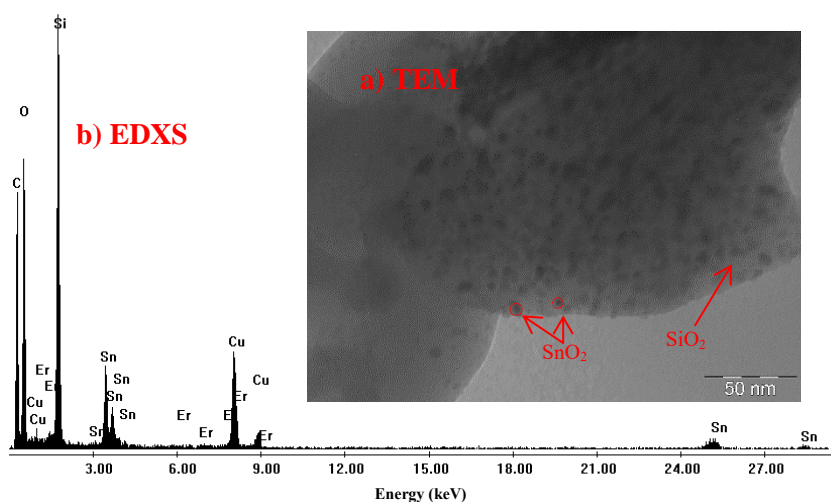


Figure 4.8 a) TEM image and b) EDXS spectrum of the 80SiO₂-20SnO₂:0.5Er³⁺ planar waveguide. In the observed grains, the black dots are SnO₂ nanocrystals while the light grey part is SiO₂ matrix

To better understand the nano/microstructure of the planar waveguides, the high-resolution STEM images were acquired. Figure 4.9 shows the HR-STEM images of the cross section of the (100-x)SiO₂-xSnO₂:0.3Er³⁺ planar waveguides (x = 10 and 15 mol%). The images reveal the homogeneous distribution of SnO₂ (dark dots) in SiO₂ (lighter color). From these cross section STEM images, it is possible to determine the thickness: 1116 nm and 1196 nm for 10 and 15 mol% planar waveguides respectively. However, there is a different nanosize-distribution of SnO₂ along depth of the multilayer planar waveguides: smaller in the outer layers and larger in the inner layers which are closer to the substrates. As already mentioned in the XRD discussion in 4.4.2, this is due to the different thermal effect time applied on the multilayers: longer from the inner layers which were deposited first. Nevertheless, as one can see the maximum size is around 20 nm but the most contribution is the SnO₂ nanocrystals with size smaller than 10 nm for both samples. The only difference is the distribution of the large SnO₂ nanocrystals (~20 nm): around 300 nm depth for the 15 mol% SnO₂ planar waveguide and 200 nm depth for the 10 mol%. This is in agreement with the XRD results: the SnO₂ XRD peaks appear higher in the 15 mol% than 10 mol%. Moreover, the depth profile of size-distributed SnO₂ provides a

complementary explanation for the different SnO_2 crystallization of the planar waveguides scoped by XRD. The higher SnO_2 rutile XRD patterns comes from the higher contribution of the large-sized SnO_2 nanocrystals in the planar waveguides. And, the different contribution of SnO_2 nanocrystals in turns is defined by the chemical kinetics of the binary systems. In addition, from Figure 4.9 b), the higher SnO_2 planar waveguide (15 mol%) exhibits a layered structure especially in the outer layers. The thickness of these layers ranges from 55 to 60 nm which is in fact corresponding to each dipping layer. This feature is observed also for the higher contents of SnO_2 planar waveguides which will be discussed in the Auger electron spectroscopy in the next subsection (see 4.4.4).

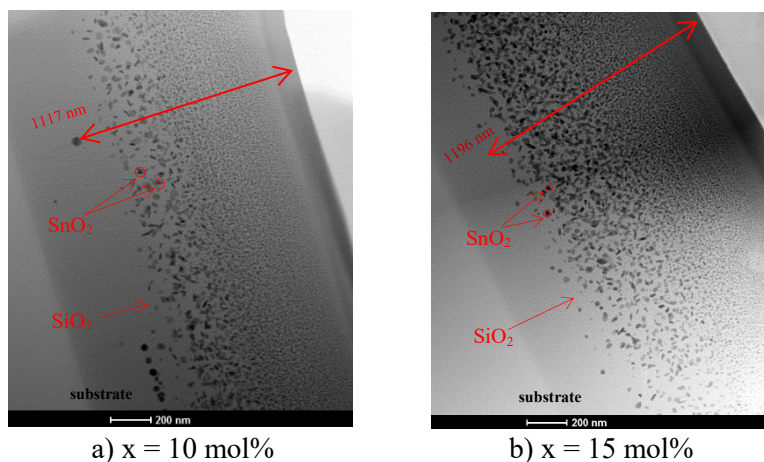


Figure 4.9 HR-STEM images of the cross section of the $(100-x)\text{SiO}_2-x\text{SnO}_2:0.3\text{Er}^{3+}$ planar waveguides: a) $x = 10 \text{ mol\%}$ and b) $x = 15 \text{ mol\%}$

Figure 4.10 shows EDXS map of the 10% and 15% planar waveguides acquired using the Super-X detector of TALOS F200S STEM instrumentation - ThermoFisher Scientific. One can see the distribution of the Sn, Si and O elements inside the specimens. Si and O are homogenously distributed inside the thin-films and the vSiO_2 substrate. Sn is mainly concentrated in the SnO_2 nanoparticles, but it also presents in all the area of the planar waveguides. The EDXS mapping of Sn in the $85\text{SiO}_2-15\text{SnO}_2:0.5\text{Er}^{3+}$ revealed a layered structure of its distribution along the depth.

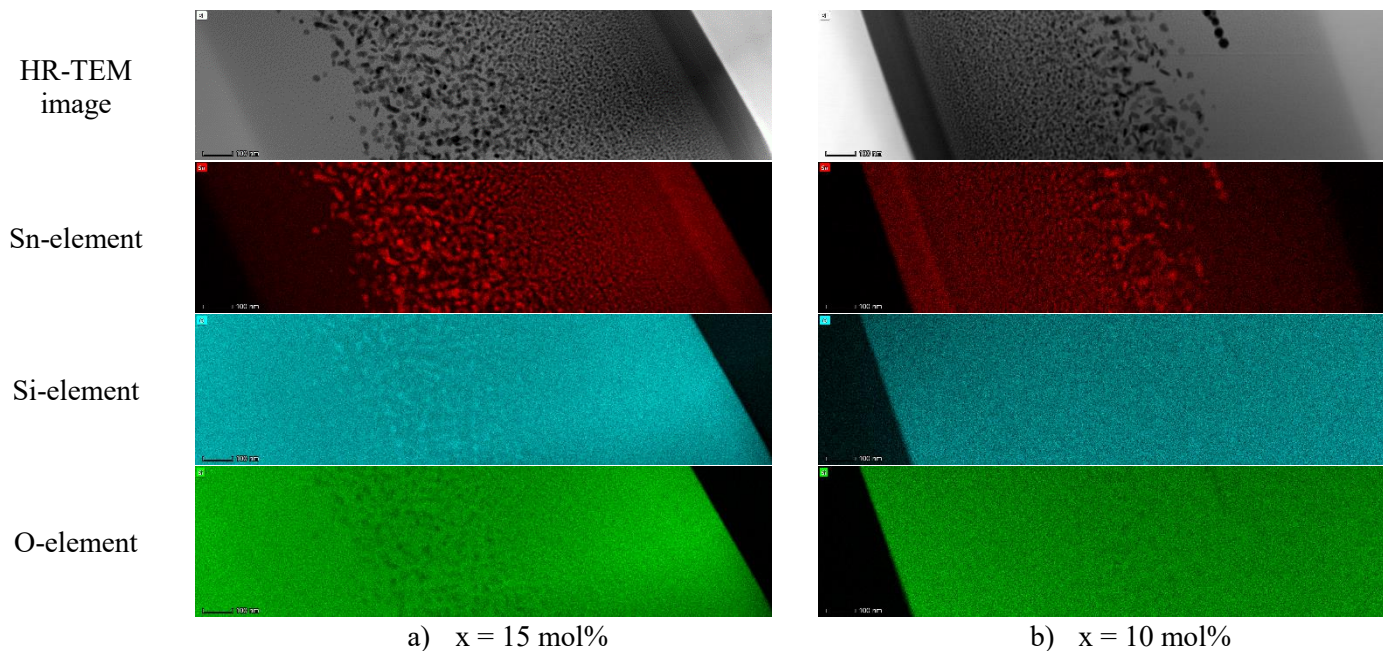


Figure 4.10 High-STEM images and the corresponding EDXS mapping of the Si, Sn and O elements in the $(100-x)\text{SiO}_2\text{-SnO}_2:0.5\text{Er}^{3+}$ planar waveguides: a) $x = 10$ and b) $x = 15 \text{ mol\%}$.

More detailed nanostructure in small-sized SnO₂ nanocrystal regions of the two planar waveguides are shown in the HR-STEM in Figure 4.11. The images a) and b) reveal the homogeneous dispersion of SnO₂ nanocrystals with grain size of less 5 nm. The particle grains shown in images c) and d) exhibit the interplanar distance of 0.32 nm corresponding to the SnO₂ rutile crystal and this confirm the crystalline structure of SnO₂ nanocrystals.

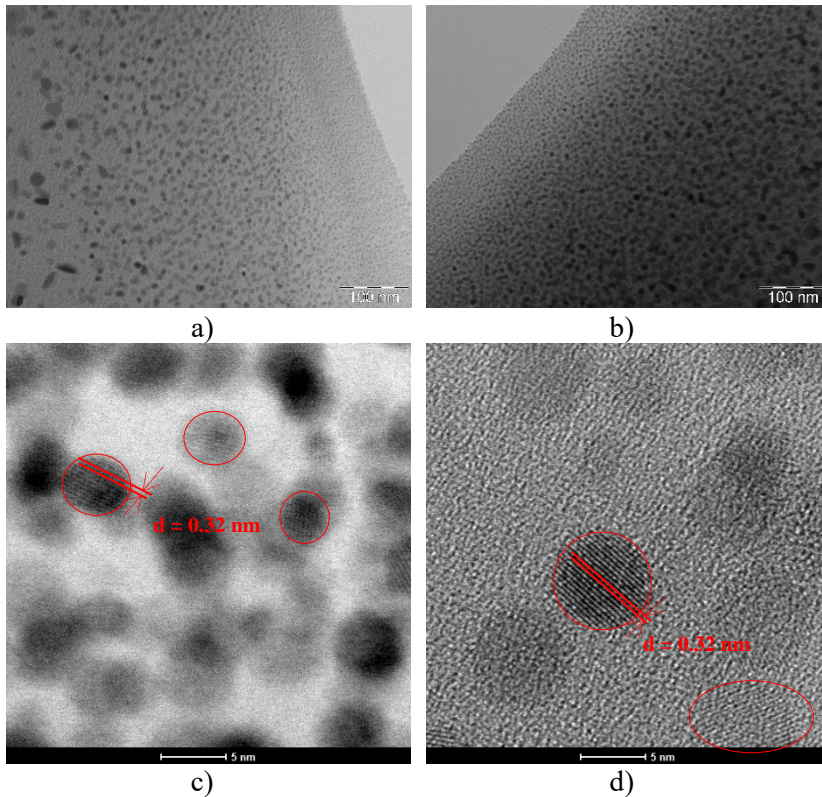


Figure 4.11 HR-STEM images of the (100-x)SiO₂-xSnO₂:0.3Er³⁺ planar waveguides: a) and c) x = 10 mol%; b) and d) x = 15 mol%.

The red circles are just for visualizing the SnO₂ particles

In case of the monoliths, Figure 4.12 show all the electron microscopical results of the 90SiO₂-10SnO₂:0.5Er³⁺. The TEM images of both monoliths show the presence of small and homogenously distributed SnO₂ nanoparticles. The dimensions of such particles are less than 10 nanometers (see Figure 4.12a and Figure 4.13a). SAEDs in figures b) indicate that the particles are SnO₂ Cassiterite nanocrystal. The EDXS

analyses in figures c) show the presence of Si, O and Sn, as principal elements and Er is also detected.

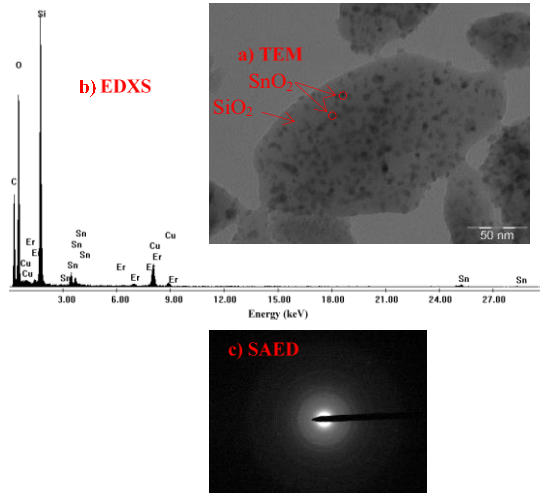


Figure 4.12 a) TEM image, b) EDXS spectrum and c) SAED patterns of the 90SiO₂-10SnO₂:0.5Er³⁺ monolith. In the TEM image of the observed grains, the black dots are SnO₂ nanocrystals while the light grey part is SiO₂ matrix

The same results are also obtained from the 95SiO₂-5SnO₂:0.5Er³⁺ as shown in Figure 4.13.

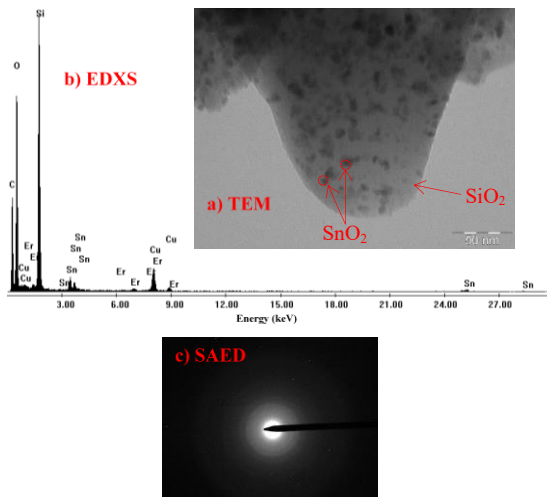


Figure 4.13 a) TEM image, b) EDXS spectrum and c) SAED patterns of the 95SiO₂-5SnO₂:0.5Er³⁺ monolith. In the TEM image of the observed grains, the black dots are SnO₂ nanocrystals while the light grey part is SiO₂ matrix

4.4.4 Auger electron spectroscopy (AES)

Considering the different size-distribution of SnO₂ along the depth of the planar waveguides, it is necessary to check the quantitative compositional along the depth to ensure the homogeneous compositional distribution of all the constituent elements. This factor affects the index profile and consequently the light confinement in the planar waveguides. Therefore, Auger electron spectroscopy was employed to explore the quantitative composition of the planar waveguides along the depth. This technique is based on the Auger effect, in which one electron from an outer-shell falls into an inner-shell hole (electron vacancy) formerly created by external sources e.g. electron beam, x-ray, and the energy released from this transition is high enough to eject another electron out of the atom [Matthew 2004]. The second ejected electron is named Auger electron. By analyzing the kinetic energies of the Auger electrons, which are the fingerprints of each element, the chemical and the composition of the sample can be probed. The elemental identification and quantification were carried out by means of PHI 4200 thin film analyzer. In this instrument, the Auger

analysis by electron beam is combined with argon sputter ion etching of the surface. By this, the elemental and compositional depth profile of the planar waveguides was acquired.

4.4.4.1 Composition

Figure 4.14 shows the AES in-depth composition profile of Si, Sn and O with respect to the erosion depth of the top-side coating of the $70\text{SiO}_2\text{-}30\text{SnO}_2\text{:}0.5\text{Er}^{3+}$ planar waveguide. As expected, Er was not detectable due to its small concentration. From this profile, one can easily see an alternating distribution of Sn and Si respectively along the depth of the sample. In other words, higher tin signal corresponds to lower silicon and vice versa. This resembles a layered structure of the planar waveguide which is in agreement with HR-STEM observation shown in Figure 4.10. The profile lost the quality when the erosion depth reached ~ 200 nm due to progressive deterioration factors, e.g. atomic mixing, roughness, diffusion, etc. Concerning the oxygen content, due to Ar^+ ion bombardment during the erosion, oxygen tends to escape from the sample surface as observed in [Yusupjanova 2016], [Ohwaki 1989]. This effect reduces the AES signal of oxygen and consequently, leads to spurious oxygen nonstoichiometry.

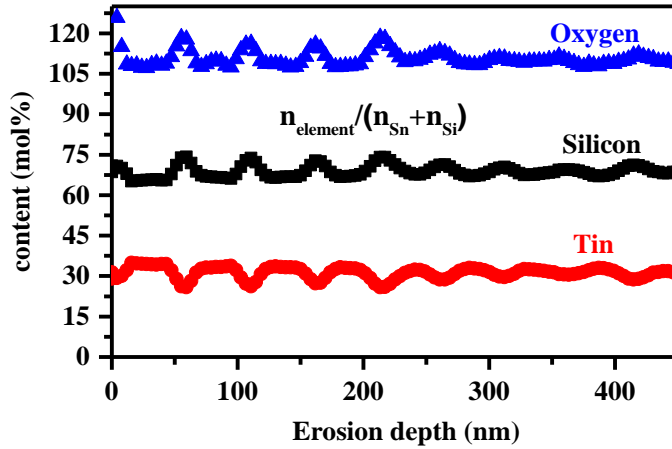


Figure 4.14 AES in-depth composition profile vs erosion depth of the top side of the $70\text{SiO}_2\text{-}30\text{SnO}_2\text{:}0.5\text{Er}^{3+}$ planar waveguide

This layered structure is also observed in the $80\text{SiO}_2\text{-}20\text{SnO}_2\text{:}0.5\text{Er}^{3+}$ planar waveguide, see Figure 4.15. Considering only one layer, SnO_2

locates mostly in the center with $\sim (21 \pm 3)$ mol% and the content on the surface is $\sim (10 \pm 1)$ mol%.

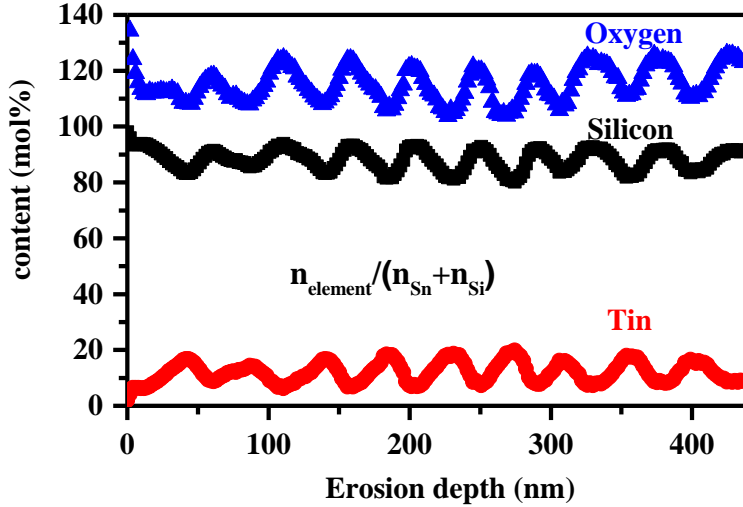


Figure 4.15 AES in-depth composition profile vs erosion depth of the top side of the $80\text{SiO}_2\text{-}20\text{SnO}_2\text{:}0.5\text{Er}^{3+}$ planar waveguide

In case of the $90\text{SiO}_2\text{-}10\text{SnO}_2\text{:}0.5\text{Er}^{3+}$ planar waveguide, the center-localized distribution of SnO_2 is less visible due to its small content of 10 mol%. However, some small fluctuation of SnO_2 content still can be seen from Figure 4.16. The SnO_2 content is determined to be $\sim (12 \pm 2)$ mol%. Measurements reveal a quite homogenous distribution of Si, O and Sn.

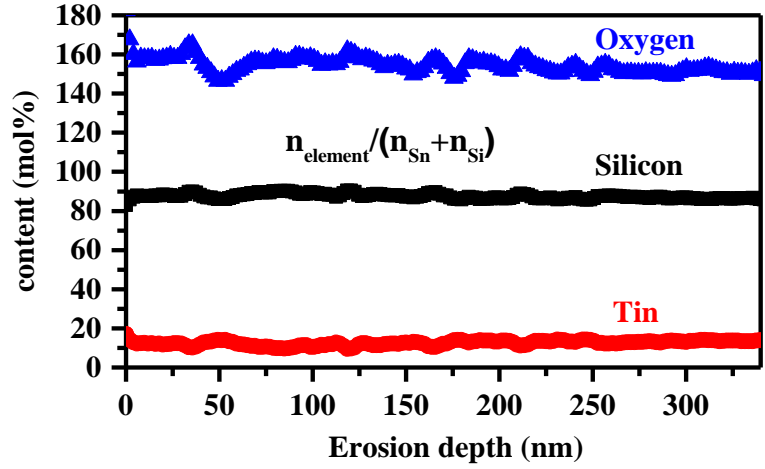


Figure 4.16 AES in-depth composition profile vs erosion depth of the top side of the $80\text{SiO}_2\text{-}20\text{SnO}_2\text{:}0.5\text{Er}^{3+}$ planar waveguide

4.4.4.2 Chemical states

However, the high-quality signal of the first four SnO_2 -rich and SiO_2 -rich layers is enough for a detailed analysis of AES profile and corresponding thicknesses of the layers, see in Figure 4.17. The results show a remarkable thickness homogeneity among these layers. Interestingly, the thickness of a pair of SnO_2 -rich and SiO_2 -rich layers is comparable with the thickness of each dipping layer (~ 54 nm). This aspect reveals that the component distribution of each dipping layer is SnO_2 -rich in the center and SiO_2 -rich on the surface. This is due to the reduction of the surface-crystal of SnO_2 which has been already observed in [Van 2015]. Instead of homogeneous dispersion of 30 mol% SnO_2 throughout the layer, the concentration of SnO_2 varies from $\sim (35 \pm 4)$ mol% in the center to $\sim (25 \pm 4)$ mol%. Moreover, the average of SnO_2 content throughout the erosion depth remains compatible with the synthesis composition of the planar waveguide with 30 mol% SnO_2 .

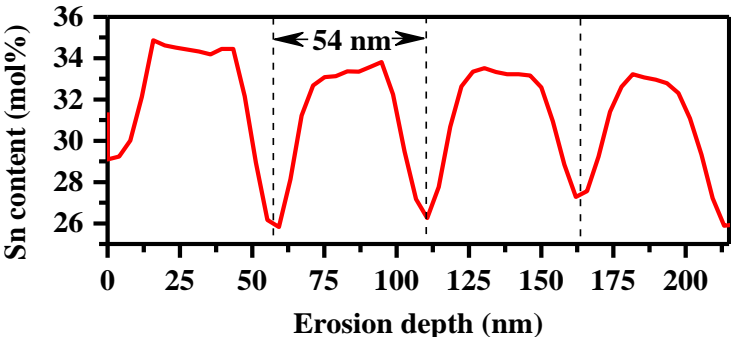


Figure 4.17 AES depth profile of tin signal of the first four SnO_x -rich and SiO_y -rich layers on the top side of the 70SiO_2 - $30\text{SnO}_2:0.5\text{Er}^{3+}$ planar waveguide

The AES spectra acquired at different depth of 268.6 and 908.5 nm in Figure 4.18 reveal the consistent chemical states of Sn, Si and O. The oxidation states of Sn and Si were detailedly determined by the energy peak shift and the shape of the principle Auger transitions: LMM for Si and MNN for Sn.

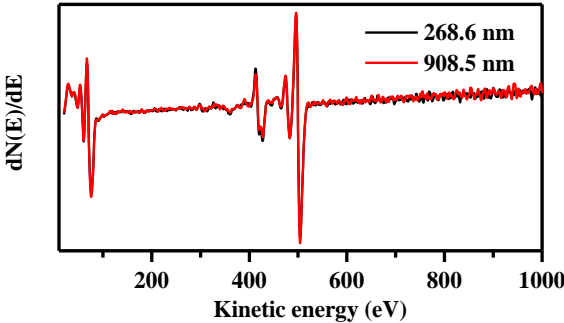


Figure 4.18 AES spectra acquired at different depth of 268.6, 908.5 nm and at the end of the depth profile of the top side of the 70SiO_2 - $30\text{SnO}_2:0.5\text{Er}^{3+}$ planar waveguide

Figure 4.19 shows different AES spectra of Si_{LMM} line shape acquired at different depths of the planar waveguide where there is the maximum, minimum signal of Sn and at the end of the depth profile in comparison with the references of Si element and in silicon oxide. The fingerprints exhibit the typical features of Si in SiO_2 matrix [Lang 1989], [Ntwaeaborwa 2006]. There is no remarkable position and shape change of the line shapes. In other words, no difference in chemical state of the element was detected.

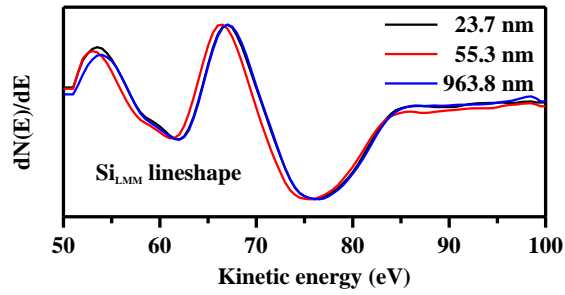


Figure 4.19 Analysis of LMM line shape of silicon at different depths of the planar waveguide: 23.7 nm (maximum of Sn signal), 55.3 nm (minimum of Sn signal) and 963.8 nm (at the end of the profile)

Concerning the chemical state of Sn, the characteristic line shapes of Sn in SnO_2 [Nehasil 2003], [Lee 2000], [Ryzhikov 2002] were indicated in Figure 4.20. The overlapping curves confirms no chemical states variation at the different depths of the profile.

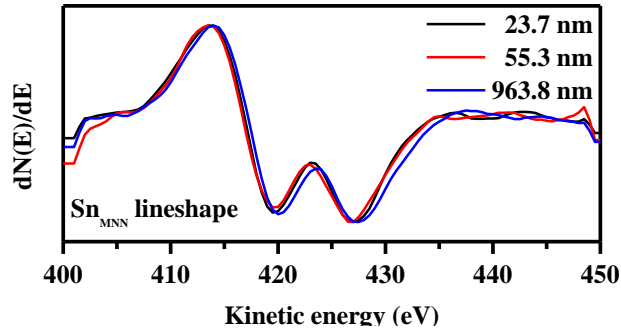


Figure 4.20 Analysis of MNN lineshape of tin at different depths of the planar waveguide: 23.7 nm (maximum of Sn signal), 55.3 nm (minimum of Sn signal) and 963.8 nm (at the end of the profile)

In addition, the line shapes of oxygen do not show significant change in energy position and shape as shown in Figure 4.21.

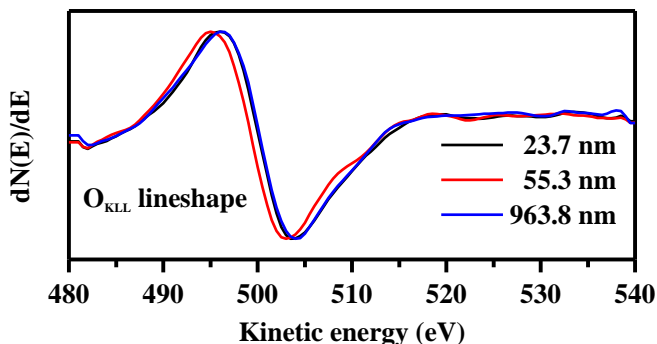


Figure 4.21 Analysis of KLL lineshape of oxygen at different depths of the planar waveguide: 23.7 nm (maximum of Sn signal), 55.3 nm (minimum of Sn signal) and 963.8 nm (at the end of the profile)

4.4.5 Surface roughness

Besides the bulk scattering losses coming from defects of the nano/microstructure of the glass-ceramics, the surface scattering is also a crucial issue, especially in optical waveguiding applied for integrated optics. Therefore, analyzing the surface roughness of the compositional planar waveguides is mandatory. The roughness of the planar waveguides is analyzed by means of Atomic force microscope (AFM). The AFM images were acquired with a Solver Px Scanning Probe Microscope from NT-MDT Spectrum Instruments (Zelenograd, Moscow, Russia). AFM data were acquired in semi-contact mode with a silicon tip ($\sim 3\text{-}30\text{ N/m}$, $\sim 310\text{ KHz}$) with a nominal radius of less than 10 nm . Analyses were performed in the “center” of each sample on different scanning areas, $30 \times 30\text{ }\mu\text{m}^2$ and $10 \times 10\text{ }\mu\text{m}^2$ with a resolution of 512×512 pixels.

The average roughness (R_a – ISO 4287/1 [nm]) and root mean square roughness (R_{MS} – ISO 4287/1 [nm]) were estimated for each scanned area. Figure 4.22 shows the 3D AFM images of the top-side coating of the thin film containing pure SiO_2 doped with 0.5 mol\% Er^{3+} and the glass-ceramic planar waveguides $(100-x)\text{SiO}_2\text{-}x\text{SnO}_2\text{:}0.5\text{Er}^{3+}$ ($x = 5, 10, 15, 20, 25$ and 30). These images show a uniform distribution of the nanocrystals on the surface. The mean values of the average roughness and root mean square roughness are calculated from three different scanned areas and they are shown in Table 4.2.

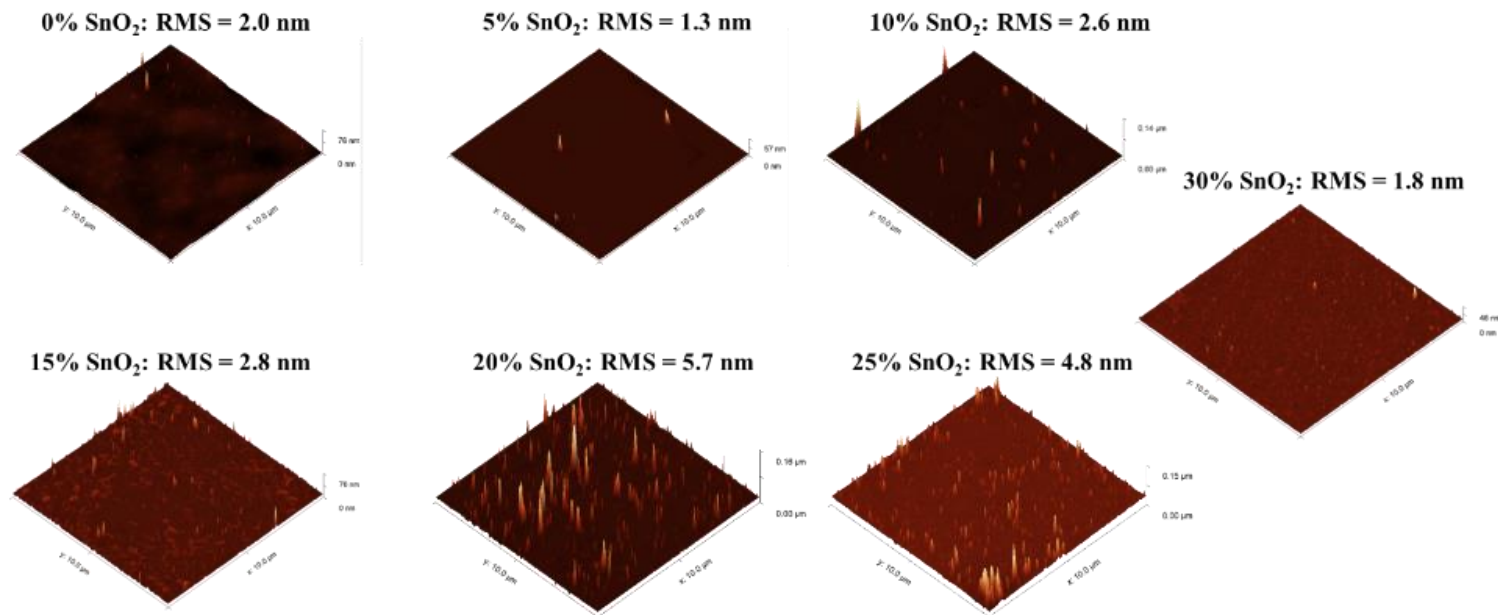


Figure 4.22 AFM images of the $(100-x)\text{SiO}_2\text{-}x\text{SnO}_2\text{:}0.5\text{Er}^{3+}$ planar waveguides ($x = 0, 5, 10, 15, 20, 25$ and 30 mol%)

Table 4.2 shows that all the contents of tin dioxide exhibit appropriate values. These values meet the requirement of 10 nm following the Rayleigh smooth-surface criterion equation (4.1) for UV-mid-IR range as suggested in the work [Jonh 2012]. Increasing SnO₂ content from 0 to 20 leads to an increase of the surface roughness to the maximum value of 5.7 nm. Then, the surface roughness decreases from 4.8 nm for the 25 mol% SnO₂ planar waveguide down to 1.8 nm for the 30 mol% one. This trend of surface is in agreement with the behavior of increasing contribution of larger-sized SnO₂ nanocrystals up to 20 mol% SnO₂ and then decreasing in 25 and 30 mol% as discussed in XRD (see 4.4.2) and HR-TEM analyses earlier (see 4.4.3). Considering the possible losses coming both in terms of bulk and surface scattering, the 30 mol% SnO₂ planar waveguide show the best performance. In addition, this is the highest SnO₂ achieved in this planar waveguide format and it is beneficial to obtain high photorefractivity and Er³⁺ luminescence sensitizing.

Table 4.2 The average roughness (Ra) and root mean square roughness (RMS) of the (100-x)SiO₂-xSnO₂:0.5Er³⁺ planar waveguides (x = 0, 5, 10, 15, 20, 25 and 30 mol%)

(100-x)SiO ₂ -xSnO ₂ :0.5Er ³⁺ (x: mol%)	average roughness Ra (nm)	root mean square roughness RMS (nm)
x = 0	1.5	2.0
x = 5	0.6	1.3
x = 10	0.7	2.6
x = 15	1.4	2.8
x = 20	1.7	5.7
x = 25	1.9	4.8
x = 30	0.8	1.8

4.5 Spectroscopic properties

Aforementioned, the spectroscopic properties of SiO₂-SnO₂:Er³⁺ are essential features which decide the lasing configuration of the systems. Exploiting the complementary information from the structural and chemical characterization, the spectroscopic properties of the glass-ceramics are studied using absorption and photoluminescence spectra.

4.5.1 Experimental set-ups

4.5.1.1 Spectrophotometer

The absorption spectra of the $\text{SiO}_2\text{-SnO}_2\text{:Er}^{3+}$ glass-ceramics were acquired using the Cary Varian 5000 spectrophotometer.

4.5.1.2 Spectrofluorometer

Edinburgh FLS980 spectrofluorometer, fully automated modular device was employed to perform the steady photoluminescence spectra. The NIR-PMT photomultiplier and monochromator slit of few micrometers (200-500 μm) was used to obtain high resolution photoluminescence emission and excitation spectra of the $\text{SiO}_2\text{-SnO}_2\text{:Er}^{3+}$. The time-resolved emission spectra were also acquired. The wide lifetime ranging from nanosecond to second and the reduced instrumental response width allow the acquisition of the time-resolved photoluminescence spectra for the investigation of the energy transfer.

4.5.1.3 Luminescence in waveguiding configuration

The photoluminescence spectra were also acquired using modular experimental set-up. By applying the prism coupling technique, excitation light was injected into the planar waveguides and the luminescence measurements were performed at the coupling mode of the excitation light. This waveguiding configuration allows increasing the photoluminescence signals and consequently obtaining the spectra with an increase of contrast [Righini 2005]. The setup schematic used for the waveguiding luminescence measurements is shown in Figure 4.23.

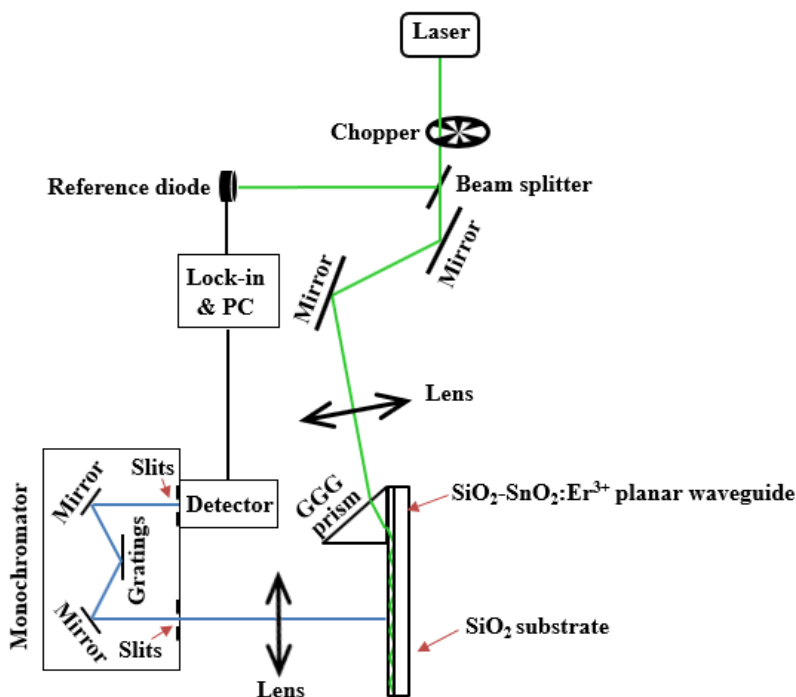


Figure 4.23 The setup schematic of luminescence measurement in waveguiding configuration

A Gadolinium gallium garnet (GGG) prism, with a refractive index of $n_p = 1.9758$ at $\lambda_L = 543.5$ nm cut at 45° - 90° - 45° was employed. The 514.5 nm coherent laser beam from the Ar^+ laser Coherent mod. Innova-Sabre TSM 15 (Santa Clara, CA, USA) was used to directly excite Er^{3+} to its $^2\text{H}_{1/2}$ excited state and the emission and time-resolved emission spectra of Er^{3+} at 1500 nm were recorded at room temperature.

4.5.1.4 Luminescence in reflection configuration

For the acquisition of the emission spectra at different excitation wavelengths, the modular photoluminescence set-up was in reflection configuration. The reflection configuration shown in Figure 4.24 was employed to perform such measurements. All the measurements were carried out at room temperature.

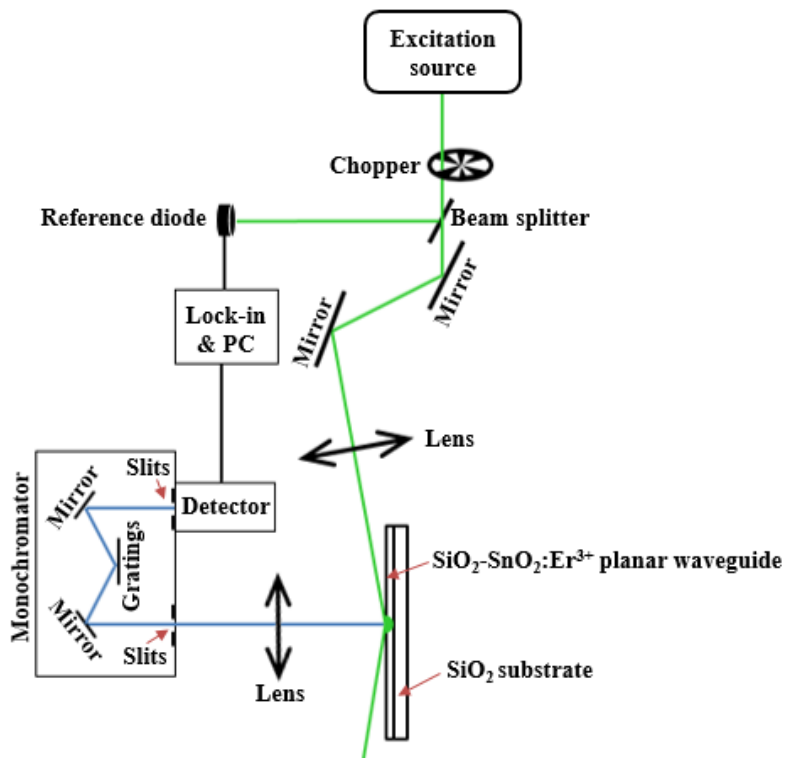


Figure 4.24 The setup schematic of luminescence measurement in reflection configuration

In this case, the Xenon lamp 450 W (Edison, NJ, USA) coupled to monochromator Horiba mod. microHR (Edison, NJ, USA) with a grating of 1200 g/mm was used as an excitation source. The original emission spectrum of the Xenon lamp is shown in Figure 4.25. The excitation range was from 300 nm to 750 nm with 1 nm scanning step and the spectral resolution of 10 nm.

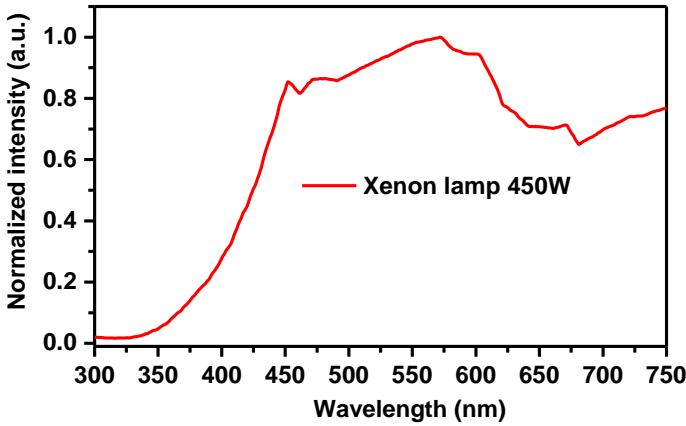


Figure 4.25 The original emission spectrum of the Xenon lamp 450W (Edison, NJ, USA)

The Thorlabs UV diode laser ($\lambda_{\text{ex}} = 340 \text{ nm}$) was also used as an excitation source for the SnO_2 band-gap excitation, i.e. indirect excitation for Er^{3+} luminescence at $1.5 \mu\text{m}$.

4.5.2 Absorption

Since the absorption spectra of planar waveguides suffer from the interference between the layers as shown in Figure 3.26, for the investigation of Er^{3+} transitions, the absorption measurements were performed only on the monolithic squares $(100-x)\text{SiO}_2-x\text{SnO}_2:0.5\text{Er}^{3+}$ ($x = 0, 5$ and $10 \text{ mol}\%$). Absorption spectra allow determining the absorption coefficients and absorption cross sections which are the fundamental factors governing the optical sensitivity of the $\text{SiO}_2\text{-SnO}_2\text{:Er}^{3+}$ glass-ceramics [Righini 2005]. Using the data from the absorption spectra, the Judd-Ofelt theory was applied to analyze the radiative properties of Er^{3+} transitions in $\text{SiO}_2\text{-SnO}_2$ glass-ceramics such as: the transition probability, radiative lifetimes and the branching ratios.

4.5.2.1 Absorption spectra

Before the discussion of absorption, it is necessary to recall the energy-level diagram of SnO_2 and Er^{3+} as shown in Figure 4.26.

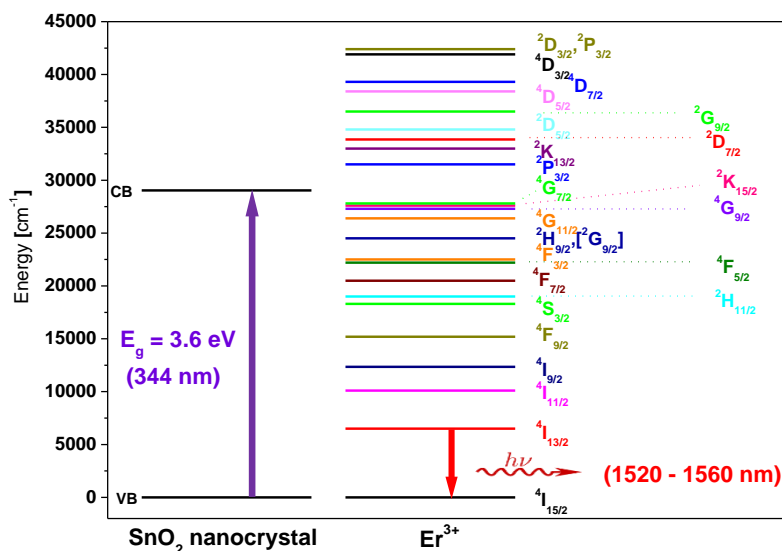
Figure 4.26 Energy-level diagram of SnO₂ and Er³⁺ transitions

Figure 4.27 shows the absorption spectra of the (100-x)SiO₂-xSnO₂:0.5Er³⁺ monoliths (x = 0, 5 and 10 mol%). The assignments of the SnO₂ interband transitions and Er³⁺ transition from the ground state ⁴I_{15/2} to an excited state were carried out based on the energy diagram shown in Figure 4.26.

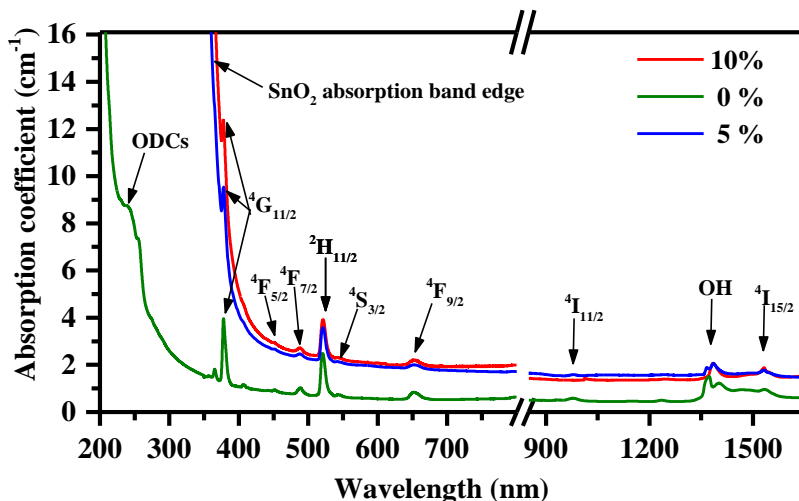


Figure 4.27 Room temperature absorption spectra of the (100-x)SiO₂-xSnO₂:0.5Er³⁺ monoliths (x = 0, 5 and 10 mol%)

Both 5 and 10 mol% SnO₂ monoliths exhibit an optical absorption band edge at around 3.5 eV (~ 350 nm) which is close to the largely accepted value of SnO₂ band gap of 3.6 eV at 300K [Mounkachi 2016], [Trani 2008], [Zur 2017b]. Increasing the SnO₂ content leads to a red-shift of the optical absorption band edge and an increase of the material absorption background as already observed in [Zur 2017b]. The pure SiO₂:0.5Er³⁺ shows the absorption band edge at > 6.2 eV of SiO₂ (~ 200 nm) with the presence of typical UV absorption band centered at 240 nm, assigned to existent oxygen deficient centers in SiO₂ [Saito 2014], [Skujia 1998], [Skujia 2012]. The bands at around 1385 nm is assigned to the two –OH stretching vibrations [Righini 2005], [Grzechnik 1998]. The presence of the residual –OH groups in the monoliths suggests that a further treatment after the current heat-treatment at 900°C for 100 h is necessary to remove completely the OH groups. The absorption bands corresponding to the transitions of Er³⁺ from the ground state ⁴I_{15/2} to other excited states are also revealed in Figure 4.27. From Figure 4.27, all the absorption spectra reveal that the absorption coefficient of the interband absorption of SnO₂ is much higher than the absorption coefficients of the Er³⁺ transitions.

In Figure 4.28, the absorption spectra of the 95SiO₂-5SnO₂:yEr³⁺ monoliths doped with different concentrations of Er³⁺ (y = 0.25, 0.50, 0.75 and 1.00 mol%) also reveal all the relevant Er³⁺ transitions as discussed ahead and SnO₂ interband absorption in the UV range. Higher Er³⁺ concentration leads to higher absorption coefficients. However, they are still much lower in comparison with the absorption coefficient of the interband SnO₂ transitions.

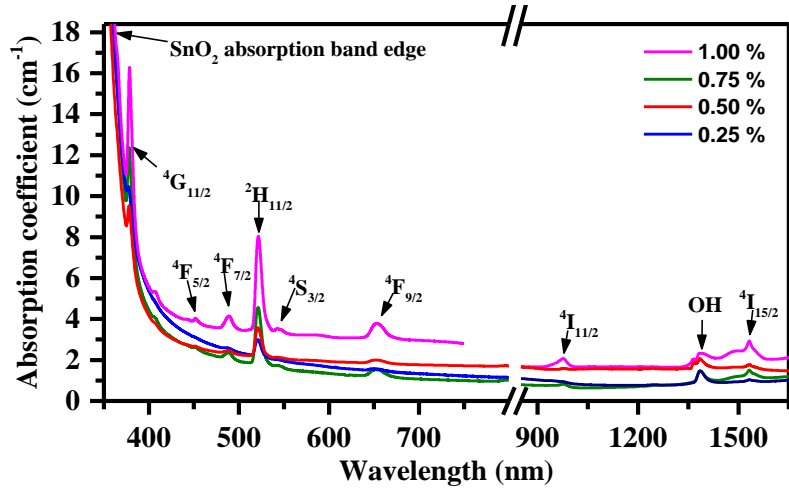


Figure 4.28 Room temperature absorption spectra of the 95SiO₂-5SnO₂:yEr³⁺ monoliths (x = 0.25, 0.50, 0.75 and 1.00 mol%)

One can find the assignment of the absorption bands and the absorption coefficients corresponding to the transitions of Er³⁺ from the ground state $^4I_{15/2}$ to an excited state of (100-x)SiO₂-xSnO₂:0.5Er³⁺ monoliths containing different SnO₂ contents (x = 0, 5 and 10 mol%) and 95SiO₂-5SnO₂:yEr³⁺ monoliths doped with different Er³⁺ concentrations (y = 0.25, 0.50, 0.75 and 1.00 mol%) in Table 4.3. These values are used for the calculation of the absorption cross sections shown in the next subsection 4.5.2.2.

Figure 4.29 shows the room temperature absorption spectra in the range of the $^4I_{15/2}$ - $^4I_{13/2}$ transition of Er³⁺ in the SiO₂-SnO₂:Er³⁺ monoliths. Concerning the (100-x)SiO₂-xSnO₂:0.5Er³⁺ monoliths (x = 0, 5 and 10 mol%), from Figure 4.29 a), it is evident that the effective absorption bandwidth is narrower in the glass-ceramics, i.e. 10 and 5 mol% SnO₂-containing monoliths than the 100SiO₂:0.5Er³⁺ glass. And the maximum absorption peaks of Er³⁺ in the glass-ceramics is at 1532 while it shifts to 1537 nm in the 100SiO₂:0.5Er³⁺ glass. This can be attributed to the reduction of the inhomogeneous broadening absorption which is greater when Er³⁺ ions locate in a disordered structure, i.e. glasses [Righini 2005]. The occupation of the active ions in more and more different microscopic environments in short-range disorder of glasses gives rises to the inhomogeneous broadening [Hehlen 1997], [Righini 2005]. In other words, in the 5 and 10 mol% SnO₂ glass-ceramics doped with 0.5 mol% Er³⁺, most of the rare earth ions locates in a higher ordered

environment than SiO_2 , i.e. SnO_2 . This effect was already observed in other glass-ceramics [Miguel 2014] when Er^{3+} ions locates in the crystalline environments. Moreover, Figure 4.29 b) shows the $^4\text{I}_{15/2}$ - $^4\text{I}_{13/2}$ absorption spectra of the 5 mol% SnO_2 glass-ceramics doped with different Er^{3+} concentrations. Although the maximum peaks of the absorption bands remain at 1533 nm representing for Er^{3+} in the glass-ceramics but increasing the Er^{3+} concentrations lead to a broader bandwidth. The higher absorption at the shorter wavelength region similar to the one of $100\text{SiO}_2:0.5\text{Er}^{3+}$ is probably due to the occupation of a higher portion of Er^{3+} ions in SiO_2 in the 95SiO_2 - SnO_2 doped with higher Er^{3+} concentrations

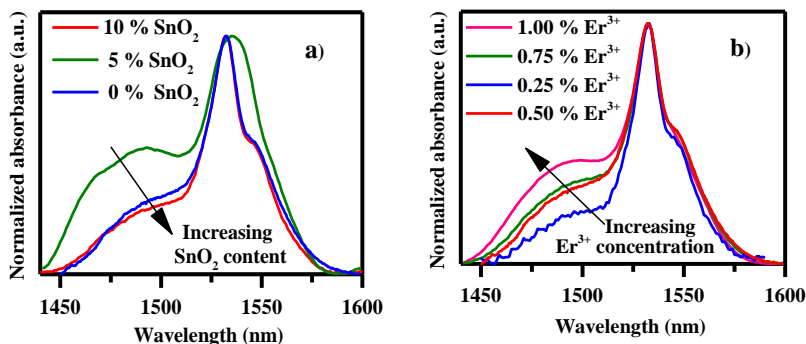


Figure 4.29 Room temperature absorption spectra of (of $^4\text{I}_{15/2}$ - $^4\text{I}_{13/2}$ transition of Er^{3+} in: a) $(100-x)\text{SiO}_2$ - $x\text{SnO}_2:0.5\text{Er}^{3+}$ monoliths containing different SnO_2 contents ($x = 0, 5$ and 10 mol%) and b) 95SiO_2 - $5\text{SnO}_2:y\text{Er}^{3+}$ monoliths doped with different Er^{3+} concentrations ($y = 0.25, 0.50, 0.75$ and 1.00 mol%)

Table 4.3 Table of the absorption bands and the absorption coefficient corresponding to the transitions of Er^{3+} from the ground state $^4\text{I}_{15/2}$ to an excited state of $(100-x)\text{SiO}_2-x\text{SnO}_2:0.5\text{Er}^{3+}$ monoliths containing different SnO_2 contents ($x = 0, 5$ and 10 mol%) and $95\text{SiO}_2-5\text{SnO}_2:y\text{Er}^{3+}$ monoliths doped with different Er^{3+} concentrations ($y = 0.25, 0.50, 0.75$ and 1.00 mol%).

Notes: GC means glass-ceramics ($x = 5$ and 10 mol%) and G means glass ($x = 0$).

Absorption bands		Absorption coefficient α (cm^{-1}) with 5 % error						
		(100-x)SiO ₂ -xSnO ₂ :0.5Er ³⁺ monoliths containing different SnO ₂ contents (x = 0, 5 and 10 mol%)			95SiO ₂ -5SnO ₂ :yEr ³⁺ monoliths doped with different Er ³⁺ concentrations (y = 0.25, 0.50, 0.75 and 1.00 mol%)			
		x = 10	x = 5	x = 0	y = 0.25	y = 0.50	y = 0.75	y = 1.00
$\lambda(\text{nm})$	transition							
378	$^4\text{I}_{15/2}-^4\text{G}_{11/2}$	1.926	1.757	2.693	0.919	1.757	3.640	6.357
451	$^4\text{I}_{15/2}-^4\text{F}_{5/2}$	0.055	0.045	0.082	0.018	0.045	0.090	0.190
488	$^4\text{I}_{15/2}-^4\text{F}_{7/2}$	0.205	0.135	0.293	0.078	0.135	0.307	0.632
521	$^4\text{I}_{15/2}-^2\text{H}_{11/2}$	1.565	1.393	1.781	0.799	1.393	2.726	4.583
542	$^4\text{I}_{15/2}-^4\text{S}_{3/2}$	0.048	0.038	0.074	0.023	0.038	0.068	0.152
652	$^4\text{I}_{15/2}-^4\text{F}_{9/2}$	0.258	0.162	0.307	0.103	0.162	0.355	0.742
1533(GC)/ 1537(G)	$^4\text{I}_{15/2}-^4\text{I}_{13/2}$	0.394	0.232	0.215	0.110	0.232	0.419	0.870

4.5.2.2 Absorption cross section

(i) Absorption cross sections of Er^{3+} transitions

For photonic application, absorption cross section is one of the fundamental factors which quantify the probability of a luminescent specie to absorb light at a certain wavelength and this is a crucial factor for optical amplification [Tanabe 1999]. In addition, as other spectroscopic properties, the absorption cross section strongly depends on the local environment of the rare-earth ions. In other words, the nature and the composition of the host material play a crucial role in tailoring the absorption cross section and the whole spectroscopic properties of the rare-earth ions through the modification of their local environment [Righini 2005], [Tanabe 1999]. The absorption coefficients from Figure 4.27 and Figure 4.28 allow calculating the absorption cross section of Er^{3+} transitions following the equation:

$$\sigma(\lambda) = \frac{\alpha(\lambda)}{N_0} \quad (4.3)$$

where $\sigma(\lambda)(\text{cm}^2)$ is the absorption cross section at a certain wavelength λ ;

$\alpha(\lambda)(\text{cm}^{-1})$ is the absorption coefficient at the wavelength λ ;

N_0 is the estimated Er^{3+} concentration (ions/ cm^3) of the $\text{SiO}_2\text{-SnO}_2\text{:Er}^{3+}$ monoliths.

Figure 4.30 shows the absorption cross sections of the $^4\text{I}_{15/2}\text{-}^4\text{I}_{13/2}$ transition of Er^{3+} in the compositional glass-ceramic monoliths. Concerning the monoliths doped with 0.5 mol%, from Figure 4.30a, the 10 mol% SnO_2 glass-ceramic monolith exhibits highest absorption cross sections compared to the 5 mol% SnO_2 and the pure SiO_2 glass. On the other hands, from Figure 4.30b of the 95 $\text{SiO}_2\text{-5SnO}_2$ glass-ceramics doped with different Er^{3+} concentrations, increasing Er^{3+} concentration results in an increase of the $^4\text{I}_{15/2}\text{-}^4\text{I}_{13/2}$ absorption cross section. However, the comparable absorption cross section at 1.5 μm of Er^{3+} in the 90 $\text{SiO}_2\text{-10SnO}_2\text{:0.5Er}^{3+}$ to the 95 $\text{SiO}_2\text{-5SnO}_2\text{:1.0Er}^{3+}$ indicate that the presence of SnO_2 nanocrystals lead to an increase of absorption cross section of Er^{3+} even at lower Er^{3+} concentration (two times less). In other words, this is an indication for tailoring the absorption cross section of Er^{3+} by changing the Er^{3+} local environment and the validity of SnO_2

nanocrystals in the glass-ceramics in increasing the optical cross section of Er^{3+} .

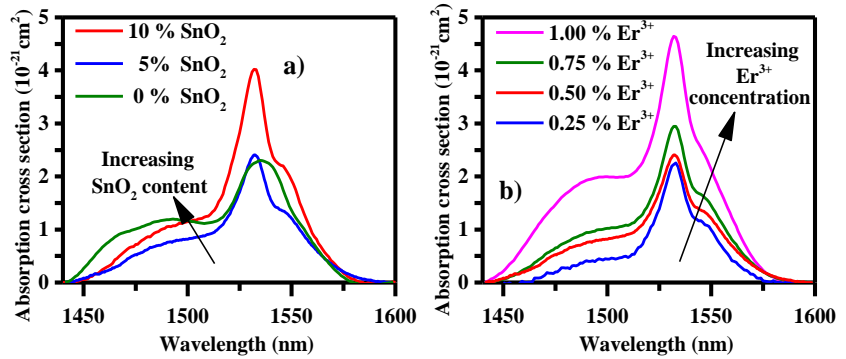


Figure 4.30 Room temperature absorption spectra of (of $^4\text{I}_{15/2}$ - $^4\text{I}_{13/2}$ transition of Er^{3+} in: a) $(100-x)\text{SiO}_2$ - $x\text{SnO}_2$: 0.5Er^{3+} monoliths containing different SnO_2 contents ($x = 0, 5$ and $10 \text{ mol}\%$) and b) 95SiO_2 - 5SnO_2 : $y\text{Er}^{3+}$ monoliths doped with different Er^{3+} concentrations ($y = 0.25, 0.50, 0.75$ and $1.00 \text{ mol}\%$)

Table 4.4 tabulates the absorption cross sections at the maximum absorption peaks of each Er^{3+} transition from the ground state $^4\text{I}_{15/2}$ to an excited state in $(100-x)\text{SiO}_2$ - $x\text{SnO}_2$: 0.5Er^{3+} monoliths containing different SnO_2 contents ($x = 0, 5$ and $10 \text{ mol}\%$) and 95SiO_2 - 5SnO_2 : $y\text{Er}^{3+}$ monoliths doped with different Er^{3+} concentrations ($y = 0.25, 0.50, 0.75$ and $1.00 \text{ mol}\%$). Although for the lasing applications of SiO_2 - SnO_2 : Er^{3+} glass-ceramics, the most desired pumping scheme is to excite the SnO_2 band gap in the UV range and exploit the luminescence sensitization, it could not be directly calculated due to lacking the concentration of emitting centers of SnO_2 . However, an attempt to estimate the cross section of the transitions occurring in SnO_2 was carried out and discussed in the next concept.

Table 4.4 Absorption cross section of the Er^{3+} transitions of from the ground state $^4\text{I}_{15/2}$ to an excited state in $(100-x)\text{SiO}_2-x\text{SnO}_2:0.5\text{Er}^{3+}$ monoliths containing different SnO_2 contents ($x = 0, 5$ and 10 mol%) and $95\text{SiO}_2-5\text{SnO}_2:y\text{Er}^{3+}$ monoliths doped with different Er^{3+} concentrations ($y = 0.25, 0.50, 0.75$ and 1.00 mol%). Notes: GC means glass-ceramics ($x = 5$ and 10 mol%) and G means glass ($x = 0$).								
Absorption bands		Absorption cross section σ ($10^{-21} \times \text{cm}^2$) with 5% error						
		$(100-x)\text{SiO}_2-x\text{SnO}_2:0.5\text{Er}^{3+}$ monoliths containing different SnO_2 contents ($x = 0, 5$ and 10 mol%)			$95\text{SiO}_2-5\text{SnO}_2:y\text{Er}^{3+}$ monoliths doped with different Er^{3+} concentrations ($y = 0.25, 0.50, 0.75$ and 1.00 mol%)			
$\lambda(\text{nm})$	transition	$x = 10$ ($N_0=9.797 \times 10^{19}$ ions/ cm^3)	$x = 5$ ($N_0=9.638 \times 10^{19}$ ions/ cm^3)	$x = 0$ ($N_0=9.366 \times 10^{19}$ ions/ cm^3)	$y = 0.25$ ($N_0=4.889 \times 10^{19}$ ions/ cm^3)	$y = 0.50$ ($N_0=9.638 \times 10^{19}$ ions/ cm^3)	$y = 0.75$ ($N_0=14.251 \times 10^{19}$ ions/ cm^3)	$y = 1.00$ ($N_0=18.736 \times 10^{19}$ ions/ cm^3)
378	$^4\text{I}_{15/2}-^4\text{G}_{11/2}$	19.66	18.23	28.75	18.79	18.23	25.54	33.93
451	$^4\text{I}_{15/2}-^4\text{F}_{5/2}$	0.56	0.47	0.87	0.37	0.47	0.63	1.02
488	$^4\text{I}_{15/2}-^4\text{F}_{7/2}$	2.09	1.41	3.12	1.59	1.41	2.16	3.37
521	$^4\text{I}_{15/2}-^2\text{H}_{11/2}$	15.98	14.45	19.01	16.35	14.45	19.13	24.46
542	$^4\text{I}_{15/2}-^4\text{S}_{3/2}$	0.49	0.40	0.79	0.46	0.40	0.48	0.81
652	$^4\text{I}_{15/2}-^4\text{F}_{9/2}$	2.63	1.68	3.28	2.10	1.68	2.49	3.96
1533(GC)/ 1537(G)	$^4\text{I}_{15/2}-^4\text{I}_{13/2}$	4.02	2.41	2.30	2.26	2.41	2.95	4.64

4.5.2.3 An attempt to estimate the absorption cross section of SnO₂

In SnO₂, there is an existence of native oxygen vacancies (OV) which acts as a shallow donor leading SnO₂ to become a n-type semiconductor with the band-gap of 3.6 eV [Batzill 2005]. As proposed in the work [Lettieri 2008], there are two types of intrinsic oxygen vacancies which act as carriers in SnO₂: (i) the bulk-like oxygen vacancies which leads to the electronic transport and the interband absorption in UV range [Zhou 2009], [Shu 2013] and (ii) the surface vacancies which attribute to a broad luminescence emission in the Vis range as usually observed in the experimental measurements [Lettieri 2008], [Van 2016]. According to this hypothesis, from Figure 4.27 and Figure 4.28, the saturation of the absorption band starting from 337 nm and 342 nm in the 10 and 5 mol% glass-ceramic monoliths respectively can be assigned to the band-defect-band transitions of the bulk-like oxygen vacancies. This aspect is still an ongoing issue. Nevertheless, disregarding the origin of the transitions leading to UV absorption of SnO₂, according to [Peelaers 2012], the calculation of absorption cross section of exciton transitions of SnO₂ based on the equation:

$$\sigma_{\text{SnO}_2}(\lambda) = \frac{\alpha_{\text{SnO}_2}(\lambda)}{N_{\text{carrier}}} \quad (4.4)$$

where $\sigma_{\text{SnO}_2}(\lambda)$ is the absorption cross section of the interband transition due to free-carriers in SnO₂ semiconductor;

$\alpha_{\text{SnO}_2}(\lambda)$ is the absorption coefficients of SnO₂ interband transitions;

N_{carrier} is the number of carriers, i.e. oxygen vacancies in SnO₂.

However, due to the lack of information of the intrinsic oxygen vacancy concentration, it was not possible to calculate the full absorption cross section of the whole absorption band edge of SnO₂.

Nevertheless, from the excitation spectra which will be discussed in 4.5.4, the most effective excitation wavelength leading to the highest luminescence signal detected at 1.5 μm emission of Er³⁺ is the UV absorption band of SnO₂, for example, at 363 nm and 353 nm for the 10 and 5 mol% SnO₂ glass-ceramic monoliths respectively. This can be explained due to much higher absorption cross section of exciton transitions in SnO₂ in comparison with other transitions between the

electronic states of Er^{3+} , e.g. $^2\text{H}_{11/2}$. With an assumption that the detected 1.5 μm emission intensity of Er^{3+} at a certain excitation wavelength is proportional to the absorption cross section of Er^{3+} at the corresponding excitation wavelength, the absorption cross section of the interband transition of SnO_2 can be estimated as follows: multiplying the known absorption cross section of Er^{3+} at the electronic state $^2\text{H}_{11/2}$ from Table 4.4 and the 1.5 μm emission intensity ratio excited at the SnO_2 UV absorption band (at 363 nm for 10 mol% SnO_2 monoliths) and at the electronic state $^2\text{H}_{11/2}$ of Er^{3+} (at 521 nm) from the excitation spectra discussed in section 4.5.4.2, taking into account the normalization of the different intensity of the light source as shown in Figure 4.25.

The results of estimated absorption cross sections of SnO_2 interband transition of in the 10 and 5 mol% glass-ceramic monoliths are tabulated in Table 4.5. The estimated values of absorption cross section of SnO_2 interband transition are reasonable in comparison with the ones from the work [Peelaers 2012].

Table 4.5 Calculated absorption cross section of RE-induced oxygen vacancy in SnO_2 of the 10 and 5 mol% glass-ceramic monoliths			
	$\alpha_{\text{abs}}(\lambda_{^2\text{H}_{11/2}})$ (cm^{-1})	1.5 μm intensity emission ratio from excitation spectra $(\frac{I_{\lambda_{\text{ex/SnO}_2}}}{I_{\lambda_{\text{ex}/^2\text{H}_{11/2}}}})$	$\sigma_{\text{SnO}_2}(\lambda)$ ($\times 10^{-21} \text{ cm}^2$)
x = 10	15.98	10^3	1.6×10^4
x = 5	14.45	10^3	1.5×10^4

4.5.2.4 McCumber-Miniscalco-Quimby estimated emission cross section

Using the McCumber model [McCumber 1964], the estimation of emission cross section of $^4\text{I}_{13/2}$ - $^4\text{I}_{15/2}$ transition, i.e. the desired 1.5 μm emission of Er^{3+} in the monoliths was carried out following the equation [Righini 2005]:

$$\sigma_e(\lambda) = \left(\exp\left(\frac{\varepsilon - \frac{hc}{\lambda}}{k_B T}\right) \right) \sigma_a(\lambda) \quad (4.5)$$

where $\sigma_e(\lambda)$ and $\sigma_a(\lambda)$ are the emission and absorption cross section of the $^4I_{13/2}$ - $^4I_{15/2}$ transition respectively;

and ε is the temperature-dependent excitation energy, which can be defined simply based on the McCumber -Miniscalco-Quimby model [Miniscalco 1991]:

$$\exp\left(\frac{\varepsilon}{k_B T}\right) = \frac{\sum_{i=1}^M \exp\left(-\frac{(i-1)E_{li}}{k_B T}\right)}{\sum_{j=1}^N \exp\left(-\frac{(j-1)E_{lj}}{k_B T}\right)} \exp\left(\frac{E_0}{k_B T}\right) \quad (4.6)$$

where M and N are the numbers of Stark manifold sublevels of the ground state $^4I_{15/2}$ and the metastable state $^4I_{13/2}$ of Er^{3+} in the host material. In case of the glasses and the rutile-like tetragonal crystal structure of SnO_2 [Miniscalco 1991], the maximum numbers of Stark splitting sublevels of the ground state $^4I_{15/2}$ and the metastable state $^3I_{13/2}$ are: M = 8 and N = 7 respectively;

E_0 is the difference in energy between the lowest energy sublevels of the ground state $^4I_{15/2}$ and the metastable state $^4I_{13/2}$. E_0 was defined by low temperature luminescence measurements in the work [Kong 2009]:

$$E_0 = h\nu_0 \text{ and } \nu_0 = 6570 \text{ cm}^{-1};$$

The E_{li} and E_{lj} are the energy gaps between the Stark components of the ground state $^4I_{15/2}$ and the metastable state $^3I_{13/2}$ respectively. These values were estimated also from the work using the average energy gaps of the Stark sublevels suggested in the work [Kong 2009]:

$$E_{li} = h\nu_{li} \text{ and } \nu_{li} = 53 \text{ cm}^{-1} \text{ and } E_{lj} = h\nu_{lj} \text{ and } \nu_{lj} = 48 \text{ cm}^{-1};$$

k_B is the Boltzmann constant: $k_B = 1.381 \times 10^{-23} \text{ (J / K)}$;

h is Plack constant: $h = 6.626 \times 10^{-34} \text{ Js}$;

T is the temperature at which the absorption measurements were carried out: $T = 300 \text{ K}$.

Figure 4.31 shows the absorption and emission cross sections of Er^{3+} at $1.5 \mu\text{m}$ in the compositional monoliths. The emission spectra show different shapes compared to the measured emission spectra which will be discussed in 4.5.3, especially for the SiO_2 - SnO_2 : Er^{3+} glass-ceramics

when there are Er^{3+} ions embedded in SnO_2 nanocrystals and the emission spectra performed under SnO_2 band gap excitation reveals Stark splitting. This is because of a simplified treatment of the Stark sublevels of this model with assumptions: all the Stark levels are equally spaced and populated [Righini 2005], [Miniscalco 1991], which is in fact different from the real systems especially in crystalline materials [Barnes 1991]. Since the emission cross section of Er^{3+} at a certain wavelength depends on the corresponding absorption cross section, it is not surprising that the 10 mol% SnO_2 glass-ceramics doped with 0.5 mol% Er^{3+} have the highest emission cross sections at 1.5 μm among the $(100-x)\text{SiO}_2-x\text{SnO}_2:0.5\text{Er}^{3+}$ monoliths containing different SnO_2 contents ($x = 0, 5$ and 10 mol%). Comparing between the 5 mol% SnO_2 monoliths doped with different Er^{3+} concentrations ($y = 0.25, 0.50, 0.72$ and 1.00 mol%), the one with highest Er^{3+} concentration, i.e. 1 mol% has the highest emission cross sections at 1.5 μm . In addition, the effective optical cross section bandwidth of $^4\text{I}_{15/2} \leftrightarrow ^4\text{I}_{13/2}$ transition of Er^{3+} in the $\text{SiO}_2\text{-SnO}_2:\text{Er}^{3+}$ monoliths was also defined [Righini 2005] as following equation:

$$\Delta\lambda = \frac{\int_{\text{band}} \alpha_e(\lambda) d\lambda}{\lambda_{\text{peak}}} \quad (4.7)$$

Table 4.6 tabulates all the absorption cross sections (σ_a) and emission cross sections (σ_e) of $^4\text{I}_{15/2} \leftrightarrow ^4\text{I}_{13/2}$ transitions of Er^{3+} in the compositional $\text{SiO}_2\text{-SnO}_2:\text{Er}^{3+}$ monoliths in the comparison with some other host matrices in the literature. These three parameters: σ_a , σ_e and $\Delta\lambda$ are crucial for the optical amplifiers in the wavelength-division-multiplexing (WDM) in fiber-optical communications [E Desurvire 1994], [Righini 2005], [Pelli 2004]. For a comparison, Table 4.6 reports the values of σ_a , σ_e and $\Delta\lambda$ of Er^{3+} in $\text{SiO}_2\text{-SnO}_2$ glass-ceramics in comparison with other glass host matrices such as phosphate and silicate glasses which were studied as rare-earth-activated gain media in the literature [Benoit 2005], [Barnes 1991], [Rolli 2003], [Miniscalco1991]. From this table, one can see that the values of σ_a , σ_e and $\Delta\lambda$ vary depending on the host material composition which governs the local environment of Er^{3+} and modifies the spectroscopic properties of the rare-earth [Righini 2005]. The absorption and emission cross section of the 10 mol% SnO_2 glass-ceramic monolith are among the highest values of the reported host materials. In particular, a comparison with other host matrices with Er^{3+} concentrations from 7×10^{19} to 10×10^{19} ions/ cm^3 , the

optical cross sections of 10 mol% SnO₂ glass-ceramic monolith are comparable to the highest ones from Baccarat [Benoit 2005]. In case of Tellurite, the highest emission cross sections of Er³⁺ were achieved thanks to their high refractive index [Rolli 2003]. This is an explanation for the higher cross sections of Er³⁺ achieved in higher SnO₂ containing glass ceramics since there is higher portion of Er³⁺ ions embedded in SnO₂ nanocrystals, i.e. higher-refractive region in the glass-ceramics. The increasing SnO₂ content may be a strategy to obtain higher optical cross section of Er³⁺ at 1.5 μm. However, in case of SiO₂-SnO₂ monoliths, the achievable SnO₂ content is 10 mol%. Therefore, the cross section at λ_{peak} of 1.5 μm emission of Er³⁺ has only an increase from 3.27×10^{-21} to 5.03×10^{-21} from the pure SiO₂:Er³⁺ glass to 90SiO₂-10SnO₂:0.5Er³⁺ glass-ceramic monoliths. However, from this behavior, in case of the glass-ceramic planar waveguides with maximum SnO₂ content of 30 mol%, higher increase of optical cross sections of Er³⁺ is expected.

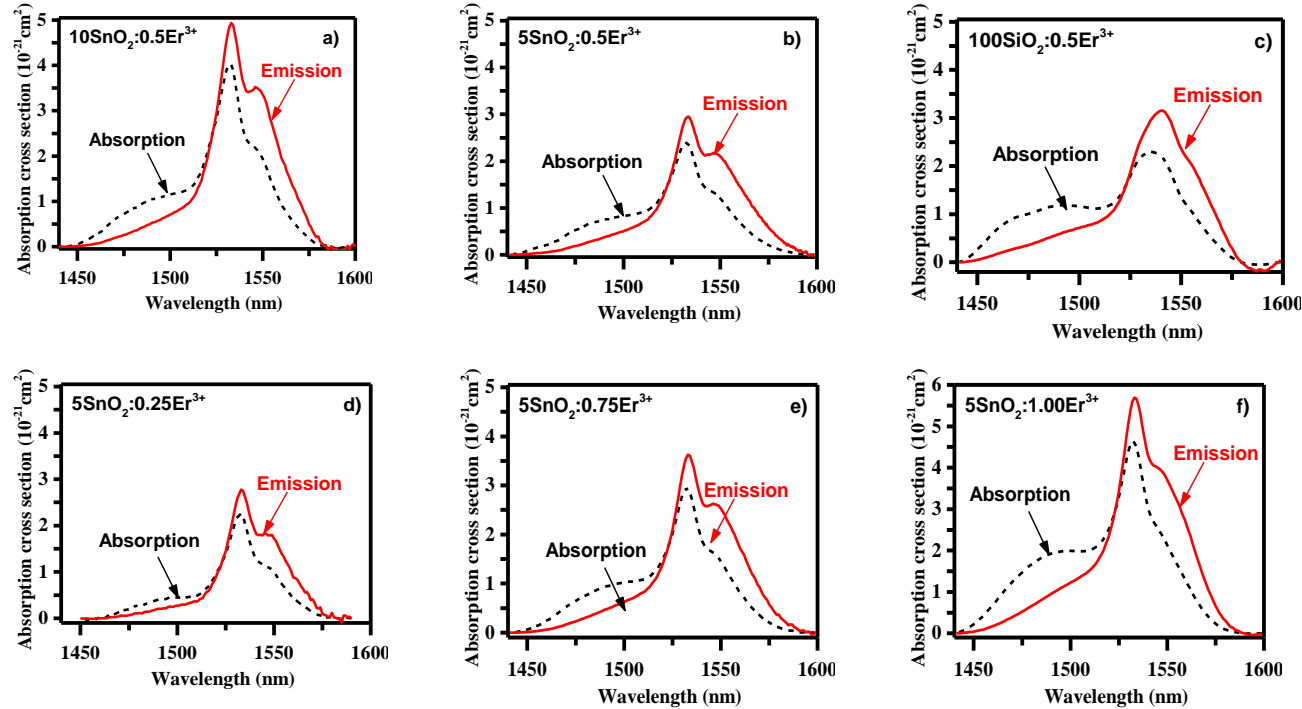


Figure 4.31 Absorption and calculated emission cross section of Er^{3+} at $1.5 \mu\text{m}$ of the monoliths: a) $90\text{SiO}_2-10\text{SnO}_2:0.5\text{Er}^{3+}$, b) $95\text{SiO}_2-5\text{SnO}_2:0.5\text{Er}^{3+}$, c) $100\text{SiO}_2:0.5\text{Er}^{3+}$, d) $95\text{SiO}_2-5\text{SnO}_2:0.25\text{Er}^{3+}$, e) $95\text{SiO}_2-5\text{SnO}_2:0.75\text{Er}^{3+}$ and f) $95\text{SiO}_2-5\text{SnO}_2:1.00\text{Er}^{3+}$

Table 4.6 Values σ_a , σ_e and $\Delta\lambda$ of $^4I_{15/2}$ - $^4I_{13/2}$ transition of Er^{3+} in $(100-x)SiO_2$ - $xSnO_2$: $0.5Er^{3+}$ monoliths containing different SnO_2 contents ($x = 0, 5$ and 10 mol%) and $95SiO_2$ - $5SnO_2$: yEr^{3+} monoliths doped with different Er^{3+} concentrations ($y = 0.25, 0.50, 0.75$ and 1.00 mol%) in comparison with other host materials in the literature

Host matrix	Er^{3+} concentration ($\times 10^{19}$ ions/cm ³)	σ_a ($\times 10^{-21}$ cm ²)	σ_e ($\times 10^{-21}$ cm ²)	λ_{peak} ± 1 nm	$\Delta\lambda$ ± 2 (nm)	Ref
$95SiO_2$ - $5SnO_2$: $0.25Er^{3+}$	4.889	2.26	2.78	1533	34	this work
$95SiO_2$ - $5SnO_2$: $0.75Er^{3+}$	14.251	2.95	3.62	1533	46	this work
$95SiO_2$ - $5SnO_2$: $1.00Er^{3+}$	18.736	4.64	5.72	1533	51	this work
$95SiO_2$ - $5SnO_2$: $0.50Er^{3+}$	9.638	2.41	2.95	1533	47	this work
$100SiO_2$: $0.50Er^{3+}$	9.366	2.30	3.27	1541	64	this work
$90SiO_2$ - $10SnO_2$: $0.50Er^{3+}$	9.797	4.02	5.03	1533	42	this work
Silicate (Baccarat)	8.900	4.3	5.1	1537	18	[Benoit 2005]
Al-P-silica	-	6.6	5.7	1531	43	[Miniscalco 1991], summarized in [Righini 2005]
Fluorophosphate L14	-	5	5	1531	63	
Silicate L22	-	5.8	7.3	1536	20	
Al_2O_3 - SiO_2	7.000	5.1	4.4	1530	55	[Barnes 1991]
GeO_2 - Al_2O_3 - SiO_2	7.000	4.7	4.4	1530		
GeO_2 - SiO_2	1.000	7.9	6.7	1530	25	
Tellurite	44.260	7.9	9.2	1532	66	[Rolli 2003]

4.5.2.5 Internal gain coefficient

From the obtained absorption and emission cross sections, it was possible to estimate the internal gain coefficient using the equation [Righini 2005]:

$$g(\lambda) = 4.343 \times (\sigma_e(\lambda)N_2 - \sigma_a(\lambda)N_1) \quad (4.8)$$

where $g(\lambda)$ is the internal gain coefficient (dB/cm);

$\sigma_e(\lambda)$ and $\sigma_a(\lambda)$ are absorption and emission cross section at a certain wavelength λ ;

N_2 and N_1 are the density of Er^{3+} ions at the upper state, i.e. the metastable state $^4\text{I}_{13/2}$ and the ground state $^4\text{I}_{15/2}$ respectively. In fact, $N_2 + N_1 = N_0$ with N_0 is the total Er^{3+} concentration in each monolith.

Figure 4.32 shows the results of calculated internal gain coefficients of Er^{3+} at 1.5 μm emission as a function of the fractional upper-state population N_2/N_0 in all the obtained monoliths: in $(100-x)\text{SiO}_2-x\text{SnO}_2:0.5\text{Er}^{3+}$ monoliths containing different SnO_2 contents ($x = 0, 5$ and 10 mol%) and $95\text{SiO}_2-5\text{SnO}_2:y\text{Er}^{3+}$ monoliths doped with different Er^{3+} concentrations ($y = 0.25, 0.50, 0.75$ and 1.00 mol%). In all the monoliths, one can see that the internal gain in the full 1500 nm emission range of Er^{3+} (1440 to 1600 nm) strongly depends on the fractional upper-state population N_2/N_0 . At low population inversion, a small amplification can be achieved in a longer wavelength range while the short wavelength range is absorbed. In this case, the monoliths behave like absorbers of the light. At higher population, a higher amplification is obtained in a wider spectral range. Concerning the full population inversion ($N_2/N_0 = 1$), the higher SnO_2 content leads to higher internal gain among the monoliths with the same 0.5 mol% dopant concentration of Er^{3+} . In case of 5 mol% glass-ceramic doped with different Er^{3+} concentrations, the internal gain increases with increasing Er^{3+} concentrations. For a comparison, at the full population inversion, the 10 mol% SnO_2 monolith has an estimated internal gain coefficient of 2.1 ± 0.2 dB/cm at 1533 nm which is comparable to the value of 2.0 dB/cm obtained in case of Er^{3+} in Baccarat in the work [Benoit 2005]. The luminescence sensitization is beneficial for the achievement of the high population inversion since the higher Er^{3+} density at $^4\text{I}_{13/2}$ excited states is expected thanks to fast energy transfer in ns scale and high energy

transfer efficiency [Lin 2014], and high absorption cross section of SnO_2 .

Thi Ngoc Lam Tran – Tin dioxide - based photonic glass-ceramics

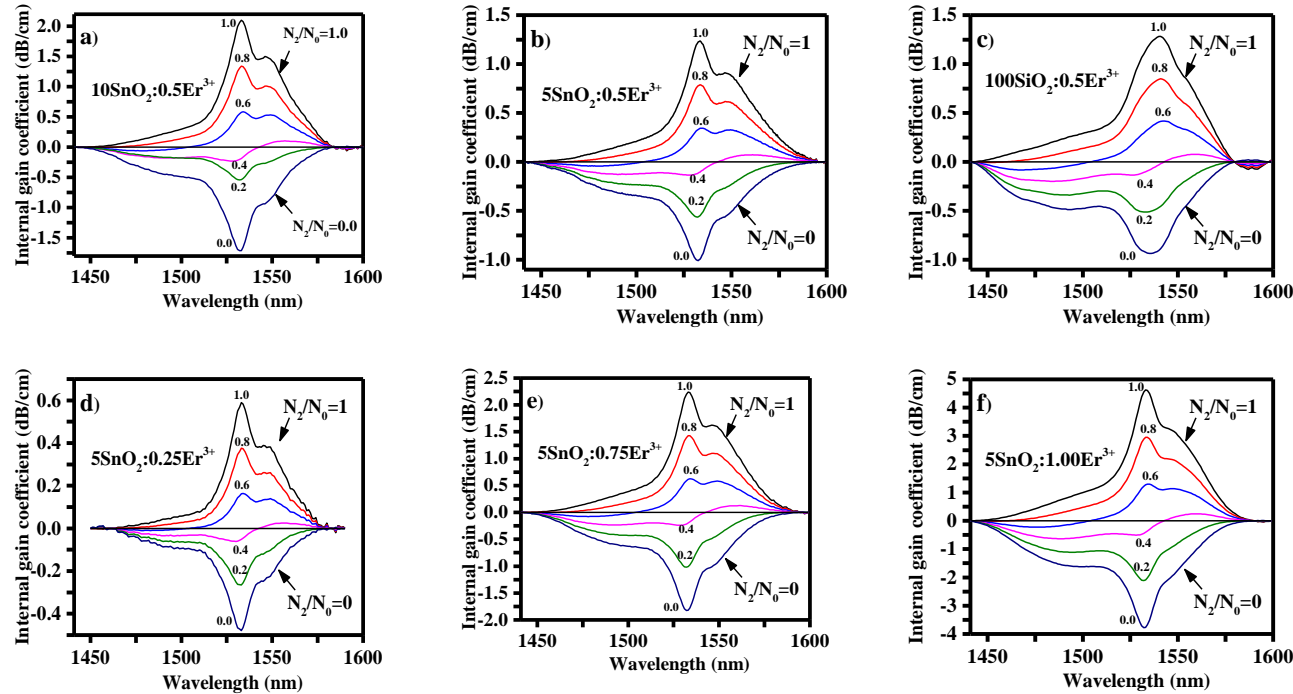


Figure 4.32 Calculated internal gain coefficient as a function of the fractional upper-state population N_2/N_0 of the a) 90SiO₂-10SnO₂:0.5Er³⁺, b) 95SiO₂-5SnO₂:0.5Er³⁺, c) 100SiO₂:0.5Er³⁺, d) 95SiO₂-5SnO₂:0.25Er³⁺, e) 95SiO₂-5SnO₂:0.75Er³⁺ and f) 95SiO₂-5SnO₂:1.00Er³⁺. $N_2/N_0=1$ is when the full population is achieved and $N_2/N_0=0$ when there is no population inversion

The results of calculated internal gain provide a very important parameter for the laser designs which will be discussed in Chapter 7 .

4.5.2.6 Judd-Ofelt analysis

To evaluate the quantum efficiency, it is required to know the radiative lifetime of Er^{3+} in the compositional monoliths. Therefore, the Judd-Ofelt theory was employed. The principles and practical examples of Judd-Ofelt theory applied for determining the radiative lifetime of rare-earth ions can be found in the literature in such works [Walsh 2006], [Ouannes 2014]. In this subsection, the interest is focused on applying the approximation of the Judd-Ofelt theoretical expression and calculated values of the oscillator strength of the electric and magnetic dipole transitions of Er^{3+} in the glass-ceramics. The Judd-Ofelt theoretical expression S_{cal} is:

$$S_{\text{cal}} = S_{\text{ed}} + S_{\text{md}} \quad (4.9)$$

$$S_{\text{ed}} = \sum_{k=2,4,6} \Omega_k |\langle \psi J \| U^k \| \psi' J' \rangle|^2 = \sum_{k=2,4,6} M_k \Omega_k \quad (4.10)$$

$$S_{\text{md}} = \frac{e^2 h^2}{16 \pi^2 m^2 c^2} |\langle \psi J \| L + 2S \| \psi' J' \rangle|^2 \quad (4.11)$$

where Ω_k ($k = 2, 4, 6$) are three Judd-Ofelt parameters;

$M_k = \langle \psi J \| U^k \| \psi' J' \rangle^2$ are the doubly reduced matrix elements in intermediate coupling approximation taken from in [H. Ebendorff-Heidepriem 2016], [Nielson 1963], [Walsh 2006] and shown in Table 4.7.

$|\langle \psi J \| L + 2S \| \psi' J' \rangle|^2$ are the matrices of LS couplings of 4f electrons of Er^{3+} which can be found in [Shortley 1940];

J and J' are the total angular momentum quantum numbers of the initial and final states, respectively;

e is the electron charge;

c is the light velocity in vacuum;

h is the Planck constant;

m is the electron mass.

On the other hand, the line strength can be obtained from the measured absorption spectra following the equation:

$$S_{\text{meas}} = \frac{3ch(2J+1)}{8\pi^3 e^2 \lambda N_o} n \left(\frac{3}{n^2 + 2} \right)^2 \int \alpha(\lambda) d\lambda \quad (4.12)$$

where $\bar{\lambda}$ is the mean wavelength of the absorption band of each transition;

N_0 is the concentration Er^{3+} ions per unit volume;

$\alpha(\lambda)$ is the measured absorption coefficient at a given wavelength λ ;

$\int \alpha(\lambda) d\lambda$ is the integral absorption coefficient of an absorption transition band of Er^{3+} calculated from the background-removed absorption spectra of the $(100-x)\text{SiO}_2-x\text{SnO}_2:y\text{Er}^{3+}$ ($x = 0, 5$ and 10 mol%, $y = 0.25, 0.50, 0.75$ and 1.00 mol% shown in Figure 4.27 and Figure 4.28. The results are tabulated in Table 4.7;

n is the refractive index of the $(100-x)\text{SiO}_2-x\text{SnO}_2:0.5\text{Er}^{3+}$ monoliths at the given wavelength λ , also tabulated in Table 4.7.

By using the standard least square fitting for the theoretical oscillator strength S_{cal} in equation (4.9) and S_{meas} in equation (4.12), the Judd-Ofelt parameters Ω_k can be derived. In addition, the root mean square (r.m.s) deviation of the oscillator strengths between the measured values (4.12) and calculated theoretical (4.9) ones were also derived using the equation:

$$\text{r.m.s} = \left[\frac{1}{N-3} \sum_{i=1}^N (S_{\text{meas}} - S_{\text{cal}})^2 \right]^{1/2} \quad (4.13)$$

As a result, the transition probability, radiative lifetimes and the branching ratios can be calculated using following equations (4.14)(4.15)(4.16).

- The transition probability is calculated by:

$$A(\psi'J', \psi J) = \frac{64\pi^4 \nu^3}{3h(2J+1)} [\chi_{\text{ed}} S_{\text{ed}} + \chi_{\text{md}} S_{\text{md}}] \quad (4.14)$$

where $A(\psi'J', \psi J)$ is the transition probability of the spontaneous emission corresponding to the transition $|\psi'J'\rangle \rightarrow |\psi J\rangle$;

χ_{ed} and χ_{md} : are the Lorent local field of electric dipole and magnetic dipole.

For absorption transition $\chi_{\text{ed}} = (n^2 + 2)^2 / 9n$; $\chi_{\text{md}} = n$ and for emission transition: $\chi_{\text{ed}} = n(n^2 + 2)^2 / 9$; $\chi_{\text{md}} = n^3$;

- Radiative lifetime of the rare earth ion at the excited state $|\psi'J'\rangle$ is calculated by:

$$\frac{1}{\tau(\psi'J')} = \sum_{\psi J} A(\psi'J', \psi J) = A_T(\psi'J') \quad (4.15)$$

where $\tau(\psi'J')$ is the radiative lifetime of the excited state $|\psi'J'\rangle$;

$A(\psi J) = \sum_j A(\psi'J', \psi J)$ is the total transition probability of the possible

transition from the excited state $|\psi'J'\rangle$ to other lower-energy states $|\psi J\rangle$

Branching ratio of a transition $|\psi'J'\rangle \rightarrow |\psi J\rangle$ is calculated using the equation:

$$\beta_R(\psi'J', \psi J) = \frac{A(\psi'J', \psi J)}{A_T(\psi'J')} \quad (4.16)$$

The chart illustrating the calculation of Judd-Ofelt parameters, transition probability, radiative lifetime and branching ratios is shown in Figure 4.33.

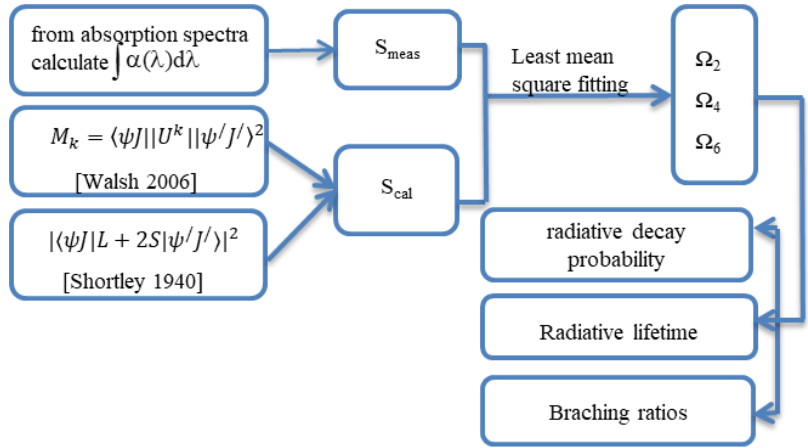


Figure 4.33 Chart illustrating the calculation of Judd-Ofelt parameters, transition probability, radiative lifetime and branching ratios

The used parameters for the calculation are tabulated in Table 4.7. The results of the measured and the theoretical oscillator strengths of Er^{3+} transitions from the ground state $^4I_{15/2}$ to an excited state in the compositional $(100-x)\text{SiO}_2-x\text{SnO}_2:y\text{Er}^{3+}$ monoliths ($x = 0, 5$ and 10 mol% and $y = 0.25, 0.50, 0.75$ and 1.00 mol%) and the corresponding r.m.s of the calculations are listed in Table 4.8. On the other hand, Table

4.9 tabulates the calculated Judd-Ofelt parameters (Ω_2 , Ω_4 , Ω_6) and transition probability from $^4I_{13/2}$ to $^4I_{15/2}$ and lifetime of the metastable state $^4I_{13/2}$, which corresponds to the 1500 nm emission of Er^{3+} .

Table 4.7 The parameters used to calculate the oscillator strengths in equations (4.12) and (4.10)

the doubly reduced matrix elements	Transition from ground state $^4I_{15/2}$ to excited state							N_0 (10^{19} ions/ cm^3)	Transition from ground state $^4I_{15/2}$ to excited state						
	$^4G_{11/2}$	$^4F_{5/2}$	$^4F_{7/2}$	$^2H_{11/2}$	$^4S_{3/2}$	$^4F_{9/2}$	$^4I_{13/2}$		$^4G_{11/2}$	$^4F_{5/2}$	$^4F_{7/2}$	$^2H_{11/2}$	$^4S_{3/2}$	$^4F_{9/2}$	$^4I_{13/2}$
	$\bar{\lambda}$ (nm)						Estimated refractive index n (based on the results in Figure 4.52)								
	$\bar{\lambda}$ (nm)						$\bar{\lambda}$ (nm)								
	378	451	488	521	542	652	1533		378	451	488	521	542	652	1533
$\langle \parallel U_2 \parallel \rangle^2$	0.9181	0	0	0.7125	0	0	0.0195								
$\langle \parallel U_4 \parallel \rangle^2$	0.5261	0	0.1468	0.4123	0	0.5354	0.1173								
$\langle \parallel U_6 \parallel \rangle^2$	0.1171	0.2233	0.6266	0.0925	0.2211	0.4619	1.4316								
	$\int_{\text{band}} \alpha(\lambda) d\lambda$ (cm^{-1}) of the transition from $^4I_{15/2}$														
(100-x)SiO ₂ -xSnO ₂ :0.5Er ³⁺ monoliths (x = 0, 5 and 10 mol%)															
x = 10	9.424	0.285	1.977	13.329	0.434	5.054	16.573	9.797	1.549	1.531	1.525	1.521	1.518	1.510	1.496
x = 5	8.508	0.197	1.335	11.631	0.345	3.152	10.899	9.638	1.509	1.494	1.489	1.486	1.484	1.477	1.465
x = 0	15.526	0.399	2.774	14.818	0.603	5.248	13.688	9.366	1.482	1.469	1.465	1.462	1.461	1.455	1.441
95SiO ₂ -5SnO ₂ :yEr ³⁺ monoliths (y = 0, 0.25, 0.50 and 1.00 mol%)															
y = 0.25	4.273	0.099	0.728	6.686	0.210	1.685	3.764	4.889	1.509	1.494	1.489	1.486	1.484	1.477	1.465
y = 0.50	8.508	0.197	1.335	11.631	0.345	3.152	10.899	9.638							
y = 0.75	18.699	0.444	3.102	22.663	0.633	6.411	19.346	14.251							
y = 1.00	33.126	0.893	6.300	38.148	1.392	13.735	44.468	18.736							

Table 4.8 Results of the oscillator strengths of Er ³⁺ transitions from the ground state ⁴ I _{15/2} to an excited state in the compositional (100-x)SiO ₂ -xSnO ₂ :yEr ³⁺ monoliths (x = 0, 5 and 10 mol% and y = 0.25, 0.50, 0.75 and 1.00 mol%). Notes: GC means glass-ceramics (x = 5 and 10 mol%) and G means glass (x = 0).													
		x = 10 & y = 0.5		x = 5 & y = 0.5		x = 0 & y = 0.5		x = 5 & y = 0.25		x = 5 & y = 0.75		x = 5 & y = 1.00	
λ(nm)	Transition	S _{meas}	S _{cal}	S _{meas}	S _{cal}	S _{meas}	S _{cal}	S _{meas}	S _{cal}	S _{meas}	S _{cal}	S _{meas}	S _{cal}
		×10 ⁻²⁰ cm ²											
378	⁴ I _{15/2} - ⁴ G _{11/2}	3.05	3.45	2.89	3.21	5.53	5.33	2.86	3.38	4.29	4.53	5.78	5.99
451	⁴ I _{15/2} - ⁴ F _{5/2}	0.08	0.17	0.06	0.12	0.12	0.16	0.06	0.07	0.09	0.14	0.13	0.25
488	⁴ I _{15/2} - ⁴ F _{7/2}	0.51	0.65	0.36	0.43	0.77	0.66	0.38	0.35	0.56	0.56	0.86	0.95
521	⁴ I _{15/2} - ² H _{11/2}	3.20	2.69	2.91	2.50	3.89	4.14	3.30	2.63	3.84	3.52	4.92	4.65
542	⁴ I _{15/2} - ⁴ S _{3/2}	0.10	0.17	0.08	0.12	0.15	0.15	0.10	0.07	0.10	0.14	0.17	0.25
652	⁴ I _{15/2} - ⁴ F _{9/2}	0.98	0.96	0.63	0.63	1.11	1.13	0.67	0.68	0.87	0.88	1.42	1.41
1532(GC) / 1537(G)	⁴ I _{15/2} - ⁴ I _{13/2}	1.38	1.30	0.94	0.90	1.24	1.27	0.64	0.65	1.13	1.12	1.98	1.91
r.m.s		0.683×10 ⁻²⁰		0.541×10 ⁻²⁰		0.352×10 ⁻²⁰		0.854×10 ⁻²⁰		0.404×10 ⁻²⁰		0.377×10 ⁻²⁰	

Table 4.9 The calculated Judd-Ofelt parameters (Ω_2 , Ω_4 , Ω_6) and transition probability from $^4I_{13/2}$ to $^4I_{15/2}$ and lifetime of the metastable state $^4I_{13/2}$					
	Ω_2 ($\times 10^{-20}$)	Ω_4 ($\times 10^{-20}$)	Ω_6 ($\times 10^{-20}$)	A (s^{-1})	$\tau(^4I_{13/2})$ ms
(100-x)SiO ₂ -xSnO ₂ :0.5Er ³⁺ monoliths (x = 0, 5 and 10 mol%)					
x = 10	3.019	1.124	0.772	277	3.6
x = 5	3.021	0.714	0.526	246	4.0
x = 0	4.855	1.504	0.699	249	4.0
95SiO ₂ -5SnO ₂ :yEr ³⁺ monoliths (y = 0, 0.25, 0.50 and 1.00 mol%)					
y = 0.25	3.076	0.983	0.333	237	4.2
y = 0.50	3.021	0.714	0.526	246	4.0
y = 0.75	4.230	1.097	0.632	255	3.9
y = 1.00	5.418	1.671	1.125	287	3.5

Generally, from Table 4.9, all the listed values of Ω_2 , Ω_4 and Ω_6 of SiO₂-SnO₂:Er³⁺ glass-ceramics and pure SiO₂:Er³⁺ glass are in range of the one obtained in host materials summarized in the work [Rolli 2003]. According to [Tanabe 1992], the Judd-Ofelt parameters can be correlated to local environment of the RE ions: the Ω_2 parameter relates to the lowering from inversion symmetry. In fact, all glass-ceramics monoliths with low dopant concentration of Er³⁺ (0.25, 0.50 and 0.75 mol%) have a lower value of Ω_2 in comparison with the pure SiO₂. In other words, this indicates that in the glass ceramic monoliths, Er³⁺ ions locate in a local electric field with higher symmetry than pure SiO₂. A similar effect was already observed in the ZnO-PbO tellurite glasses [Ramamoorthy 2014]. In the case of 95SiO₂-5SnO₂ monolith with highly doped Er³⁺ (1 mol%), the high value of Ω_2 can be attributed to the decrease of the local symmetry due to Er³⁺-Er³⁺ local field interaction. Concerning Ω_4 and Ω_6 which relate to the local basicity of rare earth sites, unclear trend of these two parameters can be due to the presence of broad distribution of Er³⁺ sites and the complexity in the glass-ceramics which will be discussed in 4.5.5. Moreover, another benefit of Judd-Ofelt analyses is that it allows to derive the values of transition probability, branching ratios and radiative lifetimes of several Er³⁺ transitions. The radiative lifetimes of the metastable state $^4I_{13/2}$ in the compositional monoliths were listed in Table 4.9. The results show that increasing SnO₂ leads to a decrease of radiative lifetime due to the effect of increasing refractive index of the local environment of Er³⁺ which will be discussed with details in section 4.5.5.1. The Judd-Ofelt

calculation also reveals the reduction radiative lifetime when Er^{3+} concentration increases. These values are important for the study of spectroscopic properties and calculating the quantum yield of Er^{3+} transitions in the glass-ceramics. Table 4.10 lists the obtained values for the transitions of Er^{3+} with 15 energy levels in the $90\text{SiO}_2\text{-}10\text{SnO}_2\text{:}0.5\text{Er}^{3+}$ glass-ceramics. Besides the information of the relevant Er^{3+} transitions corresponding to the Vis-NIR emissions, for understanding the energy transfer from SnO_2 to Er^{3+} , it is necessary to pay attention to the transitions of Er^{3+} referring to the UV emission range. The transition probabilities and the corresponding radiative lifetimes were analyzed without taking into account the thermalization effect. However, due to the small energy gap between the excited states $^4\text{G}_{9/2}$, $^2\text{K}_{15/2}$ and $^2\text{G}_{7/2}$, it is necessary to take into account the thermalization phenomenon at room temperature [Righini 2005], [Rolli 2003]. Therefore, due to the rapid thermalization, all the Er^{3+} ions at higher energy states $^2\text{K}_{15/2}$ and $^2\text{G}_{7/2}$ decay to the $^4\text{G}_{9/2}$. As a result, the absorption spectra reveal the dominant transition of only $^4\text{G}_{9/2}$ with an estimated radiative lifetime in range of few tens of microsecond. Moreover, from this $^4\text{G}_{9/2}$ excited state, the transition to the metastable state $^4\text{I}_{13/2}$ has the dominate transition probability with branching ratio of 71 %. In addition, the rapid thermalization also occurs between the two pairs of small energy gap levels: $^2\text{H}_{11/2}$ and $^4\text{S}_{3/2}$, and $^4\text{F}_{5/2}$ and $^4\text{F}_{3/2}$: all Er^{3+} ions at the higher energy states $^4\text{S}_{3/2}$ and $^4\text{F}_{3/2}$ relax to the lower energy states $^2\text{H}_{11/2}$ and $^4\text{F}_{5/2}$ respectively.

Chapter 4 Experimental assessments

Table 4.10 Values of transition probability, branching ratios and radiative lifetimes of Er^{3+} transitions in $90\text{SiO}_2\text{-}10\text{SnO}_2\text{:}0.5\text{Er}^{3+}$ glass ceramics obtained using Judd-Ofelt methods.

Transition	Wavelength (nm)	$\langle U_2 \rangle^2$	$\langle U_4 \rangle^2$	$\langle U_6 \rangle^2$	Transition probability A (s^{-1})	Branching ratio (%)	Radiative lifetime (ms)
$^4\text{I}_{13/2} - ^4\text{I}_{15/2}$	1538	0.0195	0.1173	1.4316	276.62	100.00	3.615
$^4\text{I}_{11/2} - ^4\text{I}_{13/2}$	2770	0.0331	0.1708	1.0864	55.63	43.23	7.770
$^4\text{I}_{11/2} - ^4\text{I}_{15/2}$	990	0.0282	0.0003	0.3953	73.06	56.77	
$^4\text{I}_{9/2} - ^4\text{I}_{11/2}$	4627	0.0030	0.0674	0.1271	11.75	10.02	8.528
$^4\text{I}_{9/2} - ^4\text{I}_{13/2}$	1733	0.0004	0.0106	0.7162	23.45	20.00	
$^4\text{I}_{9/2} - ^4\text{I}_{15/2}$	815	0.0000	0.1732	0.0099	82.06	69.99	
$^4\text{F}_{9/2} - ^4\text{I}_{9/2}$	3491	0.1279	0.0059	0.0281	2.09	0.26	1.235
$^4\text{F}_{9/2} - ^4\text{I}_{11/2}$	1990	0.0704	0.0112	1.2839	33.23	4.10	
$^4\text{F}_{9/2} - ^4\text{I}_{13/2}$	1158	0.0101	0.1533	0.0714	36.03	4.45	

Thi Ngoc Lam Tran – Tin dioxide - based photonic glass-ceramics

$^4F_{9/2} - ^4I_{15/2}$	661	0.0000	0.5354	0.4619	738.44	91.19	1.119
$^4S_{3/2} - ^4F_{9/2}$	3109	0.0000	0.0001	0.0228	0.32	0.04	
$^4S_{3/2} - ^4I_{9/2}$	1644	0.0000	0.0788	0.2542	34.53	3.86	
$^4S_{3/2} - ^4I_{11/2}$	1213	0.0000	0.0042	0.0739	18.73	2.10	
$^4S_{3/2} - ^4I_{13/2}$	844	0.0000	0.0000	0.3462	243.71	27.28	
$^4S_{3/2} - ^4I_{15/2}$	545	0.0000	0.0000	0.2211	596.23	66.73	0.267
$^2H_{11/2} - ^4S_{3/2}$	12557	0.0000	0.2002	0.0097	0.02	0.00	
$^2H_{11/2} - ^4F_{9/2}$	2500	0.3629	0.0224	0.0022	12.87	0.34	
$^2H_{11/2} - ^4I_{9/2}$	1449	0.2077	0.0662	0.2858	54.53	1.46	
$^2H_{11/2} - ^4I_{11/2}$	1105	0.0357	0.1382	0.0371	39.14	1.05	
$^2H_{11/2} - ^4I_{13/2}$	791	0.0230	0.0611	0.0527	66.29	1.77	
$^2H_{11/2} - ^4I_{15/2}$	522	0.7125	0.4123	0.0925	3571.48	95.38	0.474
$^4F_{7/2} - ^2H_{11/2}$	8593	0.1258	0.0164	0.3984	0.30	0.01	
$^4F_{7/2} - ^4S_{3/2}$	5102	0.0000	0.0055	0.0000	0.01	0.00	

Chapter 4 Experimental assessments

${}^4F_{7/2} - {}^4F_{9/2}$	1942	0.0121	0.0342	0.0115	89.34	4.24	
${}^4F_{7/2} - {}^4I_{9/2}$	1242	0.0163	0.0954	0.4277	68.72	3.26	
${}^4F_{7/2} - {}^4I_{11/2}$	980	0.0035	0.2648	0.1515	122.88	5.83	
${}^4F_{7/2} - {}^4I_{13/2}$	725	0.0000	0.3371	0.0001	274.95	13.04	
${}^4F_{7/2} - {}^4I_{15/2}$	493	0.0000	0.1468	0.6266	1552.95	73.63	
${}^4F_{5/2} - {}^4F_{7/2}$	6051	0.0765	0.0498	0.0998	4.16	0.27	0.648
${}^4F_{5/2} - {}^2H_{11/2}$	3551	0.0000	0.0581	0.1847	1.66	0.11	
${}^4F_{5/2} - {}^4S_{3/2}$	2768	0.0077	0.0036	0.0000	0.46	0.03	
${}^4F_{5/2} - {}^4F_{9/2}$	1464	0.0005	0.2345	0.3491	61.29	3.97	
${}^4F_{5/2} - {}^4I_{9/2}$	1032	0.0101	0.0629	0.1129	62.21	4.03	
${}^4F_{5/2} - {}^4I_{11/2}$	844	0.0000	0.0984	0.0028	68.61	4.45	
${}^4F_{5/2} - {}^4I_{13/2}$	647	0.0000	0.1794	0.3419	638.68	41.41	
${}^4F_{5/2} - {}^4I_{15/2}$	455	0	0	0.2233	705.32	45.73	
${}^4F_{3/2} - {}^4F_{5/2}$	28794	0.0605	0.0351	0.0000	0.05	0.00	0.747

Thi Ngoc Lam Tran – Tin dioxide - based photonic glass-ceramics

$^4F_{3/2} - ^4F_{7/2}$	5001	0.0027	0.0577	0.0000	0.31	0.02	
$^4F_{3/2} - ^2H_{11/2}$	3161	0.0000	0.0004	0.0025	0.04	0.00	
$^4F_{3/2} - ^4S_{3/2}$	2525	0.0266	0.0000	0.0000	2.68	0.20	
$^4F_{3/2} - ^4F_{9/2}$	1393	0.0000	0.0022	0.0616	9.99	0.75	
$^4F_{3/2} - ^4I_{9/2}$	996	0.0000	0.2338	0.0545	168.04	12.55	
$^4F_{3/2} - ^4I_{11/2}$	820	0.0000	0.0913	0.4831	473.83	35.39	
$^4F_{3/2} - ^4I_{13/2}$	632	0.0000	0.0000	0.0347	59.01	4.41	
$^4F_{3/2} - ^4I_{15/2}$	448	0.0000	0.0000	0.1255	624.89	46.67	0.613
$^2G_{9/2} - ^4F_{3/2}$	4791	0.0000	0.0188	0.0057	0.05	0.00	
$^2G_{9/2} - ^4F_{5/2}$	4107	0.0092	0.0219	0.0056	0.18	0.01	
$^2G_{9/2} - ^4F_{7/2}$	2447	0.0894	0.0483	0.0273	5.07	0.31	
$^2G_{9/2} - ^2H_{11/2}$	1904	0.0285	0.1635	0.0610	9.88	0.61	
$^2G_{9/2} - ^4S_{3/2}$	1654	0.0000	0.0036	0.0014	0.24	0.01	
$^2G_{9/2} - ^4F_{9/2}$	1079	0.0075	0.0261	0.0469	15.23	0.93	

Chapter 4 Experimental assessments

$^2G_{9/2} - ^4I_{9/2}$	825	0.0138	0.0066	0.0032	20.17	1.24	0.069
$^2G_{9/2} - ^4I_{11/2}$	700	0.0381	0.0753	0.1047	181.11	11.10	
$^2G_{9/2} - ^4I_{13/2}$	559	0.0590	0.1059	0.3531	736.59	45.16	
$^2G_{9/2} - ^4I_{15/2}$	410	0.0000	0.0243	0.2147	662.44	40.62	
$^4G_{11/2} - ^2G_{9/2}$	5022	0.2951	0.1068	0.1414	1.58	0.01	
$^4G_{11/2} - ^4F_{3/2}$	2452	0.0000	0.0232	0.0907	1.17	0.01	
$^4G_{11/2} - ^4F_{5/2}$	2260	0.0000	0.0373	0.0806	1.62	0.01	
$^4G_{11/2} - ^4F_{7/2}$	1645	0.0867	0.1264	0.0168	16.82	0.12	
$^4G_{11/2} - ^2H_{11/2}$	1381	0.0004	0.0151	0.0498	3.87	0.03	
$^4G_{11/2} - ^4S_{3/2}$	1244	0.0000	0.1282	0.0040	13.80	0.10	
$^4G_{11/2} - ^4F_{9/2}$	889	0.4283	0.0372	0.0112	349.02	2.41	
$^4G_{11/2} - ^4I_{9/2}$	708	0.0631	0.0122	0.0228	115.07	0.80	
$^4G_{11/2} - ^4I_{11/2}$	614	0.0002	0.0486	0.0133	52.63	0.36	
$^4G_{11/2} - ^4I_{13/2}$	503	0.1005	0.2648	0.2570	1197.01	8.28	

Thi Ngoc Lam Tran – Tin dioxide - based photonic glass-ceramics

$^4G_{11/2} - ^4I_{15/2}$	379	0.9156	0.5263	0.1167	12708.01	87.88	0.090
$^4G_{9/2} - ^4G_{11/2}$	10221	0.0000	0.2117	0.1516	0.75	0.01	
$^4G_{9/2} - ^2G_{9/2}$	3368	0.0251	0.0004	0.0328	0.57	0.01	
$^4G_{9/2} - ^4F_{3/2}$	1978	0.0000	0.1711	0.1124	7.77	0.07	
$^4G_{9/2} - ^4F_{5/2}$	1850	0.1650	0.0846	0.0024	20.23	0.18	
$^4G_{9/2} - ^4F_{7/2}$	1417	0.6234	0.0067	0.1194	150.50	1.36	
$^4G_{9/2} - ^2H_{11/2}$	1216	0.0237	0.3463	0.157	70.05	0.63	
$^4G_{9/2} - ^4S_{3/2}$	1109	0.0000	0.1659	0.0103	30.95	0.28	
$^4G_{9/2} - ^4F_{9/2}$	817	0.217	0.3167	0.365	519.39	4.69	
$^4G_{9/2} - ^4I_{9/2}$	662	0.0041	0.0060	0.0049	17.51	0.16	
$^4G_{9/2} - ^4I_{11/2}$	579	0.0937	0.1601	0.0168	549.56	4.97	
$^4G_{9/2} - ^4I_{13/2}$	479	1.1078	0.3672	0.0106	7865.57	71.07	
$^4G_{9/2} - ^4I_{15/2}$	365	0.0000	0.2337	0.1368	1834.89	16.58	0.914
$^2K_{15/2} - ^4G_{9/2}$	31066	0.0000	0.0056	0.0558	0.00	0.00	

Chapter 4 Experimental assessments

$^2K_{15/2} - ^4G_{11/2}$	7691	0.0998	0.0579	0.6787	0.26	0.02	
$^2K_{15/2} - ^2G_{9/2}$	3038	0.0000	0.7139	0.0822	4.15	0.38	
$^2K_{15/2} - ^4F_{3/2}$	1859	0.0000	0.1711	0.1124	5.85	0.53	
$^2K_{15/2} - ^4F_{5/2}$	1746	0.0000	0.0000	0.0472	0.92	0.08	
$^2K_{15/2} - ^4F_{7/2}$	1355	0.6234	0.0067	0.1194	107.60	9.83	
$^2K_{15/2} - ^2H_{11/2}$	1171	0.1010	0.0000	1.1445	100.40	9.17	
$^2K_{15/2} - ^4S_{3/2}$	1071	0.0000	0.0000	0.0035	0.30	0.03	
$^2K_{15/2} - ^4F_{9/2}$	796	0.0000	0.0867	0.0142	29.46	2.69	
$^2K_{15/2} - ^4I_{9/2}$	649	0.0000	0.2101	0.0969	158.54	14.48	
$^2K_{15/2} - ^4I_{11/2}$	569	0.0463	0.0017	0.2426	251.42	22.97	
$^2K_{15/2} - ^4I_{13/2}$	472	0.0001	0.0015	0.0257	29.90	2.73	
$^2K_{15/2} - ^4I_{15/2}$	361	0.0213	0.0039	0.0735	405.77	37.07	
$^2G_{7/2} - ^2K_{15/2}$	55371	0.0000	0.1203	0.0048	0.00	0.00	0.173
$^2G_{7/2} - ^4G_{9/2}$	19900	0.0034	0.1887	0.1494	0.01	0.00	

Thi Ngoc Lam Tran – Tin dioxide - based photonic glass-ceramics

$^2G_{7/2} - ^4G_{11/2}$	6753	0.0140	0.0544	0.0177	0.10	0.00	
$^2G_{7/2} - ^2G_{9/2}$	2880	0.0152	0.0052	0.0244	15.42	0.27	
$^2G_{7/2} - ^4F_{3/2}$	1799	0.0961	0.0342	0.0000	15.21	0.26	
$^2G_{7/2} - ^4F_{5/2}$	1693	0.3831	0.0017	0.0380	65.98	1.14	
$^2G_{7/2} - ^4F_{7/2}$	1323	0.1221	0.0409	0.0070	49.06	0.85	
$^2G_{7/2} - ^2H_{11/2}$	1146	0.0006	0.0393	0.271	45.93	0.79	
$^2G_{7/2} - ^4S_{3/2}$	1050	0.0475	0.1631	0.0000	76.61	1.32	
$^2G_{7/2} - ^4F_{9/2}$	785	0.0000	0.1230	0.1630	149.92	2.59	
$^2G_{7/2} - ^4I_{9/2}$	641	0.1649	0.3703	0.2168	1142.91	19.72	
$^2G_{7/2} - ^4I_{11/2}$	563	0.5073	0.2776	0.1616	3105.90	53.59	
$^2G_{7/2} - ^4I_{13/2}$	468	0.0000	0.0997	0.0310	382.70	6.60	
$^2G_{7/2} - ^4I_{15/2}$	359	0.0000	0.0200	0.1171	745.87	12.87	

4.5.3 Emission

4.5.3.1 The planar waveguides

Concerning the emission features of $\text{SiO}_2\text{-SnO}_2\text{:Er}^{3+}$ glass-ceramics, there are three main points which need to be discussed: (i) the general difference of the emission characteristics between the two excitation schemes of all the compositional planar waveguides; (ii) the difference of the emission characteristics between the compositional planar waveguides with different SnO_2 content for each excitation scheme; and (iii) the observed site-selective behavior.

(i) The general difference of the emission characteristics between the two excitation schemes:

Figure 4.34 shows the emission spectra of Er^{3+} under indirect and direct excitation of the $(100-x)\text{SiO}_2\text{-}x\text{SnO}_2\text{:}0.5\text{Er}^{3+}$ planar waveguides ($x = 5, 10, 15, 20, 25$ and 30). The emission spectra excited at $\lambda_{\text{ex}} = 330$ nm, corresponding to the absorption band edge of SnO_2 , were acquired in the reflection configuration shown in Figure 4.24 using the Xenon lamp as the excitation source. On the other hand, the emission spectra excited at 514.5 nm is the direct excitation of Er^{3+} to the $^2\text{H}_{11/2}$ excited state acquired in the waveguiding configuration shown in Figure 4.23 using the Ar^+ laser as the excitation source.

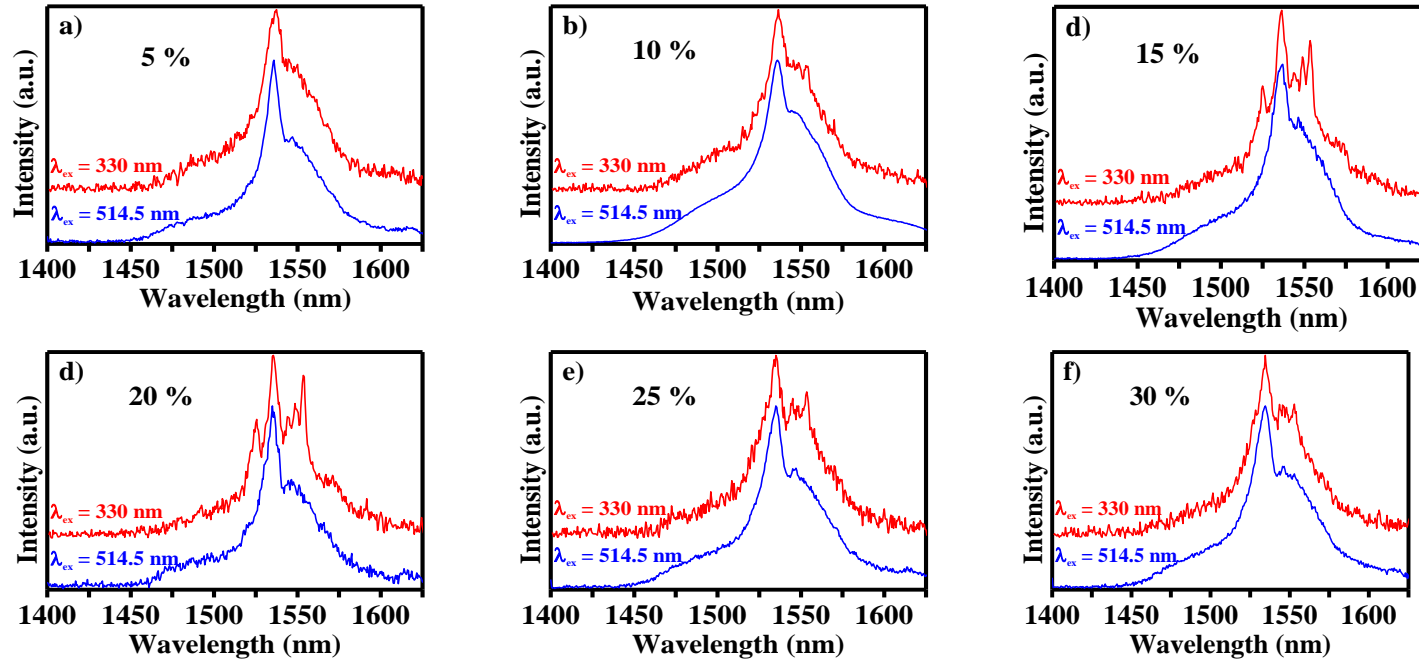


Figure 4.34 Emission spectra of the $(100-x)\text{SiO}_2-x\text{SnO}_2:0.5\text{Er}^{3+}$ planar waveguides ($x = 5, 10, 15, 20, 25$ and 30) under indirect excitation $\lambda_{\text{ex}} = 330$ nm (using Xenon Lamp source and in reflection configuration) and direct excitation $\lambda_{\text{ex}} = 514.5$ nm (using Ar^+ laser source and in waveguiding configuration)

Under the indirect excitation ($\lambda_{\text{ex}} = 330 \text{ nm}$) associated to the SnO_2 band-gap, the $^4\text{I}_{13/2} \rightarrow ^4\text{I}_{15/2}$ emission spectra exhibit Stark splitting and narrow peaks (see Figure 4.34) in the compositional planar waveguides, excepting the 5 mol% SnO_2 planar waveguides. Therefore, the shown 1500 nm emission spectra of the glass ceramic planar waveguides under the indirect excitation scheme confirm: i) the energy transfer from SnO_2 nanocrystals into Er^{3+} and ii) the evidence of Er^{3+} ions locating in crystalline environment, i.e. SnO_2 nanocrystals [Tran 2018b], [Van 2014]; [Van 2015]; [Van Tran 2012]. However, these emission features vary upon SnO_2 content which will be discussed with details in the next concept.

On the contrary, for all the compositional planar waveguides, the $^4\text{I}_{13/2} \rightarrow ^4\text{I}_{15/2}$ photoluminescence spectra obtained by directly exciting the $^2\text{H}_{11/2}$ level of the Er^{3+} ions exhibit a broad band typical of the Er^{3+} ions embedded in a disordered environment, i.e. glasses [Duverger 2001], [Righini 2005].

All the emission spectra shown in Figure 4.34 have the relatively large effective bandwidth from 42 nm to 52 nm which is comparable to other glasses [Berneschi 2006] and glass-ceramics such as $\text{SiO}_2\text{-ZrO}_2$ and $\text{SiO}_2\text{-HfO}_2$ [Zur 2017a] suitable for integrated optical amplifiers for WDM systems.

(ii) The difference of the emission characteristics between the compositional $(100-x)\text{SiO}_2\text{-}x\text{SnO}_2\text{:}0.5\text{Er}^{3+}$ glass-ceramics:

From Figure 4.34, under the direct excitation ($\lambda_{\text{ex}} = 514.5 \text{ nm}$), all the compositional planar waveguides show a similar emission features of Er^{3+} in an amorphous environment [Duverger 2001], [Righini 2005]. Under the indirect excitation ($\lambda_{\text{ex}} = 330 \text{ nm}$), the sharp and resolved feature of the emission spectra varies upon SnO_2 content. However, due to the broad excitation bandwidth (10 nm) of the Xenon lamp, the photoluminescence may include the emission features of Er^{3+} ions locating at different crystalline fields of SnO_2 nanocrystals. Therefore, the emission characteristics of the Er^{3+} ions may correlate to the structure of SnO_2 nanocrystals such as size, order level of the local field and size-distribution in the planar waveguides. In fact, there is a correlation supporting this explanation. In the 15 and 20 mol% planar waveguides with clearer SnO_2 -rutile XRD patterns, i.e. a higher

contribution of a larger sizes of SnO₂ nanocrystals, the emission spectra exhibit sharp and well-resolved peaks with the most intense peak at 1553.5 nm. This is the characteristic $^4I_{13/2} - ^4I_{15/2}$ emission of Er³⁺ ions that locate in the lattice of the crystalline environment of SnO₂ as already observed in [Tran 2018a], [Zur 2017b], [Fernández 2018]. On contrary, in the 5 mol% SnO₂ planar waveguides where there is no observable XRD pattern of SnO₂ nanocrystals, a broad emission band, which is typical from Er³⁺ ions in an amorphous environment [Righini 2005], [Duverger 2001] is observed. This suggests that the energy transfer still occurs even when Er³⁺ ions are embedded in a glass-like disordered SnO₂ environment. Furthermore, from the other smaller SnO₂ nanocrystal-containing planar waveguides, i.e 10, 25 and 30 mol% SnO₂ ones, the emission spectra show broad band together with less-pronounced Stark splitting peaks which indicates the location of Er³⁺ in the glass-like crystal field sites such as on the surface or order-broken crystalline interfaces of SnO₂ nanoparticles. This aspect can be explained due to the lattice distortions induced by the high surface to volume ratio of small nanosizes of SnO₂ in these planar waveguides [Cascales 2018].

In Figure 4.35, a similar spectral shape of 1500 nm emission of Er³⁺ is also observed in the other 30 mol% SnO₂ planar waveguides doped with different y concentrations of the rare earth (y = 0.5, 1 and 1.5 mol% Er³⁺).

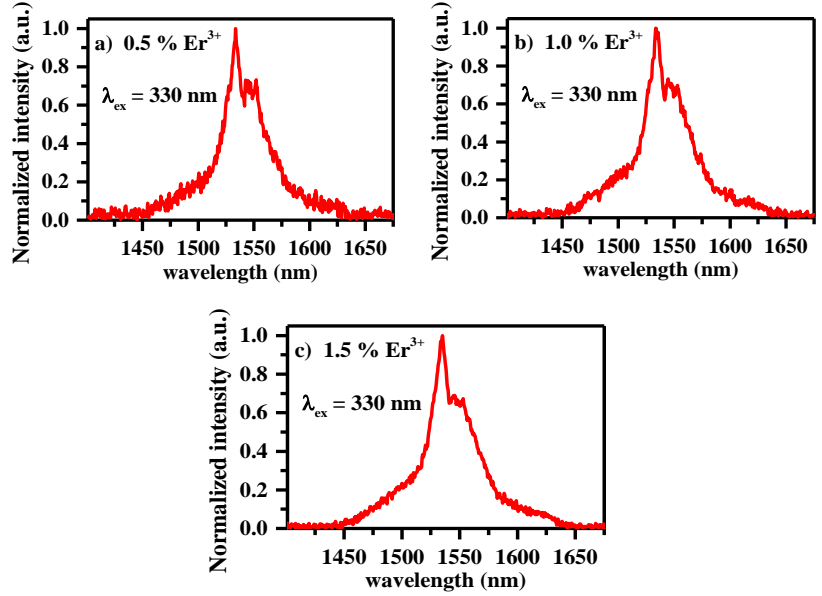


Figure 4.35 Emission spectra acquired by indirect excitation $\lambda_{\text{ex}} = 330$ nm, using Xenon Lamp in reflection configuration of the $70\text{SiO}_2\text{-}30\text{SnO}_2\text{:yEr}^{3+}$ planar waveguides doped with different y concentration of Er^{3+} ($y = 0.5, 1$ and 1.5 mol%)

(iii) *The observed site-selective behavior:*

The UV diode laser ($\lambda_{\text{ex}} = 340$ nm) was also employed to excite the planar waveguides at SnO_2 band-gap and acquire the 1500 nm Er^{3+} emission spectra. The emission spectra of three representative 10, 20 and 30 mol% SnO_2 planar waveguides upon the diode laser in comparison with the Xenon lamp are shown in Figure 4.36. The emission features of the planar waveguide containing 20 mol% SnO_2 noticeably changes under indirect excitation of the two UV sources. This is likely due to site-selective characteristic of Er^{3+} under narrow diode laser beam. As already discussed, since SnO_2 nanocrystals in the 20 mol% SnO_2 planar waveguides have higher distribution of larger nanosized SnO_2 , they provide a wider diversity of local SnO_2 sites for Er^{3+} ions: bulk-like electrical field and the distorted surface electrical fields. Therefore, under the narrow beam of the UV diode laser excitation, only one certain site of Er^{3+} in the nanocrystal is selectively excited which is confirmed by the single exponential decay curves discussed in 4.5.5. The broad and less resolved emission spectrum

reveals that the involved Er^{3+} ions locate in glass-like SnO_2 environment. On the other hand, the broad band Xenon lamp excitation involves a larger diversity of Er^{3+} sites in SnO_2 which includes the ones locating at centrosymmetric D_{2h} lattice site of Sn^{4+} as observed in [Fernández 2018]. In addition, one can see that the emission spectrum under Xenon lamp excitation is predominated by the sharp and pronounced peaks of the Er^{3+} ions locating at the D_{2h} sites. Referring to the 10 and 30 mol% planar waveguides, there is no significant change observed in the emission spectra which may be due to higher distribution of the small nanosized SnO_2 , leading to higher contribution of the emission feature of similar distorted sites of Er^{3+} in the nanocrystals.

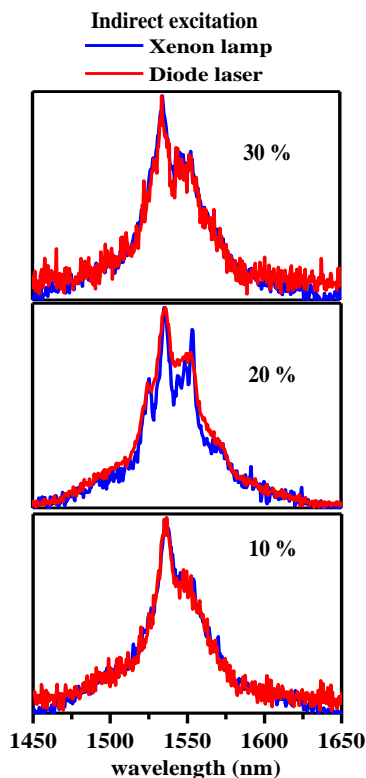


Figure 4.36 Emission spectra acquired by indirect excitation $\lambda_{\text{ex}} = 340$ nm, using diode laser and $\lambda_{\text{ex}} = 330$ nm in reflection configuration of the $(100-x)\text{SiO}_2-x\text{SnO}_2:0.5\text{Er}^{3+}$ planar waveguides ($x = 10, 20$ and 30)

However, slight differences of the Er^{3+} emission are also revealed in the $70\text{SiO}_2-30\text{SnO}_2:0.5\text{Er}^{3+}$ planar waveguides excited at different

wavelengths in the UV range ($\lambda_{\text{ex}} = 320, 330$ and 350 nm) as shown in Figure 4.37. All the measurement conditions were kept constant for the emission acquisition at different excitation wavelengths from the Xenon lamp source. One can see the different emission features at $1.5 \mu\text{m}$ of Er^{3+} due to the selectivity of Er^{3+} emission at different sites. The presence of broad distribution of Er^{3+} sites and the complexity of the site-selective spectral response of the rare earth in the distorted sites of Er^{3+} even in pure SnO_2 nanocrystals was already observed in the work [Fernández 2018].

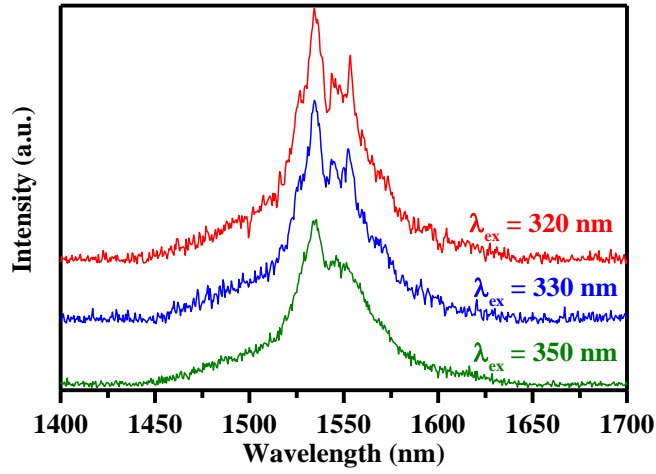


Figure 4.37 Emission spectra acquired by different indirect excitation $\lambda_{\text{ex}} = 320, 330$ and 350 nm using Xenon Lamp in reflection configuration of the $70\text{SiO}_2\text{-}30\text{SnO}_2\text{:}0.5\text{Er}^{3+}$ planar waveguides

4.5.3.2 The monoliths

Concerning the emission of the $(100-x)\text{SiO}_2\text{-}x\text{SnO}_2\text{:}0.4\text{Er}^{3+}$ monoliths shown in Figure 4.38, the similar emission behaviors to the planar waveguides are obtained: Stark-splitting and narrowing peaks under indirect excitation and a broad band emission at $1.5 \mu\text{m}$ under direct excitation as studied in [Tran 2018a], [Tran 2018b]. Due to the Stark splitting, the effective bandwidth of Er^{3+} emission at $1.5 \mu\text{m}$ under indirect excitation is 33 nm narrower than 55 nm of the direct excitation but the broad emission band still fulfils the requirements of the laser materials [Walter 2006].

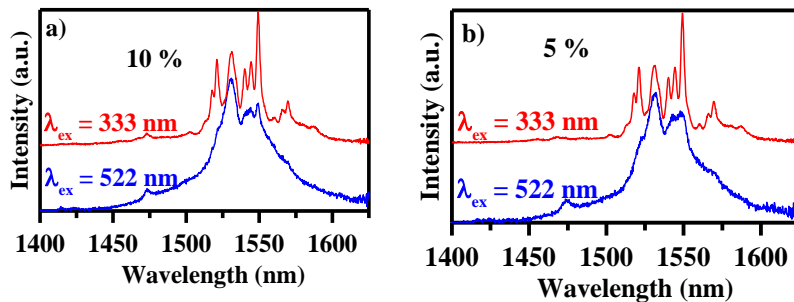


Figure 4.38 Emission spectra acquired under indirect excitation $\lambda_{\text{ex}} = 333 \text{ nm}$, using Edinburgh FLS980 spectrofluorometer of the $(100-x)\text{SiO}_2\text{-}x\text{SnO}_2\text{:}0.5\text{Er}^{3+}$ monoliths

4.5.4 Excitation

4.5.4.1 The planar waveguides

Figure 4.39 shows the excitation spectrum in the $70\text{SiO}_2\text{-}30\text{SnO}_2\text{:}0.5\text{Er}^{3+}$ planar waveguides obtained by recording the luminescence signal at 1530 nm , the fingerprint of the ${}^4\text{I}_{13/2} \rightarrow {}^4\text{I}_{15/2}$ transition of Er^{3+} . This excitation spectrum was acquired using Edinburgh FLS980 spectrofluorometer. One can see that the more intense emission from the Er^{3+} metastable state ${}^4\text{I}_{13/2}$ is evidently achieved by indirect pumping, i.e. UV excitation at the SnO_2 band-gap of around 300 nm . The direct excitation of Er^{3+} to its electronic states such as ${}^4\text{G}_{11/2}$, ${}^4\text{F}_{5/2}$, ${}^4\text{F}_{7/2}$, ${}^2\text{H}_{11/2}$, ${}^2\text{F}_{9/2}$ and ${}^4\text{I}_{11/2}$ (centered at 378 , 451 , 521 and 980 respectively) are also revealed and in agreement with the absorption spectrum in Figure 4.27. A much lower emission intensity of Er^{3+} at $1.5 \mu\text{m}$ was obtained when the sample was excited under the direct excitation. These results confirm the role of SnO_2 as an efficient Er^{3+} luminescence sensitizer.

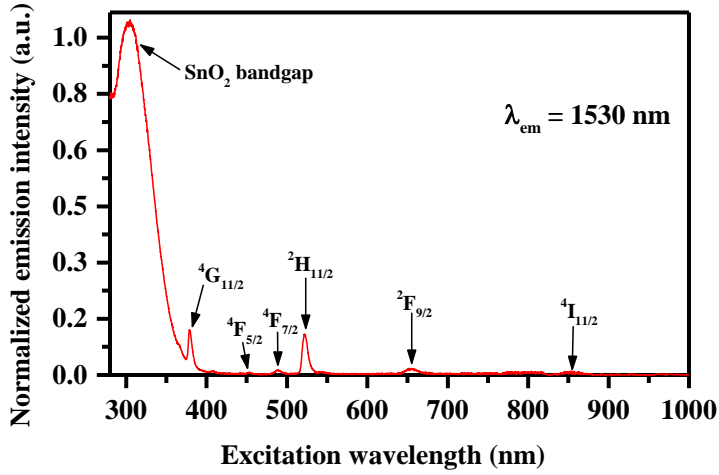


Figure 4.39 Excitation spectra acquired at emission $\lambda_{\text{em}} = 1530$ nm, using Edinburgh FLS980 spectrofluorometer of the 70SiO₂-30SnO₂:0.5Er³⁺ planar waveguides

Figure 4.40 shows the excitation spectra of all the compositional (100-x)SiO₂-xSnO₂:0.5Er³⁺ planar waveguides were acquired using the Xenon lamp as an excitation source. The normalization due to the inequal intensity at different excitation wavelength of the Xenon lamp excitation source (see Figure 4.25) was not taken into account in these excitation spectra. Even though the emission intensity of the Xenon lamp source in the UV range is much lower than the green, the excitation excited at SnO₂ band gap in the UV range leads to much higher 1.5 μm luminescence intensity of Er³⁺ in comparison with directly excited to its electronic states, e.g. ²H_{11/2} in the green as revealed in Figure 4.40. Therefore, it is evident that the energy transfer from the SnO₂ nanocrystals gives the dominant contribution to the emission of Er³⁺ at 1.5 μm in comparison with other direct excitation to Er³⁺ electronic states. The same behaviour is also obtained with the 70SnO₂-30SnO₂ doped with different Er³⁺ concentration (0.5, 1 and 1.5 mol%) as shown in Figure 4.41.

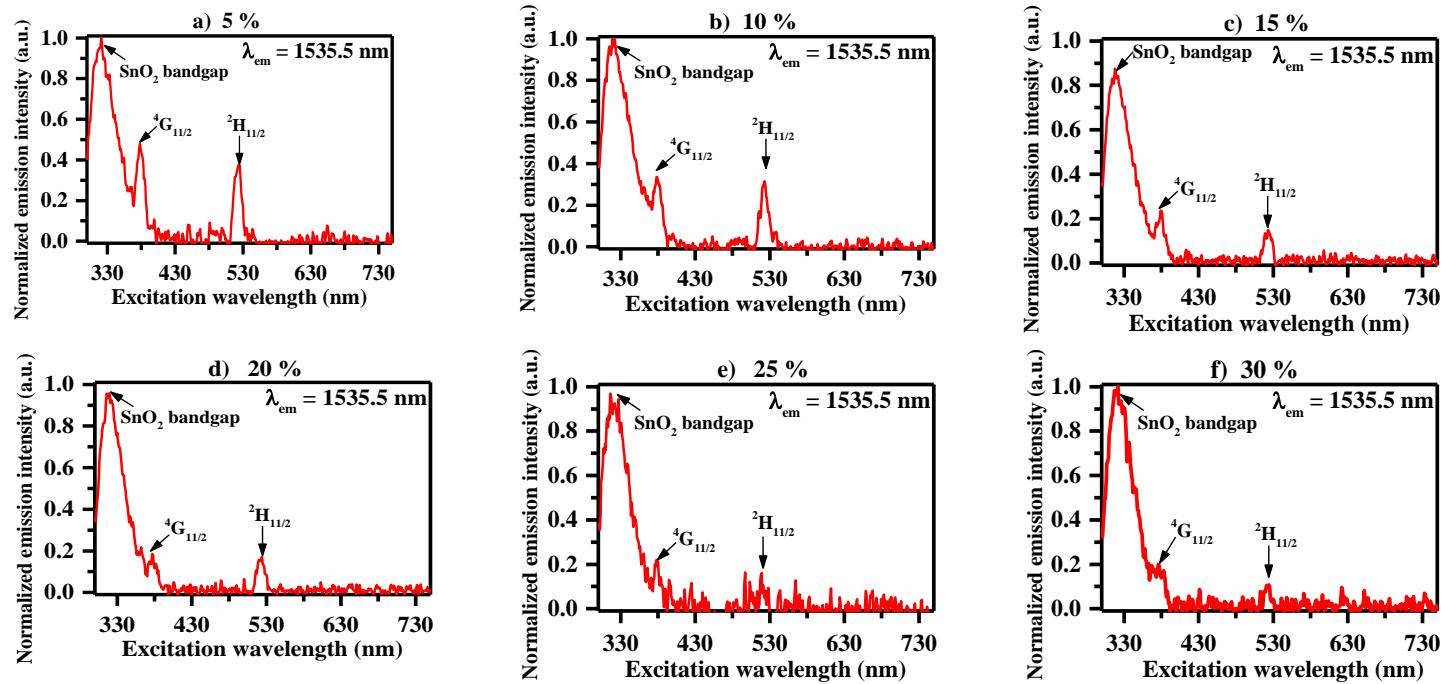


Figure 4.40 Excitation spectra of the $(100-x)\text{SiO}_2-x\text{SnO}_2:0.5\text{Er}^{3+}$ planar waveguides ($x = 5, 10, 15, 20, 25$ and 30) detected at $\lambda_{\text{em}} = 1535.5$ nm, acquired using Xenon Lamp and in reflection configuration

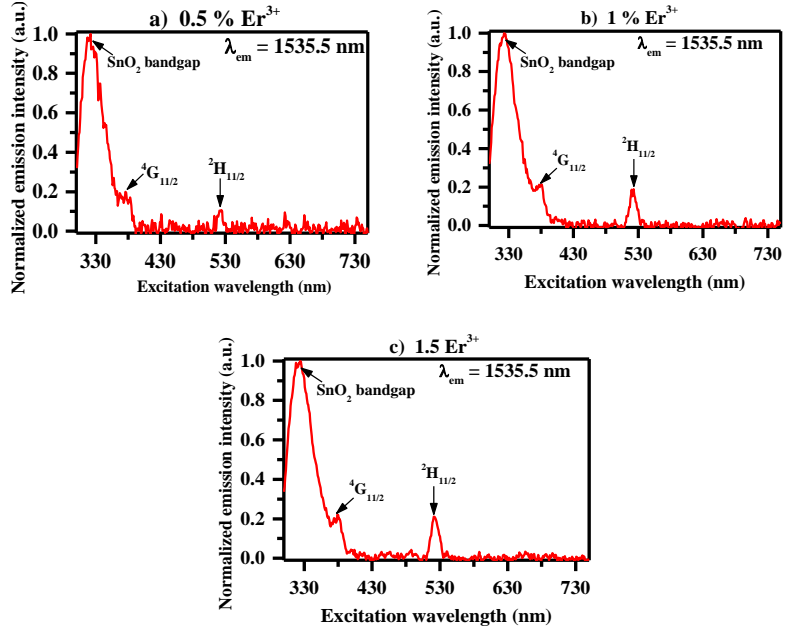


Figure 4.41 Excitation spectra of the $70\text{SiO}_2\text{-}30\text{SnO}_2\text{:yEr}^{3+}$ planar waveguides doped with different y concentration of Er^{3+} ($y = 0.5, 1$ and $1.5 \text{ mol}\%$) detected at $\lambda_{\text{em}} = 1535.5 \text{ nm}$, acquired using Xenon Lamp and in reflection configuration

4.5.4.2 The monoliths

From the excitation spectra detected at 1530 nm in the $(100-x)\text{SiO}_2\text{-}x\text{SnO}_2\text{:}0.5\text{Er}^{3+}$ monoliths ($x = 5$ and $10 \text{ mol}\%$) shown in Figure 4.42, the efficient Er^{3+} luminescence sensitizing of SnO_2 is again confirmed by the much more intense emission at $1.5 \mu\text{m}$ under indirect exciting the SnO_2 band-gap (at $\sim 300 \text{ nm}$) in comparison with directly exciting its electronic states. The most effective excitation wavelengths within the UV absorption band of SnO_2 leading to the highest luminescence signal detected at $1.5 \mu\text{m}$ emission of Er^{3+} : at 353 nm and 363 nm for the 10 and $5 \text{ mol}\%$ glass-ceramic monoliths respectively. As already discussed in section 4.5.2.2, this band may be related to the interband transitions of the carriers, i.e. oxygen vacancies in SnO_2 which plays a dominant role for the energy transfer from the nanocrystals to Er^{3+} [Cascales 2018]. Based on this, the absorption cross section of the interband transitions of SnO_2 at these most effective excitation wavelengths were estimated as discussed in section 4.5.2.2. Moreover, from Figure 4.42,

the indirect excitation scheme exhibits a much broader pump band thanks to the interband transition of SnO_2 semiconductor compared with the other direct excitations to the electronic states of Er^{3+} . In other words, $\text{SiO}_2\text{-SnO}_2\text{:0.5Er}^{3+}$ glass-ceramics with luminescence sensitisation pumping scheme are suitable for the commercially available broad-pump sources for optically pumped solid-state lasers, e.g. incandescent lamps, cw arc lamps, or flashlamps [Walter 2006].

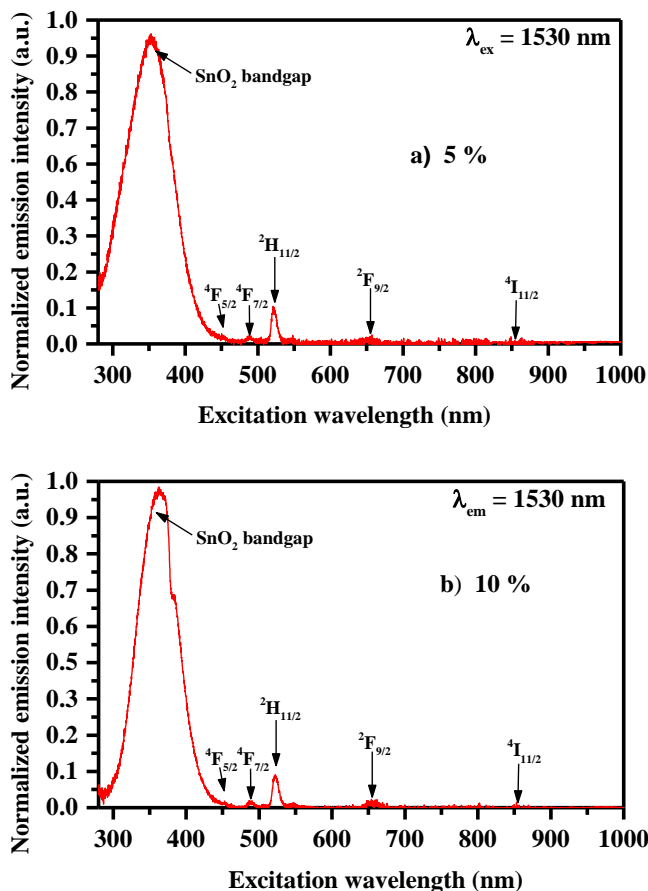


Figure 4.42 Excitation spectra acquired at emission $\lambda_{\text{em}} = 1530 \text{ nm}$, using Edinburgh FLS980 spectrofluorometer of a) $95\text{SiO}_2\text{-5SnO}_2\text{:0.5Er}^{3+}$ monolith and b) $90\text{SiO}_2\text{-10SnO}_2\text{:0.5Er}^{3+}$

In addition, for the investigation of the absorption cross section of interband transition of SnO_2 as discussed in 4.5.2.3, the excitation spectra detected at 1530 emission of Er^{3+} in the $(100-x)\text{SiO}_2\text{-xSnO}_2\text{:0.5Er}^{3+}$ monoliths ($x = 5$ and 10 mol\%) were acquired using the

Xenon lamp as an excitation source with the configuration shown in Figure 4.24. The obtained excitation spectra exhibit the same features as the ones shown in Figure 4.42. Comparing the 1.5 μm emission of Er^{3+} excited at different excitation wavelengths, the UV absorption band of SnO_2 is the one leading to the highest luminescence signal detected at 1.5 μm emission of Er^{3+} which is much higher than the ones obtained from the direct excitation to Er^{3+} electronic states. Taking into account the normalization of the different intensity of the Xenon lamp light source as shown in Figure 4.25, the 1.5 μm emission intensity when excited at the UV absorption band of SnO_2 is 3 order of magnitude higher than the one excited at 521 nm to $^2\text{H}_{11/2}$ excited state of Er^{3+} . This value was used to estimate the absorption cross section of interband transition of SnO_2 as already discussed in 4.5.2.3.

4.5.5 Time-resolved emission

To design a possible laser, it is mandatory to assess the lifetimes of Er^{3+} ions at the excited state corresponding to the desired emission signal. Therefore, the decay curves of $^4\text{I}_{13/2}$ metastable state of Er^{3+} in the compositional $\text{SiO}_2\text{-SnO}_2\text{:}0.5\text{Er}^{3+}$ are important features.

4.5.5.1 The planar waveguides

Figure 4.43 shows the time-resolved emission spectra of the $^4\text{I}_{13/2} \rightarrow ^4\text{I}_{15/2}$ photoluminescence of Er^{3+} in the $70\text{SiO}_2\text{-}30\text{SnO}_2\text{:}0.5\text{Er}^{3+}$ planar waveguide. There are two different excitation schemes: energy transfer excited at SnO_2 band-gap ($\lambda_{\text{ex}} = 306 \text{ nm}$) and directly excited Er^{3+} to its $^2\text{H}_{11/2}$ state ($\lambda_{\text{ex}} = 522 \text{ nm}$). Thanks to the large time range from nanoseconds to seconds of the Edinburgh FLS980 spectrofluorometer, the initial rise of the time-resolved emission spectra under indirect excitation was also scoped.

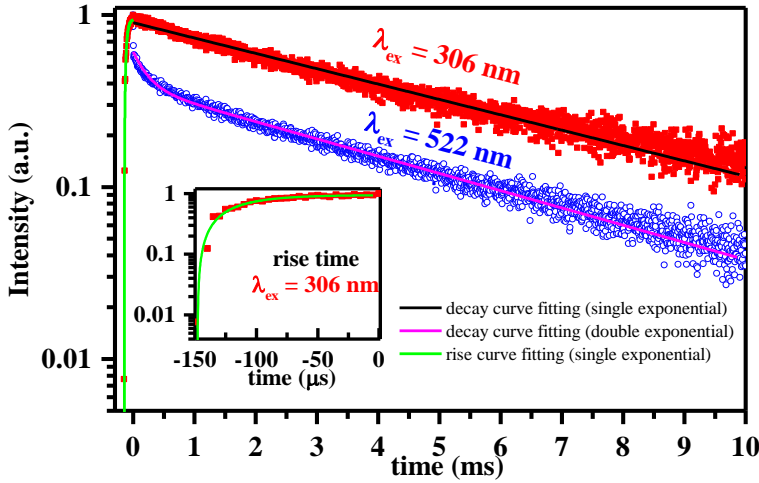


Figure 4.43 Time-resolved luminescence spectra from the $^4I_{13/2}$ metastable state of Er^{3+} excited indirectly at $\lambda_{ex} = 306$ nm and excited directly at $\lambda_{ex} = 522$ nm, acquired using Edinburgh FLS980 spectrofluorometer of the $70SiO_2-30SnO_2:0.5Er^{3+}$ planar waveguide. The inset is the rise time curve of the $^4I_{13/2}$ metastable state of Er^{3+} excited indirectly at $\lambda_{ex} = 306$ nm

Under indirect excitation, the only involved Er^{3+} ions are the ones in SnO_2 nanocrystals. The Er^{3+} ions in SnO_2 nanocrystals possess a decay curve following single exponential behavior which confirms only one site of Er^{3+} in SnO_2 nanocrystals is involved in under the narrow laser beam. Concerning the average decay time $\tau_{1/e}$, this involved Er^{3+} site in SnO_2 possesses a $^4I_{13/2}$ metastable lifetime: $\tau_{1/e} = 4.3 \pm 0.1$ ms which is much longer than the one directly excited to the $^2H_{11/2}$ state of Er^{3+} : $\tau_{1/e} = 0.6 \pm 0.1$ ms. The $^4I_{13/2}$ decay curve under the direct excitation to the $^2H_{11/2}$ level of Er^{3+} ions does not show a single exponential behavior due to more complicated spectral response of Er^{3+} due to local environment inhomogeneities [Righini 2005]. In case of $SiO_2-SnO_2:0.5Er^{3+}$ glass-ceramics, the direct excitation involves not only the ions embedded in the silica matrix but also those suffering from different local crystalline fields of SnO_2 , as it was well discussed by Joaquín Fernández et al [Fernández 2018].

Furthermore, in the indirect excitation, i.e. SnO_2 band-gap excitation at 306 nm, the rise time of the $^4I_{13/2}$ metastable state of Er^{3+} in range of 30 ± 10 μs is observed and this is not observed in the direct excitation (λ_{ex}

= 522 nm). In other words, it is a clear evidence of the exciton mediated energy transfer from SnO₂ to Er³⁺. The proposed mechanism will be discussed in the next subsection 4.5.5.2 of time-resolved spectra of the monoliths. All the values of the rise and decay times under indirect excitation and the decay time in case of direct excitation of ⁴I_{13/2} metastable state of Er³⁺ in the 70SiO₂-30SnO₂:0.5Er³⁺ planar waveguides are tabulated in Table 4.11.

Table 4.11 Table of decay time and rise time of the time-resolved luminescence from the ⁴ I _{13/2} metastable state of Er ³⁺ excited indirectly at λ _{ex} = 306 nm and directly at λ _{ex} = 522 nm, acquired using Edinburgh FLS980 spectrofluorometer of the 70SiO ₂ -30SnO ₂ :0.5Er ³⁺ planar waveguides		
Excitation scheme	Indirect (λ _{ex} = 306 nm)	Direct (λ _{ex} = 522 nm)
τ _{1/e} decay time (ms)	4.3 ± 0.1	0.6 ± 0.1
rise time (μs)	30 ± 10	0

Aforementioned, the decay function of the luminescence from the ⁴I_{13/2} metastable state of Er³⁺ under direct excitation at λ_{ex} = 522 nm does not show single exponential function. Approximately, a sum function of two exponentials were employed to describe the luminescence decay function under direct excitation as suggested in [Righini 2005]:

$$\phi(t) = A_1 \exp\left[-\frac{t}{\tau_1}\right] + A_2 \exp\left[-\frac{t}{\tau_2}\right] \quad (4.17)$$

where φ(t) is the decay function;

τ₁ and τ₂ are the two decay time components;

and A₁ and A₂ are the coefficients of the two two decay time components τ₁ and τ₂ respectively;

Table 4.12 summarizes the obtained values of A₁, τ₁, A₂, τ₂. In addition, in this table, the ratio of the numbers N₁ and N₂ of the ions which decay with the lifetime τ₁ and τ₂ respectively are also listed following the approximation of the number of the total ions:

$$N = N_1 + N_2 = A_1 \tau_1 + A_2 \tau_2 \quad (4.18)$$

Table 4.12 Table of the obtained values of A_1 , τ_1 , A_2 , τ_2 , and the ratio of $\rho = \frac{N_1}{N_1+N_2} = \frac{A_1\tau_1}{A_1\tau_1+A_2\tau_2}$ of the decay function of the luminescence from the $^4I_{13/2}$ metastable state of Er^{3+} under direct excitation at $\lambda_{ex} = 522$ nm of the 70SiO ₂ -30SnO ₂ :0.5Er ³⁺ planar waveguide										
x	A_1	ΔA_1	τ_1 (ms)	$\Delta \tau_1$ (ms)	A_2	ΔA_2	τ_2 (ms)	$\Delta \tau_2$ (ms)	ρ (%)	$\Delta \rho$ (%)
30	0.38	0.01	4.3	0.1	0.23	0.01	0.24	0.01	97	10

The results tabulated in Table 4.12 show that about 97 % of the Er^{3+} ions in the $^4I_{13/2}$ metastable state has an exponential decay of about 4.3 ms which is exactly the lifetime of Er^{3+} in SnO₂ under indirect excitation scheme shown in Table 4.11. This confirms that the majority of the Er^{3+} ions (97 %) are imbedded in the SnO₂ crystals. The short lifetime component of 0.24 ± 0.01 ms can be due to different causes such as ion-ion interaction energy transfer or Er-OH centres as also observed in [Chiasera 2011], [Tran 2018a]. Furthermore, the absence of this fast decay time under indirect excitation at SnO₂ band-gap indicates that the involved Er^{3+} ions in SnO₂ nanocrystals may not suffer from interaction energy transfer or Er-OH centres in the glass-ceramic planar waveguides. In other words, the incorporation of Er^{3+} ions in SnO₂ nanocrystals helps reducing the quenching of luminescence due to these effects. Despite lacking the information of the $^4I_{13/2}$ radiative lifetime of Er^{3+} in the SiO₂-SnO₂ glass-ceramic planar waveguides, the quantum yield is expected to be high in this system and an explanation for this will be given in section 4.5.5.2.

For further investigation of dynamic process of photoluminescence occurring in SiO₂-SnO₂ glass-ceramics activated by Er^{3+} , the decay curves of $^4I_{13/2}$ metastable state of Er^{3+} in the compositional planar waveguides were acquired both under indirect excitation and direct excitation as shown in Figure 4.44 and Figure 4.45 respectively.

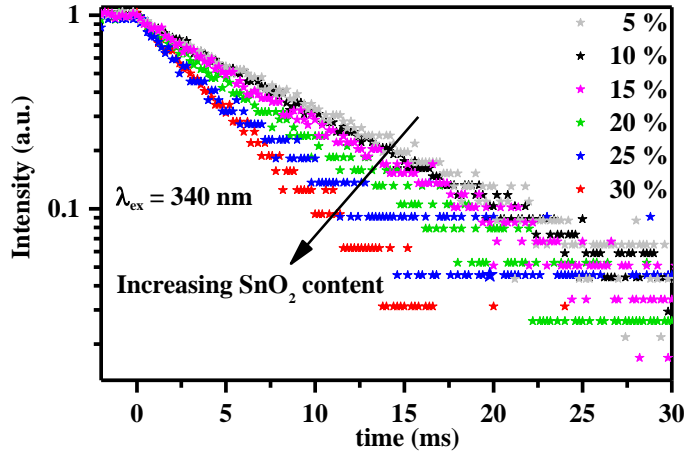


Figure 4.44 Time-resolved luminescence spectra from the $^4I_{13/2}$ metastable state of Er^{3+} excited indirectly at $\lambda_{\text{ex}} = 340 \text{ nm}$, acquired using Thorlabs UV diode laser and in reflection configuration of the $(100-x)\text{SiO}_2\text{-}x\text{SnO}_2\text{:}0.5\text{Er}^{3+}$ planar waveguides ($x = 5, 10, 15, 20, 25$ and 30)

Referring to the indirect excitation of Er^{3+} within SnO_2 band-gap ($\lambda_{\text{ex}} = 340 \text{ nm}$) using the diode laser beam, all the decay curves exhibit single exponential behavior. This evidences that for each composition, only a single site of Er^{3+} in SnO_2 is involved in this excitation scheme. The values of $1/e$ decay time of the compositional $(100-x)\text{SiO}_2\text{-}x\text{SnO}_2\text{:}0.5\text{Er}^{3+}$ are listed in Table 4.13. Considering the $70\text{SiO}_2\text{-}30\text{SnO}_2\text{:}0.5\text{Er}^{3+}$, the decay lifetime in this case is in the order of 5.0 ms which is close to the one shown in Figure 4.39.

Interestingly, increasing the content of SnO_2 in the glass-ceramics leads to a decrease of decay time from 9.3 ms for 5 mol\% down to 5.0 ms for 30 mol\% . This can be explained by the local field effects on the radiative lifetime and consequently on the measured lifetime of $^4I_{13/2}$ metastable state of Er^{3+} in the glass-ceramics with different SnO_2 content [Duan 2005]. Increasing the content of SnO_2 leads to an increase of refractive index of the medium and this changes the local field effects on Er^{3+} . The relation between the refractive index and the measured lifetime at $^4I_{13/2}$ metastable state of Er^{3+} can be described as follows:

$$\frac{1}{\tau} = \Gamma_{\text{total}} = A + A_{\text{ET}} + A_{\text{phonon}} \quad (4.19)$$

where τ is the measured lifetime at $^4I_{13/2}$ metastable state of Er^{3+} ; Γ_{total} is the total transition rate which is contributed by:

- (i) $A = A(\psi'J', \psi J)$ is the radiative transition probability already expressed in equation (4.14) and it can be written in term of refractive index of the glass-ceramic medium as following equation:

$$A = A(\psi'J', \psi J) = \frac{64\pi^4 \nu^3}{3h(2J+1)} \left[\frac{n(n^2+2)^2}{9} S_{ed} + n^3 S_{md} \right] \quad (4.20)$$

- (ii) A_{ET} is a sum of all possible unwanted energy transfer processes happening at this excited state excepting the desired $^4I_{13/2} \rightarrow ^4I_{15/2}$ transition;
- (iii) A_{phonon} is the transition probability related to the multiphonon relaxations.

By combining the two equations (4.19) and (4.20), the direct relationship between the lifetime and the local field effects in term of refractive index n is obtained:

$$\frac{1}{\tau} = \Gamma_{total} = \frac{64\pi^4 \nu^3}{3h(2J+1)} \left[\frac{n(n^2+2)^2}{9} S_{ed} + n^3 S_{md} \right] + A_{ET} + A_{phonon} \quad (4.21)$$

From (4.21), one can see that increasing the refractive index n of the $SiO_2-SnO_2:0.5Er^{3+}$ leads to a decrease of the $^4I_{13/2}$ metastable state lifetime of Er^{3+} . A similar effect was observed in case of SiO_2-HfO_2 planar waveguides activated by Er^{3+} in the work [Zampedri 2007]. In this work, both the real and virtual cavity models have been applied but the data was not reproduced. This is not surprising since in the compositional planar waveguides, the substituent parameters S_{ed} , S_{md} , A_{ET} and A_{phonon} can vary for each composition.

Table 4.13 Table of decay time of the luminescence from the $^4I_{13/2}$ metastable state of Er^{3+} excited indirectly at $\lambda_{ex} = 340$ nm, acquired using Xenon Lamp and in reflection configuration of the $(100-x)SiO_2-xSnO_2:0.5Er^{3+}$ planar waveguides ($x = 5, 10, 15, 20, 25$ and 30)						
x	5	10	15	20	25	30
$\tau_{1/e}$ (ms)	9.3 ± 0.1	8.9 ± 0.1	8.2 ± 0.1	7.0 ± 0.1	5.7 ± 0.2	5.0 ± 0.2

Considering the direct excitation scheme, the decay curves of $^4I_{13/2} \rightarrow ^4I_{15/2}$ acquired using the Ar^+ laser in the waveguiding configuration are shown in Figure 4.45. The obtained $1/e$ decay times of the compositional planar waveguides are listed in Table 4.14. Under this direct excitation,

the decay times of the compositional planar waveguides also exhibit the local field effect dependence: increasing the SnO₂ content induces the decrease of ⁴I_{13/2} metastable state lifetime of Er³⁺.

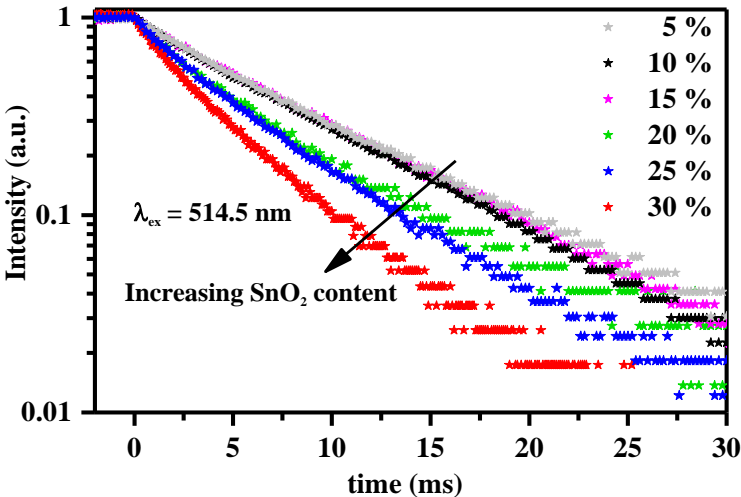


Figure 4.45 Time-resolved luminescence spectra from the ⁴I_{13/2} metastable state of Er³⁺ excited directly at λ_{ex} = 514.5 nm, acquired using Ar⁺ laser source and in waveguiding configuration of the (100-x)SiO₂-xSnO₂:0.5Er³⁺ planar waveguides (x = 5, 10, 15, 20, 25 and 30)

Table 4.14 Table of decay time of the luminescence from the ⁴ I _{13/2} metastable state of Er ³⁺ excited directly at λ _{ex} = 514.5 nm, using Ar ⁺ laser source and in waveguiding configuration of the (100-x)SiO ₂ -xSnO ₂ :0.5Er ³⁺ planar waveguides (x = 5, 10, 15, 20, 25 and 30)						
x	5	10	15	20	25	30
τ _{1/e} (ms)	8.6 ± 0.1	8.3 ± 0.1	8.0 ± 0.1	7.0 ± 0.1	5.8 ± 0.1	4.6 ± 0.1

Comparing the values listed in Table 4.13 and Table 4.14, one can see that the ⁴I_{13/2} metastable state lifetime of Er³⁺ under the direct excitation are slightly less but comparable to the ones under indirect excitation. Since the direct excitation involves Er³⁺ at different sites, the high similarity of decay times between the two excitation schemes reveals that majority of Er³⁺ ion locates in the SnO₂ nanocrystals as in case of 30 mol% SnO₂ shown and discussed in Figure 4.43 and in Table 4.12. For integrated optics, obtaining high Er³⁺ concentration is an important demand to achieve high luminescence signal over a short distance.

Therefore, different concentrations of Er^{3+} were introduced into 70SiO_2 - 30SnO_2 planar waveguides, i.e. the highest SnO_2 content ones of this planar waveguide format. However, the higher concentrations of Er^{3+} (1.0 and 1.5 mol%) result in a slight luminescence quenching due to Er^{3+} ion-ion interaction with shorter decay times of the $^4\text{I}_{13/2}$ metastable state of Er^{3+} as shown in Figure 4.46 and Table 4.15.

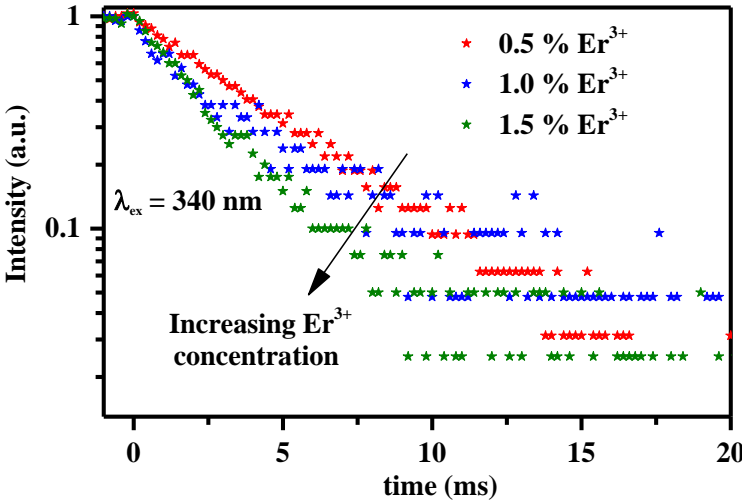


Figure 4.46 Time-resolved luminescence spectra from the $^4\text{I}_{13/2}$ metastable state of Er^{3+} excited directly at $\lambda_{\text{ex}} = 340$ nm, acquired using Xenon lamp source and in reflection configuration of the 70SiO_2 - 30SnO_2 : $y\text{Er}^{3+}$ planar waveguides doped with different y Er^{3+} concentration ($y = 0.5, 1.0$ and 1.5 mol%)

Table 4.15 Table of decay time of the luminescence from the $^4\text{I}_{13/2}$ metastable state of Er^{3+} excited indirectly at $\lambda_{\text{ex}} = 340$ nm, acquired using diode laser and in reflection configuration of the 70SiO_2 - 30SnO_2 : $y\text{Er}^{3+}$ planar waveguides ($y = 0.5, 1.0$ and 1.5 mol%)			
y	0.5	1.0	1.5
$\tau_{1/e}$ (ms)	5.0 ± 0.2	3.4 ± 0.2	2.4 ± 0.2

4.5.5.2 The monoliths

Figure 4.47 shows the time-resolved emission spectra ($\lambda_{\text{ex}} = 330$ nm) of the $^4\text{I}_{13/2} \rightarrow ^4\text{I}_{15/2}$ photoluminescence of Er^{3+} in the 90SiO_2 - 10SnO_2 : 0.5Er^{3+} monolith, acquired using the Edinburgh FLS980

spectrofluorometer. Compared to the planar waveguides, under the indirect excitation, the involved Er^{3+} ions in SnO_2 nanocrystals exhibit more complexity of the decay curve. The complexity of the decay curve can be attributed to the remaining OH groups in the monolith as revealed with the absorption peaks at 1300 nm in absorption spectrum in the Figure 4.27. Under indirect excitation, the $1/e$ decay time of Er^{3+} at $^4\text{I}_{13/2}$ metastable state is around 1.2 ms which is higher than directly excited Er^{3+} to its $^4\text{H}_{11/2}$ electronic state with lifetime of 0.08 ms. Although the quenching due to ion-ion interaction and OH groups still exists in the bulk samples, Er^{3+} embedded in SnO_2 suffer less these cross relaxation processes. This means the presence of SnO_2 helps reducing these cross relaxation processes and thus increase the luminescence efficiency. In addition, using the radiative lifetime derived using Judd-Ofelt theory as discussed in 4.5.2.6, the quantum yields of the $^4\text{I}_{13/2}$ metastable state of Er^{3+} of the monolith under the two excitation schemes were calculated. In fact, the quantum efficiency of the $^4\text{I}_{13/2}$ metastable state of Er^{3+} is higher under indirect excitation than the direct one. Table 4.16 lists the values of the decay time and the corresponding quantum yield of the $^4\text{I}_{13/2}$ metastable state of Er^{3+} in the $10\text{SiO}_2\text{-}90\text{SnO}_2\text{:}0.5\text{Er}^{3+}$ monolith under the two excitation schemes.

Under this indirect excitation, the rise time of Er^{3+} at $^4\text{I}_{13/2}$ metastable state is also revealed in range of $20 \pm 10 \mu\text{s}$ comparable to the planar waveguide as shown in Figure 4.43. This again confirms the energy transfer from SnO_2 to Er^{3+} .

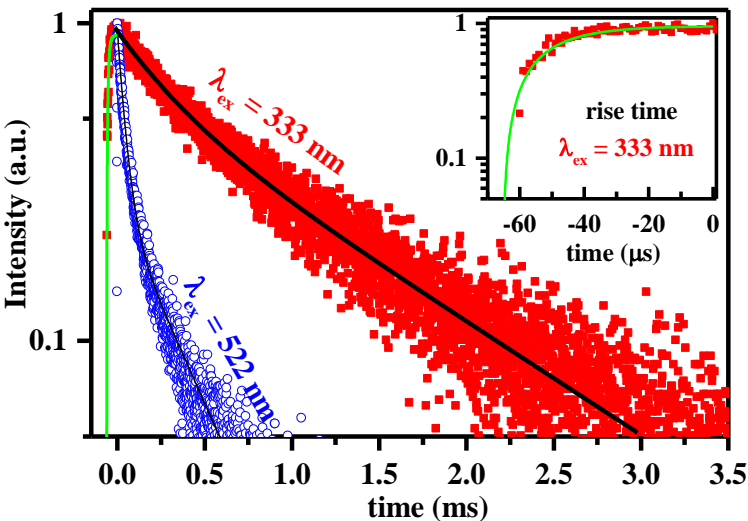


Figure 4.47 Time-resolved luminescence spectra from the $^4I_{13/2}$ metastable state of Er^{3+} excited indirectly at $\lambda_{ex} = 333$ nm and excited directly at $\lambda_{ex} = 522$ nm, acquired using Edinburg FLS980 spectrofluorometer of the $90SiO_2$ - $10SnO_2$: $0.5Er^{3+}$ monolith. The inset is the rise time curve of the $^4I_{13/2}$ metastable state of Er^{3+} excited indirectly at $\lambda_{ex} = 333$ nm

Table 4.16 Table of decay time and rise time of the 1.5 μm luminescence from the $^4I_{13/2}$ metastable state of Er^{3+} excited indirectly at $\lambda_{ex} = 306$ nm and directly at $\lambda_{ex} = 522$ nm, acquired using Edinburg FLS980 spectrofluorometer of the $90SiO_2$ - $10SnO_2$: $0.5Er^{3+}$ monolith and the corresponding quantum efficiencies of the $^4I_{13/2}$ metastable state of Er^{3+} under two excitation schemes		
Excitation scheme	Indirect ($\lambda_{ex} = 333$ nm)	Direct ($\lambda_{ex} = 522$ nm)
average decay time (ms)	1.2 ± 0.3	0.08 ± 0.01
rise time (μs)	20 ± 10	0
Quantum efficiency $\eta = \frac{\tau_{1/2}}{\tau_{Judd-Oftel}}$	$33 \pm 3 \%$	$2.0 \pm 0.5 \%$

Concerning the compositional $(100-x)SiO_2$ - SnO_2 : $0.5Er^{3+}$ monoliths ($x = 5$ and 10 mol%), the decay curves of Er^{3+} $^4I_{13/2}$ metastable state were acquired using the diode laser as an excitation source at SnO_2 bandgap ($\lambda_{ex} = 340$ nm). From Figure 4.48, one can see these $^4I_{13/2}$ decay curves

of the monoliths possess more complex exponential behavior as already discussed above for Figure 4.47. The $1/e$ decay time and the corresponding quantum efficiency of the $^4I_{13/2}$ metastable state of Er^{3+} are listed in Table 4.17. Among these two samples, the 10 mol% SnO_2 monolith exhibits longer lifetime 1.2 ms than the 5 mol% one with 0.5 ms. Consequently, the quantum yield of the 1500 nm emission is higher for the 10 mol% SnO_2 monolith $33 \pm 3 \%$ in comparison with $14 \pm 2 \%$ in the 5 mol% SnO_2 monolith. The complexity of the $^4I_{13/2}$ decay curves of the compositional monoliths are distributed by different factors such as: (i) OH groups; (ii) concentration quenching effect due to Er^{3+} ions-ions interaction. Therefore, the more serious quenching effect in the $95SiO_2-5SnO_2:0.5Er^{3+}$ monoliths indicates the higher contribution of the ion-ion interaction and effect of Er-OH centers. The more serious concentration quenching in the 5 mol% SnO_2 can be explained that the higher Er^{3+}/SnO_2 content ratio in this sample leads a smaller control of Er^{3+} partition induced by SnO_2 nanocrystals in the monoliths. Therefore, it is necessary to compromise the Er^{3+}/SnO_2 content ratio in the monoliths. These effects can be described in detail in time resolved emission spectra of the 5 mol% SnO_2 monoliths doped with different Er^{3+} concentrations shown in Figure 4.49.

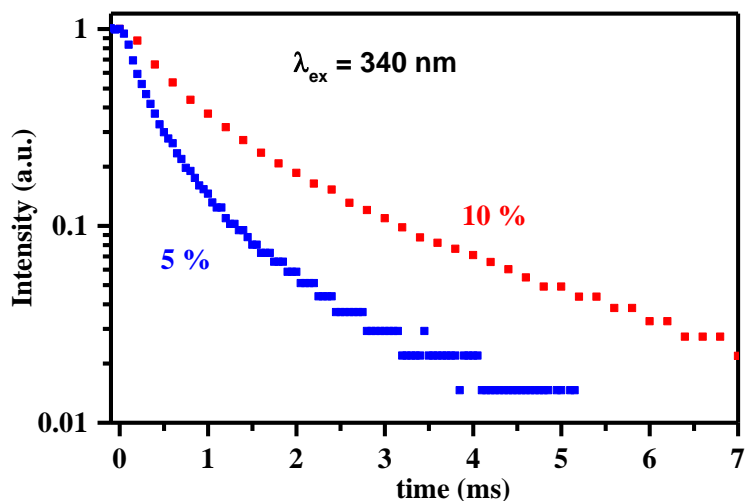


Figure 4.48 Time-resolved luminescence spectra from the $^4I_{13/2}$ metastable state of Er^{3+} excited indirectly at $\lambda_{ex} = 340$ nm, acquired using Thorlabs UV diode laser and in reflection configuration of the $(100-x)SiO_2-xSnO_2:0.5Er^{3+}$ monoliths ($x = 5$ and 10)

Table 4.17 Table of decay time of the luminescence from the $^4I_{13/2}$ metastable state of Er^{3+} excited indirectly at $\lambda_{ex} = 340$ nm, acquired using diode laser and in reflection configuration of the $(100-x)SiO_2-xSnO_2:0.5Er^{3+}$ planar waveguides ($x = 5$ and 10) and their corresponding quantum efficiencies of the $^4I_{13/2}$ metastable state of Er^{3+}		
x	10	5
$\tau_{1/e}$ (ms)	1.2 ± 0.3	0.5 ± 0.1
Quantum efficiency $\eta = \frac{\tau_{1/e}}{\tau_{Judd-Ofelt}}$	$33 \pm 3 \%$	$14 \pm 2 \%$

Figure 4.49 shows the $^4I_{13/2}$ decay curves of the $95SiO_2-5SnO_2$ activated by Er^{3+} with different concentrations (0.25, 0.50, 0.75 and 1.00 mol%). The $1/e$ decay times of $^4I_{13/2}$ metastable state of Er^{3+} are tabulated in Table 4.18. The decrease of the lifetime with increasing Er^{3+} concentration reveals the contribution of the quenching effect due to ion-ion interaction as discussed ahead. Therefore, with 5 mol% SnO_2 monoliths, among different doped Er^{3+} concentration, the 0.25 mol% is the optimal choice of Er^{3+}/SnO_2 content ratio which has the moderate Er^{3+} concentration with less effect of ion-ion quenching effect. Therefore, the quantum yield in this $95SiO_2-5SnO_2:0.25Er^{3+}$ composition shows the highest value with $48 \pm 4 \%$.

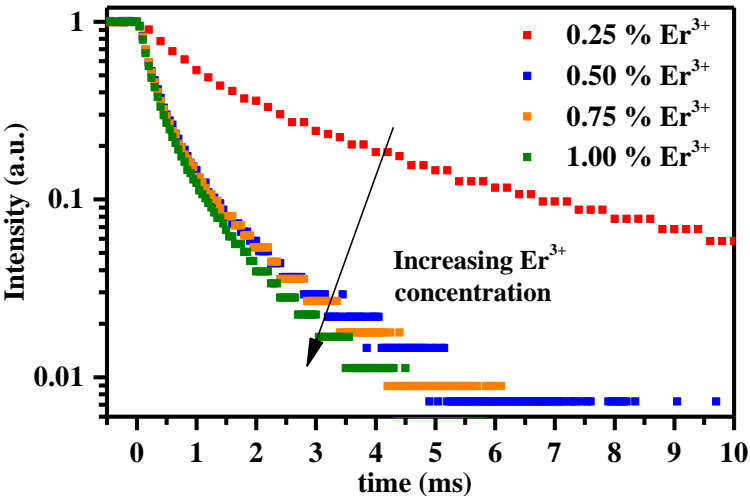


Figure 4.49 Time-resolved luminescence spectra from the $^4I_{13/2}$ metastable state of Er^{3+} excited indirectly at $\lambda_{ex} = 340$ nm, acquired using Thorlabs UV diode laser and in reflection configuration of the $95SiO_2-5SnO_2:yEr^{3+}$ monoliths ($y = 0.25, 0.50, 0.75$ and 1.0)

Table 4.18 Table of decay time of the luminescence from the $^4I_{13/2}$ metastable state of Er^{3+} excited indirectly at $\lambda_{ex} = 340$ nm, acquired using Xenon Lamp and in reflection configuration of the $95SiO_2-5SnO_2:yEr^{3+}$ planar waveguides ($y = 0.5, 1.0$ and 1.5 mol%) and their corresponding quantum efficiencies of the $^4I_{13/2}$ metastable state of Er^{3+}				
y	0.25	0.50	0.75	1.00
$\tau_{1/e}$ (ms)	2.0 ± 0.3	0.5 ± 0.1	0.4 ± 0.1	0.4 ± 0.1
Quantum efficiency $\eta = \frac{\tau_{1/e}}{\tau_{Judd-Ofelt}}$	$48 \pm 4 \%$	$14 \pm 2 \%$	$9 \pm 1 \%$	$9 \pm 1 \%$

Comparing with an erbium-activated modified silica glass (Baccarat) [Benoit 2005] which was reported to have a high quantum efficiency of the $^4I_{13/2}$ metastable state of Er^{3+} with 62.5 %, the $95SiO_2-5SnO_2:0.5Er^{3+}$ with $48 \pm 4 \%$ and $90SiO_2-10SnO_2:0.50Er^{3+}$ with 33% have acceptably moderate quantum efficiency. However, as discussed ahead, the presence of OH groups are one of the factors which attribute to lower the quantum yield of the SiO_2-SnO_2 monoliths. Therefore, higher

quantum yields of the SiO₂-SnO₂ monoliths can be achieved with the removal of OH groups simply by a further heat-treatment. Concerning this factor in the compositional planar waveguides, as already discussed in the subsection 4.5.5.1 of the time-resolved 1500 nm emission spectra, the involved Er³⁺ ions under indirect excitation do not suffer from the addressed quenching effect and thus, they are expected to have higher quantum yield efficiencies of the ⁴I_{13/2} metastable state of Er³⁺.

4.5.5.3 A possible scheme for Er³⁺ luminescence sensitization at 1.5 μm

For understanding the energy transfer from SnO₂ into Er³⁺ ions, a simplified energy-level diagram of both SnO₂ and Er³⁺ are illustrated in Figure 4.50. According to the works [Cascales 2018], [Kong 2009], the energy transfer from SnO₂ to Er³⁺ is proposed to be mediated by either band-to-band or band-to-defect-state transitions of oxygen vacancies in SnO₂. The study of real mechanism of SnO₂-RE energy transfer is still under investigation. Nevertheless, as reported in the work [Cascales 2018], [Lin 2014], the relaxation occurring in SnO₂ and the energy transfer from SnO₂ to Er³⁺ is in nanosecond scale while the observed rise time of the ⁴I_{13/2} is longer in few tens of microsecond. This indicates that there may be other involved processes in the luminescence sensitization: possibly transitions between the electronic states of Er³⁺ occurring after the Er³⁺ ion receives the energy from SnO₂. Therefore, an attempt to understand more Er³⁺ luminescence sensitization at 1.5 μm was carried out based on the observed lifetime of the ⁴I_{13/2} metastable state and the Judd-Ofelt calculated radiative decay time of the excited states ⁴G_{9/2}. From Figure 4.50, one can see that the broad absorption band of SnO₂ is resonance with the excited states ⁴G_{9/2}, ²K_{15/2} and ²G_{7/2}. As discussed, due to the rapid thermalization, all the Er³⁺ ions at higher states ²K_{15/2} and ²G_{7/2} decay to the ⁴G_{9/2} at room temperature. Therefore, the consideration is paid on the ⁴G_{9/2} level. From the sections 4.5.2.6 and 4.5.5, it is noticeable that the observed values of the rise time of the ⁴I_{13/2} metastable state and the Judd-Ofelt calculated radiative decay time of the excited states ⁴G_{9/2} are in the same time scale: few tens of microsecond. Moreover, high branching ratio of 71 % of the transition from ⁴G_{9/2} to the metastable state ⁴I_{13/2} allows suggesting of the Er³⁺ luminescence sensitization scheme as follows:

- (i) The excitation at the UV range leads to either the band-to-band or band-to-defect-state transitions of SnO_2 . Afterwards, the relaxation occurs in SnO_2 and transfers energy from SnO_2 to Er^{3+} . These two processes were observed to happen in nanosecond scale [Cascales 2018], [Lin 2014]. In addition, the energy transfer efficiency from SnO_2 to Er^{3+} was estimated to be 63.4 % [Lin 2014].
- (ii) Thanks to the energy resonance, Er^{3+} after receiving the transferred energy undergoes the transition from the ground state $^4\text{I}_{15/2}$ to an excited state which can be any of the following states: $^4\text{G}_{9/2}$, $^2\text{K}_{15/2}$ or $^2\text{G}_{7/2}$. Due to the rapid thermalization as discussed in section 4.5.2.6, Er^{3+} ion which is at any of the higher energy states (either $^2\text{K}_{15/2}$ or $^2\text{G}_{7/2}$) decays first to the lowest energy level $^4\text{G}_{9/2}$. And then, from $^4\text{G}_{9/2}$, Er^{3+} relaxes to the metastable states $^4\text{I}_{13/2}$ with high branching ratio (71 % see section 4.5.2.6). This process occurs in few tens of microsecond.
- (iii) Finally, from the metastable states $^4\text{I}_{13/2}$, Er^{3+} relaxes to the ground state $^4\text{I}_{15/2}$ and emits the photon at 1.5 μm .

Overall, based on the influential factors involved in the whole process of Er^{3+} luminescence sensitization: (i) the high absorption cross section of SnO_2 interband transition (see 4.5.2.2), (ii) high energy transfer efficiency from SnO_2 to Er^{3+} (63.4 % [Lin 2014]), (iii) high branching ratios from $^4\text{G}_{9/2}$ to the metastable state $^4\text{I}_{13/2}$ (71 % see 4.5.2.6) and (iv) relatively high quantum efficiency at 1500 nm emission of Er^{3+} under indirect excitation (48 ± 4 % for the $95\text{SiO}_2\text{-}5\text{SnO}_2\text{:}0.25\text{Er}^{3+}$ and 33 ± 3 % for $90\text{SiO}_2\text{-}10\text{SnO}_2\text{:}0.50\text{Er}^{3+}$), it is reasonable to confirm the role of SnO_2 as an efficient Er^{3+} luminescence sensitizers. Moreover, this indicates the promising of an efficient laser exploiting this luminescence sensitization as a pumping scheme.

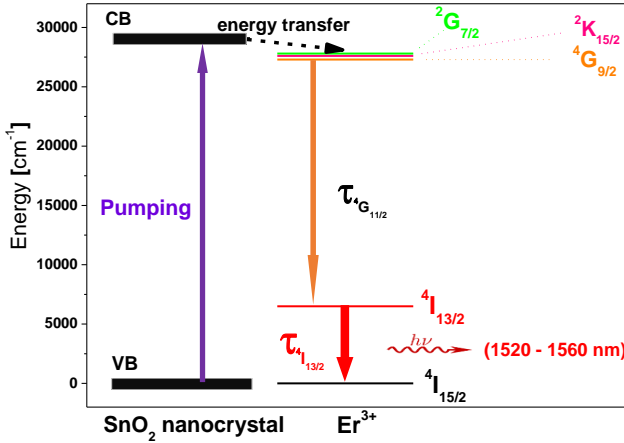


Figure 4.50 Energy-level diagram of SnO_2 and Er^{3+} and a possible Er^{3+} luminescence sensitization scheme.

4.6 Optical waveguiding characterization

Concerning the $\text{SiO}_2\text{-SnO}_2\text{:}0.5\text{Er}^{3+}$ planar waveguides, the optical waveguiding characterization is an essential task. In this planar waveguiding format, the electromagnetic waves need to be confined and directed in the region of $\text{SiO}_2\text{-SnO}_2\text{:}0.5\text{Er}^{3+}$ medium. Therefore, the thickness, refractive index and index profile of the $(100\text{-}x)\text{SiO}_2\text{-}x\text{SnO}_2\text{:}0.5\text{Er}^{3+}$ are the first three fundamental parameters which determine the light confinement. The propagation loss measurement is another key validation to evaluate whether the planar waveguides are appropriate for integrated optics. All these characteristics in turns provide the fundamental data for the appropriate design and strategy for future fabrication of integrated planar waveguide laser.

4.6.1 Refractive index and thickness measurement

4.6.1.1 M-line spectroscopy

For the measurements of refractive index and thickness of the compositional $(100\text{-}x)\text{SiO}_2\text{-}x\text{SnO}_2\text{:}0.5\text{Er}^{3+}$ planar waveguides, the m-line technique was employed. The fundamentals and the prism coupling working principle of this m-line technique can be found in the intensive studies [Monneret 2000], [Ulrich 1973] or review papers in the

literature [Monneret 2000], [Righini 2005]. The instrumentations used for these measurements are two Metricon mod. 2010 apparatuses [Metricon Corporation]: the first one with two He-Ne lasers with 632.8 and 543.5 nm lines and the second one with the 632.8, 1330 and 1540 nm lines integrated with a fiber optic probe and photodetector for losses measurement option. Briefly, in these measurements, the planar waveguides were placed and kept in contact with a prism by a pneumatically-operated coupling head. A laser beam was incidented into one base of the prism. The measurements then were carried out by rotating the sample-prism configuration together. In the out-of-coupling condition [Monneret 2000], the laser beam is totally reflected and recorded by photodetector. When the incident angle meets the coupling condition, a certain discrete value, photons can tunnel across the air gap between the measured planar waveguide and the prism. Therefore, at this incident angle, called mode angle, the laser beam can enter into a guided optical propagation mode and this causes a sharp drop in the intensity of reflected light reaching the detector. The planar waveguides need to have at least two modes for acquiring the values of refractive index and thickness [Ulrich 1973].

4.6.1.2 Results of refractive index and thickness

Figure 4.51 shows an example of m-line measurement for the $70\text{SiO}_2\text{-}30\text{SnO}_2\text{:}0.5\text{Er}^{3+}$ planar waveguide acquired at different wavelengths (543.5, 632.8, 1319 and 1542 nm). The dropping points of the laser beam intensity reflected onto the photodetector are indicators for the coupling modes as already described above. As one can see, all the modes at different wavelengths are well-confined. In particular, for the applications in integrated optics, the confined single mode at desired wavelength is required. In fact, the $70\text{SiO}_2\text{-}30\text{SnO}_2\text{:}0.5\text{Er}^{3+}$ planar waveguide meets this requirement with a well-confined single mode at 1542 nm.

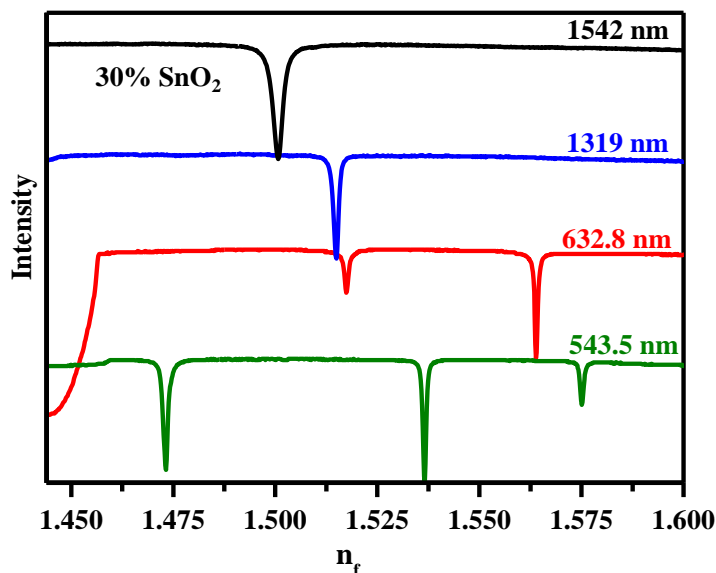


Figure 4.51 M-line measurement of the $70\text{SiO}_2\text{-}30\text{SnO}_2\text{:}0.5\text{Er}^{3+}$ at TE modes of 543.5, 632.8, 1319 and 1542 nm

Similar results of m-line measurements were obtained for other compositional $(100-x)\text{SiO}_2\text{-}x\text{SnO}_2\text{:}0.5\text{Er}^{3+}$ planar waveguides ($x = 5, 10, 15, 20, 25$ and 30 mol%). Since the 5 mol% SnO_2 planar waveguide has small refractive index with respect to the vSiO_2 substrate, only one mode in the visible (both 543.5 and 632.8 nm) was supported. Therefore, the refractive index and thickness of this sample were not experimentally acquired. On the other hand, the other compositional planar waveguides (starting from 10 mol% SnO_2), at least two propagation modes were supported in the visible. As consequence, the refractive indices and thicknesses of these samples were measured and listed in Table 4.19. Increasing SnO_2 content leads to a linear increase of the refractive indices which follow the Lorentz-Lorenz equation. The m-line measurements do show significant variation between the thickness values of planar waveguides of which the average is $1.3 \pm 0.1 \mu\text{m}$.

Table 4.19 Table of the measured refractive index and average thickness of the $(100-x)\text{SiO}_2-x\text{SnO}_2:0.5\text{Er}^{3+}$ planar waveguides ($x = 10, 15, 20, 25$ and 30 mol%)

(100-x)SiO ₂ - xSnO ₂ :0.5Er ³⁺ (x: mol%)	Refractive index (± 0.001)								Average thickness (± 0.1 μm)
	543.5 nm		632.8 nm		1319 nm		1542 nm		
	TE	TM	TE	TM	TE	TM	TE	TM	
x = 5	1.484	1.479	1.484	1.480					
x = 10	1.518	1.518	1.513	1.512	1.498	1.499	1.495	1.496	1.2
x = 15	1.542	1.542	1.538	1.538	1.523	1.525	1.520	1.522	1.2
x = 20	1.561	1.560	1.555	1.554	1.537	1.537	1.533	1.534	1.3
x = 25	1.580	1.578	1.574	1.572	1.556	1.555	1.552	1.550	1.3
x = 30	1.592	1.590	1.586	1.584	1.569	1.567	1.565	1.564	1.3

4.6.2 Dispersion curves

From the measured refractive index, it was possible to obtain the dispersion curves of the compositional planar waveguides using Sellmeier equation [Mito 1997], [Fujino 1997] as shown in Figure 4.52. The values of 5 and 0 % SnO₂ sol-gel derived samples were obtained using the extrapolating the Lorentz-Lorenz equation discussed in the next section. From the results, the corresponding dispersion curves were obtained as shown in Figure 4.52.

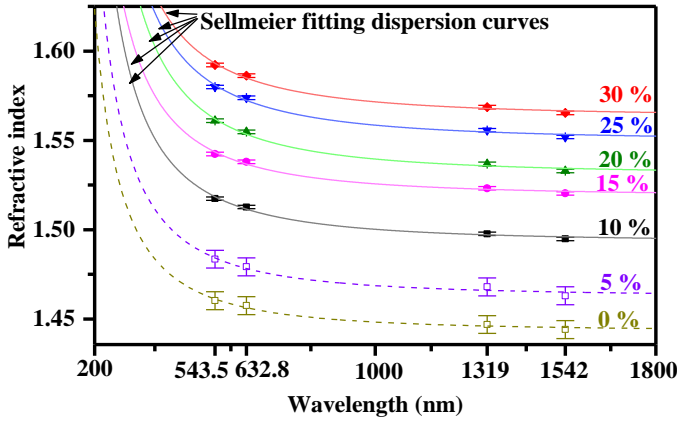


Figure 4.52 Sellmeier fitted dispersion curves obtained from the measured refractive indices of the (100-x)SiO₂-xSnO₂:0.5Er³⁺ planar waveguides (x = 5, 10, 15, 20, 25 and 30 mol%) and the 100SiO₂:0.5Er³⁺ thin film (x = 0 mol%).

4.6.3 Lorentz-Lorenz

The linearly increasing behavior of the refractive index of the compositional planar waveguides with respect to SnO₂ content are described by Lorentz-Lorenz relation [Bonin 1997]:

$$\frac{n^2(\lambda)-1}{n^2(\lambda)+2} = \frac{4\pi}{3} \sum_k \frac{N_k \alpha_k(\lambda)}{V} \quad (4.22)$$

where $n(\lambda)$ is the refractive index of the material at the wavelength λ ;

N_k is the number of the k^{th} kind molecules;

α_k is the polarizability of the k^{th} kind molecules;

V is the volume of the material, strictly related to its density.

In case of SiO_2 - SnO_2 binary glass-ceramics, the relation (4.22) can be shorten into two components:

$$\frac{n^2(\lambda)-1}{n^2(\lambda)+2} = \frac{4\pi}{3} \rho_{\text{SiO}_2/\text{GC}} \alpha_{\text{SiO}_2/\text{GC}}(\lambda) + \rho_{\text{SnO}_2/\text{GC}} \alpha_{\text{SnO}_2/\text{GC}}(\lambda) \quad (4.23)$$

where $\rho_{\text{SiO}_2/\text{GC}}$, $\alpha_{\text{SiO}_2/\text{GC}}$ and $\rho_{\text{SnO}_2/\text{GC}}$, $\alpha_{\text{SnO}_2/\text{GC}}$ are the molecular density and polarizability of the two components: SiO_2 and SnO_2 respectively in the compositional glass-ceramics.

The calculations of the molecular densities of SiO_2 and SnO_2 in the compositional glass-ceramics are described using these following equations:

$$\rho_{\text{SnO}_2/\text{GC}} = \frac{x \times A}{100 \left(\frac{x \times M_{\text{SnO}_2}}{\rho_{\text{SnO}_2}} + \frac{(100-x) \times M_{\text{SiO}_2}}{\rho_{\text{SiO}_2}} \right)} \quad (4.24)$$

$$\rho_{\text{SiO}_2/\text{GC}} = \frac{(100-x) \times A}{100 \left(\frac{x \times M_{\text{SnO}_2}}{\rho_{\text{SnO}_2}} + \frac{(100-x) \times M_{\text{SiO}_2}}{\rho_{\text{SiO}_2}} \right)} \quad (4.25)$$

where $\rho_{\text{SiO}_2} = 2.196 \text{ g/cm}^3$ and $M_{\text{SiO}_2} = 60.50 \text{ g/mol}$

and $\rho_{\text{SnO}_2} = 6.950 \text{ g/cm}^3$ and $M_{\text{SnO}_2} = 150.71 \text{ g/mol}$

By substituting the individual values of $\rho_{\text{SiO}_2/\text{GC}}$ and $\rho_{\text{SnO}_2/\text{GC}}$, and the measured refractive index for each $(100-x)\text{SiO}_2x\text{SnO}_2$ composition, a fitting based on the equation (4.23) was acquired. A very well-fitted result of the Lorentz-Lorenz relation is shown in Figure 4.53. There are two main values attained from this Lorentz-Lorenz relation:

- (i) Thanks to this linear increase behavior, the refractive index tailoring in a wide dynamic range of the glass-ceramics can be easily achieved by changing only SnO_2 content;
- (ii) The good agreement between the Lorentz-Lorenz relation and the measured refractive indices of the glass-ceramics indicates a high densification achieved in the compositional SiO_2 - SnO_2 : Er^{3+} planar waveguides as suggested in the work [Gonçalves 2004] in case of SiO_2 - HfO_2 .

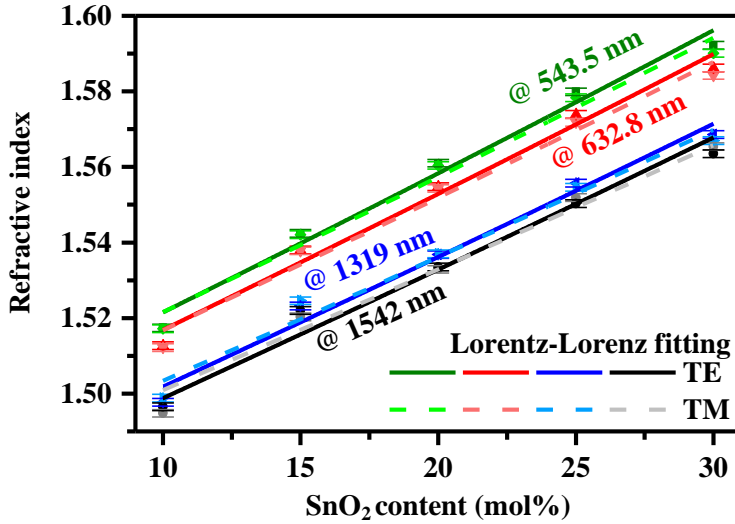


Figure 4.53 Lorentz-Lorenz fitting of the refractive indices of the $(100-x)\text{SiO}_2-x\text{SnO}_2:0.5\text{Er}^{3+}$ planar waveguides ($x = 10, 15, 20, 25$ and 30 mol%)

Moreover, the obtained Lorentz-Lorenz equations allows to derive the refractive index of any composition of the $(100-x)\text{SnO}_2-\text{SnO}_2:0.5\text{Er}^{3+}$ glass-ceramics. For example, the 5 and 0 % SnO_2 sol-gel derived samples when the refractive index could not be measured by m-line.

4.6.3.1 Index profile and confinement

The three propagation modes of $70\text{SiO}_2-30\text{SnO}_2:0.5\text{Er}^{3+}$ planar waveguide allow obtaining the index profiles in the visible (543.5 and 632.8 nm) as shown in Figure 4.54. One can see that the $70\text{SiO}_2-30\text{SnO}_2:0.5\text{Er}^{3+}$ planar waveguide exhibits step-index profile which leads to a good confinement for the light propagating inside the planar waveguides.

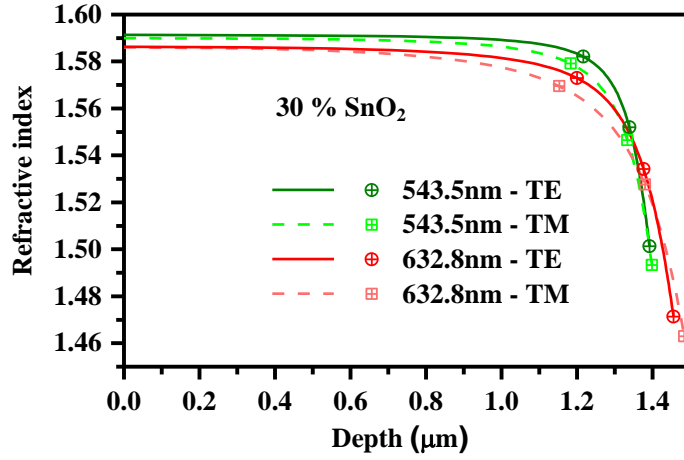


Figure 4.54 Index profile of the 70SiO₂-30SnO₂:0.5Er³⁺ planar waveguide

Figure 4.55 is the demonstration of the distribution of electric field energy at 1542 nm - TE₀ mode in the 70SiO₂-30SnO₂:0.5Er³⁺ planar waveguide. In fact, based on the distribution, the calculated confinement at the desired optical signal, i.e. 1542 nm is about 82% which is sufficient for integrated optic application.

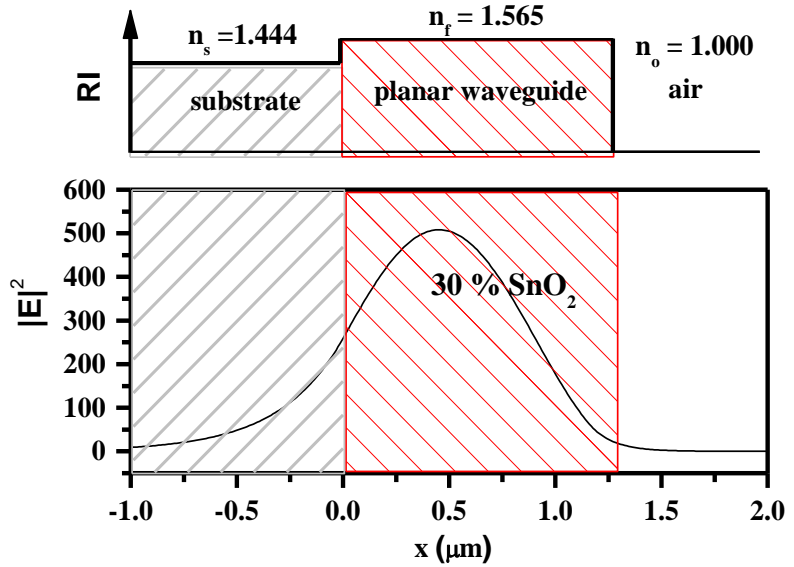


Figure 4.55 Distribution of electric field energy at 1542 nm - TE₀ mode in the planar waveguide configuration

4.6.4 Propagation losses

The fiber optic probe and photodetector embedded in the Metricon apparatus allow measurements for propagation losses. This method is based on measuring the light scattered out from the surface of the planar waveguides. In this method, the scattered light intensity is assumed to be proportional to the light propagating inside the planar waveguides. Therefore, the attenuation rate of the scattered light is assumed to be equal to the propagating light in the planar waveguides. Then the measurements of losses were carried out by scanning the fiber optic probe, along the surface of the planar waveguides. By using exponential fit of the equation (4.26) below, the power attenuation coefficients of the planar waveguides were obtained

$$I(z) = I_0 10^{-\frac{\alpha}{10}z} \quad (4.26)$$

where z is the distance in the longitudinal propagating direction (in cm) and $I(z)$ is the scattered light intensity along the z direction of the propagation. I_0 is the first point of the propagation.

However, it is necessary to pay attention to the data processing to obtain the attenuation coefficient of the planar waveguides. In case that there are some scattered centers due to imperfections, i.e. macro defects on the surface of the planar waveguides, the behavior of the scattered light at these points are not mimicking the propagating light inside the glass-ceramic planar waveguides. Therefore, to obtain the reliable values of the attenuation coefficient of the planar waveguides, it is mandatory to avoid these scattered centers for the fittings of the decay curves. In addition, the data used for the fittings should follow the linear behavior in the log scale. For most of the samples, the decay curves were fitted on the propagating length of about 1 cm and these data length are fixed for all the wavelengths of each sample. Based on these conditions, the fitting acquisition of the decay curves was carried out as shown in Figure 4.56.

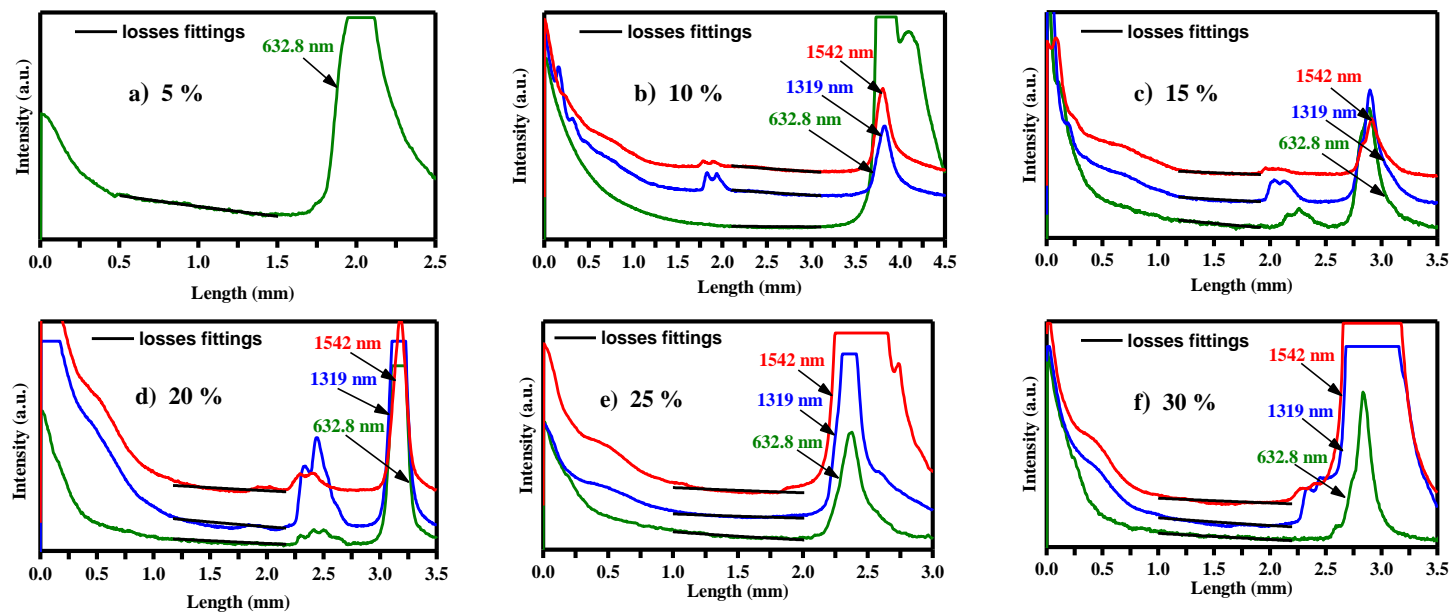


Figure 4.56 Propagation losses measurements and the losses fittings using the equation (4.26) of the $(100-x)\text{SiO}_2-x\text{SnO}_2:0.5\text{Er}^{3+}$ planar waveguides ($x = 5, 10, 15, 20, 25$ and 30 mol%)

The obtained attenuation coefficients of the compositional planar waveguides are listed in Table 4.20. From these results, there is no clear trend of the dependence of the propagation losses on SnO₂ contents. However, this is not surprising since the losses are attributed by different factors as already mentioned in section 4.2.1 about the optical losses. Therefore, the interpretation of the propagation losses needs to be elaborated with the consideration of possible factors from the structural, chemical and morphological properties for each composition of the glass-ceramic planar waveguides. Considering the surface roughness as well as SnO₂ nanocrystals of the glass-ceramic planar waveguides, the obtained values are low and within the applicable range of integrated optics as discussed in 4.4.5. In other words, they may play a minor impact on the propagation losses. Taking into account the losses from material absorption, this factor also shows different trend in comparison with the obtained values of the attenuation coefficients of the compositional planar waveguides. This implies that the influence of the structural defect causing losses is not a crucial factor causing losses. Another possible influential factor of the losses of the planar waveguides is imperfection which can happen during the sol-gel fabrication process. This factor is, in fact, driven by the chemical kinetics of the synthesized solution, dipping process and capillary force during the solvent evaporation of each compositional planar waveguides.

Concerning the behavior of losses at different propagation wavelengths of each composition planar waveguides (excepting 5 mol%), the attenuation coefficient is lower in the visible (at 632.8 nm), higher in the infrared and especially the highest at 1319 nm. This higher attenuation at 1542 nm can be attributed to the absorption of erbium. Furthermore, the high losses value at 1319 nm can be attributed to some residual water absorption. Nevertheless, the 70SiO₂-SnO₂:0.5Er³⁺ exhibits low propagation losses at 1542 nm of around 0.6 ± 0.2 dB/cm. The image of the propagation in the red (at 632.5 nm) of the low loss 70SiO₂-SnO₂:0.5Er³⁺ planar waveguide is revealed in the Figure 4.57.

Table 4.20 Table of measured propagation losses of the (100-x)SiO ₂ -xSnO ₂ :0.5Er ³⁺ planar waveguides (x = 5, 10, 15, 20, 25 and 30 mol%) at TE ₀ modes at 632.8, 1319 and 1542 nm			
(100-x)SiO ₂ -xSnO ₂ :0.5Er ³⁺	Propagation losses (± 0.2 dB/cm)		
	632.8 nm -TE ₀	1319 nm -TE ₀	1542 nm -TE ₀
x = 5	1.0	X	X
x = 10	0.2	1.0	1.0
x = 15	0.6	1.9	1.5
x = 20	0.5	1.0	0.8
x = 25	1.8	1.7	1.4
x = 30	0.3	1.0	0.6



Figure 4.57 The image of the propagation in the red (at 632.5 nm) of the low loss 70SiO₂-SnO₂:0.5Er³⁺ planar waveguide. The bright point marked by the blue circle is the indication for the output of the propagating light

4.7 Conclusions

In summary, a comprehensive photonic assessment of the structural, chemical, morphological, spectroscopic and optical waveguiding properties of the SiO₂-SnO₂:Er³⁺ monoliths and planar waveguides systems was achieved for the validation of the glass-ceramics.

From the structural characterizations, the densification of the glass-ceramics was checked. The results show that the planar waveguides reach high densification. On the other hand, from Raman feature, the heat-treatment at 900 °C for 100 h induces the densification of monoliths but there is still the presence of some residual OH groups in the bulks in the absorption spectra. The compositional and chemical analyses of the planar waveguides were performed by Auger Electron Spectroscopy and EXDS techniques to avoid chemical contaminants. The XRD analyses and HR-STEM observations revealed the homogeneous distribution of small sized SnO₂ in the glass-ceramics and in majority SnO₂ nanocrystals are less than 10 nm. However, in case of the planar waveguides, there is a small portion of larger sized SnO₂ nanocrystals (up to maximum 20 nm) in the inner layers due to the size-distribution induced by the different thermal effect time on the deposited multilayers. The planar waveguides have smooth surfaces and the value of root mean square roughness varies depending on the SnO₂ contents. Specifically, the 30 mol% SnO₂ planar waveguides have the smoothest surface with the root mean square roughness of around 1.8 nm which fulfil the requirement for integrated optics [Jonh 2012]. The planar waveguides are transparent from UV to NIR range. Increasing SnO₂ content leads to a significant increase of refractive index in a wide dynamic range. The well-fitted Lorentz-Lorenz relation of the refractive indices is beneficial for refractive index tailoring of the compositional planar waveguides. Concerning the optical waveguiding properties, the planar waveguides have confined propagation modes, step-index profile with high confinement (82 % for 30 mol% SnO₂ planar waveguides at 1542 nm) and specially, low losses (around 0.6 ± 0.2 dB/cm).

Considering the spectroscopic properties, from the absorption measurements on the monoliths, the absorption and emission cross sections, internal gain and the radiative lifetime were derived. The results show that the local environment change of Er³⁺ in the glass-ceramics leads to an increase of absorption cross section, and consequently an increase of emission cross section of Er³⁺ at 1.5 μm. The 10 mol% SnO₂ glass-ceramic monoliths exhibit high absorption, emission cross section and the estimated internal gain coefficient of 2.1 ± 0.2 dB/cm is comparable with Er³⁺ in Baccarat [Benoit 2005]. The evidence of the energy transfer from SnO₂ to Er³⁺ in the glass-ceramics was demonstrated based on the comparison between the emission spectra excited indirectly and directly. Especially the rise time of about

few tens of microsecond of $^4I_{13/2}$ metastable state under exciting at SnO_2 band edge is the clear evidence of the energy transfer. Based on the observed rise times and the Er^{3+} transitions features obtained from Judd Ofelt analyses, a possible scheme of the energy transfer processes from SnO_2 to Er^{3+} was proposed to understand Er^{3+} luminescence sensitization at 1.5 μm . The more effective luminescence sensitizing scheme of SnO_2 for Er^{3+} compared with direct excitation scheme of the rare earth was revealed by the excitation spectra. The time-resolved emission spectra of Er^{3+} under the indirect excitation show that the decay time of the metastable $^4I_{13/2}$ decreases from 10 ms to 5 ms when SnO_2 content increases from 5 to 30 mol% in the compositional glass-ceramic planar waveguides. In addition, it is demonstrated that most of Er^{3+} ions locate in SnO_2 nanocrystals in the planar waveguides. The time-resolved emission spectra were also used to define the $^4I_{13/2}$ decay time of Er^{3+} under indirect excitation in SiO_2 - SnO_2 monoliths: 1.2 ms for 90SiO_2 - 10SnO_2 : 0.5Er^{3+} and 2 ms for 95SiO_2 - 5SnO_2 : 0.25Er^{3+} . The corresponding quantum yields are relatively high: the 95SiO_2 - 5SnO_2 : 0.25Er^{3+} with $48 \pm 4\%$ and 90SiO_2 - 10SnO_2 : 0.50Er^{3+} with 33%. A comparison of the $^4I_{13/2}$ lifetimes under the indirect excitation and direct excitation indicates that the incorporation of Er^{3+} in SnO_2 nanocrystals helps reducing the effect of cross relaxation processes due to ion-ion interaction and the formation of Er-OH centers and thus leads to a higher luminescence efficiency.

The influential factors involved in the whole process of Er^{3+} luminescence sensitization were also considered: (i) the high absorption cross section of SnO_2 interband transition, (ii) high energy transfer efficiency from SnO_2 to Er^{3+} (63.4 % [Lin 2014]), (iii) high branching ratios from $^4G_{9/2}$ to the metastable state $^4I_{13/2}$ (71 % see 4.5.2.6) and (iv) relatively high quantum efficiency at 1500 nm emission of Er^{3+} under indirect excitation ($48 \pm 4\%$ for the 95SiO_2 - 5SnO_2 : 0.25Er^{3+} and $33 \pm 3\%$ for 90SiO_2 - 10SnO_2 : 0.50Er^{3+}), it is reasonable to confirm the role of SnO_2 as efficient Er^{3+} luminescence sensitizers. Moreover, this indicates the promising of an efficient laser exploiting this luminescence sensitization as a pumping scheme.

Overall, all the photonic assessment demonstrates viability of the SiO_2 - SnO_2 : Er^{3+} monoliths and planar waveguides for construction of a compact solid state laser and integrated laser respectively. The data obtained from experimental assessments provide important parameters for the laser designs. To understand more the SnO_2 : Er^{3+} nanostructure,

next chapter is dedicated for the simulation studies on the location of Er^{3+} in SnO_2 and the corresponding $\text{SnO}_2:\text{Er}^{3+}$ nanostructure using Density Functional Theory (DFT). A model for understanding $\text{SnO}_2:\text{Er}^{3+}$ nanostructure and the relaxation dynamic of the electronic states supporting for the proof of concept of the considered devices will be developed.

References

- [Armellini 1999] Armellini C., Ferrari M., Montagna M., Pucker G., Bernard C., & Monteil A., “Terbium (III) doped silica-xerogels : effect of aluminium (III)”, *Journal of Non-Crystalline Solids*, 245(1-3), pp. 115–121(1999), doi: 10.1016/S0022-3093(98)00856-4.
- [Barnes 1991] Barnes W. L., Laming R. I., Tarbox E. J., & Morkel P. R., “Absorption and Emission Cross Section of Er^{3+} Doped Silica Fibers”, *IEEE Journal of Quantum Electronics*, 27(4), pp. 1004–1010(1991), doi: 10.1109/3.83335.
- [Batzill 2005] Batzill M., & Diebold U., “The surface and materials science of tin oxide”, *Progress in Surface Science*, 79(2–4), pp. 47–154(2005), doi: 10.1016/j.progsurf.2005.09.002.
- [Benoit 2005] Benoit V., Bhaktha S. N. B., Boulard B., Chaussedent S., Chiappini A., Chiasera A., Duval E., Etienne S., Ferrari M., Gaillard-Allemand B., Jestin Y., Mattarelli M., Montagna M., Monteil A., Moser E., Conti G. N., Pelli S., Portales H., Rao D. N., Righini G. C., Vishunubhatla K. C., “Optical and spectroscopic properties of erbium-activated modified silica glass with 1.54 μm high quantum efficiency”, *Proceeding of SPIE 5723, Optical Components and Materials II*, 5723, pp. 79–88(2005), doi: 10.1117/12.590252.
- [Berneschi 2006] Berneschi S.; Bettinelli M.; Brenci M.; Calzolari R.; Chiasera A.; Ferrari M.; Matterelli M.; Montagna M.; Nunzi Conti. G.; Pelli S.; Sebastiani S.; Siligardi S.; Speghini A.; Righini G. C. (2006). “Optical and spectroscopic properties of a new erbium-doped soda-lime-alumino-silicate glass for integrated optical amplifiers”. *Proceedings of SPIE Volume 6025, ICO20: Optical Communication*, 60251M(1–8) (2006), doi: 10.1117/12.667070.
- [Bohren 2007] Bohren C. F. & Huffman D. R. (1983). “Absorption and Scattering of light by small particles”, *John Wiley & Sons* (2007), doi: 10.1002/9783527618156.

- [Bonin 1997] Bonin Keith D. & Vitaly V Kresin, “General properties of the linear polarizability”, Electric-dipole polarizabilities of atoms, molecules, and clusters., pp. 9–32(1997), doi 10.1142/2962.
- [Bouajaj 1997] Bouajaj A., Ferrari M., & Montagna M., “Crystallization of silica xerogels: A study by Raman and Fluorescence spectroscopy”, Journal of Sol-Gel Science and Technology, 395, pp. 391–395(1997), doi: 10.1023/A:1026480212567.
- [Cascales 2018] Cascales, C., Balda, R., Lezama, L., & Fernández, J. (2018), “Site symmetry and host sensitization-dependence of Eu^{3+} real time luminescence in tin dioxide nanoparticles”, Optic Express, 26(13), pp. 16155–16170, doi: 10.1364/OE.26.016155.
- [Chiasera 2011] Alessandro Chiasera, Guillaume Alombert-Goget, Maurizio Ferrari, Simone Berneschi, Stefano Pelli, Brigitte Boulard, Claire Duverger-Arfuso, “Rare earth-activated glass-ceramic in planar format”, Optical Engineering, 50(7), pp. 071105 (2011). doi:10.1117/1.3559211.
- [Demtröder 2015] Demtröder W., “Laser Raman Spectroscopy”, Laser Spectroscopy 2: Experimental techniques”, Springer-Verlag Berlin Heidelberg, pp. 149–181(2015).
- [Diéguez 2001] Diéguez A., Romano-Rodríguez A., Vilà A., & Morante J. R., “The complete Raman spectrum of nanometric SnO_2 particles”, Journal of Applied Physics, 90(3), pp. 1550–1557(2001), doi: 10.1063/1.1385573.
- [Dietrich 1969] Dietrich Marcuse, “Mode conversion caused by surface imperfection of a dielectric slab waveguide”, The Bell System Technical Journal, 48(10), pp. 3187–3215(1969), doi: 10.1002/j.1538-7305.1969.tb01742.x.
- [Duan 2005] Duan C.-K., F.Reid M., & Wang Z., “Local field effects on the radiative lifetime of emitters in surrounding media: Virtual- or real-cavity model?”, Physics Letters A, 343(6), pp. 474–480(2005), doi: 10.1016/j.physleta.2005.06.037.
- [Duverger 2001] C. Duverger, M. Montagna, R. Rolli, S. Ronchin, L. Zampedri, M. Fossi, S. Pelli, G. C. Righini, A. Monteil, C. Armellini, M. Ferrari, “Erbium-activated silica xerogels: Spectroscopic and optical properties”, Journal of Non-Crystalline Solids, 280(1–3), pp. 261–268(2001), doi: 10.1016/S0022-3093(00)00383-5.
- [Duverger 1999] Duverger C., Nedelec J. M., Benatsou M., M. Bouazaoui, B. Capoen, M. Ferrari, Turrell, S., “Waveguide Raman spectroscopy: a non-destructive tool for the characterization of

amorphous thin films”, *Journal of Molecular Structure*, 480–481, pp. 169–178(1999), doi: 10.1016/S0022-2860(98)00694-2.

[E Desurvire 1994] E Desurvire., “Erbium-Doped Fiber Amplifiers: Principles and Applications”, John Wiley, New York(1994).

[Fazio 2012] Fazio E., Neri F., Savasta S., Spadaro S., & Trusso S. “Surface-enhanced Raman scattering of SnO₂ bulk material and colloidal solutions”, *Physical Review B - Condensed Matter and Materials Physics*, 85(19), pp. 1–7(2012), doi: 10.1103/PhysRevB.85.195423.

[Fernández 2018] Fernández, J., García-Revilla, S., Balda, R., & Cascales, C., “Rare-earth-doped wide-bandgap tin-oxide nanocrystals: Pumping mechanisms and spectroscopy”, *Proceedings of SPIE Volume 10528, Optical Components and Materials XV*; pp. 1052805 (2018). doi:10.1117/12.2290170.

[Fujino 1997] Fujino, S., & Morinaga, K., “Material dispersion and its compositional parameter of oxide glasses”, *Journal of Non-Crystalline Solids*, 222, pp.316–320(1997), doi: 10.1016/S0022-3093(97)90130-7.

[Galeener 1985] Galeener, F. L., “Raman and ESR studies of the thermal history of amorphous SiO₂”, *Journal of Non-Crystalline Solids*, 71(1–3), pp. 373–386(1985), doi: 10.1016/0022-3093(85)90308-4.

[Gonçalves 2004] Gonçalves, R. R., Carturan, G., Montagna, M., ... Messaddeq, Y. , “Erbium-activated HfO₂-based waveguides for photonics”, *Optical Materials*, 25(2), pp. 131–139(2004), doi: 10.1016/S0925-3467(03)00261-1.

[Grzechnik 1998] Grzechnik, A., & Mcmillan, P. F., “Temperature dependence of the OH - absorption in SiO₂ glass and melt to 1975 K”, *American Mineralogist*, 83(3–4), pp. 331–338(1998), doi: 10.2138/am-1998-3-417.

[H. Ebendorff-Heidepriem 2016] H. Ebendorff-Heidepriem, Ehrh D., Bettinelli M., & Speghini A., “Effect of Glass Composition on Judd-Ofelt Parameters and Radiative Decay Rates of Er³⁺ in Fluoride Phosphate and Phosphate Glasses”, *Journal of Non-Crystalline Solids*, 240(1–3), pp. 66–78(2016), doi: 10.1016/S0022-3093(98)00706-6.

[Hehlen 1997] Hehlen, M., Cockroft, N., Gosnell, T., & Bruce, A., “Spectroscopic properties of Er³⁺- and Yb³⁺-doped soda-lime silicate and aluminosilicate glasses”, *Physical Review B*, 56(15), 9302–9318(1997), doi: 10.1103/PhysRevB.56.9302.

[Henderson 1985] Henderson, G. S., Bancroft, G. M., Fleet, M. E., & Roger, D. J. “Raman spectra of gallium and germanium substituted

silicate glasses: variations in intermediate range order”, *American Mineralogist*, 70, pp. 946–960(1985).

[Jonh 2012] Jonh C. Stover., “Quantifying surface roughness. Optical scattering: measurement and analysis”, Third edition, SPIE Press(2012).

[Kinowski 2001] Kinowski, C., Bouazaoui, M., Bechara, R., & Hench, L. L., “Kinetics of densification of porous silica gels : a structural and textural study”, *Journal of Non-Crystalline Solids*, 291, pp. 143–152(2001).

[Kong 2009] Kong, J., Zhu, H., Li, R., Luo, W., & Chen, X. (2009). “Carrier-mediated 1.55 μm photoluminescence from single Er^{3+} center in SnO_2 nanocrystals”, *Optics Letters*, 34(12), pp. 1873–1875 (2009).

[Lang 1989] Lang, B., “Build-up and annealing of damage induced by ion and electron beams at SiO_2 surfaces: an AES study”, *Applied Surface Science*, 37, pp. 63–77(1989).

[Lee 2000] Lee, S. W., Tsai, P. P., & Chen, H., “Comparison study of SnO_2 thin- and thick-film gas sensors”, *Sensors and Actuators B: Chemical*, 67(1–2), pp. 122–127(2000).

[Leonhardt 2013] Leonhardt, C., Brumm, S., Seifert, A., ... Mehring, M., “Tin oxide nanoparticles and $\text{SnO}_2/\text{SiO}_2$ hybrid materials by twin polymerization using tin(IV) alkoxides”, *ChemPlusChem*, 78(11), pp.1400–1412(2013).

[Lettieri 2008] Lettieri, S., Causà, M., Setaro, A., ... P. Maddalena., “Direct role of surface oxygen vacancies in visible light emission of tin dioxide nanowires”, *Journal of Chemical Physics*, 129(24), pp. 244710(2008).

[Lin 2014] Lin, T., Zhang, X., Lin, T., ... Chen, K., “Highly efficient near-infrared emission in Er^{3+} doped silica films containing size-tunable SnO_2 nanocrystals”, *Optics Express*, 22(1), pp. 369–376(2014).

[Matthew 2004] Matthew, J., “Surface analysis by Auger and x-ray photoelectron spectroscopy”, Edited by D. Briggs and J. T. Grant, IMPublications, Chichester, UK and SurfaceSpectra, Manchester, UK, (2003).

[McCumber 1964] McCumber, D. E., “Einstein relations connecting broadband emission and absorption spectra”, *Physical Review*, 136(4A), pp. A954(1964).

[McMillan 1986] McMillan, P. F., & Remmele, R. L. J., “Hydroxyl sites in SiO_2 glass: A note on infrared and Raman spectra”, *The American Mineralogist*, 71, pp. 772–778(1986).

- [Metricon Corporation] Metricon Corporation. (n.d.). <https://www.metricon.com/model-2010-m-overview/>.
- [Miguel 2014] Miguel, A., Morea, R., Arriandiaga, M. A., ... Balda, R., “Structural, optical, and spectroscopic properties of Er^{3+} -doped $\text{TeO}_2 - \text{ZnO} - \text{ZnF}_2$ glass-ceramics”, 34, pp. 3959–3968(2014).
- [Miniscalco 1991] Miniscalco, W. J., & Quimby, R. S., “General procedure for the analysis of Er^{3+} cross sections. Optics Letters, 16(4), pp. 258(1991).
- [Mito 1997] Mito, T., Fujino, S., Takebe, H., Morinaga, K., Todoroki, S., & S. Sakaguchi, “Refractive index and material dispersions of multi-component oxide glasses”, Journal of Non-Crystalline Solids, 210, pp.155–162(1997).
- [Monneret 2000] Monneret, S., Huguet-Chantôme, P., & Flory., F., “M-lines technique: Prism coupling measurement and discussion of accuracy for homogeneous waveguides”, Journal of Optics A: Pure and Applied Optic, 2(3), pp. 188(2000).
- [Montagna 2004] Montagna, M., “Characterization of Sol–Gel Materials by Raman and Brillouin Spectroscopies”, Handbook of Sol-gel science and technology: Processing, Characterization and Applications. Volume II: Characterization and properties of Sol-gel materials and products, Edited by S. Sakka, Kluwer Academic Publishers, pp. 99–117(2004).
- [Mounkachi 2016] Mounkachi, O., Salmani, E., Lakhal, M., Ez-zahraouy, H., & Hamedoun, M., “Band-gap engineering of SnO_2 ”, Solar Energy Materials & Solar Cells, 148, pp. 34–38(2016).
- [Mundy 1974] Mundy, W. C., Roux, J. A., & Smith, A. M.. “Electromagnetic scattering on spherical polydispersions”, Journal of the Optical Society of America, 64(12), pp. 1593–1597(1974).
- [Nehasil 2003]Nehasil, V., Janeček, P., Korotchenkov, G., & Matolín, V. “Investigation of behaviour of Rh deposited onto polycrystalline SnO_2 by means of TPD, AES and EELS”, Surface Science, 532–535, pp. 415–419(2003).
- [Nielson 1963] Nielson, C. W., & Koster, G. F., “Spectroscopic coefficients for the pn, dn, and fn configurations”, Cambridge, Mass., M. I. T. Press(1963).
- [Ntwaeaborwa 2006] Ntwaeaborwa, O. M., Swart, H. C., Kroon, R. E., Holloway, P. H., & Botha, J. R. “Enhanced luminescence and degradation of $\text{SiO}_2\text{:Ce,Tb}$ powder phosphors prepared by a sol-gel

process”, *Journal of Physics and Chemistry of Solids*, 67(8), pp. 1749–1753(2006).

[Ohwaki 1989] Ohwaki, T., & Taga, Y. “Effects of sputtered particle energy on the properties of SiO₂ films”, *Applied Physics Letters*, 55(9), pp. 837–839(1989).

[Okuno 2005] Okuno, M., Zotov, N., Schmücker, M., & Schneider, H., “Structure of SiO₂–Al₂O₃ glasses: Combined X-ray diffraction, IR and Raman studies”, *Journal of Non-Crystalline Solids*, 351(12–13), pp. 1032–1038(2005).

[Ouannes 2014] Ouannes, K., Soltani, M. T., Poulain, M., ... Lebbou., K., “Spectroscopic properties of Er³⁺-doped antimony oxide glass.” *Journal of Alloys and Compounds*, 603, pp.132–135(2014).

[Peelaers 2012] Peelaers, H., Kioupakis, E., & Van De Walle, C. G., “Fundamental limits on optical transparency of transparent conducting oxides: Free-carrier absorption in SnO₂”, *Applied Physics Letters*, 100, pp. 011914 (2012), doi:10.1063/1.3671162

[Peercy 1973] Peercy, P. S., & Morosin, B., “Pressure and temperature dependences of the Raman-active phonons in SnO₂”, *Physical Review B*, 7(6), pp. 2779–2786(1973).

[Pelli 2004] Pelli, S., Bettinelli, M., Brenci, M., ... Righini, G. C., “Erbium-doped silicate glasses for integrated optical amplifiers and lasers”, *Journal of Non-Crystalline Solids*, 345–346, pp.372–376(2004).

[Ramamoorthy 2014] Ramamoorthy, R. K., Bhatnagar, A. K., Rocca, F., Dalba, G., Mattarelli, M., & Montagna, M., “Er³⁺ local structure and its optical properties in ZnO-PbO tellurite glasses”, *Journal of Non-Crystalline Solids*, 383, pp. 153–156(2014).

[Righini 2005] Righini, G. C., & Ferrari, M., “Photoluminescence of rare-earth-doped glasses”, *Rivista Del Nuovo Cimento*, 28(12), pp. 1–53(2005).

[Rolli 2003] Rolli, R., Rolli, R., Montagna, M., ... Ferrari, M., “Erbium-doped tellurite glasses with high quantum efficiency and broadband stimulated emission cross section at 1.5 μm”, *Optical Materials*, 21, pp. 743–748(2003).

[Rossi 2018] Rossi, B., & Masciovecchio, C. “GISR 2017: Present and future of Raman researches in Italy”, *Journal of Raman Spectroscopy*, 49, pp.909–912(2018).

[Ryzhikov 2002] Ryzhikov, A. S., Vasiliev, R. B., Rumyantseva, M. N., ... Gaskov, A. M., “Microstructure and electrophysical properties of SnO₂, ZnO and In₂O₃ nanocrystalline films prepared by reactive

magnetron sputtering”, *Materials Science and Engineering B: Solid-State Materials for Advanced Technology*, 96(3), pp.268–274(2002).

[Saito 2014] Saito, M., D’Amico, F., Bencivenga, F., ... Masciovecchio, C., “Spatial correlation between chemical and topological defects in vitreous silica: UVresonance Raman study”, *The Journal of Chemical Physics*, 140, pp. 244505(1-5) (2014).

[Shortley 1940] Shortley, G. H., “The computation of quadrupole and magnetic dipole transitions”, *Physics Review*, 57, pp.225–237(1940).

[Skuja 1998] Skuja, L., “Optically active oxygen-deficiency-related centers in amorphous silicon dioxide.” *Journal of Non-Crystalline Solids*, 239(1–3), pp. 16–48(1998).

[Skuja 2012] Skuja, L., Kajihara, K., Hirano, M., & Hosono, H., “Oxygen-excess-related point defects in glassy/amorphous SiO₂ and related materials”, *Nuclear Instruments and Methods in Physics Research- Section B: Beam Interactions with Materials and Atoms.*, 286, pp.159–168 (2012).

[Smith 2013] Smith, E., & Dent, G. (2013) “Modern Raman spectroscopy - A practical approach”, John Wiley & Sons (2013).

[Tanabe 1999] Tanabe, S., “Optical transitions of rare earth ions for amplifiers: How the local structure works in glass”, *Journal of Non-Crystalline Solids*, 259(1–3), pp.1–9(1999).

[Tanabe 1992] Tanabe, S., Ohyagi, T., Soga, N., & Hanada, T., “Compositional dependence of Judd-Ofelt parameters of Er³⁺ ions in alkali-metal borate glasses”, *Physical Review B*, 46, pp. 3305(1992).

[Tong2014] Tong, X. C., “Advanced Materials for Integrated Optical Waveguides”, Springer International Publishing(2014), doi: 10.1007/978-3-319-01550-7

[Tran 2018a] Tran T.N. L., Massella D., Zur L., Chiasera A., Varas S., Armellini C., Righini C. G., Lukowiak A., Zonta D., Ferrari M., “SiO₂-SnO₂:Er³⁺ glass-ceramic monoliths”. *Applied Sciences*, 8(8), pp. 1335(1-8) (2018), doi: 10.3390/app8081335.

[Tran 2018b] L. T. N. Tran, L. Zur, D. Massella, B. Derkowska-Zielinska, A. Chiasera, S. Varas, C. Armellini, A. Martucci, D. Zonta, T. T. V. Tran, A. Lukowiak, S. Taccheo, D. Dorosz, G. C. Righini, Y. G. Boucher, M. Ferrari, “SiO₂-SnO₂:Er³⁺ transparent glass-ceramics: fabrication and photonic assessment”, *Proceeding of SPIE. 10683, Fiber Lasers and Glass Photonics: Materials through Applications*, 10638, pp. 106832C(1-10), doi: 10.1117/12.2306767.

- [Trani 2008] Trani, F., Causà, M., Ninno, D., Cantele, G., & Barone, V., “Density functional study of oxygen vacancies at the SnO₂ surface and subsurface sites”, *Physical Review B*, 77(245410), pp. 1–8(2008).
- [Tricoli 2012] Tricoli, A., “Structural stability and performance of noble metal-free SnO₂-based gas sensors”, *Biosensors*, 2(2), pp. 221–233(2012).
- [Ulrich 1973] Ulrich, R., and R. T. “Measurement of thin film parameters with a prism coupler”, *Applied Optics*, 12(12), pp. 2901–2908(1973).
- [Van 2010] Van T. T., Turrell S., Eddafi M., Capoen B., Bouazaoui M., Roussel P., Berneschi S., Righini G., Ferrari M., Bhaktha S. N. B., Cristini O., Kinowski C., “Investigations of the effects of the growth of SnO₂ nanoparticles on the structural properties of glass-ceramic planar waveguides using Raman and FTIR spectroscopies”, *Journal of Molecular Structure*, 976(1–3), pp. 314–319(2010), doi: 10.1016/j.molstruc.2010.04.010.
- [Van 2012] Van Tran, T. T., Si Bui, T., Turrell, S., ... Kinowski, C. (2012), “Controlled SnO₂ nanocrystal growth in SiO₂-SnO₂ glass-ceramic monoliths. *Journal of Raman Spectroscopy*, 43(7), pp. 869–875(2012).
- [Van 2014] Tran T. T. Van, S. Turrell, B. Capoen, Le V. H., M. Ferrari, Davor R., Boussekey L., Kinowski C., “Environment segregation of Er³⁺ emission in bulk sol-gel-derived SiO₂-SnO₂ glass ceramics”, *Journal of Materials Science*, 49(24), 8226–8233(2014), doi: 10.1007/s10853-014-8531-6.
- [Van 2015] Van T. T. T., Turrell S., Capoen B., Vinh L. Q., Cristini-Robbe O., Bouazaoui M., D’Acapito F., Ferrari M., Ristic D., Lukowiak A., Almeida R., Santos L., Kinowski C., “Erbium-Doped Tin-Silicate Sol–Gel-Derived Glass-Ceramic Thin Films: Effect of Environment Segregation on the Er³⁺ Emission”, *Science of Advanced Materials*, 7(2), pp. 301–308(2015), doi: 10.1166/sam.2015.2022.
- [Van 2016], Van Tran, T. T., Ly Nguyen, T., Giang Le, T. T., & Dung Cao, T. M., “Tin Dioxide Nanocrystals as an Effective Sensitizer for Erbium Ions in Er-Doped SnO₂ Systems for Photonic Applications”, *Journal of Nanomaterials*, 2016, pp. 6050731(1-5) (2016), doi:10.1155/2016/6050731
- [Walsh 2006] Walsh, B. M., “Judd-Ofelt theory: principles and practices.” In B. Di Bartolo & O. Forte, eds., *Advances in Spectroscopy for Lasers and Sensing*, pp. 403–433(2006).

- [Walter 2006] Walter Koechner, “Properties of Solid-State Laser Materials”, Solid-State Laser Engineering, New York: Springer, pp. 38–101 (2006).
- [Wiscombe 1980] Wiscombe, W. J., “Improved Mie scattering algorithms”, Applied Optics, 19(9), pp. 1505–1509(1980).
- [Woodward 1967] Woodward, L. A., Raman Spectroscopy, New York: Plenum Press(1967).
- [Yusupjanova 2016] Yusupjanova, M. B., Tashmukhamedova, D. A., & Umirzakov, B. E., “Composition, morphology, and electronic structure of the nanophases created on the SiO₂ Surface by Ar⁺ ion bombardment”, Technical Physics, 61(4), pp.628–630(2016).
- [Zampedri 2003] Zampedri, L., Ferrari, M., Armellini, C., ... Gonçalves, R. R., “Erbium-activated silica-titania planar waveguides”, Journal of Sol-Gel Science and Technology, 26(1–3), pp. 1033–1036(2003).
- [Zampedri 2007] Zampedri, L., Mattarelli, M., Montagna, M., & Gonçalves, R. R. “Evaluation of local field effect on the ⁴I_{13/2} lifetimes in Er-doped silica-hafnia planar waveguides”, Physical Review B - Condensed Matter and Materials Physics, 75(7), pp. 2–5(2007)..
- [Zhu 2014] Zhu, Y., Chen, J., Li, H., Zhu, Y., & Xu, J., “Synthesis of mesoporous SnO₂-SiO₂ composites and their application as quartz crystal microbalance humidity sensor”, Sensors and Actuators, B: Chemical, 193, pp. 320–325 (2014).
- [Zur 2017a] Zur, L., L. T. N. Tran, Meneghetti M., Varas S., Armellini C., Ristic D., Chiasera A., Scotognella F., Pelli S., Nunzi C. G., Boulard B., Zonta D., Dorosz D., Lukowiak A., Righini G. C., Ramponi R., Ferrari M., “Glass and glass-ceramic photonic systems”. In Proceeding of SPIE 10106, Integrated Optics: Devices, Materials, and Technologies XXI, Vol. 10106, p. 1010603(1-12) (2017), doi: 10.1117/12.2254965.
- [Zur 2017b] Zur, L., Tran, L. T. N., Meneghetti, M., Tran V. T. T., Lukowiak A., Chiasera A., Zonta D., Ferrari M., Righini, G. C. “Tin-dioxide nanocrystals as Er³⁺ luminescence sensitizers: Formation of glass-ceramic thin films and their characterization”, Optical Materials, 63, pp. 95–100(2017), doi: 10.1016/j.optmat.2016.08.041.

Chapter 5 Numerical calculation on SnO₂:Er³⁺

5.1 Introduction

To better understand the spectral response of Er³⁺ in SiO₂-SnO₂ glass-ceramics, it is necessary to figure out the nature of the surrounding environments of the rare-earth ions in this two phase material. With the aim of exploiting the role of SnO₂ as Er³⁺ luminescence sensitizer, a study on the structure of pure SnO₂ activated by Er³⁺ is important to understand more the local environment and spectroscopic properties of Er³⁺ embedded in the nanocrystals. Therefore, this chapter is dedicated to the numerical calculation of the location of Er³⁺ in pure SnO₂ crystalline environment, the electronic structure, density of states (DOS) and the relaxation dynamic of the electronic states using Density Functional Theory approach.

5.2 Fundamentals

5.2.1 Brief overview of location of rare-earth in SnO₂ studies

As discussed in 4.5, the pronounced Stark splitting of the Er³⁺ photoluminescence spectra exciting at the SnO₂ band gap observed in the SiO₂-SnO₂:Er³⁺ monoliths and some planar waveguides (15 and 20 mol% SnO₂) is the clear evidence that the involved Er³⁺ ions are embedded in the crystalline environment of SnO₂. However, the exact location of Er³⁺ ions in SnO₂ is still under investigation. Looking at the literature, the substitution of Er³⁺ for Sn⁴⁺ was evidenced by the EXAFS measurements in the work [Van 2014] without specification of the site symmetry of the substitution. However, there are two widely suggested sites in which Er³⁺ can locate in SnO₂: one with symmetry C_{2h} and another with symmetry D_{2h} as discussed in [Lin 2014]. In the work [Morais 2002], the author suggested a substitution of the RE ions to the Sn⁴⁺ ions in the C_{2h} sites of the cassiterite structure based on the splitting into three Stark components of the emission spectra corresponding to the transitions ⁴I_{13/2}-⁴I_{15/2} of Er³⁺. On the other hand, based on the absence of the electric dipole transitions from ⁴I_{15/2} ground state, the authors in the works [Fernández 2018], [Kong 2009] suggested that Er³⁺

incorporated at the centrosymmetric D_{2h} lattice site of Sn^{4+} in SnO_2 . However, also in [Fernández 2018], the complex spectral response of the Er^{3+} in SnO_2 is highly suggested the presence of broad distribution of Er^{3+} sites in the nanocrystals. In fact, to understand this, the experimental approaches exploiting site-selective spectroscopic measurements are mandatory to well define more suitable pumping schemes for laser design. Moreover, it is necessary to combine the experimental results of more selective spectroscopic measurements and the theoretical model of the possible location of the rare-earths in SnO_2 nanocrystals. Therefore, the numerical study carried out in this chapter is to develop a model for understanding $\text{SnO}_2:\text{Er}^{3+}$ structure and the relaxation dynamic of the electronic states supporting the proof of concept of the considered devices. Moreover, the modification of the intra band gap of SnO_2 induced by the introduction of Er^{3+} into SnO_2 is of particular interest. In addition, the presence of defect bands in the band-gap induced by Er^{3+} incorporation can change the relaxation dynamic of the crystal and must be considered during the device design.

5.2.2 Crystalline structure of pure SnO_2

5.2.2.1 Rutile-like structure of SnO_2

SnO_2 is a semiconductor with a rutile-like crystalline structure. It has a tetragonal symmetry with cell parameters of $a = b = 4.737 \text{ \AA}$; $c = 3.186 \text{ \AA}$ [Bolzan 1997]. In this structure, the Sn atoms are surrounded by a slightly distorted octahedron of O atoms. The basic cell of SnO_2 consists of two Sn atoms coordinating at $(0,0,0)$ and $(\frac{1}{2}, \frac{1}{2}, \frac{1}{2})$ and four O atoms placed at $\pm(x, x, 0)$ and $\pm(x + \frac{1}{2}, x - \frac{1}{2}, \frac{1}{2})$ with $x = 0.3056$ [Bolzan 1997]. Figure 4.34 shows the rutile-like crystal structure of SnO_2 unit cell with Sn atoms in grey and O atoms in red, obtained using crysden program [Kokalj 2003].

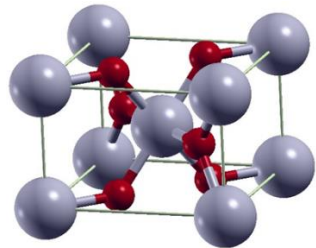


Figure 5.1 Figure of a unit cell of SnO₂ rutile-like crystalline structure (Sn atoms in grey and O atoms in red), obtained using crysden program [Kokalj 2003]

5.2.2.2 The C_{2h} and D_{2h} symmetry groups

With a rutile-like structure, SnO₂ belongs to the D_{4h}¹⁴ (P4₂/mmn) space group [Tiwari 2016] which has two Wyckoff positions for Sn⁴⁺ cation: D_{2h} for the lattice position [Evarestov 2012] and one C_{2h} for the interstitial position [Santilli 1994], [Choi 2014], [Ma 2011]. The C_{2h} symmetry group has a C₂ higher order rotational symmetry axis and a σ_h reflection plane perpendicular to the rotational symmetry axis. The D_{2h} group has two C₂ higher order rotational symmetry axis and a σ_h reflection plane perpendicular to one of the C₂ rotation axis, as demonstrated in Figure 5.2.

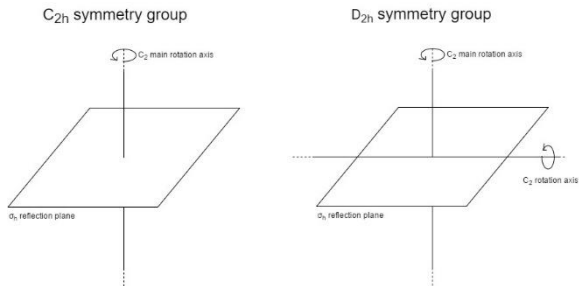


Figure 5.2 Schematic representation of the C_{2h} and D_{2h} symmetry groups of SnO₂
The character tables of the C_{2h} and D_{2h} symmetry groups of SnO₂ are reported in Table 5.1 and in Table 5.2.

Table 5.1 Character table of the C_{2h} group

C _{2h}	E	C ₂	i	σ _h		
A _g	1	1	1	1	R _z	x ² , y ² , z ² , xy
B _g	1	-1	1	-1	R _x , R _y	xz, yz
A _u	1	1	-1	-1	z	
B _u	1	-1	-1	1	x, y	

Table 5.2 Character table of the D_{2h} group

D_{2h}	E	$C_2(z)$	$C_2(y)$	$C_2(x)$	i	$\sigma(xy)$	$\sigma(xz)$	$\sigma(yz)$		
A_g	1	1	1	1	1	1	1	1	R_z	x^2, y^2, z^2
B_{1g}	1	1	-1	-1	1	1	-1	-1		xy
B_{2g}	1	-1	1	-1	1	-1	1	-1		xz
B_{3g}	1	-1	-1	1	1	-1	-1	1		yz
A_u	1	1	1	1	-1	-1	-1	-1	R_x	
B_{1u}	1	1	-1	-1	-1	-1	1	1		z
B_{2u}	1	-1	1	-1	-1	1	-1	1		y
B_{3u}	1	-1	-1	1	-1	1	1	-1		x

5.3 Comparison between EXAFS data and a model including C_{2h} symmetry site for RE ions

Based on the EXAFS data from [Van 2014], important information about the distance between erbium and nearby atoms in the SnO_2 nanocrystals is obtained. Using the crystallographic data for the cassiterite structure [Downs 2003], [Bolzan et al. 1997], the structure of SnO_2 with only D_{2h} symmetry is displayed in Figure 5.3 using the VESTA software from JP-minerals [Momma 2011].

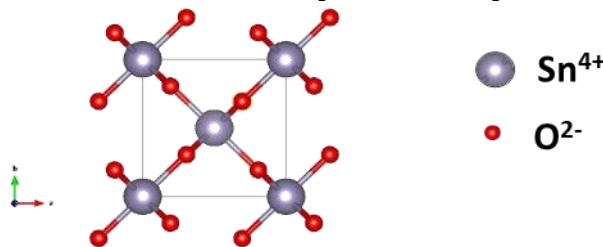


Figure 5.3 Structure of tin dioxide, viewed along the c axis, obtained by using the VESTA software from JP-minerals [Momma 2011]

Based on the Bilbao Crystallographic Server [Aroyo 2011], the crystallographic coordinates for the Wyckoff positions with C_{2h} ($2/m$) were obtained as follows: $(0, \frac{1}{2}, 0), (0, \frac{1}{2}, \frac{1}{2}), (\frac{1}{2}, 0, \frac{1}{2}), (\frac{1}{2}, 0, 0)$. An interstitial Sn atom was included at one of these coordinates in the structure of SnO_2 as shown in Figure 5.4.

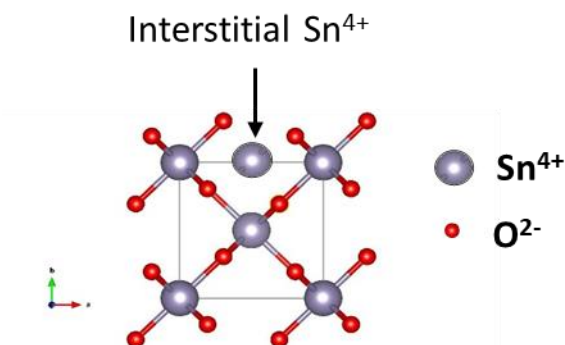


Figure 5.4 Structure of tin dioxide with interstitial tin, viewed along the c axis, obtained by using the VESTA software from JP-minerals [Momma 2011]

Based on the two structures (with and without interstitial tin), the Sn – Sn and Sn – O distances belonging to the first two coordination shells of Er^{3+} were calculated [Meneghetti 2016] and compared with the EXAFS data [Van 2014]. As first approximation, the lattice distortion induced by Er^{3+} substitution and the radius difference between Er^{3+} and Sn^{4+} were not considered for the calculation of the distances. The results can be summarized as follows:

- (i) In the model without interstitial tin, Er^{3+} has one possible site, D_{2h} symmetry site, to substitute for Sn^{4+} . From this model, the result showed that the bond lengths of a Sn – O first shell and a Sn – O second shell are comparable: 2.048 Å and 2.058 Å which makes difficulty to distinguish these two shells and can be considered as one single first shell with a total coordination number of 6. Therefore, the next Sn–Sn bond can be considered as the second shell and its bond length of 3.709 Å and coordination number of 8 was also defined.
- (ii) In the model with interstitial Sn^{4+} , there are two possibilities for Er^{3+} substitution: at D_{2h} lattice site and at C_{2h} interstitial site. For the Sn^{4+} with D_{2h} lattice site locating far from interstitial Sn^{4+} ions, the similar results were obtained as in case of the model without interstitial Sn^{4+} : Sn – O first shell ranging from 2.048 Å to 2.058 Å and coordination number of 6 and Sn–Sn second shell with a bond length of 3.709 Å and coordination number of 8. On the other hand, for the Sn^{4+} with D_{2h} lattice site locating nearby an interstitial Sn^{4+} , the distance of Sn – O first shell remains the same with bond

length of 2.048 - 2.058 Å and coordination number of 6 but Sn–Sn second shell has a shorter bond length of 2.369 Å and coordination number of 4. For the C_{2h} interstitial site, the Sn – Sn first shell with a bond length of 1.593 Å and coordination number of 2 and a Sn – O second shell with a bond length of 1.716 Å and coordination number of 2 were obtained.

Table 5.3 shows a comparison between these results and the EXAFS data from the paper [Van 2014]. As one can see the distances of the first two shells of the D_{2h} lattice site in the model without interstitial Sn^{4+} are in good agreement with the EXAFS data. This result was obtained also for the Sn^{4+} ions with D_{2h} lattice site locating far from interstitial Sn^{4+} ions in the model with interstitial Sn^{4+} . On the contrary, this model shows a noticeable difference in the distances of the first two shells compared to the EXAFS data for both C_{2h} symmetry sites and the Sn^{4+} ions with D_{2h} lattice site locating nearby an interstitial Sn^{4+} ions. This suggested that the substitution of most of Er^{3+} ion occurs at the D_{2h} lattice site of Sn^{4+} in SnO_2 . And the interstitial Sn^{4+} ions if present, are not influential. However, the information of the interstitial Sn^{4+} case is also important for further investigation especially in a boundary SnO_2 structure, e.g. nanocrystals where the surface distortion occurs

These results are also confirmed by DFT calculation on the structure in which the lattice distortion and the different atomic radius were considered. This confirms two points: (i) erbium substitutes for Sn at the lattice site and (ii) the distortion of the lattice due to the substitution perturbs only the first shell (the second shell distances are the same in both DFT, EXAFS and simplified model).

Table 5.3 The distance of the 1 st shell and the 2 nd shell of the SnO_2 structure at the two sites			
	Site	1 st shell (Å)	2 nd shell (Å)
Model with interstitial Sn^{4+} (this work)	C_{2h}	1.593	1.761
	D_{2h}	2.048-2.058	2.369 (nearby interstitial C_{2h} Sn^{4+})
		2.048-2.058	3.709 (far from interstitial C_{2h} Sn^{4+})
Model without interstitial Sn^{4+} (this work)	D_{2h}	2.048-2.058	3.709
DFT	D_{2h}	2.15	3.71
EXAFS [Van 2014]		2.2	3.7

5.4 DFT simulated band-structure and density of states of SnO₂:Er³⁺

5.4.1 Methodology

To investigate the SnO₂ crystal structure and the role of rare earth activation on its density of states, the Density Functional Theory (DFT) were applied. The overview including the principles and applied cases can be found in [Yang 2003], [Gross 2013]. Briefly, the aim of the Density Functional Theory (DFT) is to give a computationally efficient solution to the static electronic many-body problem, which is to find the solutions of the static Schrödinger equation for a system of N interacting non-relativistic electrons [Yang 2003]. The band-structure and the density of state of the SnO₂ crystal were investigated using the open software Quantum espresso [Giannozzi 2009], [Giannozzi 2017].

Based on the numerical calculation results of location of Er³⁺ in SnO₂, the DFT simulation was carried on SnO₂ crystal with one Er³⁺ substituting for Sn⁴⁺ at a D_{2h} lattice site. The image of the cell used for calculation is shown in Figure 5.5. The cell consists of 2×2×2 unit cell, leading to 62-atom basic cell. In this calculation, the charge compensation induced by the substitution of Er³⁺ for Sn⁴⁺ was taken into account. The DFT calculations were carried out to find the modifications and the consequent characteristics of SnO₂ band-structure induced by Er³⁺ substitution. Two regimes were applied for these calculations: (i) unrelaxed structure, in which the atoms stay steady at their position and (ii) relaxed structure in which the atoms move around their position with the local density approximation (LDA) using Ultra-Soft-Pseudo-Potential [Schlipf 2015], [Setten 2018].

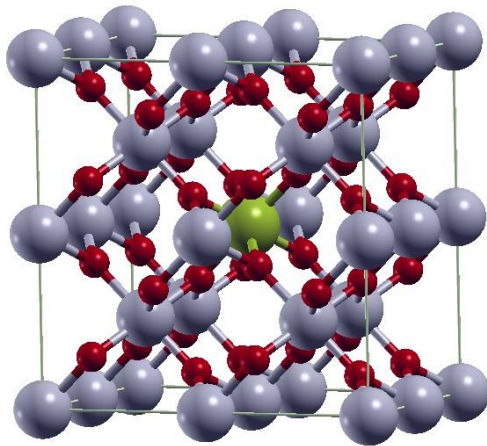


Figure 5.5 Figure of the cell of SnO₂ rutile-like crystalline structure (Sn atoms in grey, O atoms in red and substituting Er³⁺ in green) used for DFT calculation, obtained using crysden program [Kokalj 2003].

5.4.2 Un-relaxed structure

The first calculation is performed on the pure crystal of single unit cell displayed in Figure 5.4. The results are reported in Figure 5.6. They are coherent with what expected for a semiconductor crystal. In fact, the Fermi energy lies in the band gap between conduction and valence bands. The shape of both Bands and Density of States is coherent with the one found in the literature for similar calculations [Errico 2007]. The band-gap evaluated is of $E_g = 1$ eV, compared to an experimental value of 3.6 eV. This is a well-known issue of DFT to underestimate band-gap value, in [Errico 2007] the band-gap is evaluated at 1.7eV while in [Liu 2010] the band-gap value is 0.134 eV. These values are obtained with different codes and different approaches but the big difference between them expresses the difficulty to obtain a reliable value of energy band-gap for semiconductors using DFT. For this reason, in this work the obtained energy band-gap is not comparable to the experimental value. However, this does not affect the meaning in term of the modification

of the band-structure and density of states induced by the substitution of Er³⁺ for Sn⁴⁺.

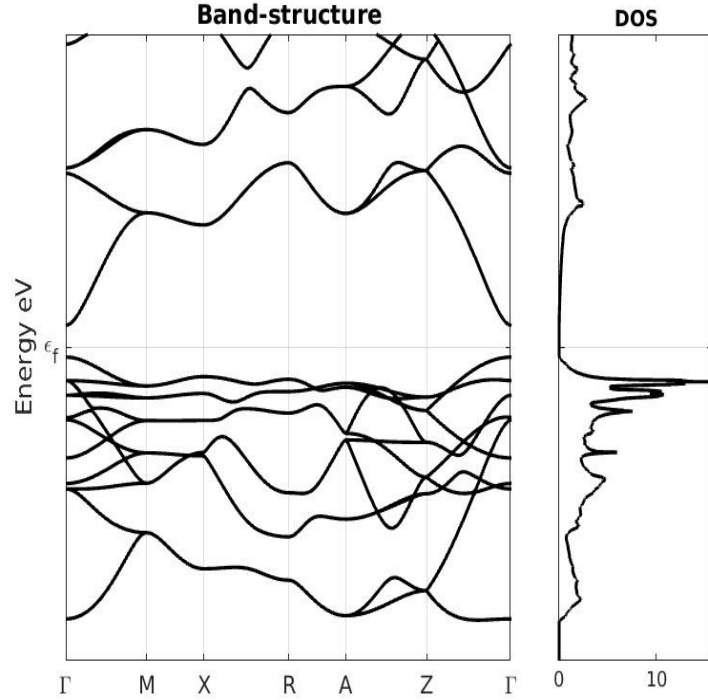


Figure 5.6 Band-diagram and Density of States of a single cell calculation of pure SnO₂. Energy units are in eV but they are defined up to a constant, so the only relevant quantities are difference in Energies. The line ϵ_f represents the Fermi energy evaluated in this case [Massella 2018].

In the un-relaxed regime, the DFT calculated density of states of SnO₂ crystal with the substitution of Er³⁺ for Sn⁴⁺ is shown in Figure 5.7. The obtained density of state is not significantly different from the one of a pure crystal. This is similar to the one obtained for Ga doping [Rivera 2014]. A noticeable result is a change in the Fermi energy, now it is within the valence band. This means that the conduction properties of the material can be changed by the doping. Unfortunately, it was not possible to calculate the band-structure of this configuration due to hardware limitations.

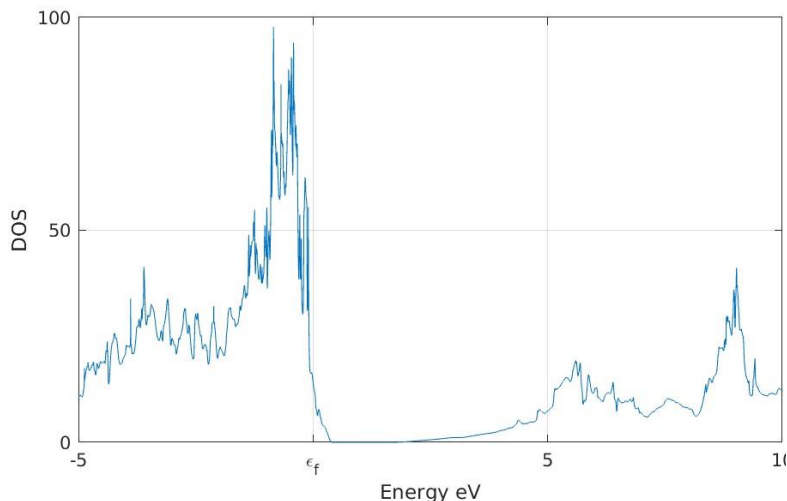


Figure 5.7 Density of States of a $2 \times 2 \times 2$ cell calculation of a single Er^{3+} ion doped (~ 6 mol%) shown in Figure 5.5. Energy units are in eV but they are defined up to a constant, so the only relevant quantities are difference in Energies. The line ϵ_f represents the Fermi energy evaluated in this case [Massella 2018]

5.4.3 Relaxed structure

Relaxed simulations were performed in the same system and with the same parameters on both pure SnO_2 and on 6 mol% Er^{3+} doped crystal as shown in Figure 5.5. The relaxation calculation revealed the same distances of the first shells as shown in section 5.3, which again confirmed the substitution of Er^{3+} for Sn^{4+} at the D_{2h} lattice site. Using the positions obtained from the relaxed calculation, it was possible to calculate again the DOS of the pure and doped SnO_2 crystals. The results in the band-gap region is shown in Figure 5.8. From Figure 5.8a), there is a small difference of DOS between the doped and the pure SnO_2 crystals. However, it is noticeable that there are also states of the valence band above the Fermi energy in these two relaxed cases as already observed in the un-relaxed case (see Figure 5.7). The strong modification of DOS is observed at around -6 eV (negative) in the doped SnO_2 compared to the pure one. Although this modification has no significant consequence in the behaviour of the material, it is the main contribution to the lowering of the Fermi energy. Figure 5.8b) reveals clearer the differences of DOS in the band-gap region. The band-gap of the doped SnO_2 crystal is slightly larger than the pure SnO_2 crystal.

However, since the number of states between the fermi energy and the band-gap region is very small which makes the experimental proof of the difference between the two cases challenging.

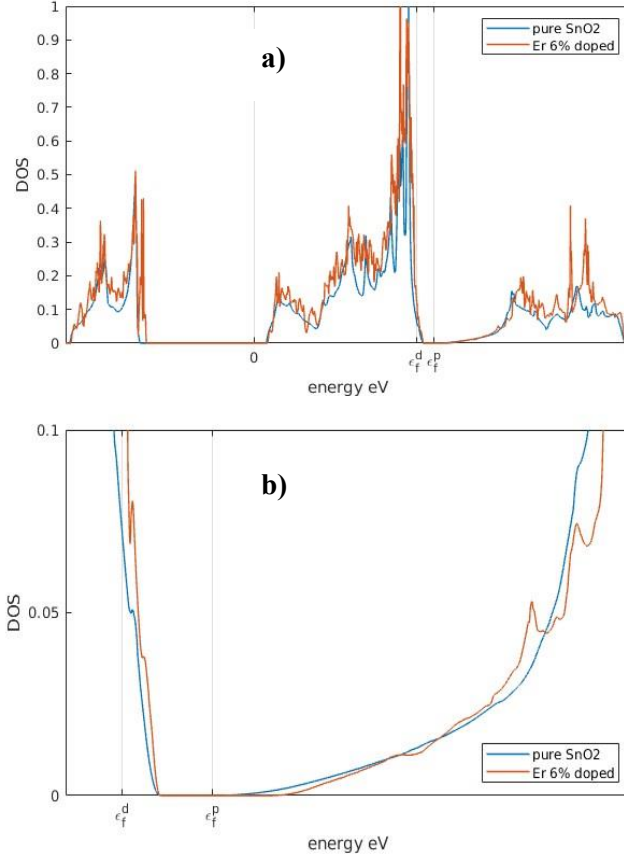


Figure 5.8 Density of States of a $2 \times 2 \times 2$ relaxed cell calculation of a single Er³⁺ ion doped (~ 6 mol%) and pure SnO₂ crystals: a) in a large energy range of band structure; b) only in the band-gap region.

Energy units are in eV but they are defined up to a ϵ_f^d is the fermi energy in the doped case and ϵ_f^p is the fermi energy in the pure crystal[Massella 2018].

The unchanged region of the band-structure can be explained by recalling the partial DOS of SnO₂ obtained by Errico [Errico 2007] as shown in Figure 5.9. As one can see from the graphs of the partial DOS, the main contribution in the band-gap region of SnO₂ crystal is due to oxygen, this means that the substitution of Sn by other ions has a low impact on the band-gap.

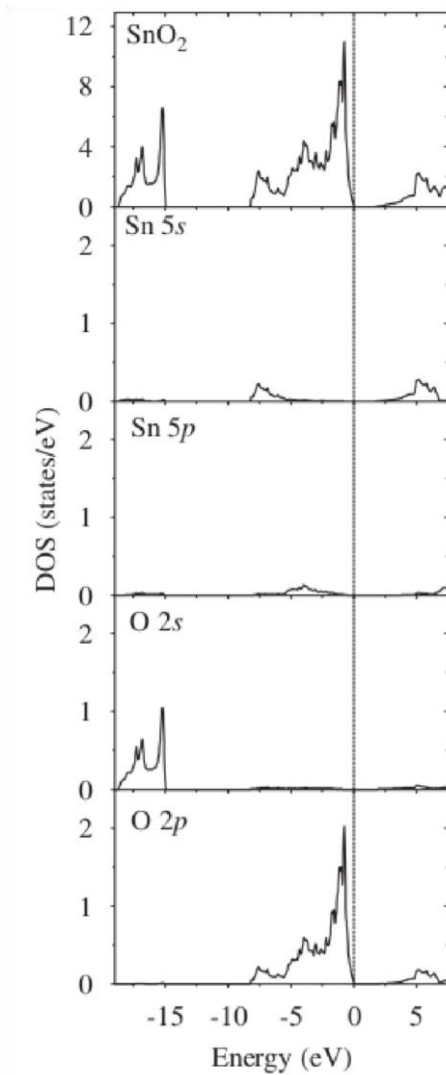


Figure 5.9 Partial and total DOS adopted from the work [Errico 2007]. The main contribution in the band-gap region is due to O. This explains why the calculation considering only the substitution of Er^{3+} for Sn^{4+} show a small modification of SnO_2 band structure

The calculation with other element leads to a similar response [Rivera 2014]. This suggests that a possible source of intra-band-gap state can be due to oxygen vacancies. The substitution of Er^{3+} for Sn^{4+} leads to the oxygen vacancies in the lattice to compensate the charge difference between Er^{3+} and Sn^{4+} . This result is in agreement with the prediction in

the work [Freeman 1990] for the oxygen vacancies creation as a substitutional solution of trivalent dopants for Sn⁴⁺. Moreover, the RE luminescence sensitization occurs in rare-earth doped SnO₂ are suggested to be associated with RE-related oxygen vacancies [Cascales 2018], [Bouzidi 2009].

5.5 Conclusions

As presented in this chapter, a numerical calculation for distances of the first two shells of SnO₂ crystals with and without the consideration of the interstitial Sn⁴⁺ at C_{2h} symmetry site, i.e. a kind of point defects in SnO₂ was carried out. A comparison between the calculation results and the EXAFS data from the work [Van 2014] confirmed the substitution of Er³⁺ for Sn⁴⁺ at D_{2h} lattice site and the interstitial Sn⁴⁺ ions if present, are not influential in this no-boundary SnO₂ structure. However, the information of the interstitial Sn⁴⁺ case is also important especially in case of a boundary SnO₂ structure, e.g. nanocrystals where the surface distortion occurs. A model for understanding SnO₂:Er³⁺ structure and the relaxation dynamic of the electronic states using DFT approach was also developed. The obtained models predicted that the substitution of Er³⁺ for Sn⁴⁺ occurs with the oxygen vacancy creation. This is in agreement with other computational modeling studies [Freeman 1990], [Errico 2007], [Rivera 2014] and also experimental studies but for the case of other dopants: Eu³⁺ [Cascales et al. 2018]. All the obtained numerical calculation and modelling provide complementary information for understanding more local environment and spectral response spectroscopic properties of Er³⁺ embedded in the nanocrystals, especially in case the Stark-splitting features are evident as discussed in the spectroscopic properties of the glass-ceramics in the section 4.5. The results of these numerical calculation and modelling on the no-boundary SnO₂ crystal are essential bricks for further investigation with more intensive computational studies on the boundary SnO₂ crystals with the consideration of surface distortion symmetry which is similar to the experimentally obtained SnO₂ nanocrystals in the glass-ceramics. All these approaches together with the experimental results are crucial for defining suitable pumping schemes for the laser design based on the fabricated SiO₂-SnO₂:Er³⁺ glass-ceramics exploiting the role of SnO₂ as Er³⁺ luminescence sensitizers. Besides the advantage of luminescence sensitisation, SiO₂-SnO₂:Er³⁺ glass-ceramics also exhibit another innovative property: photorefractivity which allows applying the robust

direct laser photoinscription technique on the systems to fabricate Bragg gratings and channel waveguides for waveguide integrated laser. And, this is the topic of the next chapter: Chapter 6: Photorefractivity investigation.

References

- [Aroyo 2011] Aroyo, M. I., Perez-Mato, J. M., Orobengoa, D., Tasci, E., De La Flor, G., & Kirov, A. “Crystallography online: Bilbao crystallographic server”, *Bulgarian Chemical Communications*, 43(2), pp. 183–197(2011)..
- [Bolzan 1997] Bolzan, A. A., Fong, C., Kennedy, B. J., & Howard, C. J. “Structural Studies of Rutile-Type Metal Dioxides”, *Acta Crystallographica Section B*, 53(3), pp. 373–380(1997).
- [Bouzidi 2009] Bouzidi, C., Elhouichet, H., Moadhen, A., & Oueslati, M., “Sensitisation of erbium emission by silicon nanocrystals-doped SnO₂”, *Journal of Luminescence*, 129(1), pp. 30–33(2009).
- [Cascales 2018] Cascales, C., Balda, R., Lezama, L., & Fernández, J., “Site symmetry and host sensitization-dependence of Eu³⁺ real time luminescence in tin dioxide nanoparticles”, *Optic Express*, 26(13), pp. 16155–16170(2018).
- [Choi 2014] Choi, Y. I., & Sohn, Y., “Photoluminescence profile mapping of Eu(III) and Tb(III / IV)-embedded in quantum size SnO₂ nanoparticles”, *RSC Advances*, 4, pp. 31155–31161(2014).
- [Downs 2003] Downs, R. T., & Hall-Wallace, M., “The American Mineralogist crystal structure database”, *American Mineralogist*, 88(1), pp. 247–250(2003).
- [Errico 2007] Errico, L. A. “Ab initio FP-LAPW study of the semiconductors SnO and SnO₂”, *Physica B: Condensed Matter*, 389(1), pp. 140–144(2007).
- [Evarestov 2012] Evarestov, R., & Smirnov, V. P. “Site symmetry in crystals: theory and applications”, *Springer Science & Business Media* (2012).
- [Fernández 2018] Fernández, J., García-Revilla, S., Balda, R., & Cascales, C., “Rare-earth-doped wide-bandgap tin-oxide nanocrystals: Pumping mechanisms and spectroscopy”, *Proceedings of SPIE Volume 10528, Optical Components and Materials XV*; pp. 1052805 (2018). doi:10.1117/12.2290170.

- [Freeman 1990] Freeman, C. M., & Catlow, C. R. A., “A computer modeling study of defect and dopant states in SnO₂”, *Journal of Solid State Chemistry*, 85(1), pp. 65–75(1990).
- [Giannozzi 2017] Giannozzi, P., Andreussi, O., Brumme, T., ... Baroni, S., “Advanced capabilities for materials modelling with quantum espresso”, *Journal of Physics: Condensed Matter*, 29(46), pp. 465901(2017).
- [Giannozzi 2009] Giannozzi, P., Baroni, S., Bonini, N., ... Wentzcovitch, R. M., “Quantum espresso: a modular and open-source software project for quantum simulations of materials. *Journal of Physics: Condensed Matter*, 21(39), pp. 395502(1-19) (2009).
- [Gross 2013] Gross, E. K., & Dreizler, R. M. “Density functional theory”, (Vol. 337), Springer Science & Business Media(2013).
- [Kokalj2003] Kokalj, A., “Computer graphics and graphical user interfaces as tools in simulations of matter at the atomic scale”, *Computational Materials Science*, 28(2), pp. 155–168(2003).
- [Kong 2009] Kong, J., Zhu, H., Li, R., Luo, W., & Chen, X. (2009). “Carrier-mediated 1.55 μm photoluminescence from single Er³⁺ center in SnO₂ nanocrystals”, *Optics Letters*, 34(12), pp. 1873–1875 (2009).
- [Lang 1989] Lang, B., “Build-up and annealing of damage induced by ion and electron beams at SiO₂ surfaces: an AES study”, *Applied Surface Science*, 37, pp. 63–77(1989).
- [Lin 2014] Lin, T., Zhang, X., Lin, T., ... Chen, K., “Highly efficient near-infrared emission in Er³⁺ doped silica films containing size-tunable SnO₂ nanocrystals”, *Optics Express*, 22(1), pp. 369–376(2014).
- [Liu 2010] Liu, Q.-J., Liu, Z.-T., & Feng, L.-P., “First-principles calculations of structural, electronic and optical properties of tetragonal SnO₂ and SnO”, *Computational Materials Science*, 47(4), pp. 1016–1022(2010).
- [Ma 2011] Ma, C., Brik, M. G., Kiisk, V., Kangur, T., & Sildos, I., “Spectroscopic and crystal-field analysis of energy levels of Eu³⁺ in SnO₂ in comparison with ZrO₂ and TiO₂”, *Journal of Alloys and Compounds*, 509(8), pp. 3441–3451(2011).
- [Massella 2018] Massella D., “SiO₂-SnO₂:Er³⁺ planar waveguide: Computational and Optical assessment”, Master thesis, Department of Physics, University of Trento (2018).
- [Meneghetti 2016] Massella D., “Tin dioxide nanocrystals as Er³⁺ luminescence sensitizers: sol-gel fabrication of transparent glass-

ceramics and their characterization”, Master thesis, Department of Physics, University of Trento (2016).

[Momma 2011] Momma, K., & Izumi, F., “VESTA 3 for three-dimensional visualization of crystal, volumetric and morphology data”, *Journal of Applied Crystallography*, 44(6), pp. 1272–1276(2011).

[Morais 2002] Morais, E., José, S., Ribeiro, L., ... Messaddeq, Y. “Optical characteristics of Er^{3+} – Yb^{3+} doped SnO_2 xerogels”, *Journal of Alloys and Compounds*, 344(1), pp. 217–220 (2002).

[Rivera 2014] Rivera, R., Marcillo, F., Chamba, A., Puchaicela, P., & Stashans, A., “Quantum chemical study of point defects in tin dioxide”, *Transactions on Engineering Technologies*, Springer, Dordrecht, pp. 13–24 (2014).

[Santilli 1994] Santilli, C. V, Pulcinelli, S. H., Fernando, L., & Oliveira, C. De., “Spectroscopic characterization of SnO_2 gels”, *Journal of Sol-Gel Science and Technology*, 2(1-3), pp. 263-267 (1994), doi:10.1007/BF00486253.

[Schlipf 2015] Schlipf, M., & Gygi, F., “Optimization algorithm for the generation of oncv pseudopotentials”, *Computer Physics Communications*, 196, pp.36–44(2015).

[Setten 2018] Setten, M. J. van, Giantomassi, M., Bousquet, E., ... Rignanese, G.-M. “The pseudodojo: Training and grading a 85 element optimized norm-conserving pseudopotential table”, *Computer Physics Communications*, 226, pp. 39–54(2018).

[Shu 2013] Shu Sheng Pan, Siu Fung Yu, Yun Xia Zhang, Yuan Yuan Luo, Shuan Wang, Jun Min Xu, and Guang Hai Li, “Crystallite size-modulated exciton emission in SnO_2 nanocrystalline films grown by sputtering”, *Journal of Applied Physics*, 113, pp. 143104 (2013).

[Tiwari 2016] Tiwari, A., Gerhardt, R. A., & Szutkowska, M. “Advanced Ceramic Materials”, John Wiley & Sons(2016), doi:10.1002/9781119242598.

[Van 2015] Van T. T. T., Turrell S., Capoen B., Vinh L. Q., Cristini-Robbe O., Bouazaoui M., D’Acapito F., Ferrari M., Ristic D., Lukowiak A., Almeida R., Santos L., Kinowski C., “Erbium-Doped Tin-Silicate Sol-Gel-Derived Glass-Ceramic Thin Films: Effect of Environment Segregation on the Er^{3+} Emission”, *Science of Advanced Materials*, 7(2), pp. 301–308(2015), doi: 10.1166/sam.2015.2022.

[Yang 2003] Yang, W., & Ayers, P. W., “Density-functional theory”, *Computational Medicinal Chemistry for Drug Discovery*, pp. 103–132(2003).

[Zhou 2009] Weichang Zhou, Ruibin Liu, Qiang Wan, Qinglin Zhang, A. L. Pan, Lin Guo, and Bingsuo Zou, “Bound Exciton and Optical Properties of SnO₂ One-Dimensional Nanostructures”, J. Phys. Chem. C, 113, 1719–1726(2009).

Chapter 6 Photorefractivity investigation

6.1 Introduction

For different applications in laser photonics and integrated optics, refractive index-tailored materials are surely of great interest and play an important role in miniaturization of devices and fabrication of functional photonic structures such as complex gratings and waveguides. In case of some specific glasses, the refractive index is modified significantly and permanently through a non-elastic light-matter interaction, named photorefractivity. In this chapter, one will find a brief introduction to the photorefractivity and some examples of photorefractive glasses. Aiming to exploit this special property for the writing of the channels and mirrors in case of waveguide integrated laser, the photorefractive effect under the UV pulsed KrF excimer laser ($\lambda = 248$ nm) of $\text{SiO}_2\text{-SnO}_2\text{:Er}^{3+}$ glass-ceramics will be demonstrated. Moreover, the first results of gratings fabrication on the planar waveguide using the CW frequency doubled argon laser: $\lambda = 244$ nm will be also shown.

6.2 Background

6.2.1 Refractive index

When light enters a matter with an angle, it is refracted. How much the path of light is refracted in a material is determined by the index of refraction, i.e. refractive index denoted by n and described by the Snell law.

From the atomic scale, the refraction of light is related to the polarization of the molecules constituting the material. In nonmagnetic dielectric materials, a light with an electric field component E induces a dipole moment in each molecule:

$$p_k(\lambda) = \alpha_k(\lambda)E(\lambda) \quad (6.1)$$

where:

$E(\lambda)$ is the electric field component of the light at wavelength λ ;

k is the k^{th} kind of the molecules constituting the material;

$\alpha_k(\lambda)$ is the molecular polarizability of the k^{th} kind molecule which in fact is constructed by the polarizabilities of the constituent ions and bonds.

$p_k(\lambda)$ is the induced dipole moment of the k^{th} kind molecule under the external electric field $E(\lambda)$.

In a homogeneous medium, the relation between refractive index and the total polarizability of molecules constituting the material is expressed by Lorentz-Lorenz relation [Bonin 1997]:

$$\frac{n^2(\lambda)-1}{n^2(\lambda)+2} = \frac{4\pi}{3} \sum_k \frac{N_k \alpha_k(\lambda)}{V} \quad (6.2)$$

where $n(\lambda)$ is the refractive index of the material at the wavelength λ ;

N_k is the number of the k^{th} kind molecules;

α_k is the polarizability of the k^{th} kind molecules;

V is the volume of the material, strictly related to its density.

6.2.2 Photorefractivity

From relation (6.2), one can see that refractive index of a material depends on the polarizabilities of the constituent molecules and their density within the material. Any change of these two factors results in a refractive index change which can be either transient or permanent. Photorefractivity version to be covered in this thesis is the property of a material which changes its refractive index when it is exposed to light. The polarizability modification can be altered by changing of the structure of the material itself, e.g. the breaking of bonds or by the creation new phase or simply changing of the density in the material. The complexity and diversity of photorefractive manifestation have been an ongoing challenge for defining a mechanism for it. Varied glass composition, fabrication history and irradiation condition, e.g. irradiation source, power and frequency can induce varied photorefractive responses. Therefore, the specific origin of the photorefractivity needs to be discussed in a specified glass composition and irradiation condition. In the next section, this aspect will be revealed in the short review of photorefractivity of tin dioxide based glasses and glass-ceramics. One can find that although in the same binary material composed of tin dioxide and silica, the photorefractive responses are

completely different depending on the composition and irradiation condition.

6.2.3 Short review of photorefractivity of tin dioxide - silica glasses and glass-ceramics

Briefly, the potential of tin dioxide for photorefractivity was first realized in tin-codoped germanosilicate [Dong 1995b] and phosphosilicate [Dong 1995a], [Laurence 1997], optical fibers. By introducing tin in such silicate glasses, the strong photorefractive gratings with enhanced photorefractivity up to $\sim 1.2\text{-}1.4 \times 10^{-3}$ was obtained. These results led the numerous researches on developing only tin-doped silica and exploiting its photorefractivity.

6.2.3.1 Photorefractivity of tin-doped silica glasses

One of the first photorefractivity measurements on tin-single-doped silica glasses was reported on $\text{SnO}_2\text{:SiO}_2$ optical fibres produced by modified chemical vapor deposition (MCVD) [Brambilla 2000]. However, due to the SnO_2 volatilization during the high temperature preparation of MCVD, the content of SnO_2 in SiO_2 matrix was limited to 0.15 mol%. Despite the low tin-doped content, a positive refractive index change of 3×10^{-4} was achieved and it was comparable with the one of 10% mol GeO_2 doped silica optical fibres under the same condition of 248 nm UV pulse irradiation (cumulative dose of 20 kJ/cm^2 , pulse fluency of 80 mJ/cm^2 and repetition rate of 20 Hz).

The microstructure was demonstrated to be involved in photorefractivity of tin-doped silica bulk samples with different tin contents explored in [Chiodini 2001], [Chiodini 2002], [Chiodini 2003a], [Chiodini 2003b]. Concerning the tin-doped silica glasses [Chiodini 2001], the very small content of tin (between 0.4 and 0.5 mol%) was introduced into silica to support the formation of only diluted tin substituting for silicon in SiO_2 matrix without any segregation of SnO_2 nanocrystals. In this case, the substitutional tin-doped silica glasses were obtained, and these glasses have a positive refractive index change. It is also found that by increasing tin content higher than 0.5 mol%, a segregation of SnO_2 nanocrystals occurred and formed the tin-silicate glass-ceramic composites [Chiodini 2002a]. In the work [Chiodini 2001], the 0.5

mol% SnO₂ thin film showed the presence of doping-related oxygen deficient centers (ODC's) absorption band (around 5 eV ~ 248nm) while the 0.4 mol% SnO₂ thin film did not. After 5000 pulses (fluency: 34 mJ/cm² and frequency: 10Hz) of 266 nm UV irradiation, the detectable ODC 0.5 mol% SnO₂ thin film exhibited a positive refractive index change (Δn) at 980nm of around 2×10^{-4} , twice less than the 0.4 mol% SnO₂ one with 4×10^{-4} . Therefore, the laser induce bleaching of the ODC absorption band was proved to be unessential for the photorefractivity of the thin films. Indeed, the structural units involved in the photorefractive process were suggested to be the substitutional Sn-(SiO₄)_n rings, of which the dimensions were reduced during UV exposure. And, this was suggested to be the main factor governing the photorefractive response of the tin-doped silica glasses [Chiodini 2001].

6.2.3.2 Photorefractivity of tin dioxide-silica glass ceramics

Chiodini et.al. found that by increasing tin content higher than 0.5 mol%, a segregation of SnO₂ nanocrystals occurred and formed the tin-silicate glass-ceramic composites [Chiodini 2002a]. Contrary to the tin-doped silica glasses, the glass-ceramics have negative refractive index change and the mechanism induced the negative refractive index change was proven to be related to the surface modification of SnO₂ nanoclusters and consequently decreased their crystalline size. After 1000 pulses (fluency of 150 mJ/cm² and frequency of 10 Hz) of 266nm UV irradiation, 5 mol% SnO₂ glass ceramic sample showed the refractive index change $\Delta n = - 6 \times 10^{-4}$.

The photorefractivity was also explored on SiO₂-SnO₂ doped with Eu³⁺ planar waveguides after the irradiation using CW UV laser (at 266nm) [Bhaktha 2010] and KrF excimer laser (at 248nm) [Berneschi 2010], [Lukowiak 2017]. In Ref [Berneschi 2010], [Lukowiak 2017], the photorefractivity measurements were performed on the 25 mol% SnO₂. After a cumulative dose of 7.6 kJ/cm², using a 248nm KrF excimer laser pulse with frequency of 10 Hz, the refractive index change was negative with a saturated value of $- 1.5 \times 10^{-3}$ at 1550 nm (absolute value). Indeed, the first cumulative dose of 1.5 kJ/cm² was acquired with the pulse fluency of 38mJ/cm² and the rest was with 76 mJ/cm² to reach the mentioned saturated Δn . Based on the differential Lorentz-Lorenz formula, the two factors, volume expansion and polarizability were demonstrated to contribute to the change of refractive index.

From all the mentioned works, the photorefractivity of $\text{SiO}_2\text{-SnO}_2$ glasses and glass-ceramics have shown the refractive index change applicability for efficient top-down fabrication of channel waveguides and Bragg gratings. Therefore, based on the interest of the integrated lasers, the photorefractivity of $\text{SiO}_2\text{-SnO}_2$ planar waveguides and monoliths doped with Er^{3+} is assessed to provide sufficient data for the device design which will be discussed in Chapter 7 . Moreover, the fabrication of gratings exploiting the photorefractivity of $\text{SiO}_2\text{-SnO}_2$ is also targeted.

6.3 Photorefractivity measurement

6.3.1 Experimental setup and characterization techniques

6.3.1.1 Setup schematic

The photorefractivity under UV irradiation was explored by using an KrF excimer laser (Lambda Physik Compex 110, Coherent Inc., Santa Clara, CA, USA), which emits at 248 nm. Figure 6.1 shows the setup scheme for the UV irradiation.

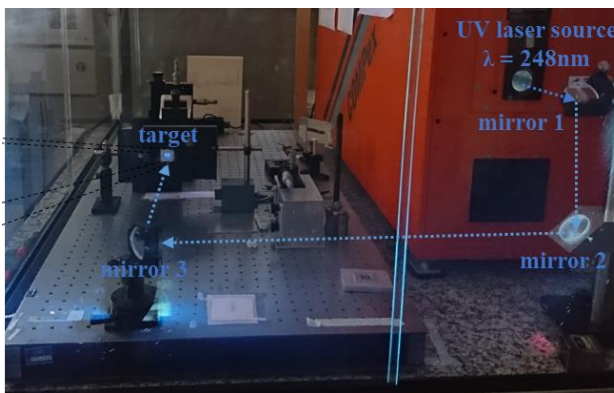


Figure 6.1 The experimental setup of the UV irradiation for the photorefractivity measurements

After successive reflections through a series of three mirrors, the laser beam reaches the target section. This is represented by a black metal

panel, on which a square slit of around $1\text{ cm} \times 1\text{ cm}$ has been made. The sample surface was masked with an aluminum sheet, having a square aperture with a size close to that of the slit adopted for the UV irradiation. The specimen was positioned and fixed on the back of the black panel (with respect to the laser beam inlet direction), taking care to align these two masks (the one of the UV irradiations on the panel and that represented by the aluminum sheet on the sample).

Figure 6.2 shows the photos of the sample preparation and the target section of the UV irradiation on the planar waveguides. The aluminum mask on the planar waveguide serves principally to delimit the coupling area during the effective index measurement by means of prism coupling technique which will be discussed afterwards. In fact, the irradiated region is close to the area of the coupling face of the prism. This reduces the uncertainty related to the position of the coupling point during the measurement.

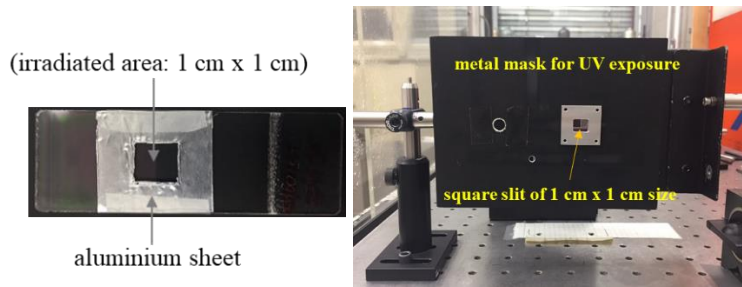


Figure 6.2 The photos of the masked planar waveguide and the target section for the UV irradiation

Two different compositions of glass-ceramic planar waveguides were employed for the photorefractivity investigation: $70\text{SiO}_2\text{-}30\text{SnO}_2\text{:}0.5\text{Er}^{3+}$ and $80\text{SiO}_2\text{-}20\text{SnO}_2\text{:}0.5\text{Er}^{3+}$. The used UV irradiation condition for the planar waveguides is the pulse fluency of 30 mJ/cm^2 . For both samples, the first cumulative of 22.5 J/cm^2 was achieved with pulse frequency of 10 Hz . Afterwards, the pulse frequency of 50 Hz was employed to reach the final cumulative dose of 9 kJ/cm^2 for ensuring that the saturated effective index change of the samples was obtained. For the mode effective index measurements supported by the planar waveguides, a home-made instrument developed in IFAC-CNR and based on prism coupling technique, with a nominal resolution on the measured effective refractive index of about 5×10^{-5} , was employed to test the guiding properties of the planar waveguides before and after

each UV exposure. Before the UV irradiation, a statistical measurement on the effective refractive index of the modes supported by the planar waveguide were performed at different wavelengths. The measurements were repeated 7 times by removing and inserting the sample in the coupling region with the prism. In this way, the standard deviation on the mode effective index measurement was determined to be: 7×10^{-5} and 2×10^{-4} at 635 nm and 1550 nm, respectively for $70\text{SiO}_2\text{-}30\text{SnO}_2\text{:}0.5\text{Er}^{3+}$; and 2×10^{-5} and 2×10^{-4} at 635 nm and 1550 nm, respectively for $80\text{SiO}_2\text{-}20\text{SnO}_2\text{:}0.5\text{Er}^{3+}$. This difference on the uncertainty of the mode effective index measurement at the two wavelengths of interest can be attributed to the broadening of the mode linewidth at the wavelength of 1550 nm due to the absorption of the erbium ions.

For the $95\text{SiO}_2\text{-}5\text{SnO}_2\text{:}0.5\text{Er}^{3+}$ monolith, the sample is simply attached to a sample holder and placed at the target section as shown in Figure 6.3. The UV irradiation condition, for the monolith case, are the following: 20 Hz as pulse frequency; 17 mJ/cm² as pulse fluency and 3.264 kJ/cm² as cumulative dose.

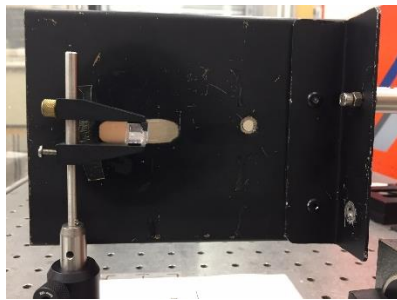


Figure 6.3 The photos of the masked planar waveguide and the target section for the UV irradiation

6.3.1.2 Characterization techniques

After the last exposure, the planar waveguides were characterized with different techniques. The UV absorption spectra were performed by means of Cary Varian 5000 spectrometer with resolution of 1 nm. The surface morphology of the planar waveguides was also scoped by Solver P47H and Solver Pro SPM atomic force microscopy (AFM). The X-ray diffraction patterns were acquired using X'PERT PRO diffractometer equipped with a Cu X-ray tube. The absorption spectra and XRD patterns of the monolith were also acquired to understand more the

photorefractive effect on $\text{SiO}_2\text{-SnO}_2\text{:Er}^{3+}$ glass-ceramics. Moreover, to check the structural modification, the micro-Raman spectra were also acquired using Labram Aramis (Horiba Jobin-Yvon) equipped with an optical microscope and a 100 \times objective and a He-Ne laser source of 632 nm as the excitation source.

6.3.2 Results and discussion

6.3.2.1 Measured effective index of the planar waveguides

6.3.2.1.1 70SiO₂-30SnO₂:0.3Er³⁺ planar waveguide

Figure 6.4 shows the change of effective index of the 70SiO₂-30SnO₂:0.5Er³⁺ planar waveguide as a function of the cumulative dose of the UV irradiation for the fundamental mode at the wavelength of 1550 nm. One can see from the figure that the effective index change of the 70SiO₂-30SnO₂:0.5Er³⁺ planar waveguide is negative. The 30 mol% SnO₂ glass-ceramic planar waveguide had a very fast photorefractive response, after the first dose of 0.003 kJ/cm², the effective index already had a significant change of -1.1×10^{-3} . And, the effective index change reached its saturated value just after 0.3 kJ/cm².

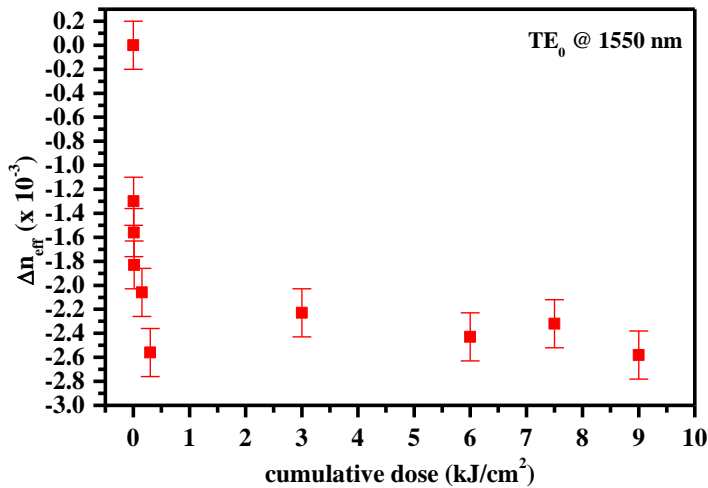


Figure 6.4 The effective index changes for the TE₀ modes supported by the 70SiO₂-30SnO₂:0.5Er³⁺ planar waveguide at the wavelength of 1550 nm as a function of cumulative dose

The change of the effective index of the 70SiO₂-30SnO₂:0.5Er³⁺ planar waveguide can be revealed from the pattern of the TE₀ mode at the wavelength of 1550 nm before UV irradiation and after 1st UV irradiation with cumulative dose of 0.003 kJ/cm² and after 10th UV irradiation with cumulative dose of 0.3 kJ/cm² in Figure 6.5.

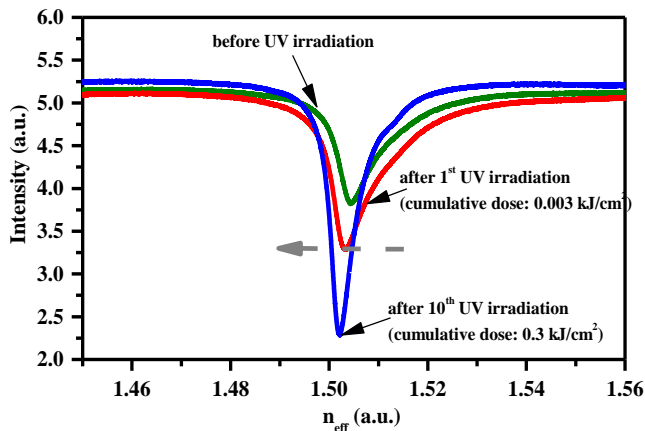


Figure 6.5 The shift to lower values of TE₀ mode at the wavelength of 1550 nm of the 70SiO₂-30SnO₂:0.5Er³⁺ before UV irradiation and after 1st UV irradiation with cumulative dose of 0.003 kJ/cm² and after 10th UV irradiation with cumulative dose of 0.3 kJ/cm²

The effective index changes of the TE modes at 635 nm of the 70SiO₂-30SnO₂:0.5Er³⁺ planar waveguide were also measured. Figure 6.6 shows the patterns of the 635 nm -TE modes before UV irradiation and after 1st UV irradiation with cumulative dose of 0.003 kJ/cm², and after 14th UV irradiation with cumulative dose of 9.0 kJ/cm². The negative effective index changes of the 635 nm -TE modes are revealed by the shift to lower values as also shown in Figure 6.6.

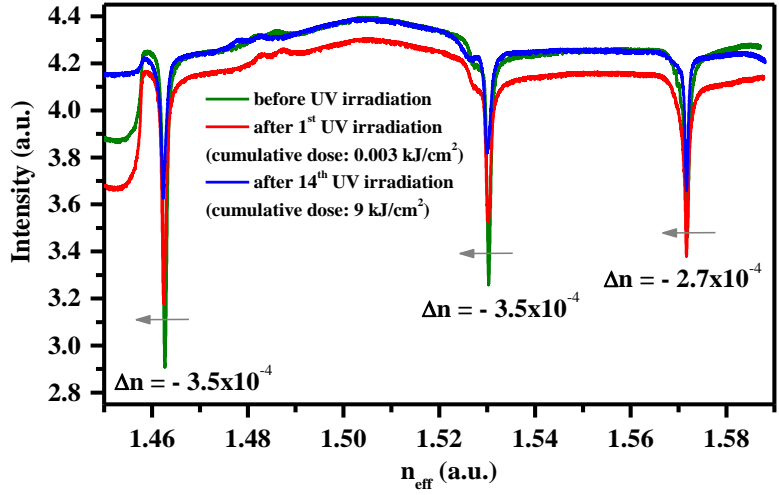


Figure 6.6 The shift to lower values of the 635 nm TE modes of the 70SiO₂-30SnO₂:0.5Er³⁺ planar waveguide before UV irradiation and after 1st UV irradiation with cumulative dose of 0.003 kJ/cm² and after 14th UV irradiation with cumulative dose of 9.0 kJ/cm²

The overall effective index change of the fundamtenal TE₀ modes of the 70SiO₂-30SnO₂:0.5Er³⁺ planar waveguide are summarized in Table 6.1. From the table, one can see that the effective index changes exhibit spectral dependence behavior: higher effective index change at 1550 nm and smaller at 635 nm. A possible explanation for this spectral dependence of the effective index change will be discussed in the section 6.3.2.4.

Table 6.1 The overall effective index change of the 70SiO ₂ -30SnO ₂ :0.5Er ³⁺ planar waveguide after UV irradiation (cumulative dose of 9 kJ/cm ²)	
Wavelength (nm)	Δn_{eff}
635 nm	$-(0.35 \pm 0.07) \times 10^{-3}$
1550 nm	$-(2.60 \pm 0.20) \times 10^{-3}$

6.3.2.1.2 80SiO₂-20SnO₂:0.3Er³⁺ planar waveguide

A negative effective index change of the fundamental mode TE₀ at the wavelength of 1550 nm is also observed in the 80SiO₂-20SnO₂:0.3Er³⁺ planar waveguide as shown in Figure 6.7. The fast effective index change of 20 mol% SnO₂ glass-ceramic planar waveguide was also observed. After the first dose of 0.003 kJ/cm², the effective index had a significant decrease of -0.7×10^{-3} . And, after the cumulative dose of only 0.3 kJ/cm², it reached rapidly the value of -1.6×10^{-3} which is very close to its saturated effective index change of -2.10×10^{-3} . From Figure 6.8, one can see the shift of the 1550 nm TE₀ mode of the 80SiO₂-20SnO₂:0.5Er³⁺ planar waveguide before UV irradiation and after 1st UV irradiation with cumulative dose of 0.003 kJ/cm², and after 14th UV irradiation with cumulative dose of 0.3 kJ/cm².

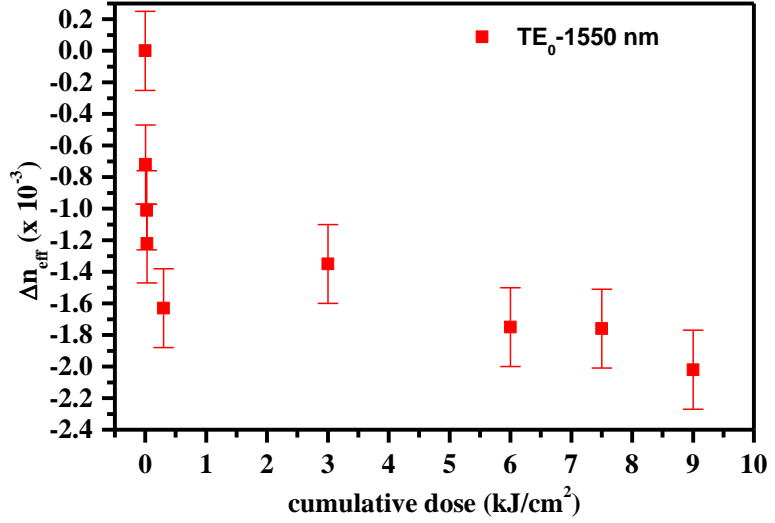


Figure 6.7 The effective index changes for the TE₀ mode supported by the 80SiO₂-20SnO₂:0.5Er³⁺ planar waveguide at the wavelength of 1550 nm as a function of cumulative dose

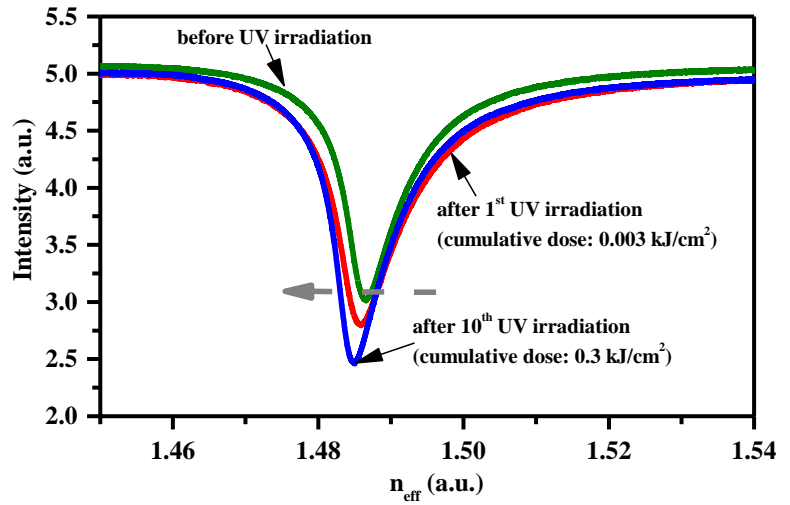


Figure 6.8 The shift to lower values of TE₀ mode at the wavelength of 1550 nm of the 80SiO₂-20SnO₂:0.5Er³⁺ before UV irradiation and after 1st UV irradiation with cumulative dose of 0.003 kJ/cm² and after 10th UV irradiation with cumulative dose of 0.3 kJ/cm²

The patterns and the changes of the effective indices of the 635 nm TE modes of the $80\text{SiO}_2\text{-}20\text{SnO}_2\text{:}0.5\text{Er}^{3+}$ planar waveguide are shown in Figure 6.9. Comparing with the effective index change of the 1550 nm TE_0 mode, the effective index changes of the 635 nm TE modes are also smaller with only -2.8×10^{-4} . In other words, this 20 mol% SnO_2 planar waveguide also exhibits a spectral dependence for the effective index change.

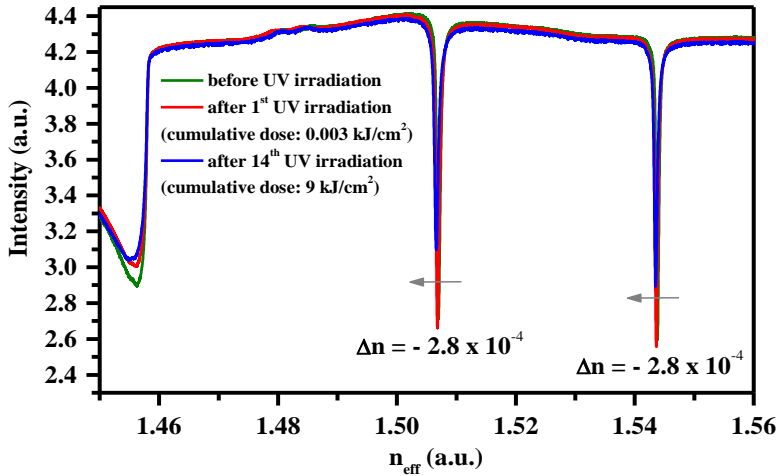


Figure 6.9 The shift to lower values of the 635 nm TE modes of the $80\text{SiO}_2\text{-}20\text{SnO}_2\text{:}0.5\text{Er}^{3+}$ planar waveguide before UV irradiation and after 1st UV irradiation with cumulative dose of 0.003 kJ/cm^2 , and after 14th UV irradiation with cumulative dose of 9.0 kJ/cm^2

The overall effective index changes of the fundamental TE_0 modes at the wavelengths of 635 nm and 1550 nm after reaching saturated values are summarized in Table 6.2. A comparison between the 30 mol % and 20 mol% planar waveguides shows that both samples exhibit a spectral dependence for the effective index change: lower at 635 nm (in the order of 10^{-4}) and higher at 1550 nm (in the order of 10^{-4}). Furthermore, the higher SnO_2 content leads to higher effective index change, i.e. higher photorefractivity.

Table 6.2 The overall effective index change of the 80SiO ₂ -20SnO ₂ :0.5Er ³⁺ planar waveguide after UV irradiation (cumulative dose of 17 kJ/cm ²)	
Wavelength (nm)	Δn_{eff}
635 nm	$-(0.28 \pm 0.04) \times 10^{-3}$
1550 nm	$-(2.00 \pm 0.20) \times 10^{-3}$

6.3.2.2 Calculated refractive index of the planar waveguides

6.3.2.2.1 Method

The effective indices of first two TE₀ and TE₁ modes at 635 nm allow defining the refractive indices of the planar waveguides before and after UV irradiation based on the dispersion equation [Ulrich 1973] for a step-index model planar waveguide:

For TE polarization

$$\omega(n_f, n_m) = \frac{\lambda}{2\pi\sqrt{n_f^2 - n_m^2}} \left[m\pi + \tan^{-1} \left(\frac{\sqrt{n_m^2 - n_o^2}}{\sqrt{n_f^2 - n_m^2}} \right) + \tan^{-1} \left(\frac{\sqrt{n_m^2 - n_s^2}}{\sqrt{n_f^2 - n_m^2}} \right) \right] \quad (6.3)$$

where m is the mode order: $m = 0$ (fundamental mode), 1, 2, 3, ...;

$n_o = 1$ is the refractive index of the air;

n_f is the refractive index of the thin film;

n_m is the effective index at m -order mode;

n_s is the refractive index of the substrate: $n_s = 1.4575$ at 635 nm;

The approach used here is to plot the value of $\omega(n_f, n_m)$ for the TE₀ and TE₁ as a function of n_f in a certain range following the equation (6.3). The coordination of the cross point of the two the functions $\omega(n_f, n_m)$ for TE₀ and TE₁ modes are in fact the the refractive index and thickness of the planar waveguide. An example of defining the refractive index at 635 nm and thickness of the 70SiO₂-SnO₂:0.5Er³⁺ based on the measured refractive index is demonstrated in Figure 6.10. In addition, with the obtained value of the thickness, the refractive indices at 1550 nm of the

70SiO₂-SnO₂:0.5Er³⁺ and 80SiO₂-SnO₂:0.5Er³⁺ were also derived. The obtained values are shown in Table 6.3.

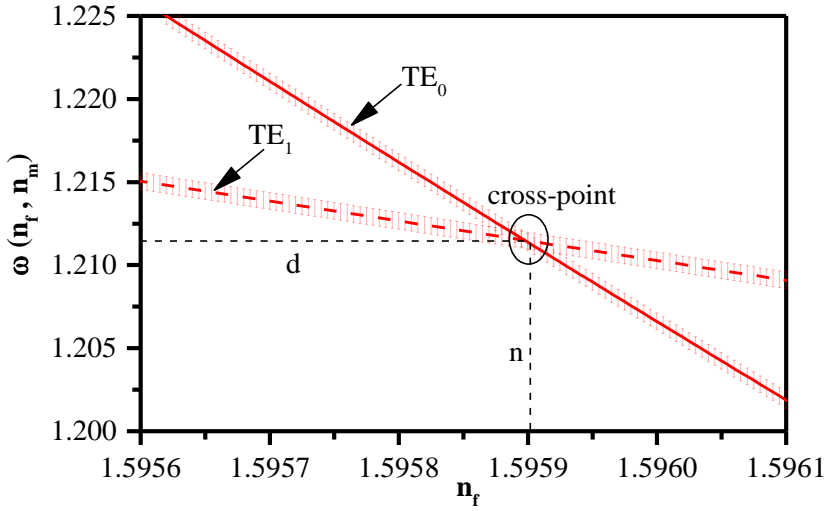


Figure 6.10 Graphic solution for defining the refractive index of the 70SiO₂-30SnO₂:0.5Er³⁺ planar waveguide before and after the final UV irradiation using (6.3)

6.3.2.2.2 Results

Table 6.3 tabulates the calculated refractive indices at the wavelengths of 635 and 1550 nm of the 70SiO₂-30SnO₂:0.5Er³⁺ and 80SiO₂-20SnO₂:0.5Er³⁺ planar waveguides before and after UV irradiation (cumulative dose of 9.0 kJ/cm²) and the corresponding refractive index changes. From the results, one can see that the values of calculated refractive index changes are approximately equal to the measured effective index changes. The results confirm again the spectral dependence of the refractive index change of the SiO₂-SnO₂ glass-ceramics: smaller at 635 nm (in range of 10⁻⁴) and higher at 1550 nm (in range of 10⁻³). Higher content of SnO₂ leads to higher photorefractivity: refractive index change at 1550 nm is $-(2.8 \pm 0.2) \times 10^{-3}$ for 30 mol% SnO₂ planar waveguide and $-(2.3 \pm 0.2) \times 10^{-3}$ for the 20 mol% SnO₂ planar waveguide.

Table 6.3 The calculated refractive indices at the wavelengths of 635 and 1550 nm of the 70SiO ₂ -30SnO ₂ :0.5Er ³⁺ and 80SiO ₂ -20SnO ₂ :0.5Er ³⁺ planar waveguides before and after UV irradiation (cumulative dose of 9 kJ/cm ²) and the corresponding refractive index changes			
70SiO ₂ -30SnO ₂ :0.5Er ³⁺ planar waveguide			
Wavelength (nm)	n _{before}	n _{after}	Δn
635 nm	1.58590	1.58561	- (0.00029 ± 0.00007)
1550 nm	1.5566	1.5538	- (0.0028 ± 0.0002)
80SiO ₂ -20SnO ₂ :0.5Er ³⁺ planar waveguide			
635 nm	1.55627	1.55599	- (0.00028 ± 0.00002)
1550 nm	1.5319	1.5294	- (0.0023 ± 0.0002)

6.3.2.3 Characterization of the irradiated samples

To understand the photorefractive effect, the XRD, Raman spectroscopy, absorption and AFM analysis were performed on the 70SiO₂-30SnO₂:0.5Er³⁺ planar waveguide before and after UV irradiation. In case of the monolith, the absorption spectra are acquired for the sample before and after irradiation. However, XRD patterns are performed on the front and back face referring to the laser beam penetration path of the irradiated monolith. Although the refractive index of the 95SiO₂-5SnO₂:0.5Er³⁺ monolith has not experimentally measured, from the characterization, the photorefractive effect is still revealed based on the same photorefractive response compared with the 70SiO₂-30SnO₂:0.5Er³⁺ planar waveguide. In addition, based on the overview discussed in 6.2.3, with 5 mol% SnO₂, the refractive index change of the monolith is expected to be negative as other SiO₂-SnO₂ glass-ceramics.

6.3.2.3.1 AFM

To check the effect of UV irradiation on the surface morphology of the sample, AFM images are acquired on the 70SiO₂-30SnO₂:0.5Er³⁺ planar waveguide before and after irradiation as shown in Figure 6.11.

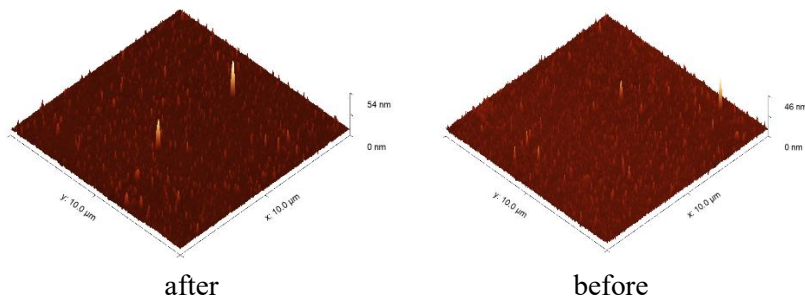


Figure 6.11 3D AFM images of the surface of the 70SiO₂-30SnO₂:0.5Er³⁺ planar waveguide before and after UV irradiation

Both images show a uniform distribution of SnO₂ nanocrystals appearing on the surface. The measured surface roughnesses of the sample are listed in Table 6.4. Although the root mean square roughness of the 70SiO₂-30SnO₂:0.5Er³⁺ planar waveguide after UV irradiation is slightly smaller in comparison with the one before UV irradiation, the average roughness remains unchanged. In other words, AFM images does not reveal a remarkable change related to the decomposition of SnO₂.

Table 6.4 The roughness of the 70SiO ₂ -30SnO ₂ :0.5Er ³⁺ planar waveguide before and after UV irradiation		
Sample	Root mean square roughness RMS (nm)	Average roughness (R _a : nm)
Before	1.8 ± 0.7	0.8 ± 0.6
After	1.4 ± 0.6	0.8 ± 0.6

6.3.2.3.2 XRD

Figure 6.12 and Figure 6.13 show XRD patterns performed on the irradiated planar waveguide and monolith respectively. Since the size of SnO₂ nanocrystals is very small (< 6 nm) in the two systems as shown in Chapter 4 the XRD patterns are employed to check if there is any significant change in SnO₂ crystallization. In fact, from Figure 6.12, one can see no big difference of the XRD patterns of the 70SiO₂-30SnO₂:0.5Er³⁺ planar waveguide before and after UV irradiation.

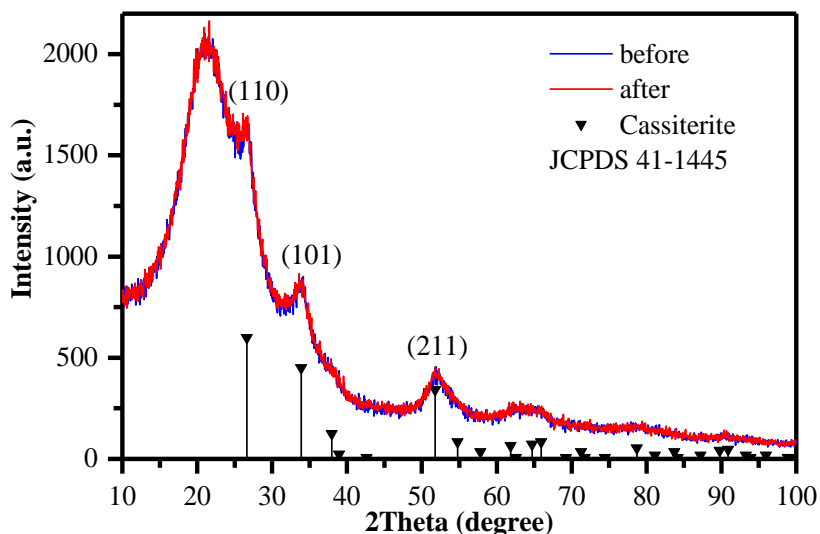


Figure 6.12 XRD patterns of the 70SiO₂-30SnO₂:0.5Er³⁺ planar waveguide before and after UV irradiation, indexed as SnO₂ Cassiterite (JCPDS 41-1445)

Due to the volume aspect of a bulk material, it is sufficient to check the effect of UV irradiation by comparing the XRD patterns of the front and back face of the irradiated monolith shown in Figure 6.13. One should disregard the background of the two patterns because it is strongly affected by the different surface geometry of the two faces. An attempt on checking the Scherrer formula-calculated size of SnO₂ nanocrystals using the FWHM of the diffraction peaks was made and listed in Table 4.1 indicating no noticeable reduction of SnO₂ nanocrystals.

However, due to the high error of XRD measurements on small nanosized crystals, the indication of reduced SnO₂ crystallization from this technique needs to be discussed in combination of the other techniques, e.g. AFM and absorption spectra.

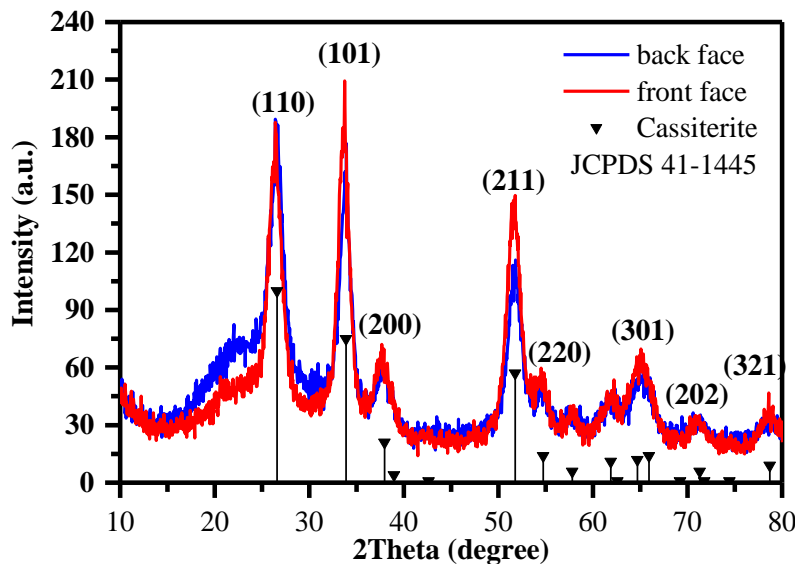


Figure 6.13 XRD patterns of the 95SiO₂-5SnO₂:0.5Er³⁺ monolith in the front side and back side, indexed as SnO₂ Cassiterite (JCPDS 41-1445). Front face is the face where the laser beam incidents

Table 6.5 The calculated average size using Scherrer formula of SnO ₂ nanocrystals in the front face and back face of the irradiated monolith				
Plane (hkl)	Front face		Back side face	
	FWHM (degree)	d _{hkl} (nm)	FWHM (degree)	d _{hkl} (nm)
(110)	1.64187	5.35	1.51711	5.49
(101)	1.30645	7.24	1.04465	7.16
(211)	1.80700	7.02	1.60549	7.00
Average size (nm)	6.5 ± 0.7		6.6 ± 0.7	

6.3.2.3.3 Absorption

Figure 6.14 shows the absorption spectra in UV-Vis range of the planar waveguide before and after UV irradiation. In the UV absorption range of Figure 6.14a), there is no observable change of absorption band edge like in the case of SiO₂-SnO₂:Eu³⁺ planar waveguides in the work

[Berneschi 2010]. However, Figure 6.14b shows a change in the oscillating profile of the absorbance which indicates a change either in refractive index or thickness or both. In case there is a change of the thickness, this change must be small so that it is not sufficient to induce an observable absorbance change in the absorption band edge.

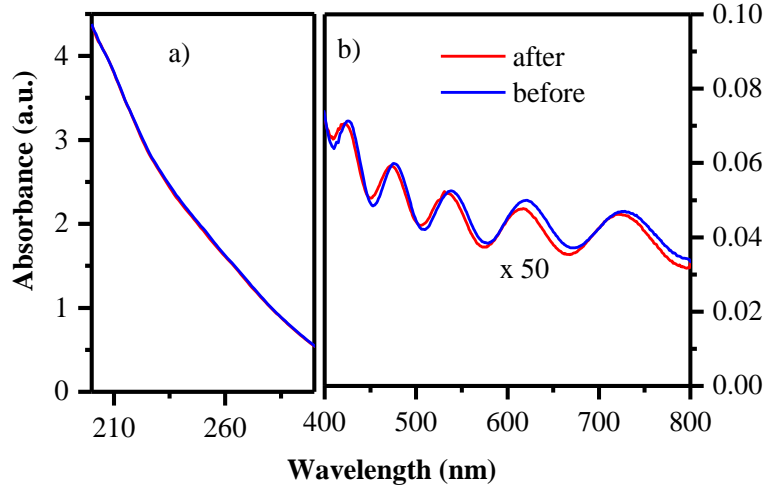


Figure 6.14 Absorption spectra of the $70\text{SiO}_2\text{-}30\text{SnO}_2\text{:}0.5\text{Er}^{3+}$ planar waveguide before and after UV irradiation

Referring to the monolith, a decrease in absorption coefficient is observed from absorption edge in the range 350 - 375 nm as one can see in Figure 6.15. This change can be related to a small reduction of SnO_2 crystallization which could not be scoped by means of XRD due to the high error of XRD measurements on small nanosized crystals. The relation between the absorption and refractive index change will be discussed with detail in the next subsection 6.3.2.3.4.

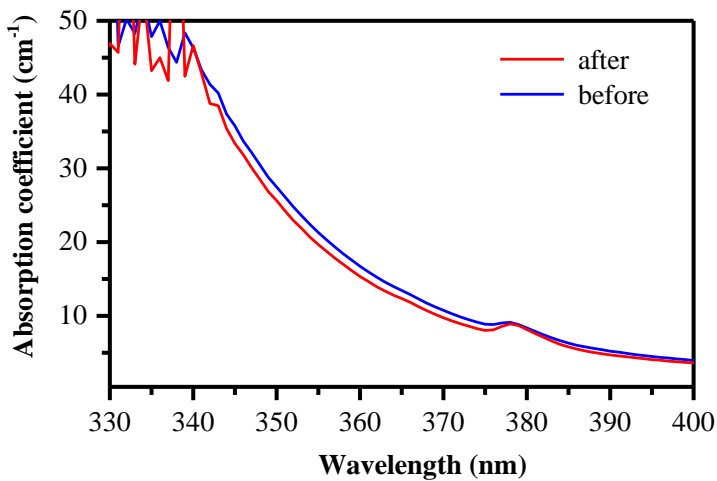


Figure 6.15 Absorption spectra of the $95\text{SiO}_2\text{-}5\text{SnO}_2\text{:}0.5\text{Er}^{3+}$ monolith before and after UV irradiation

6.3.2.3.4 Mirco-Raman

Figure 6.16 shows the Raman spectra of the $95\text{SiO}_2\text{-}5\text{SnO}_2\text{:}0.5\text{Er}^{3+}$ monolith before and after UV irradiation with cumulative dose of 3.264 kJ/cm^2 . From these spectra, one can see that the irradiated monolith exhibits all the Raman features of the monolith before irradiation but there is contribution of a strong fluorescence background to the Raman spectrum of the irradiated sample. In the irradiated planar waveguides, Raman spectra were also performed and revealed a strong fluorescence background. The presence of this fluorescence background in Raman spectra was also observed in UV-irradiated tin-silica films fabricated by MCVD method in the work [Chen 2004] and the authors suggested that it is due to the breaking of Sn-related network bonds [Chiodini 2000].

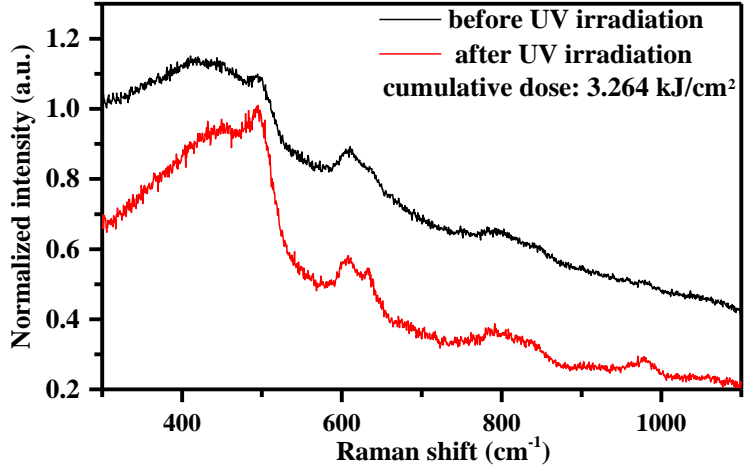


Figure 6.16 Raman spectra of the 95SiO₂-5SnO₂:0.5Er³⁺ monolith before and after UV irradiation with cumulative dose of 3.264 kJ/cm²

6.3.2.4 Discussion on photorefractive effect

To understand the photorefractive response of the SiO₂-SnO₂:Er³⁺ glass-ceramic planar waveguides in this work, the deviation form of Lorentz-Lorenz equation (6.2) is used with an assumption that the change of the material volume does not induce a change of the molecular polarizability of the material:

$$\frac{\Delta n}{n} = \frac{(n^2 - 1)(n^2 + 2)}{6n^2} \left(-\frac{\Delta V}{V} + \frac{\Delta \alpha}{\alpha} \right) \quad (6.4)$$

where n is the refractive index of the material; α is the mean molecular polarizability of the material; and V is the volume of the material and in the planar waveguides: $\frac{\Delta V}{V} = \frac{\Delta d}{d}$ with d is the thickness of the planar waveguide.

From equation (6.4), one can think first that the negative refractive index change of the SiO₂-SnO₂:Er³⁺ glass-ceramic planar waveguides is a consequence of a volume expansion which in fact was observed in our prior work [Lukowiak 2017] on SiO₂-SnO₂:Eu³⁺ glass-ceramic planar waveguides. However, the causes inducing the volume expansion and

the structural factors originating the photorefractive response of in the SiO₂-SnO₂ glass-ceramics were not well-reported. Nevertheless, if the refractive index change is a result of only the volume expansion, based on equation (6.4) the following condition should valid for all the wavelengths:

$$\frac{\Delta n}{n} \frac{6n^2}{(n^2 - 1)(n^2 + 2)} = -\frac{\Delta d}{d} = \text{const} \tan t \quad (6.5)$$

From (6.5), the refractive index changes should be comparable for the two wavelengths of 635 nm and 1550 nm. However, it is not the case of the SiO₂-SnO₂:Er³⁺ glass-ceramic planar waveguides since there is the observed spectral dependence of the refractive index change. Moreover, the big difference (with a factor of 10) between the refractive index change at 635 nm and 1550 nm indicates that the material polarizability change is the real cause of the refractive index change as also suggested in the works [Lukowiak 2017] and [Berneschi 2010]. Therefore, this work focused on the investigation of the structural modification which can explain for the negative refractive index change in the SiO₂-SnO₂ glass-ceramics.

Since the obtained refractive index change is negative, there is a possibility of the decomposition of SnO₂ nanocrystals. In the works [Chiodini 2003b], [Chiodini 2002a], the authors suggested that the laser beam at 266 nm (4.7 eV) induced the modification of the nanosized crystalline part of SnO₂ and decreased their crystalline size. However, concerning the irradiated planar waveguide, as discussed in 6.3.2.3.1 the XRD patterns and AFM images show no remarkable change of SnO₂ crystallinity either in the bulk or on the surface of the planar waveguide. In case of the irradiated monolith, this decomposition effect of SnO₂ nanocrystals induced by UV irradiation is implied only by the reduction of absorption edge coefficient in Figure 6.15. This change if present can originate the polarizability change and consequently change the refractive index. The change of absorption can be correlated to the refractive index change using the complex refractive index:

$$\tilde{n}(\lambda) = n(\lambda) + ik(\lambda) \quad (6.6)$$

where $\tilde{n}(\lambda)$ is complex refractive index;

$n(\lambda)$ is the real refractive index;

and $\kappa(\lambda)$ is the extinction coefficient, which relates to absorption coefficient as follows: $\alpha(\lambda) = \frac{4\pi\kappa(\lambda)}{\lambda}$.

Moreover, according to Kramers-Kronig relation, the real refractive index $n(\lambda)$ relates to the extinction coefficient, i.e. absorption as follows:

$$n(\lambda) - 1 = \frac{1}{2\pi} \int_0^{\infty} \frac{\lambda' \kappa(\lambda') d\lambda'}{\lambda^2 - \lambda'^2} \quad (6.7)$$

Based on the relation (6.7), one can see that any change of the absorption results in the change of refractive index. In addition, this relation can be used to explain the spectral dependence of the refractive index change at 635 nm and 1550 nm since there is absorption of Er^{3+} at 1550 nm.

On the other hand, the observed fluorescence background in the Raman spectra of the irradiated monoliths from Figure 6.16, and also in the planar waveguides indicates another possible factor attributing to the polarizability change of $\text{SiO}_2\text{-SnO}_2\text{:Er}^{3+}$ glass-ceramics: breaking Sn-related network bonds [Chen 2004], [Chiodini 2000].

Last but not least, the photorefractivity measurements show that higher SnO_2 content leads to a higher refractive index change. This is because there are photorefractive centers derived by SnO_2 in the $\text{SiO}_2\text{-SnO}_2$ glass ceramics [Chiodini 2002a]. This behavior was also observed in [Gaff 2000] in the germanium-free tin doped silica thin films were deposited by helicon activated reaction evaporation process (HARE).

6.4 Inscription of gratings

Exploiting the photorefractivity, gratings were fabricated on the $70\text{SiO}_2\text{-}30\text{SnO}_2\text{:}0.5\text{Er}^{3+}$ planar waveguide layer employing a CW frequency doubled argon laser: $\lambda = 244$ nm with a writing fluence of 1 kJ/cm^2 . Using a $\sim 5 \text{ }\mu\text{m}$ MFD (Mode-field diameter) spot, the gratings formed with $5 \mu\text{m}$ pitch raster pattern over $4 \times 4 \text{ mm}^2$ area were fabricated on a small piece of the sample as shown in Figure 6.17. One can see the colors due to the interference patterns scattering from the gratings based on the Bragg law.

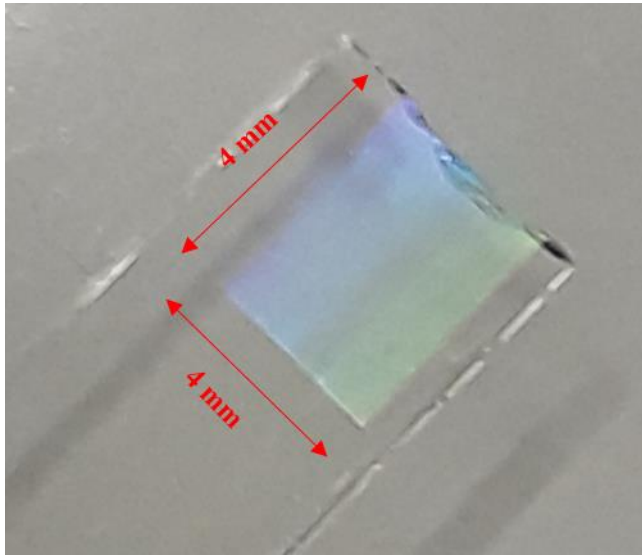


Figure 6.17: The image of the gratings fabricated by CW frequency doubled argon laser: $\lambda = 244$ nm

However, under this irradiation condition of the CW frequency doubled argon laser ($\lambda = 244$), the obtained variation of the refractive index in the gratings structure is positive and this is still under investigate. Nevertheless, a high average refractive index increase of 4.3×10^{-3} was measured via a prism coupling technique at both 633 nm and 1550 nm. It is noteworthy to emphasize the energy-efficient and consequently less time-consuming aspects of the grating fabrication on the $\text{SiO}_2\text{-SnO}_2\text{:Er}^{3+}$ glass-ceramic planar waveguide in comparison with hydrogen loaded germanoborosilicate glasses. To obtain the same value of refractive index change, the energy density needed for hydrogen loaded germanoborosilicate glasses, as that used in fiber sensors, is 10 - 15 kJ/cm^2 . In other words, typical photosensitive materials require 10 - 15 times higher energy compared to the $\text{SiO}_2\text{-SnO}_2\text{:Er}^{3+}$. This result strengthens the case for tin dioxide based glasses for use in integrated photonics. Concerning the magnitude of refractive index change, [Dong 1995b] demonstrated that the presence of tin induced a refractive index change of 3 times larger than the one of the pure germanosilicate. In the work by [Brambilla 2000], a detailed comparison between $\text{GeO}_2\text{-SiO}_2$ and $\text{SnO}_2\text{-SiO}_2$ fibers demonstrated that under similar UV intensity, the same photorefractivity could be obtained with the fibers containing very

low SnO₂ contents: two orders of magnitude less than GeO₂. Moreover, tin-doping helped avoiding hydrogen loading, which is time-consuming and induces high losses in the 1.5 μm region. And finally, SnO₂-SiO₂ fibers potentially provides a lower numerical aperture and higher thermal stability [Brambilla 2002].

6.5 Conclusions

The photorefractive effect of SiO₂-SnO₂:Er³⁺ glass-ceramics are assessed on both the planar waveguides and monoliths. The UV irradiation using the pulsed KrF excimer laser ($\lambda = 248 \text{ nm}$) leads to a negative refractive index change at 1550 nm. Higher SnO₂ content leads to a greater saturated refractive index change: $-(2.8 \pm 0.1) \times 10^{-3}$ for the 30 planar waveguides and $-(2.3 \pm 0.2) \times 10^{-3}$ for the 20 mol% planar waveguides. According to Kramers-Kronig relation, the spectral dependence of the refractive index change can be attributed to the absorption of Er³⁺ at 1550 nm. Concerning the causes leading to the photorefractivity of the SiO₂-SnO₂ glass-ceramics in terms of the structural modification, the clearly observed fluorescence background in the Raman spectra of both irradiated monoliths and planar waveguides revealed that the breaking Sn-related network bonds is involved in the photorefractive response under this UV irradiation condition. Besides, an absorption coefficient decrease in the absorption edge of the SiO₂-SnO₂ monolith suggested that there is a possibility of the contribution from a small SnO₂ decomposition to the photorefractivity of the glass-ceramics. The higher average refractive index variation at 1553 nm of 4.3×10^{-3} is obtained by using the CW frequency doubled argon laser: $\lambda = 244 \text{ nm}$ for grating inscription on SiO₂-SnO₂:Er³⁺ glass-ceramic planar waveguide. The results reveal that by exploiting the photorefractivity, the gratings fabrication on SiO₂-SnO₂:Er³⁺ glass-ceramics is 10-15 times energy-efficient, i.e. less time-consuming in comparison with hydrogen loaded germanoborosilicate glasses. This shows the outstanding photorefractivity of SiO₂-SnO₂:Er³⁺ glass-ceramics for integrated optics. The results of photorefractivity provide the refractive index variation value which is an important parameter for the design of a possible integrated laser structure discussed in Chapter 7 Device designs. This chapter is also dealt with

the calculation of the lasing threshold for the solid state laser using the lateral pumping scheme applied on the obtained cylinders.

References

- [Bhaktha 2010] B. N. Shivakiran Bhaktha, Berneschi S. Conti G. N., Righini G. C., Chiappini A., Chiasera A., Ferrari M., Turrell S., (2010). “Spatially localized UV-induced crystallization of SnO₂ in photorefractive SiO₂-SnO₂ thin film”, *Proceeding of SPIE Volume 7719, Silicon Photonics and Photonic Integrated Circuits II*, pp. 77191B– (2010), doi: 10.1117/12.854894(1-5).
- [Berneschi 2010] Berneschi, S., Bhaktha, B. N. S., Chiappini, A., ... Righini, G. C., “Highly photorefractive Eu³⁺ activated sol-gel SiO₂-SnO₂ thin film waveguides”. *Proceedings of SPIE 7604*, pp. 76040Z(1–6) (2010), doi: 10.1117/12.843210.
- [Bonin 1997] Bonin Keith D. & Vitaly V Kresin, “General properties of the linear polarizability”, *Electric-dipole polarizabilities of atoms, molecules, and clusters*, pp. 9–32(1997), doi 10.1142/2962.
- [Brambilla 2000] Brambilla G., Pruneri V., & Reekie L, “Photorefractive index gratings in SnO₂:SiO₂ optical fibers”, *Applied Physics Letters*, 76(7), pp. 807-809 (2000), doi:10.1063/1.125591.
- [Brambilla 2002] Brambilla, G., & Rutt, H. (2002). “Fiber Bragg gratings with enhanced thermal stability”. *Applied Physics Letters*, 80(18), pp. 3259–3261 (2002), doi: 10.1063/1.1475366.
- [Chen 2004] Chen, G. H., Li, Y. G., Liu, L. Y., He, Y. J., Xu, L., & Wang, W. C., “The photosensitivity and ultraviolet absorption change of Sn-doped silica film fabricated by modified chemical vapor deposition”, *Journal of Applied Physics*, 96(11), pp. 6153–6158(2004).
- [Chiodini 2001a] Chiodini N., Ghidini S. & Paleari A., “Mechanisms responsible for the ultraviolet photosensitivity of SnO₂ -doped silica” *Physical Review B*, 64(7), pp. 073102(1-3) (2001), doi: 10.1103/PhysRevB.64.073102.
- [Chiodini2000] Chiodini, N., Ghidini, S., Paleari, A., Brambilla, G., & Pruneri, V., “Photoinduced processes in Sn-doped silica fiber preforms”, *Applied Physics Letters*, 77(23), pp. 3701–3703(2000).
- [Chiodini 2002a] Chiodini N., Paleari A., Brambilla G., & Taylor, E. R., “Erbium doped nanostructured tin-silicate glass-ceramic composites”, *Applied Physics Letters*, 80(23), pp. 4449–4451 (2002), doi: 10.1063/1.1485105.

[Chiodini 2002b] Chiodini, N., Paleari, A., Spinolo, G., Chiasera A., Ferrari M., Brambilla G., Taylor, E. R. (2002c), “Photosensitive erbium doped tin-silicate glass”, *Journal of Non-Crystalline Solids*, 311(3)1–6(2002), doi: /10.1016/S0022-3093(02)01419-9.

[Chiodini 2003a] Chiodini N., Paleari A., & Spinolo G., “Photorefractivity in Nanostructured Tin-Silicate Glass Ceramics : A Radiation-Induced Nanocluster Size Effect”, *Physical Review Letters*, 90(5), pp. 055507 (1-4) (2003), doi: 10.1103/PhysRevLett.90.055507.

[Chiodini2003b] Chiodini, N., Paleari, A., Spinolo, G., & Crespi, P., “Photorefractivity in SiO₂:SnO₂ glass-ceramics by visible light”, *Journal of Non-Crystalline Solids*, 322(1–3), pp. 266–271(2003).

[Dong 1995a] Dong L., Cruz J. L., Tucknott J. A., Reekie L., & Payne, D. N., “Strong photosensitive gratings in tin-doped phosphosilicate optical fibers”. *Optics Letters*, 20(19), pp. 1982-1984 (1995), doi: 10.1364/OL.20.001982.

[Dong 1995b] Dong L., Reekie L., Xu M. G., Payne D. N., & Cruz J. L., “Enhanced Photosensitivity in Tin-Codoped Germanosilicate Optical Fibers”, *IEEE Photonics Technology Letters*, 7(9), pp. 1048–1050 (1995), doi: 10.1364/OL.20.001982.

[Gaff 2000] Gaff, K., Durandet, A., Weijers, T., Love, J., & Boswell, R., “Strong photosensitivity in tin-doped silica films” *Electronics Letters*, 36(9), pp. 842–843(2000).

[Laurence 1997] Laurence R. & Liang D., “Material considerations for Bragg fiber gratings”, *Proceedings Volume 2998, Photosensitive Optical Materials and Devices*, pp. 2–10(1997), doi: 10.1117/12.264168.

[Lukowiak 2017] Lukowiak, A., Zur, L., Tran, T. N. L., Meneghetti M., Berneschi S., Conti G. N., Pelli S., Trono C., Bhaktha B.N. S., Zonta D., Taccheo S., Righini G. C., Ferrari M., “Sol–Gel-Derived Glass-Ceramic Photorefractive Films for Photonic Structures”, *Crystals*, 7(61), pp. 1-7 (2017), doi: 10.3390/cryst7020061.

[Ulrich 1973] Ulrich, R., and R. T. “Measurement of thin film parameters with a prism coupler”, *Applied Optics*, 12(12), pp. 2901–2908(1973).

Chapter 7 Device designs

7.1 Introduction

In this chapter, a design for solid state laser with lateral pumping scheme is discussed and evaluated. In addition, a possible integrated laser structure is also studied using the Transfer Matrix Formalism (TMF). Moreover, the details of the investigation of a simple Bragg grating and the evaluation of laser conditions in $\text{SiO}_2 - \text{SnO}_2\text{:Er}^{3+}$ planar waveguides are discussed.

7.2 Solid state laser design

7.2.1 Solid state laser design with a lateral pumping scheme

From the experimental assessments discussed in Chapter 4 , the spectroscopic properties of the $\text{SiO}_2\text{-SnO}_2\text{:0.5Er}^{3+}$ glass-ceramic monoliths fulfil the requirement of materials for laser operation as mentioned in [Walter 2006]:

- (i) A broad luminescence band with sharp Stark splitting when excited at SnO_2 band-gap;
- (ii) An acceptable quantum efficiency (30 % for the 10 mol% SnO_2 cylinders);
- (iii) Strong and broad absorption band corresponding to the interband transition of SnO_2 semiconductor compared with the other direct excitations to the electronic states of Er^{3+} .

All the obtained results demonstrate the viability of $\text{SiO}_2\text{-SnO}_2\text{:0.5Er}^{3+}$ glass-ceramics for a solid state construction. Therefore, a design for a solid state laser with a lateral pumping scheme on the $90\text{SiO}_2\text{-}10\text{SnO}_2\text{:0.5Er}^{3+}$ cylinders was carried as shown in Figure 4.34. The designed laser is constructed from three main elements:

- (i) A Xenon flash lamp is used as a pump source. With the aim of exploiting the role of SnO_2 as luminescence sensitizers in the laser, the exploited pump wavelength of the laser can be fitted in the UV range corresponding to SnO_2 band-gap, i.e. around 300 to 350 nm.

- (ii) A gain medium which is constructed by the obtained $90\text{SiO}_2\text{-}10\text{SnO}_2\text{:}0.5\text{Er}^{3+}$ cylinders (see the photo in Figure 7.2)
- (iii) Two mirrors for forming an optical resonator: one fully reflective mirror (reflectivity: $R_1 = 1$) and one partially reflective mirror (a chosen reflectivity: $R_2 = 0.8$)

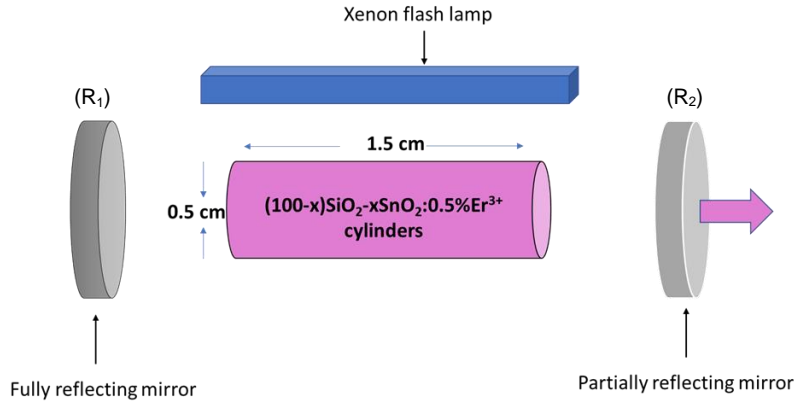


Figure 7.1 A sketch for illustrating the design of a solid state laser with a lateral pumping scheme applied on the obtained $90\text{SiO}_2\text{-}10\text{SnO}_2\text{:}0.5\text{Er}^{3+}$ cylinders

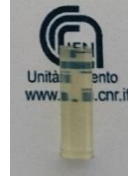


Figure 7.2 Photo of the obtained $90\text{SiO}_2\text{-}10\text{SnO}_2\text{:}0.5\text{Er}^{3+}$ cylinder used for the laser design: with the diameter: $r = 0.5$ cm and length of $L = 1.5$ cm

7.2.2 Estimation of lasing pump power threshold

7.2.2.1 Fundamentals

For the evaluation of the laser condition according to the design above, the lasing threshold power is estimated. First, it is necessary to recall briefly the relevant physical concepts related to a laser operation. The laser physics can be easily found in the books [Walter 2006], [H. Haken

1984], [A.E. Siegman 1986]. Here is a summary of some fundamental concepts from these books which are necessary to calculate the laser threshold.

7.2.2.1.1 General rate equation

There are three different processes of the interaction between light and matter which underly the operation of a laser: absorption, spontaneous emission and stimulated emission. Figure 7.3 show a demonstration of the three processes with the transition example between two levels: the metastable state $^4I_{13/2}$ and $^4I_{15/2}$ of Er^{3+} .

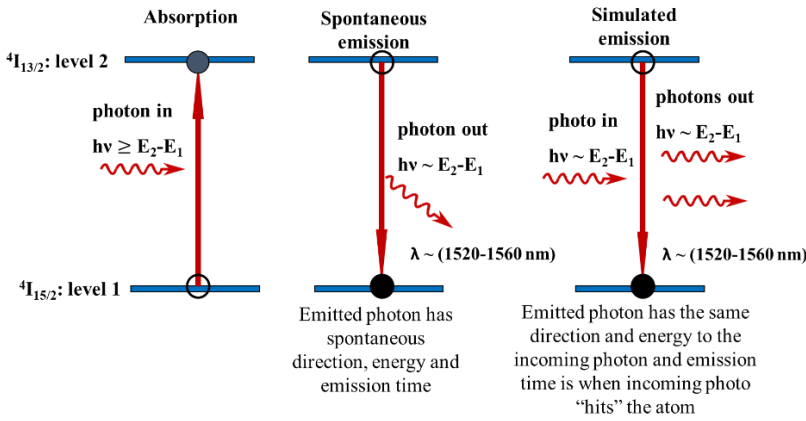


Figure 7.3 Demonstration of the three processes with the transition example between the metastable state $^4I_{13/2}$ and $^4I_{15/2}$ of Er^{3+} [A.E. Siegman 1986]

Without considering any quantum mechanical treatment, the rate equation of the three processes can be described simply as the following rate equations:

- (i) for spontaneous emission

$$\frac{dN_2}{dt} = -AN_2 = -\frac{N_2}{\tau_2} \quad (7.1)$$

- (ii) for stimulated emission

$$\frac{dN_2}{dt} = -W_{21}N_2 \quad (7.2)$$

- (iii) for stimulated absorption

$$\frac{dN_2}{dt} = +W_{12}N_1 \quad (7.3)$$

where

N_1, N_2 are the density of Er^{3+} ions at the level 1 and level 2 respectively; considering the lasing operation wavelength at $1.5 \mu\text{m}$, level 1 is the ground state $^4\text{I}_{15/2}$ and level 2 is the metastable state $^4\text{I}_{13/2}$.

A (s^{-1}) is the transition probability of the spontaneous emission which is related to the level 2 decay time: $A = \frac{1}{\tau_2}$

W_{21} and W_{12} are the transition rates (s^{-1}) of the stimulated emission and absorption respectively, which depends on the pumping process and the probability of absorbing an optical pump photon:

$$W_{21} = \sigma_{21} \Phi_{\text{photon}} \quad (7.4)$$

$$W_{12} = \sigma_{12} \Phi_{\text{photon}} \quad (7.5)$$

where σ_{21}, σ_{12} are the stimulated emission and absorption cross sections and Φ_{photon} is the flux of the pump photons.

7.2.2.1.2 Rate equations for a 3-level laser

For the design of a solid state laser, the simplest laser model: 3-level laser was applied for $\text{SiO}_2\text{-SnO}_2\text{:Er}^{3+}$ as shown in Figure 7.4.

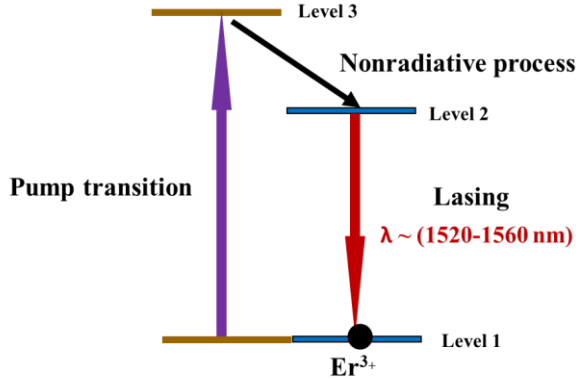


Figure 7.4 3-level energy diagram applied for $\text{SiO}_2\text{-SnO}_2\text{:Er}^{3+}$

(i) Under threshold condition

Based on the same manner of the addressed general equations between two levels as shown in section 7.2.2.1.1, the rate equations for a 3-level system under the threshold can be described in simplified forms as follows:

Considering the condition of a steady-state, i.e. the stimulated emission equal to the absorption rate:

$$W_p N_1 = \frac{N_2}{\tau} \quad (7.6)$$

$$\text{and } N_2 + N_1 = N_T$$

The obtained pump rate and the population inversion are:

$$W_p = \frac{\sigma_p P_p}{A_p \left(h \frac{c}{\lambda_p} \right)} = \sigma_p \Phi_p \quad (7.7)$$

$$\Delta N = N_2 - N_1 = \frac{W_p \tau}{1 + W_p \tau} N_T \quad (7.8)$$

where W_p (s^{-1}) is the pump rate;

τ is the lifetime of level 2;

σ_p is the absorption cross section at pump wavelength;

P_p is the pump power;

A_p is the area of the pump beam

$h \frac{c}{\lambda_p}$ is the photon energy of the pump at the wavelength λ_p ;

Φ_p is the pump flux;

ΔN is the population inversion;

(ii) *At threshold condition*

At threshold condition, the gain is equal to the loss during a round trip of the cavity as illustrated in Figure 7.5.

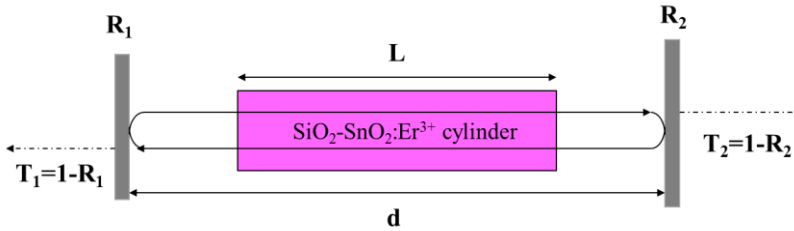


Figure 7.5 The sketch of a round trip lasing operating of the cavity at the threshold condition

In this condition, the light enters twice into the active $\text{SiO}_2\text{-SnO}_2\text{:Er}^{3+}$ cylinder. ΔN is equal to the population inversion at threshold condition. With an assumption that laser emission and absorption cross section are equal and notated now as one symbol σ_L . The laser gain is defined as follow:

$$G = \exp\{[g(\lambda) - \alpha_s]2L\} \quad (7.9)$$

G is the laser gain after around travel ($2L$) of a ring;

σ_L is the laser emission and absorption cross section, i.e. stimulated emission and absorption cross section which are assumed to be equal to the spontaneous $1.5 \mu\text{m}$ emission cross section of Er^{3+} corresponding to the $^4I_{13/2} - ^4I_{15/2}$ transition;

α_s is attenuation coefficient of the active material;

$g(\lambda) = \sigma_L(\lambda)\Delta N_{\text{th}}$ is the gain coefficient of the active medium that is proportion to the stimulated absorption cross section and the population inversion;

From equation (7.9), one can see that the laser gain is reduced by the intrinsic optical losses of the active material, e.g. scattering, absorption, etc... This, in fact, is an expression of the demand for good optical quality of the laser material discussed ahead and in section 4.2. However, besides the intrinsic optical losses from the active material, the laser gain is affected by loss from the mirrors and interface active material [Walter 2006]. For the theoretical estimation of the laser threshold, the round trip condition is applied, which means the laser power, i.e. gain after one round trip is constant. Therefore, the equation (7.9) is rewritten with the introduction of the reflectivity of the two mirrors (R_1 and R_2):

$$G = R_1 R_2 \exp\{[g(\lambda) - \alpha_s]2L\} = 1 \quad (7.10)$$

From equation (7.10), the gain coefficient of a laser can be estimated:

$$g(\lambda) = \alpha_s - \frac{\ln(R_1 R_2)}{2L} \quad (7.11)$$

And, the population inversion at the threshold can be also calculated:

$$\Delta N_{\text{th}} = \frac{g(\lambda)}{\sigma_L} = \frac{1}{\sigma_L} \left[\alpha_s - \frac{\ln(R_1 R_2)}{2L} \right] \quad (7.12)$$

At the steady-state of the laser operation, the threshold pump rate is calculated as follows:

$$W_{p,\text{th}} = \frac{N_2}{N_1 \tau} = \frac{1}{\tau} \frac{N_t + \Delta N}{N_t - \Delta N} \quad (7.13)$$

And the pump power is also calculated:

$$P_{p,\text{th}} = W_{p,\text{th}} A_p \frac{E_p}{\sigma_p} = A_p \frac{\left(h \frac{c}{\lambda_p} \right)}{\sigma_p \tau} \frac{1 + \Delta N}{1 - \Delta N} \quad (7.14)$$

The maximum gain and population inversion can be estimated by neglecting the attenuation coefficient(α_s). Therefore, the equations (7.11) and (7.12) are simplified as follows:

$$g(\lambda) = \frac{\ln(R_1 R_2)}{2L} \quad (7.15)$$

$$\Delta N_{th} = \frac{g(\lambda)}{\sigma_L} = -\frac{\ln(R_1 R_2)}{\sigma_L 2L} \quad (7.16)$$

Combining the equations (7.13), (7.14) , (7.15) and (7.16), the threshold pump power can be estimated as follows:

$$P_{p,th} = W_{p,th} A_p \frac{E_p}{\sigma_p} = A_p \frac{hc}{\lambda_p \sigma_p} \frac{1}{\tau} \frac{1 - \frac{\ln(R_1 R_2)}{N_t \sigma_L 2L}}{1 + \frac{\ln(R_1 R_2)}{N_t \sigma_L 2L}} \quad (7.17)$$

7.2.2.2 Results

Using the equation (7.17), the threshold pump power for the laser constructed on the 90SiO₂-10SnO₂:0.5Er³⁺ cylinder was estimated. The used parameters for the calculation and the results are listed Table 7.1:

Table 7.1 The used parameters for the calculation of the threshold pump power for the laser constructed on the 90SiO ₂ -10SnO ₂ :0.5Er ³⁺ cylinders were estimated	
Parameter	Value
N_t (ions/m ³)	0.980×10^{26}
τ (s)	1.2×10^{-3}
L (m)	1.5×10^{-2}
R_1	1
R_2	0.8
$A_p = 2rL$ (m ²) ($r = 0.5 \times 10^{-2}$ m & $L = 1.5 \times 10^{-2}$ m): surface area of the cylinders	3.75×10^{-5}
c (m/s)	3×10^8
λ_p (m)	363×10^{-9}
h (m ² kg/s)	6.626×10^{-34}
σ_p (m ²)	1.6×10^{-21}
σ_L (m ²)	5.03×10^{-25}
Estimated threshold (W)	14.5

In summary, the threshold pump power is estimated to be 14.5 W for the solid state laser constructed by the 10 mol% SnO₂ glass-ceramic cylinders doped with 0.5 mol% Er³⁺.

7.3 Integrated waveguide laser design

This section is dedicated to put the basic for an integrated waveguide laser design by using Transfer Matrix Formalism (TMF). The theory and principles of this method can be found in the study [Boucher 2006]. For the integrated waveguide laser design, it was mandatory to carry out: (i) the investigation of a suitable simple Bragg grating and (ii) evaluation of the laser condition operating at 1.55 μm on SiO₂-SnO₂:Er³⁺ planar waveguides. The design was applied on the 80SiO₂-20SnO₂:0.5Er³⁺ of which the preliminary photorefractivity result was applied with the effective index change $\Delta n_{\text{eff}} = (1.1 \pm 0.2) \times 10^{-3}$.

7.3.1 Brief introduction to Transfer Matrix Formalism

The basic idea behind Transfer Matrix Formalism is to divide the structure into several smaller sections. In each section the physical parameters are constants and assumed to be homogeneous. In this approach, the incoming and outcoming fields can be related using a matrix. Besides, linearity of Electromagnetism ensures that between two arbitrary abscissas z_1 and z_2 , the vector fields are connected by a linear relationship, well expressed through a (2×2) matrix [Boucher 2006] as reported in equation (7.18) and displayed in figure 5.1.

$$\begin{bmatrix} E_0^+ \\ E_0^- \end{bmatrix} = \begin{bmatrix} M_{11} & M_{21} \\ M_{21} & M_{22} \end{bmatrix} \begin{bmatrix} E_s^+ \\ E_s^- \end{bmatrix} \quad (7.18)$$

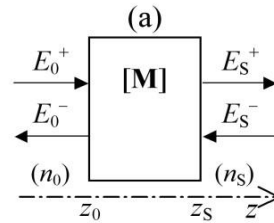


Figure 7.6 Basic idea of the transfer matrix formalism [Boucher 2006], the fields on one side of the media are related to the ones on the other side by the matrix

The principle of the (TMF) is that for a given wavelength, a given incidence and a given eigen-state of polarisation (TE/TM), the two components of the fields are determined only by (E^+, E^-) respectively propagating to the right or to the left. Once the matrix $[M]$ is known it is possible to evaluate experimental observables quantities, such as transmittance and reflection.

7.3.2 Used parameters

Based on the prior work [Boucher 2019], TMF was applied for asymmetric single-mode slab waveguide and used for in calculating the modes of the $\text{SiO}_2\text{-SnO}_2\text{:Er}^{3+}$ waveguide. The modal gain of the active planar waveguide is estimated based on the equation:

$$g_{\text{mod}} = C g_{\text{mat}} \quad (7.19)$$

where, g_{mod} is the modal gain;

g_{mat} is the gain of the $\text{SiO}_2\text{-SnO}_2\text{:Er}^{3+}$ bulk material;

C is the confinement of the $80\text{SiO}_2\text{-}20\text{SnO}_2\text{:}0.5\text{Er}^{3+}$ at $1.55 \mu\text{m}$:

$C = 78 \%$ (TE) and $C = 74 \%$ (TM).

Based on equation (7.19), the possible achievable gain in the $80\text{SiO}_2\text{-}20\text{SnO}_2\text{:}0.5\text{Er}^{3+}$ structure was estimated: $g_{\text{mod}} = 18\text{m}^{-1}$ using the following parameters:

- (i) the Er^{3+} density is: $N_{\text{tot}} = 1.18 \times 10^{26} \text{ m}^{-3}$;
- (ii) the emission cross section for Er^{3+} at $1.55 \mu\text{m}$ is $\sigma \approx 2 \times 10^{-25} \text{ m}^2$;
- (iii) the maximum material gain is $g_{\text{mat}} = \sigma N_{\text{tot}} = 23 \text{ m}^{-1}$.

7.3.3 Distributed Feedback structures

Two topologies which showed the best compromise between efficiency and simplicity were exploited for the design of the gratings (see Figure 7.7):

- (i) The first one is Distributed Feedback Structure (DFB);
- (ii) The second one is Quarter-Wave phase Shift DFB (QWS-DFB)

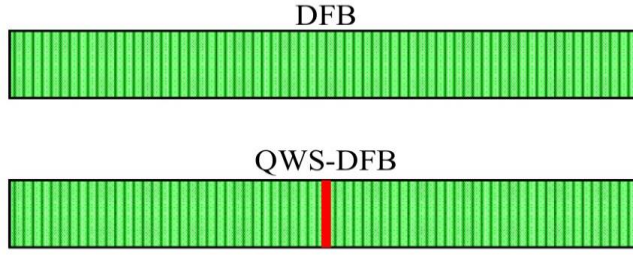


Figure 7.7 Two different topologies associated to active zones and inscribed index grating: active Distributed Feedback Structure (DFB) and Quarter-Wave phase Shift DFB (QWS-DFB). The second structure is characterized by a defect layer in the center [Boucher 2019].

Comparing the two topologies, the QWS-DFB has a lower threshold and also the spectral feature is intrinsically single-wavelength. One can see this from the transmission in the propagation direction of DFB and QWS-DFB structures in the pump-off condition in Figure 7.8 and Figure 7.9 respectively.

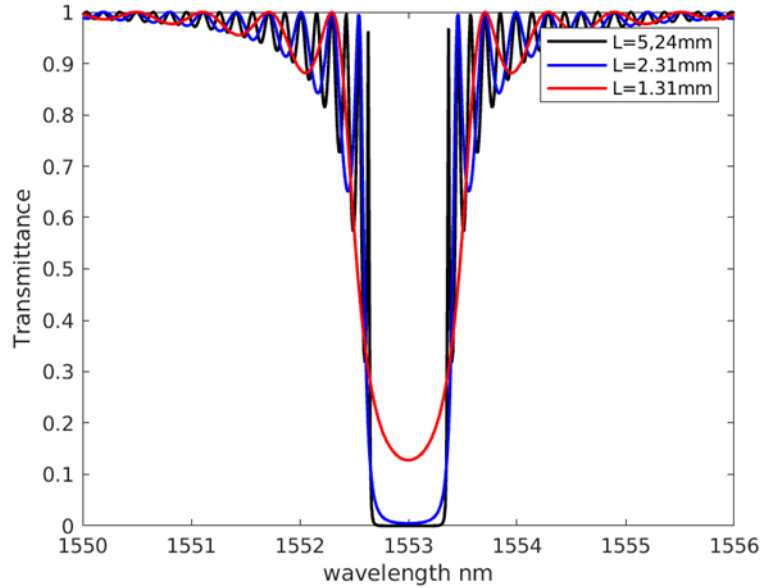


Figure 7.8 Transmission spectra in the propagation direction of a DFB structure in the pump-off condition. The spectra is obtained with different length of the structure and thus different number of periods. The photorefractivity of 20%SnO₂ – 80%SiO₂ planar waveguide was used: $\Delta n_{\text{eff}} = 1.1 \times 10^{-3}$ [Massella 2018].

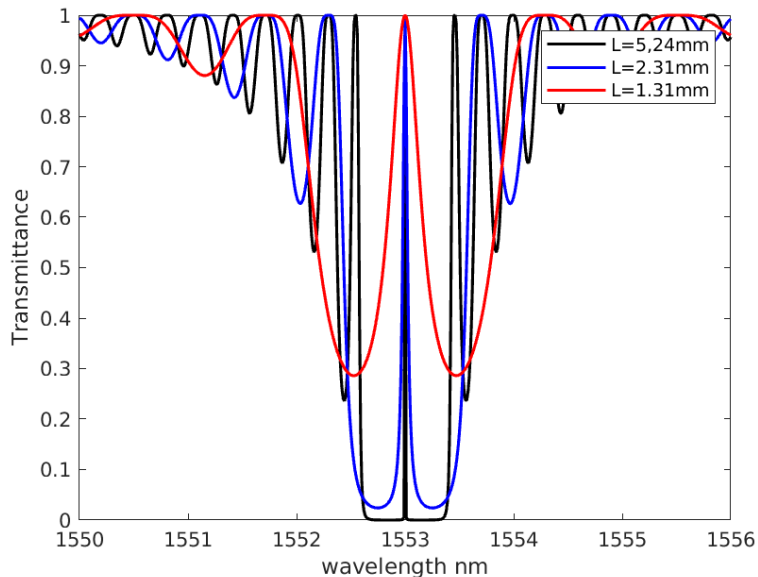


Figure 7.9 Transmission spectra in the propagation direction of a QWS-DFB structure in the pump-off condition. The spectra are obtained with different length of the structure and thus different number of periods. The photorefractivity of 20%SnO₂ – 80%SiO₂ planar waveguide was used: $\Delta n_{\text{eff}} = 1.1 \times 10^{-3}$. It is highlighted that the central peak thanks to the defect layer located in the middle of the structure, becomes more pronounced when the length of the structure increases [Massella 2018].

From Figure 7.9 , the defect layer in the QWS-DFB structure is a key element since it creates a resonance with the central wavelength and traps field intensity inside. The transmission spectra in Figure 7.8 and Figure 7.9 were investigated in respect to different length of the system. This quantity, the length, is crucial for the calculation of the threshold gain.

7.3.4 Threshold conditions: numerical calculations

Since QWS-DFB in Figure 7.9 showed better performance as discussed ahead, the threshold conditions were investigated on this structure. The idea is to use a transfer matrix for the boundary condition applied at the resonance wavelength in different QWS-DFB structure. Afterwards, by

comparing between the solution of boundary condition and achievable gain for each QWF-DFB length, the threshold condition was evaluated. Figure 7.10 shows the results of the behaviour of the $\alpha_{th}L$ vs L for different length of the structure (blue dots). α_{th} is obtained by the solution of boundary condition for each QWF-DFB length. The orange line represents the maximum achievable gain of the $80\text{SiO}_2\text{-}20\text{SnO}_2\text{:}0.5\text{Er}^{3+}$ planar waveguide. From Figure 7.10, the condition for the laser operation is when the achievable gain of the material is higher than the solution of boundary condition of QWF-DFB. In other words, when the length of QWF-DFB is longer than 6 mm, the threshold condition is easily satisfied.

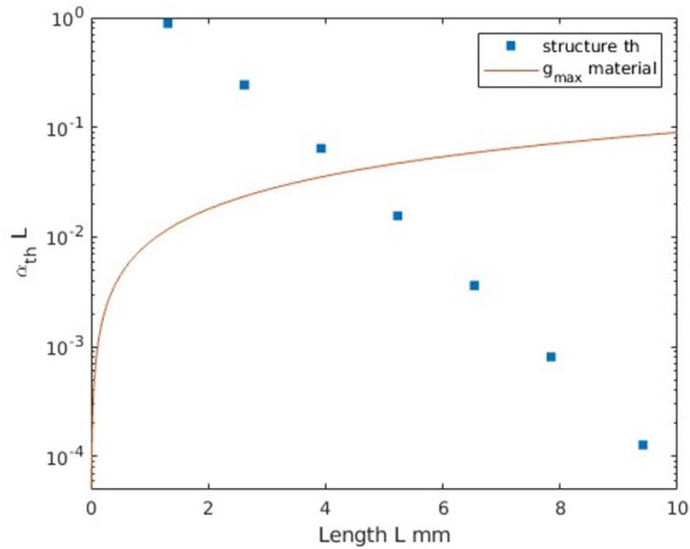


Figure 7.10 Behaviour of the $\alpha_{th}L$ vs L for different length of the structure (blue dots). α_{th} is obtained by the solution of boundary condition for each QWF-DFB length. The orange line represents the maximum achievable gain of the $80\text{SiO}_2\text{-}20\text{SnO}_2\text{:}0.5\text{Er}^{3+}$ planar waveguide [Massella 2018].

7.4 Conclusions

This chapter shows the designs for a solid state laser with lateral pumping scheme applied on the $\text{SiO}_2\text{-SnO}_2\text{:Er}^{3+}$ cylinders. The laser pumping power threshold was roughly estimated to be 14.5 W for the 10 mol% SnO_2 glass-ceramic cylinders doped with 0.5 mol% Er^{3+} . In addition, a possible integrated laser structure is also studied on the $\text{SiO}_2\text{-}$

SnO₂:Er³⁺ planar waveguides. The investigation focused on transmission spectra of a possible index-grating structure and of the threshold gain necessary to achieve a SiO₂-SnO₂:Er³⁺ waveguide laser. All these results are used as a proof of concept for the viability of applying SiO₂-SnO₂:Er³⁺ glass-ceramics for both solid state laser and integrated waveguide laser fabrication. The next chapter, i.e. Chapter 8 Optical waveguides fabricated by laser micromachining will show another practical demonstration of exploiting femtosecond laser micromachining for the fabrication of optical waveguides on the SiO₂-SnO₂:Er³⁺ monolithic squares.

References

- [A.E. Siegman 1986] A.E. Siegman., “Lasers”, University Science Books, Mill Valley, CA (1986).
- [Boucher 2006] Boucher, Y., “Theoretical investigation of amplified spontaneous emission in an active structure by extended (3x3) transfer matrix formalism: the case of a nonuniform longitudinal distribution of emitters”, Journal of the European Optical Society-Rapid Publications, 1, pp. 06027(1-6) (2006), doi:10.2971/jeos.2006.06027.
- [Boucher 2019] Boucher, Y. G., Zur, L., & Ferrari, M., “Modal properties of an erbium-doped asymmetric single-mode slab waveguide in the glass-ceramics SnO₂ –SiO₂ system” , Optical Materials, 87, pp. 90–93(2019).
- [H. Haken1984] H. Haken., “Laser Theory”, Springer, Berlin Heidelberg(1984).
- [Massella 2018] Massella D., “SiO₂-SnO₂:Er³⁺ planar waveguide: Computational and Optical assessment”, Master thesis, Department of Physics, University of Trento (2018).
- [Walter 2006] Walter Koechner., “Properties of Solid-State Laser Materials”, Solid-State Laser Engineering, New York: Springer, pp. 38–101(2006).

Chapter 8 Optical waveguides fabricated by laser micromachining

8.1 Introduction

Besides the photorefractivity as discussed in Chapter 6 , another approach which can be used to tailor the refractive index of $\text{SiO}_2\text{-SnO}_2$ glass-ceramics is femtosecond laser micromachining. Therefore, this chapter demonstrates the fabrication of optical waveguiding structures on the $90\text{SiO}_2\text{-}30\text{SnO}_2\text{:}0.5\text{Er}^{3+}$ monolithic square exploiting the femtosecond laser micromachining. The effects of the fabrication parameters such as the laser power and the scanning speeds were elaborated to avoid material ablation due to void creation. The continuous optical waveguiding structures were obtained. Moreover, the waveguiding tests on the obtained continuous optical waveguides were carried out by coupling the light at 635 nm and acquiring the near field intensity profiles in different regions of the modified zones. To understand the structural modification induced by the femtosecond laser inscription, the Raman spectroscopy was studied.

8.2 Advantages of femtosecond laser micromachining

Femtosecond laser micromachining is a high-precision technique for fabricating 3D micro-optical elements on transparent materials for applications in photonic devices [Lucas 2012], [Little 2008], [Righini 2014]. One should mention first the fabrication potential of optical waveguides by using femtosecond laser micromachining in a great diversity of transparent optical materials; both glasses such as fused silica [Little 2008], [Varkentina 2016], silicate [Martínez-Vázquez 2005], [Sotillo 2017], phosphate [Fletcher 2009], [Chan 2003] and crystalline materials such as LiNbO_3 and $\text{KGd(WO}_4)_2$ [Vishnubhatla 2008].

In general, the advantages of femtosecond laser machining over other processing techniques are: (i) no mask needed and direct fabrication; (ii) the technique can be applied to a wide variety of materials both absorptive and transparent thanks to non-linear absorption [Lucas 2012]; (iii) possibility to fabricate complex geometry thanks to the focalized volume confinement in combination with laser beam scanning.

According to review paper [Lucas 2012], the effect of femtosecond laser on materials can carry out thanks to not only the multi-photon absorption of the laser beam of the materials but also several consequent physical processes which occur afterwards. All of these mentioned processes lead to the modification of the materials. Firstly, the electrons absorb part of pulse energy and transfer to the lattice in few picoseconds. Secondly, there is a generation of pressure or shock wave aparting from the hot focal volume in nanosecond scale. Thirdly, there is a thermal energy diffusion out of the focal volume leading to a permanent structural modification. Depending on the materials and fabrication conditions, different material modifications can be achieved. Both positive and negative refractive index change can be obtained, and the spatial inhomogeneity of index modification is still under study [Lucas 2012]. Nevertheless, several factors can be attributed to this feature such as: stress-induced changes, densification, changes in effective fictive temperature, and colour-centre formation. Therefore, the investigation of fs-laser induced structural modification should be elaborated together with a specific case of material and fabrication conditions.

8.3 Experiments

8.3.1 Experimental setup and methodology

Optical channel waveguides were fabricated by Light Conversion Pharos amplified Yb:KGW femtosecond laser with single pulse duration of 230 fs at the operating wavelength of 515 nm and the repetition rate of 500 kHz. The used pulse energy ranges from 0.10 to 0.50 μJ lower than the damage threshold of fused silica [Little 2008]. The laser pulse was focused inside the $\text{SiO}_2\text{-SnO}_2\text{:Er}^{3+}$ monolithic square beneath the surface of around 200 μm , perpendicular to the desired waveguide axis using a 30 \times Olympus Plan Achromat oil immersion objective lens (NA:

0.4). The focused beam width is around 2 μm . The polished 90SiO_2 - 10SnO_2 : 0.5Er^{3+} monolithic square, i.e. the highest SnO_2 content one was chosen for fabricating optical waveguides as shown in Figure 8.1.



Figure 8.1 Photo of the polished 90SiO_2 - 10SnO_2 : 0.5Er^{3+} monolithic square chosen for the fabrication of waveguides ($1 \times 1 \text{ cm}^2$)

The optical waveguiding testing of the femtosecond laser written structures was carried out by injecting the diode laser beam at 635 nm using single-mode fiber. The output intensities were imaged with a $60\times$ aspheric lens (5721-H-B, Newport) on a beam profiler (SP620U, Spiricon) to acquire the near field intensity mode-profiles. In addition, by simply translating the input fiber laterally, the 635 nm laser beam was coupled into different regions of the modified zones and the corresponding near field intensity mode-profiles were obtained (see the section 8.3.3.1 Optical waveguiding testing).

To understand the structural modification induced by the femtosecond laser, micro-Raman spectroscopy was employed. The micro-Raman spectra was acquired using a Labram Aramis (Horiba Jobin-Yvon) equipped with an optical microscope and a $100\times$ objective. The excitation source was a He-Ne laser at 632 nm.

8.3.2 Results of femtosecond laser written structures

Five groups of continuous tracks were fabricated using different scanning speeds, writing laser powers and the corresponding pulse energies as listed in Table 8.1.

Table 8.1 Writing parameters used for the fabrication of continuous tracks in group A			
Group A	Laser power P (mW)	Pulse energy $\frac{P}{f_{\text{repetition}}}$ (μJ)	Scanning speed
Group A1	50	0.1	1, 5 and 10 mm/s
Group A2	100	0.2	
Group A3	150	0.3	
Group A4	200	0.4	
Group A5	250	0.5	

Figure 8.2 and Figure 8.3 show the optical microscope images from the white light transmission of the written structure from the top view and side view as a function of the laser powers (250, 200, 150, 100 and 50 mW) and the scanning speeds (1, 5 and 10 mm/s). In these images, the dark regions due to lack of light propagating are attributed to the lower refractive index region while the brighter regions are referring to the higher refractive index ones. From these top view images, one can see that exploiting the femtosecond laser micromachining, it was possible to obtain the continuous tracks. From the side view images, one can see that increasing the laser power or decreasing the scanning speed led to the broadening of the transverse width of the written structure. This can be explained due to good 3D heat flow during the laser fabrication with the high laser power or slow scanning speed as suggested by Sotillo in the work [Sotillo 2017]. Furthermore, one can use this as an indication of the moderate high thermal conductivity of SiO₂-SnO₂ glass-ceramics comparable to other silicate glasses [Sotillo 2017]. However, the laser powers higher than 175mW led to the ablation or void creation of the material. Therefore, to obtain the good quality waveguides suitable for photonic applications, it was necessary to avoid the material damage.

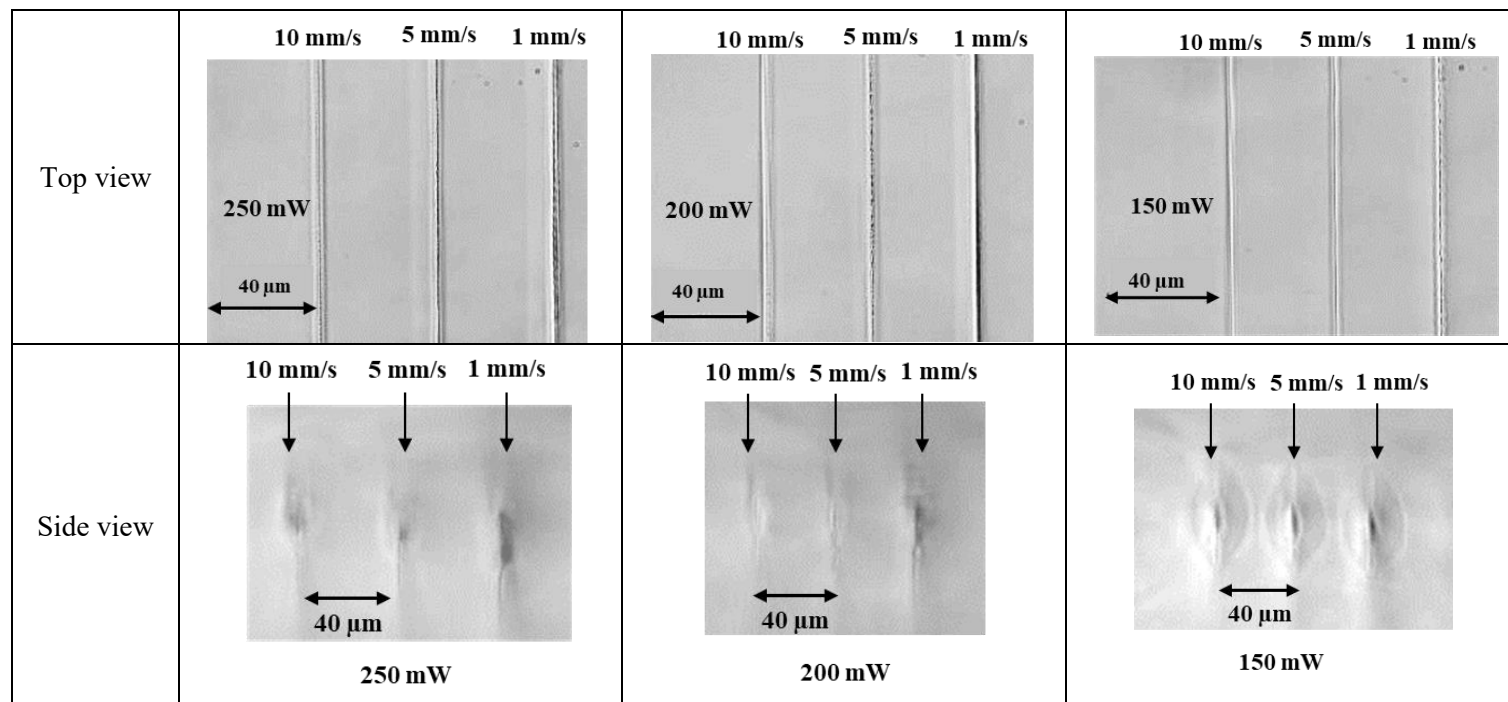


Figure 8.2 Transmission optical microscope images of the top view and side view of the continuous tracks fabricated by Femtosecond laser as a function of the laser powers of 250, 200 and 150 mW with different scanning speeds (1, 5 and 10 mm/s)

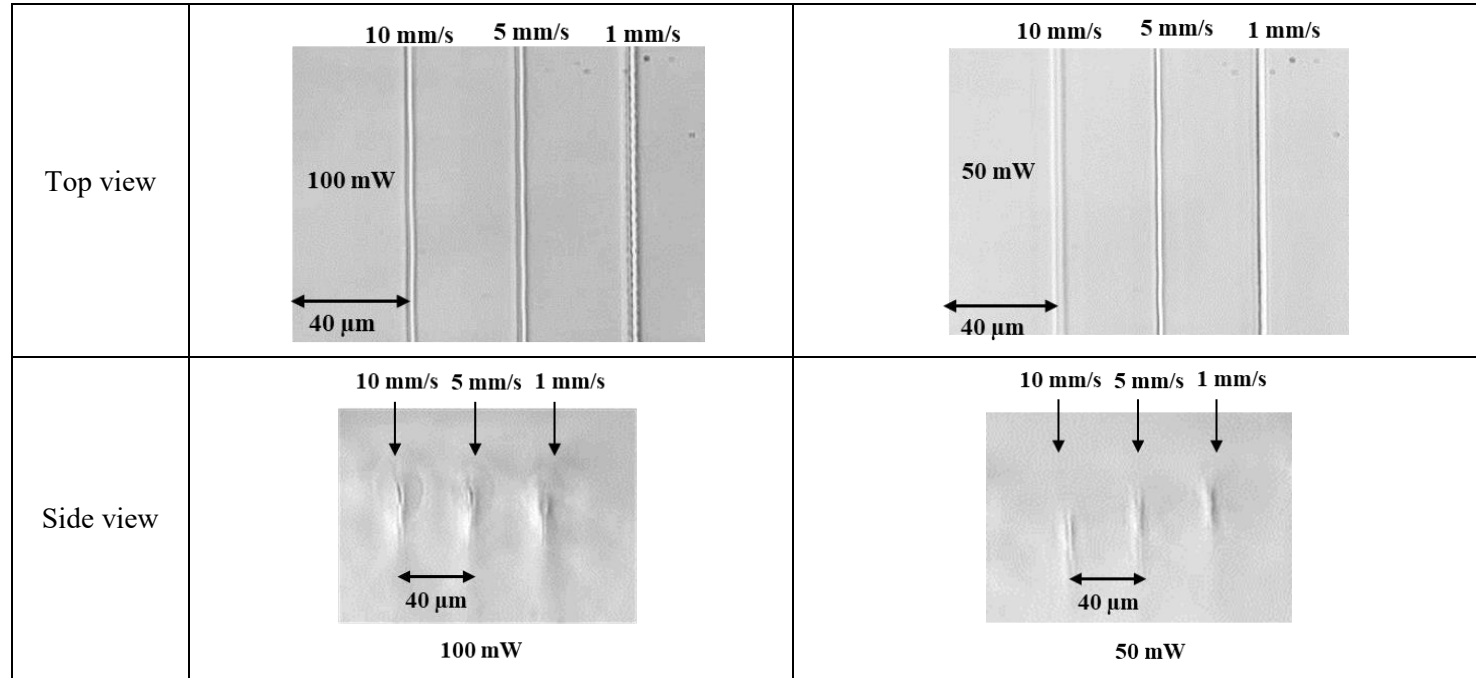


Figure 8.3 Transmission optical microscope images of the top view and side view of the continuous tracks fabricated by Femtosecond laser as function of the laser powers of 100 and 50 mW with different scanning speeds (1, 5 and 10 mm/s)

For this reason, the fabrication conditions for the optical waveguide inscription in the $90\text{SiO}_2\text{-}10\text{SnO}_2\text{:}0.5\text{Er}^{3+}$ glass-ceramic were elaborated with more parameters of laser power and scanning speed. The explored fabrication parameters are tabulated in Table 8.2. Continuous tracks were obtained, and their transmission optical microscope images of the side view are shown in Figure 8.4.

Table 8.2 Writing parameters used for the fabrication of continuous tracks in group B			
Group B	Laser power P (mW)	Pulse energy $\frac{P}{f_{\text{repetition}}}$ (μJ)	Scanning speed
Group B1	50	0.10	1, 5, 10 and 25 mm/s
Group B2	75	0.15	
Group B3	100	0.20	
Group B4	125	0.25	
Group B5	150	0.30	
Group B6	175	0.35	
Group B7	200	0.40	
Group B8	225	0.45	
Group B9	250	0.50	

Figure 8.4 shows that the undesirable damage indicated by black or dark grey color due to void creation or material ablation of the modified regions was observed at the laser power of 175 mW and higher. This value can be considered as the threshold damage of the investigated $90\text{SiO}_2\text{-}10\text{SnO}_2\text{:}0.5\text{Er}^{3+}$ monoliths. Therefore, the laser powers of less than 175 mW were employed for further investigation of the femtosecond laser written waveguides.

Thi Ngoc Lam Tran – Tin dioxide - based photonic glass-ceramics

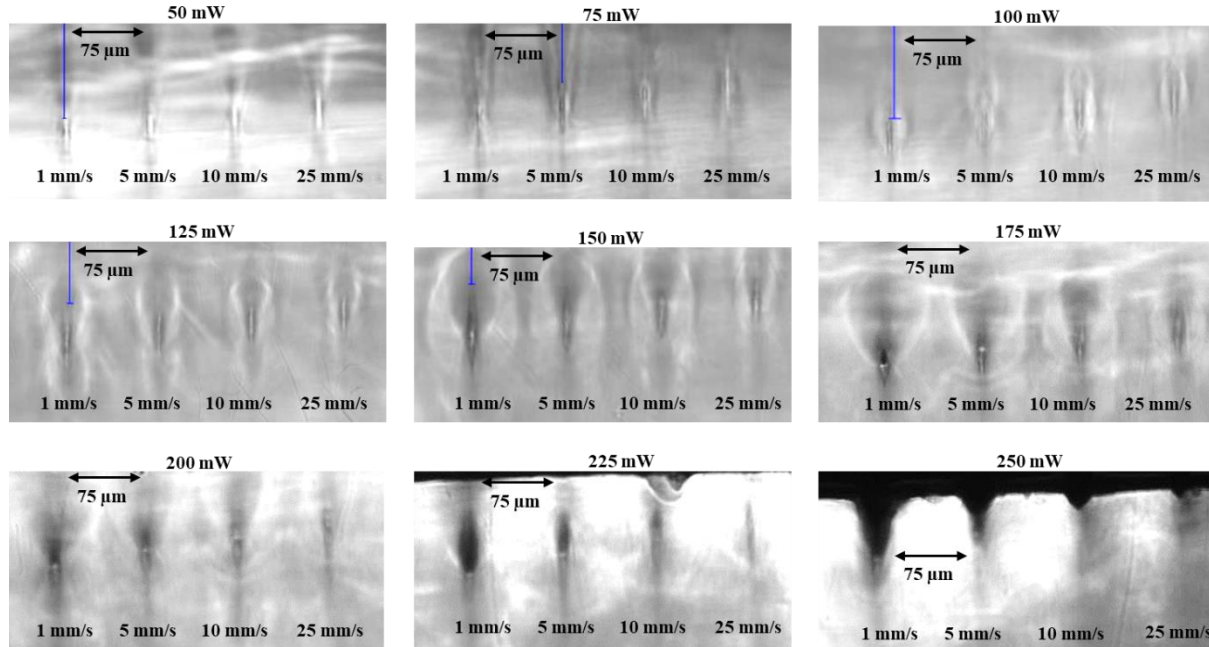


Figure 8.4 Transmission optical microscope images of the side view of the continuous tracks fabricated by Femtosecond laser as function of the laser powers of 250, 225, 200, 175, 150, 125, 100, 75 and 50 mW with different scanning speeds (1, 5, 10 and 25 mm/s)

8.3.3 Characterization of femtosecond laser written optical waveguides

8.3.3.1 Optical waveguiding testing

Four laser powers lower than damaged threshold: 150, 125, 100 and 50 mW were used to fabricate the optical waveguide structures in the $90\text{SiO}_2\text{-}10\text{SnO}_2\text{:}0.5\text{Er}^{3+}$. For each laser power, all the scanning speeds of 1, 5, 10 and 25 mm/s were employed. The near field intensity mode-profiles of all the obtained optical waveguides were acquired. Figure 8.5 and Figure 8.6 show the side view images of the four representative optical waveguides fabricated at the four laser powers and their corresponding near field intensity mode-profiles at 635 nm. Depending on the fabrication conditions, different optical waveguides yield different modified structures as demonstrated by the distribution of dark and bright regions in their side view images: the darker, the lower the refractive index. However, for all the optical waveguides, the brighter regions corresponding to the higher refractive index are locating surrounding regions, i.e. regions outside the modified zones. Furthermore, it is evidenced by the near field intensity mode-profiles at 635 nm since the light was guided in the surrounding regions outside of the modified zones in all the obtained optical waveguides disregarding the fabrication conditions. The similar behavior, i.e. optical waveguiding in surrounding regions of the laser-modified zones has been already observed in $\text{TiO}_2\text{-SiO}_2$ based silicate glass [Sotillo 2017], phosphate glasses [Fletcher 2009], [Chan 2003] and crystalline materials such as LiNbO_3 and $\text{KGd(WO}_4)_2$ [Vishnubhatla 2008]. In these works, the volume expansion of the laser-modified zones led to the compression on the surrounding regions. Therefore, the surrounding regions have higher refractive index where the light can be guided.

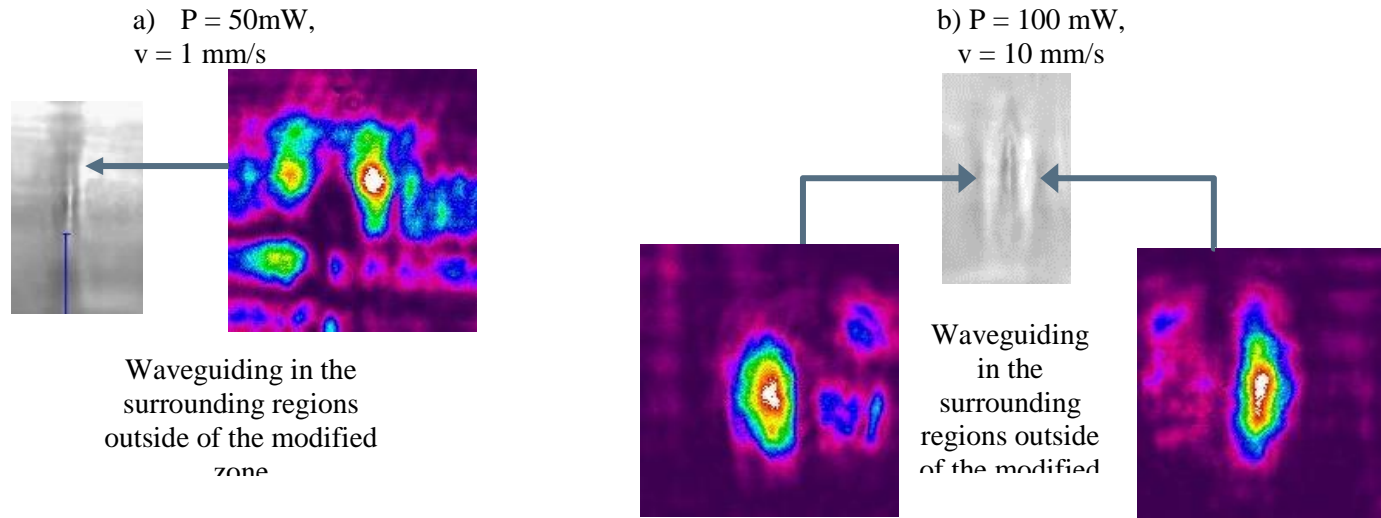


Figure 8.5 Transmission optical microscope image of the optical waveguiding structure fabricated with the laser power and writing speed: a) $P = 50\text{ mW}$ and $v = 1\text{ mm/s}$ and b) $P = 100\text{ mW}$ and $v = 10\text{ mm/s}$, and the corresponding near field intensity mode-profiles at 635 nm , revealing that the light was guided in the surrounding regions outside the modified zone

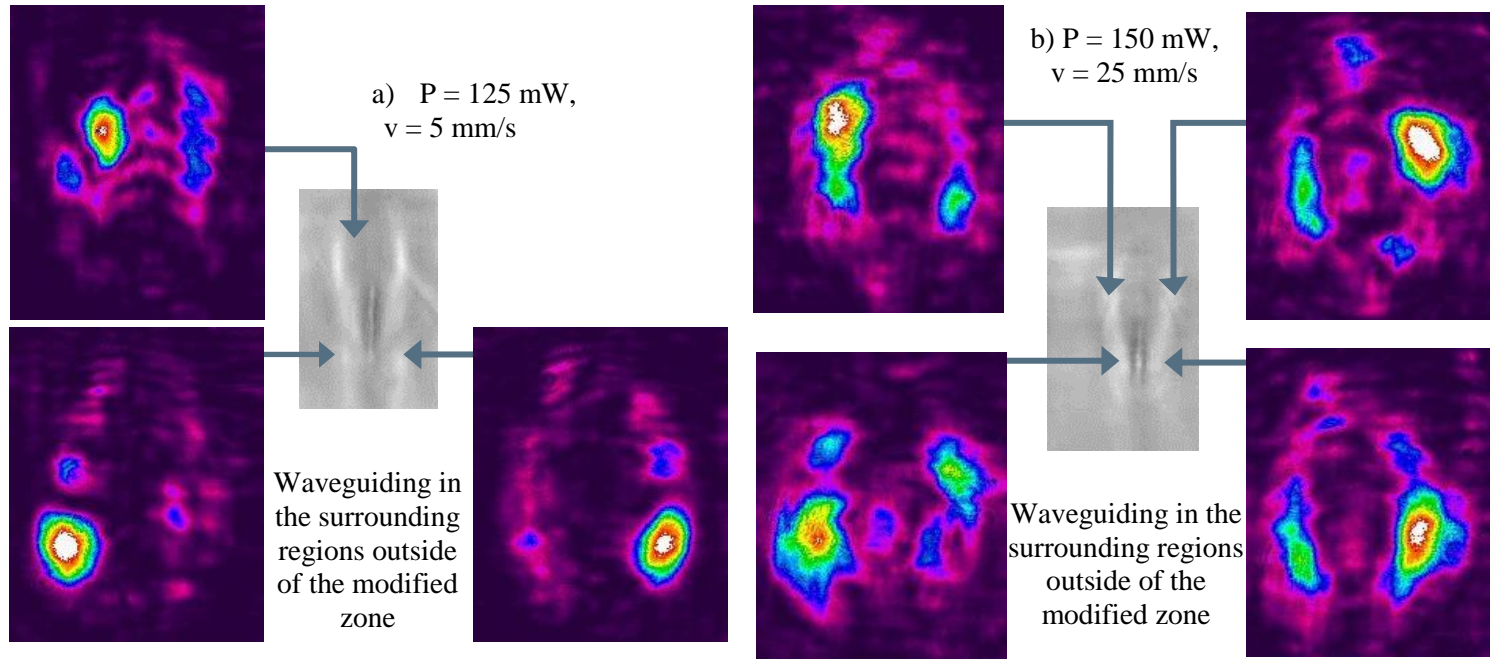


Figure 8.6 Transmission optical microscope image of the optical waveguiding structure fabricated with the laser power and writing speed: a) $P = 125 \text{ mW}$ and $v = 5 \text{ mm/s}$ and b) $P = 150 \text{ mW}$ and $v = 25 \text{ mm/s}$, and the corresponding near field intensity mode-profiles at 635 nm, revealing that the light was guided in the surrounding regions outside the modified zone

8.3.3.2 Raman spectroscopy of femtosecond laser written optical waveguides

For the study of structural modification induced by the femtosecond laser, the micro-Raman spectra ($\lambda_{\text{ex}} = 632 \text{ nm}$) were acquired each $0.5 \mu\text{m}$ across regions of the fabricated optical waveguides where the waveguiding tests were performed. Figure 8.7 illustrates an example of the acquisition scheme of the Raman spectra in the waveguiding region of optical waveguide (fabrication condition: $P = 50 \text{ mW}$ and $v = 1 \text{ mm/s}$) which is indicated by the black square in Figure 8.7a). Figure 8.7b) specifies the corresponding optical microscope image of the waveguiding region. In this image, the blue dots are the focused areas where the Raman spectra were acquired.

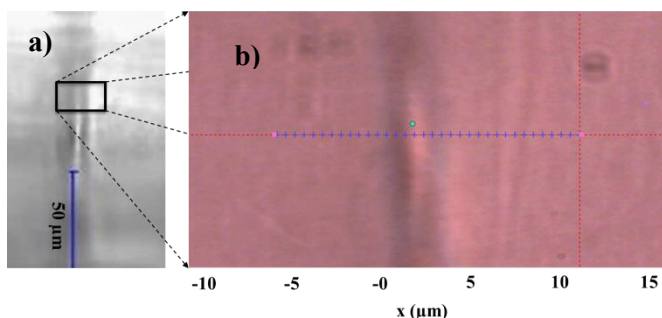


Figure 8.7 Transmission optical microscope images of a) the whole optical waveguiding structure (fabrication conditions: $P = 50 \text{ mW}$ and $v = 1 \text{ mm/s}$) and b) the characterized region where the Raman spectra were acquired across the modified zone indicated by red line. The blue dots (step = $0.5 \mu\text{m}$) are the focused areas where the Raman spectra were performed.

Figure 8.8 shows a representative Raman spectrum obtained in all the focused areas across the modified zones of the fabricated optical waveguides, covering both the modified zones and the surrounding regions. In fact, the Raman features are similar to the $90\text{SiO}_2\text{-}10\text{SnO}_2\text{:}0.5\text{Er}^{3+}$ monolith before the laser irradiation shown in section 4.4.1.1. This indicates there is no serious modification of the glass-ceramic structure induced during the femtosecond laser inscription.

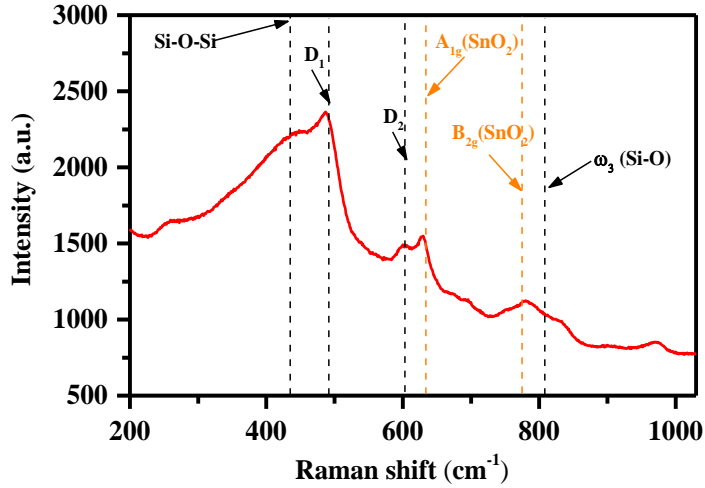


Figure 8.8 The representative Raman spectrum obtained for all the focused areas across the modified zones of the fabricated optical waveguide

However, a change of silica matrix is revealed by the difference of the intensity ratios of D_2 peak with respect to the ω_3 peak across the modified zone as shown in Figure 8.9. As one can see, the D_2/ω_3 intensity ratios are higher in the surrounding areas corresponding to the waveguiding regions than the modified zone. In particular, the two areas A and B with the two locally highest D_2/ω_3 intensity ratios are corresponding to the two observed waveguiding zones shown in the inset image. The band ω_3 at 800 cm^{-1} is assigned to a complex motion of Si atoms against the bridging oxygen atoms in O-Si-O in silica network [Armellini 1999], [Okuno 2005] and the D_2 peak is attributed to presence of three- membered rings in the normal six- membered rings of SiO_2 network [Galeener 1985], [Bouajaj 1997], [Kinowski 2001]. This behavior is in agreement with the SiO_2 local densification related to higher 3-membered rings concentration formed during the femtosecond laser treatment in the work [Little et al. 2008], [Chan 2003], [Bressel 2011], [Okuno 1999]. In case of $\text{SiO}_2\text{-SnO}_2$, the observable higher refractive index in the surrounding regions can be explained due to the locally SiO_2 densification induced by the volume expansion of the laser-modified zones which is similar to another silicate glass studied in the work [Sotillo 2017]. All the tested optical waveguides shown in Figure 8.5 and Figure 8.6 also exhibit the similar characteristics of the surrounding regions of the modified zone.

However, concerning the modified zone, it was not possible by using the Raman measurement to put an evidence of a significant change in compared with the pristine sample. The further investigations are necessary to identify the structural modification in the irradiated zones. Nevertheless, the volume expansion of SnO₂ nanoclusters in the modified region was revealed in the previous study [Paleari 2006] on SiO₂-SnO₂ glass-ceramics under femtosecond laser micromachining. The authors suggested that the volume expansion is due to SnO₂ amorphization triggered the refractive index change of the modified zone. This can be an explanation for the volume expansion of the laser-modified zone leading to the compression densification of the surrounding regions.

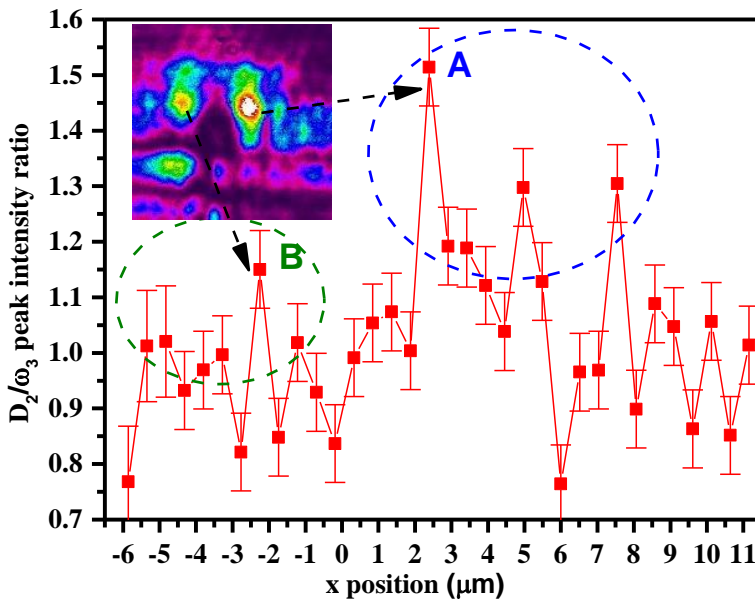


Figure 8.9 a) and b) Transmission optical microscope images of the optical waveguiding structure (fabrication conditions: $P = 50$ mW and $v = 1$ mm/s) and the characterized region respectively; c) the graph of D_2/ω_3 peak intensity ratios along the characterized points indicated by blue dots in the image from Figure 8.7b).

8.4 Conclusions

This chapter has shown the possibility of fabricating optical waveguiding structure in the $90\text{SiO}_2\text{-}10\text{SnO}_2\text{:}0.5\text{Er}^{3+}$ monolithic square using femtosecond laser machining. The elaboration of fabrication condition using different laser power and scanning speed helped to avoid the material ablation or void creation. Moreover, the continuous optical waveguides were obtained. The waveguiding properties of the fabricated optical waveguides were tested. The micro Raman spectroscopy shows that the refractive index change is due to the local densification of the surrounding area of the modified zones. Furthermore, the obtained optical waveguides fabricated by femtosecond laser micromachining are proofs of concept for the writing of channel waveguides and Bragg gratings in $\text{SiO}_2\text{-SnO}_2\text{:}0.5\text{Er}^{3+}$ glass-ceramic bulks. Last but not least, together with the photorefractivity, these results of femtosecond laser micromachining on $\text{SiO}_2\text{-SnO}_2\text{:}0.5\text{Er}^{3+}$ glass-ceramics provide solutions for the issue of writing of channels and mirrors for the integrated lasers or circuits and this strengthens more the competition of $\text{SiO}_2\text{-SnO}_2\text{:Er}^{3+}$ glass-ceramics in the applications in integrated optics.

References

- [Armellini 1999] Armellini C., Ferrari M., Montagna M., Pucker G., Bernard C., & Monteil A., “Terbium (III) doped silica-xerogels : effect of aluminium (III)”, *Journal of Non-Crystalline Solids*, 245(1-3), pp. 115–121(1999), doi: 10.1016/S0022-3093(98)00856-4.
- [Bouajaj 1997] Bouajaj, A., Ferrari, M., & Montagna, M., “Crystallization of silica xerogels: A study by Raman and Fluorescence spectroscopy”, *Journal of Sol-Gel Science and Technology*, 395, pp. 391–395(1997).
- [Chan 2003] Chan, J. W. “Waveguide fabrication in phosphate glasses using femtosecond laser pulses”, *Applied Physics Letters*, 82(82), pp. 2371–2373(2003).
- [Chan 2003] Chan, J. W., Huser, T. R., Risbud, S. H., & D. M. Krol, “Modification of the fused silica glass network associated with waveguide fabrication using femtosecond laser pulses,.” *Applied Physics A*, (76), pp. 367–372(2003).

- [Fletcher 2009] Fletcher, L. B., Witcher, J. J., Reichman, W. B., Arai, A., Bovatsek, J., & Krol, D. M., “Changes to the network structure of Er–Yb doped phosphate glass induced by femtosecond laser pulses”, *Journal of Applied Physics*, 106, pp. 083102(1-5) (2009).
- [Galeener 1985] Galeener, F. L. “Raman and ESR studies of the thermal history of amorphous SiO₂”, *Journal of Non-Crystalline Solids*, 71(1–3), pp. 373–386(1985).
- [Kinowski 2001] Kinowski, C., Bouazaoui, M., Bechara, R., & Hench, L. L. “Kinetics of densification of porous silica gels : a structural and textural study”, *Journal of Non-Crystalline Solids*, 291, pp.143–152(2001).
- [Little 2008] Little, D. J., Ams, M., Dekker, P., Marshall, G. D., Dawes, J. M., & Withford, M., “Femtosecond laser modification of fused silica: the effect of writing polarization on Si-O ring structure”, *Optics Express*, 16(24), pp. 20029(1–37) (2008).
- [Lucas 2012] Lucas, L., & Zhang, J., “Femtosecond laser micromachining: a back-to-basics primer”, *Industrial Laser Solutions*, 24(4), pp.29 (2012).
- [Martínez-Vázquez 2005] Martínez-Vázquez, R., Osellame, R., Cerullo, G., ... Spinolo, G., “Fabrication of guiding structures in nanostructured tin-silicate glass ceramic by a focused femtosecond laser” *Journal of Non-Crystalline Solids*, 351(21–23), pp. 1855–1859(2005).
- [Okuno 2005] Okuno, M., Zotov, N., Schmücker, M., & Schneider, H. “Structure of SiO₂–Al₂O₃ glasses: Combined X-ray diffraction, IR and Raman studies”, *Journal of Non-Crystalline Solids*, 351(12–13), pp. 1032–1038(2005).
- [Paleari 2006] Paleari, A., Franchina, E., Chiodini, N., & Lauria, A., “SnO₂ nanoparticles in silica : Nanosized tools for femtosecond-laser machining of refractive index patterns”, *Applied Physics B: Lasers and Optics*, 88, pp. 131912(1-3) (2006).
- [Righini 2014] Righini, G. C., & Chiappini, A. “Glass optical waveguides: a review of fabrication techniques”, *Optical Engineering*, 53(7), pp. 071819(2014).
- [Sotillo 2017] Sotillo, B., Chiappini, A., Bharadwaj, V., ... Eaton, S. M., “Raman spectroscopy of femtosecond laser written low propagation loss optical waveguides in Schott N-SF8 glass”, *Optical Materials*, 72, pp. 626–631(2017).
- [Varkentina 2016] Varkentina, N., Dussauze, M., Royon, A., Ramme, M., Petit, Y., & Canioni, L., “High repetition rate femtosecond laser

irradiation of fused silica studied by Raman spectroscopy”, *Optical Materials Express*, 6(1), pp. 79(2016).

[Vishnubhatla 2008] Vishnubhatla, K. C., Venugopal Rao, S., Raavi, S. S. K., ... Narayana Rao, D., “Micro-Raman mapping of micro-gratings in ‘BACCARAT’ glass directly written using femtosecond laser”, *Proceeding of SPIE Volume 6881, Commercial and Biomedical Applications of Ultrafast Lasers VIII*; pp. 688114 (2008).

Chapter 9 Conclusions and perspectives

Looking at state of the art of optical devices, it is evident that glass-based rare-earth-activated optical structures represent the technological pillar of a huge of photonic applications covering Health and Biology, Structural Engineering, Environment Monitoring Systems, Lighting, Laser sources and Quantum Technologies. Among different glass-based systems, a strategic place is assigned to transparent glass-ceramics, nanocomposite materials, which offer specific characteristics of capital importance in photonics. Following this strategy, this PhD thesis exploits tin dioxide (SnO_2)-based glass-ceramic activated by erbium ions (Er^{3+}) to put the basis for the fabrication of solid state and integrated lasers. Moreover, the well-known requirements in terms of losses and homogeneity, two crucial points are decisive in the development of an optically pumped rare-earth-based laser: (i) the low absorption cross section of the rare-earth ions; (ii) the writing of channels and mirrors in the case of waveguide integrated laser. The research discussed in my PhD thesis gives a possible solution to these points thanks to the demonstration of two innovative and unique characteristics of SnO_2 -based transparent glass-ceramics, i.e. luminescence sensitizing and photosensitivity. The role of SnO_2 nanocrystals as rare-earth ion luminescence sensitizers allows to overcome the low absorption cross section of the Er^{3+} ion. The photosensitivity of SnO_2 allows applying the robust direct laser photoinscription technique on the systems to fabricate Bragg gratings and channel waveguides for waveguide integrated laser. Last but not least, the developed transparent glass-ceramics prevent luminescence quenching effect due to rare-earth clustering, effectively optimizing the photoluminescence quantum yield of the system. Based on an application-oriented approach, a comprehensive study on SiO_2 - SnO_2 : Er^{3+} glass-ceramic planar waveguides and monoliths has been carried out in this research thesis. The work covers different research stages and aspects from the material preparation to a complete assessment of systems for the applications employing a rich number and variety of experimental techniques. Based on the stated research objectives, the research achievements of my work can be summarized as follows:

- (i) Concerning the fabrication, reliable sol-gel synthesis protocols with defined thermal processes have been

developed to prepare both the compositional photonic monoliths and planar waveguides. The homogeneous and transparent glass-ceramic monoliths were obtained with SnO_2 content up to 10 mol%. Three different bulk forms were produced for the desired applications: the cylinders for solid state laser construction, the monolithic squares for writing channel waveguides and big pillars for the usages for fiber preforms. Referring to the planar waveguides, high SnO_2 content up to 30 mol% was successfully introduced in SiO_2 matrix. The densified compositional planar waveguides were obtained with low surface roughnesses and high transparency. All the glass-ceramic planar waveguides and monoliths are imbedded by small SnO_2 nanocrystals with average size less than 10 nm, which do not induce scattering losses that can reduce the suitability of the system for photonic applications.

- (ii) A complete photonic assessment of the glass-ceramic systems has been obtained, based on various characterization techniques. The assessments of the structural, chemical and morphological properties of obtained transparent systems were carried out. The compositional glass-ceramic planar waveguides and monoliths fulfill the requirements of good optical materials such as densification, crack-free and contamination-free. The small nano-sized SnO_2 nanocrystals were observed by HR-STEM images and confirmed to have sizes of less than 10 nm in average. The refractive index of the $\text{SiO}_2\text{-SnO}_2\text{:Er}^{3+}$ can be easily tuned by changing SnO_2 contents since it can be expressed using the Clausius-Mossotti equation. Specifically, concerning the optical waveguiding properties, the planar waveguides have confined propagation modes, step-index profile with high confinement (82 % for 30 mol% SnO_2 planar waveguides at 1542 nm) and specially, low losses (around 0.6 dB/cm). The spectroscopic measurements demonstrate: (i) energy transfer from SnO_2 to Er^{3+} is demonstrated, (ii) most of Er^{3+} ions embedded in SnO_2 nanocrystals with high absorption, emission cross section, internal gain and quantum yield for the emission at 1.5 μm . A possible scheme for the

luminescence sensitization was proposed, and the consideration of the influential factors involved shows: (i) the high absorption cross section of SnO_2 interband transition, (ii) high energy transfer efficiency from SnO_2 to Er^{3+} (and 63.4 % [Lin 2014]), (iii) high branching ratios from $^4\text{G}_{9/2}$ to the metastable state $^4\text{I}_{13/2}$ (71 % see 4.5.2.6) and (iv) relatively high quantum efficiency at 1500 nm emission of Er^{3+} under indirect excitation (48 ± 4 % for the $95\text{SiO}_2\text{-}5\text{SnO}_2\text{:}0.5\text{Er}^{3+}$ and 33 ± 3 % for $90\text{SiO}_2\text{-}10\text{SnO}_2\text{:}0.50\text{Er}^{3+}$). These factors confirmed the role of SnO_2 as an efficient Er^{3+} luminescence sensitizers and the promising of an efficient laser exploiting this luminescence sensitization as a pumping scheme.

- (iii) A model for understanding $\text{SnO}_2\text{:Er}^{3+}$ nanostructure and the relaxation dynamic of the electronic states supporting for the realization the proof of concept of the considered devices was developed.
- (iv) The assessment of the photorefractivity of the monoliths and waveguides were carried out. High induced refractive index change at 1550 nm is demonstrated to be from 2×10^{-3} to 4×10^{-3} depending on the SnO_2 content and irradiation condition. Higher SnO_2 content leads to higher refractive index change. The first results of gratings fabrication were obtained as a proof of concept for the direct grating inscription exploiting the photorefractivity. The gratings fabrication on $\text{SiO}_2\text{-SnO}_2\text{:Er}^{3+}$ glass-ceramics is 10-15 times energy-efficient in comparison with hydrogen loaded germanoborosilicate glasses. All these achievements show the outstanding photorefractivity of $\text{SiO}_2\text{-SnO}_2\text{:Er}^{3+}$ glass-ceramics.
- (v) Another important research outcome is the design of a solid state laser with lateral pumping scheme and of an integrated waveguide laser in two different distributed feedback structures using all the parameters measured during the experimental activity.
- (vi) The fabrication of optical waveguiding structures on the monolithic squares were obtained exploiting femtosecond laser machining. And, together with the photorefractivity, these results of femtosecond laser micromachining on $\text{SiO}_2\text{-}$

$\text{SnO}_2\text{:Er}^{3+}$ glass-ceramics provide solutions for the issue of writing of channels and mirrors for the integrated lasers or circuits. These results again strengthen more the competition of $\text{SiO}_2\text{-SnO}_2\text{:Er}^{3+}$ glass-ceramics in the applications in integrated optics.

Overall, the research outcomes have fulfilled all the research objectives of this thesis. The obtained results not only demonstrate the viability and outstanding properties of the $\text{SiO}_2\text{-SnO}_2\text{:Er}^{3+}$ glass-ceramics for photonic applications but also put the basis for the fabrication of solid state and integrated lasers. The next steps of the research are the fabrication of the channels and mirrors exploiting the obtained photorefractivity with a proper pumping scheme and checking the lasing action and corresponding functional characteristics. Referring to the $\text{SiO}_2\text{-SnO}_2\text{:0.5Er}^{3+}$ monoliths, the current results are reasonably qualified for the checking of lasing action with the designed lateral pumping scheme as a proof of concept. Nevertheless, a prolonged heat-treatment will be beneficial to remove completely the OH groups for both the small cylinders and especially, big pillars for fiber preforms. An elaboration of femtosecond laser micromachining fabrication to single mode optical waveguides is demanded for the channel waveguides for optical circuits. There are still some fantastic open questions that are important for the device optimization i.e.: (i) the dynamic of the exciton-mediated energy transfer from the nanocrystal to the rare earth ion and (ii) the reason of the spatial and optical density distribution in the femtosecond laser written channel waveguides.

Research outcomes

<i>Journal papers</i>	
1.	L.T.N. Tran , D. Massella, L. Zur, A. Chiasera, S. Varas, C. Armellini, G.C. Righini, A. Lukowiak, D Zonta, M. Ferrari, “SiO ₂ -SnO ₂ :Er ³⁺ Glass-Ceramic Monoliths”, <i>Applied Science</i> 2018, 8 (8), 1335, DOI: 10.3390/app8081335.
2.	L. Zur, T. N. L. Tran , M. Meneghetti, T. T. V. Tran, A. Lukowiak, A. Chiasera, D. Zonta, M. Ferrari, G. C. Righini, “Tin-dioxide nanocrystals as Er ³⁺ luminescence sensitizers: formation of glass-ceramics thin films and their characterization”, <i>Optical Materials</i> 2017, 63, pp.95-100, DOI: 10.1016/j.optmat.2016.08.041
3.	A. Lukowiak, L. Zur, T. N. L. Tran , M. Meneghetti, S. Berneschi, G. N. Conti, S. Pelli, C. Trono, B.N. S. Bhaktha, D. Zonta, S. Taccheo, G. C. Righini and M. Ferrari, “Sol–Gel-Derived Glass-Ceramic Photorefractive Films for Photonic Structures”, <i>Crystals</i> 2017, 7(2), pp.61(1-7), DOI: 10.3390/cryst7020061
4.	D. J. Jovanovic, A. Chiappini, L. Zur, T. V. Gavrilovic, T. N. L. Tran , A. Chiasera, A. Lukowiak, K. Smits, M. D. Dramicanin, M. Ferrari, “Synthesis, structure and spectroscopic properties of luminescent GdVO ₄ :Dy ³⁺ and DyVO ₄ particles, <i>Optical Materials</i> 2018, 76, pp. 308-316”, DOI: 10.1016/j.optmat.2017.12.046
<i>Book chapter</i>	
1.	L. Zur, T. N. L. Tran , M. Meneghetti, M. Ferrari, “SnO ₂ based photonic glasses”, <i>Handbook of Sol-Gel Science and Technology</i> , Springer International Publishing (2017), p1-19, DOI: 10.1007/978-3-319-19454-7_116-1
<i>Peer-reviewed conference papers</i>	
1.	T. N. L. Tran , M. Meneghetti, L. Zur, T. T. V. Tran, A. Lukowiak, D. Zonta, G. C. Righini, M. Ferrari, “SnO ₂ based photonic glasses: A viable photonic system”, 18th Italian National Conference on Photonic Technologies (Fotonica 2016), DOI: 10.1049/cp.2016.0895
2.	L.T.N. Tran , L. Zur, D. Massella, B. Derkowska-Zielinska, A. Chiasera, S. Varas, C. Armellini, A. Martucci, D. Zonta, T.T.V. Tran, A. Lukowiak, S. Taccheo, D. Dorosz, G.C. Righini, Y. G. Boucher, M. Ferrari, “SiO ₂ -SnO ₂ :Er ³⁺ transparent glass-ceramics: fabrication and photonic assessment”, <i>Proc. SPIE</i>

	10683, Fiber Lasers and Glass Photonics: Materials through Applications, 106832C (17 May 2018), DOI: 10.1117/12.2306767
3.	Lidia Zur, Lam Thi Ngoc Tran , Damiano Massella, Alessandro Vaccari, Andrea Chiappini, Alessandro Chiasera, Stefano Varas, Cristina Armellini, Alessandro Carpentiero, Brigitte Boulard, Dominik Dorosz, Stefano Pelli, Cosimo Trono, Simone Berneschi, Gualtiero Nunzi Conti, James Gates, Pier-John Sazio, Barbara Rossi, Erica Iacob, Victor Micheli, Giorgio Speranza, Gloria Ischia, Francesco Prudenzano, Anna Lukowiak, Daniele Zonta, Roberta Ramponi, Giancarlo C. Righini, Maurizio Ferrari “SiO ₂ -SnO ₂ transparent glass-ceramics activated by rare earth ions”, submitted paper to Photonics West 2019, San Francisco, US
4.	L. Zur, L. T. N. Tran , M. Meneghetti, S. Varas, C. Armellini, D. Ristic, A. Chiasera, F. Scotognella, S. Pelli, G. N. Conti, B. Boulard, D. Zonta, D. Dorosz, A. Lukowiak, G. C. Righini, R. Ramponi, M. Ferrari, “Glass and glass-ceramic photonic systems”, Proceedings Volume 10106, Integrated Optics: Devices, Materials, and Technologies XXI; 1010603 (2017), DOI:10.1117/12.2254965
5.	D. J. Jovanović, A. Chiappini, L. Zur, T. V. Gavrilović, T. N. L. Tran , A. Chiasera, A. Lukowiak, M. D. Dramićanin, M. Ferrari, “Synthesis, structure and spectroscopic assessment of luminescent GdVO ₄ :Dy ³⁺ and DyVO ₄ nanoparticles”, Proc. SPIE 10683, Fiber Lasers and Glass Photonics: Materials through Applications, 106831Y (17 May 2018), DOI: 10.1117/12.2306124
Invited talks/Oral presentations	
1.	L. T. N. Tran , D. Massella, L. Zur, M. Meneghetti, A. Chiasera, C. Armellini, A. Chiappini, S. Varas, T. T. V. Tran, A. Vaccari, A. Lukowiak, D. Zonta, R. Ramponi, G. C. Righini, M. Ferrari, “Tin dioxide based photonic systems”, Oral presentation at CLEO®/Europe-EQEC 2017, June 24-29 th , 2017, Munich, Germany
2.	L. T. N. Tran , D. Massella, L. Zur, G. Ischia, A. Chiasera, S. Varas, C. Armellini, A. Chiappini, E. Iacob, V. Micheli, G. Speranza, D. Dorosz, C. Trono, S. Berneschi, G. Nunzi Conti, J. Gates, P.J. Sazio, B. Rossi, F. Prudenzano, A. Lukowiak, D. Zonta, R. Ramponi, G.C. Righini, M. Ferrari, "Fabrication and photonic assessments of SiO ₂ -SnO ₂ :Er ³⁺ glass-ceramic planar waveguides ", Oral communication at the 1 st International Conference on Dielectric Photonic Devices and Systems Beyond Visible (D-photon), October 1 st -2 nd , 2018, Bari, Italy

3.	D. Massella, L.T.N. Tran , L. Zur, A. Vaccari, A. Quandt, Y. G. Boucher, F. Prudeniano, T.T.V. Tran, A. Lukowiak, D. Zonta, R. Ramponi, G.C. Righini, M.Ferrari, " SiO ₂ -SnO ₂ :Er ³⁺ glass-ceramics: band-structure and the density of states ", Oral communication at the 1 st International Conference on Dielectric Photonic Devices and Systems Beyond Visible (D-photon), October 1 st -2 nd , 2018, Bari, Italy
4.	L. Zur, T. N. L. Tran , A. Chiasera, Y. G. Boucher, A. Vaccari, F. Prudeniano, D. Massella, C. Meroni, F. Enrichi, S. Varas, C. Armellini, A. Chiappini, A. Carpentiero, M. Mazzola, A. Quandt, D. Dorosz, A. Lukowiak, B. Boulard, D. Zonta, R. Ramponi, G. C. Righini, M. Ferrari, " Glass and Glass-Ceramic Photonic Systems: advances and perspectives ", Invited talk at Tsukuba Global Science Week (TGSW) symposium, September 20 th -22 nd , 2018, Tsukuba, Japan
5.	L. Zur, L. T. N. Tran , D. Massella, B. Derkowska-Zielinska, A. Vaccari, Y. G. Boucher, A. Chiappini, A. Chiasera, C. Armellini, S. Varas, T. T. V. Tran, A. Lukowiak, W. A. Pisarski, D. Dorosz, B. N. Shivakiran Bhaktha, B. Rossi, D. Zonta, G. C. Righini, M. Ferrari, " SiO ₂ -SnO ₂ glass-ceramics activated by Er ³⁺ ions for photonics applications ", Invited talk at the 11 th Seminar Porous Glasses-Special Glassees, PGL'2018, September 12 nd -16 th , 2018, Wroclaw-Szklarska Poreba, Poland
6.	T. N. L. Tran , D. Massella, L. Zur, A. Lukowiak, A. Chiasera, A. Chiappini, F. Prudeniano, S. Varas, C. Armellini, A. Carpentiero, D. Zonta, B. Boulard, D. Dorosz, J. Gates, P. Sazio, B. Rossi, S. Berneschi, G. Nunzi Conti, G. C. Righini, M. Ferrari, " Photonics glass-ceramics ", Invited talk at the 5th International Conference on the Physics of Optical Materials and Devices (ICOM), 27-31.08.2018, Igalo, Montenegro
7.	L. T. N. Tran , L. Zur, D. Massella, A. Vaccari, Y. G. Boucher, A. Chiappini, A. Chiasera, C. Armellini, S. Varas, T. T. V. Tran, A. Lukowiak, D. Dorosz, B. N. Shivakiran Bhaktha, B. Rossi, D. Zonta, G. C. Righini, M. Ferrari, " SiO ₂ -SnO ₂ glass-ceramics activated by rare earth ions for photonics ", Oral communication at the 5th International Conference on the Physics of Optical Materials and Devices (ICOM), August 27 th -31 st , 2018, Igalo, Montenegro
8.	T. N. L. Tran , C. Meroni, D. Massella, L. Zur, A. Chiasera, A. Chiappini, Y. G. Boucher, A. Vaccari, V. Piccolo, S. Varas, C. Armellini, A. Carpentiero, D. Zonta, B. Boulard, D. Dorosz, B. Rossi, A. Lukowiak, R. Ramponi, G. C. Righini, M. Ferrari, " Light management in glass photonics: structures and applications", Invited talk at the 5th International Conference

	on RARE EARTH MATERIALS (REMAT) Advances in Synthesis, Studies and Applications, June 16 th -18 th , 2018, Wroclaw, Poland
9.	L. Zur, T. N. L. Tran , C. Meroni, D. Massella, A. Chiasera, A. Chiappini, Y. G. Boucher, A. Vaccari, V. Piccolo, S. Varas, C. Armellini, A. Carpentiero, D. Zonta, B. Boulard, D. Dorosz, B. Rossi, A. Lukowiak, R. Ramponi, G.C. Righini, M. Ferrari, “Light management in glass photonics: from structures to applications”, Oral communication at the Topical meeting of COST Action MP1401, June 11 th -12 nd , 2018, Milan, Italy
10.	L.T.N. Tran , L. Zur, D. Massella, B. Derkowska-Zielinska, A. Chiasera, S. Varas, C. Armellini, A. Martucci, D. Zonta, T.T.V. Tran, A. Lukowiak, S. Taccheo, D. Dorosz, G.C. Righini, Y. G. Boucher, M. Ferrari, “SiO ₂ -SnO ₂ :Er ³⁺ transparent glass-ceramics: fabrication and photonic assessment”, Invited talk , SPIE Photonics Europe 2018, Conference 10683, Fiber Lasers and Glass Photonics: Materials through Applications, April 22 nd – 26 th 2018, Strasbourg, France
11.	A. Chiasera, T. N. L. Tran , L. Zur, A. Lukowiak, Y. G. Boucher, A. Vaccari, D. Massella, C. Meroni, S. Varas, C. Armellini, A. Chiappini, A. Carpentiero, D. Ristic, M. Ivanda, F. Scotognella, S. Pietralunga, S. Taccheo, D. Zonta, D. Dorosz, R. Ramponi, G.C. Righini, M. Ferrari, “Glass-based photonic structures: advances and perspectives”, Keynote oral presentation , 6 th International conference on Photonics, Optics and Laser Technology, January 25 th - 27 th , 2018, Funchal, Madeira - Portugal
12.	L. Zur, L. T. N. Tran , D. Massella, B. Derkowska-Zielinska, A. Vaccari, Y. Boucher, A. Chiasera, S. Varas, T. T. V. Tran, A. Lukowiak, W. A. Pisarski, B. N. Shivakiran Bhaktha, D. Zonta, R. Ramponi, G. C. Righini, M. Ferrari, “Silica - tin dioxide systems activated by rare earth ions for PV applications”, Oral communication at 6th International Workshop Plasmonics and nanoantennas for solar cells, November 30 th -December 2 th , 2017, Rome, Italy

13.	L. Zur, T. N. L. Tran , A. Chiasera, Y. G. Boucher, A. Vaccari, D. Massella, C. Meroni, F. Enrichi, S. Varas, C. Armellini, A. Chiappini, A. Carpentiero, M. Mazzola, D. Ristic, F. Scotognella, S. Taccheo, D. Zonta, A. Quandt, D. Dorosz, A. Lukowiak, R. Ramponi, G. C. Righini, B. Boulard and M. Ferrari, “Glass photonic structures for photon management applications”, Keynote oral presentation at International conference of Spectral shaping for biomedical and energy applications (SHIFT 2017), November 13th-17th, 2017, Tenerife, Canary Islands, Spain
14.	L. Zur, T. N. L. Tran , M. Meneghetti, S. Varas, C. Armellini, D. Ristic, A. Chiasera, F. Scotognella, S. Pelli, G. N. Conti, B. Boulard, D. Zonta, D. Dorosz, A. Lukowiak, G. C. Righini, R. Ramponi, M. Ferrari, “Glass and Glass-Ceramic Photonic Systems”, Invited communication at SPIE Photonic West 2017, Integrated Optics: Devices, Materials, and Technologies XXI, January 28 th - 2 nd February California, United States
15.	L. Zur, T. N. L. Tran , M. Meneghetti, S. Varas, C. Armellini, A. Chiappini, A. Chiasera, F. Scotognella, D. Zonta, D. Dorosz, A. Lukowiak, B. Boulard, G. C. Righini, R. Ramponi, M. Ferrari, “RED photonic glasses and confined structures”, Invited communication at Italian - Mexican Nanophotonics workshop January 15-19 th , 2017 Tequisquiapan Queretaro – Mexico
16.	L. Zur, T. N. L. Tran , M. Meneghetti, A. Vaccari, A. Chiasera, C. Armellini, S. Varas, T. T. V. Tran, A. Lukowiak, D. Zonta, S. Taccheo, R. Ramponi, G. C. Righini, M. Ferrari, “Silica-tin dioxide glass-ceramic photonic systems”, Oral communication at 3rd MC meeting and 2nd Annual conference, March 1 st -2 nd , 2017, University of Tel-Aviv, Tel-Aviv- Yafo, Israel
17.	T. N. L. Tran , L. Zur, A. Lukowiak, A. Chiasera, Y. G. Boucher, A. Vaccari, D. Massella, C. Meroni, F. Enrichi, S. Varas, C. Armellini, A. Chiapini, A. Carpentiero, D. Ristic, F. Scotognella, S. Pietralunga, S. Taccheo, D. Zonta, A. Quandt, B. Boulard, D. Dorosz, R. Ramponi, G. C. Righini, M. Ferrari, “Glasses for up- and down-conversion for PV applications”, Invited communication at PLESC meeting, University of Witwatersrand, Johannesburg, South Africa- May 09 th , 2017

18.	T. N. L. Tran , L. Zur, A. Lukowiak, A. Chiasera, Y. G. Boucher, A. Vaccari, D. Massella, C. Meroni, F. Enrichi, S. Varas, C. Armellini, A. Chiapini, A. Carpentiero, D. Ristic, F. Scotognella, S. Pietralunga, S. Taccheo, D. Zonta, A. Quandt, B. Boulard, D. Dorosz, R. Ramponi, G. C. Righini, M. Ferrari, S. Soria, “Glass and Glass-ceramics for photonics: advances and perspectives”, Invited communication at Photonics North conference on June 6-8 th , 2017, Ottawa, Canada
19.	L. Zur, L. T. N. Tran , D. Massella, A. Vaccari, A. Chiasera, S. Varas, C. Armellini, M. Sołtys, D. Zonta, T. T. V. Tran, A. Lukowiak, W.A. Pisarski, S. Taccheo, R. Ramponi, G.C. Righini, Y. G. Boucher, M. Ferrari, “Er-doped SiO ₂ -SnO ₂ glass ceramics for photonics – from the synthesis to the device”, The SIXTH International Workshop on Advanced Spectroscopy and Optical Materials, 9-14 th July, 2017, Gdańsk, Poland
20.	T. N. L. Tran , L. Zur, A. Lukowiak, A. Chiasera, S. Varas, C. Armellini, A. Chiappini, A. Carpentiero, D. Ristic, M. Ivanda, F. Scotognella, S. Pietralunga, S. Taccheo, D. Zonta, D. Dorosz, G. C. Righini, R. Ramponi, B. Boulard, M. Ferrari, “Glasses and Glass-ceramics for photonics: advances and perspectives”, Keynote presentation at International Conference on Molecular Spectroscopy (ICMS2017) 3-7 September, 2017 - Białka Tatrzańska, Poland
21.	D. Massella, L. T. N. Tran , L. Zur, B. Derkowska-Zielinska, A. Vaccari, A. Chiasera, S. Varas, C. Armellini, D. Zonta, T. T. V. Tran, A. Lukowiak, S. Taccheo, R. Ramponi, G. C. Righini, Y. G. Boucher, M. Ferrari, SiO ₂ -SnO ₂ :Er ³⁺ glass-ceramics for photonics: advances and perspectives, Oral communication at The 4th MC meeting 3rd Annual conference of COST Action, 17-20.09.2017, Jena, Germany
22.	Lidia Zur, L. T. N. Tran , Damiano Massella, Stefano Varas, Cristina Armellini, Alessandro Vaccari, Anna Lukowiak, Daniele Zonta, Maurizio Ferrari, Giancarlo C. Righini, “Synthesis and characterization of Er ³⁺ -doped tin dioxide glass-ceramics produced by sol-gel route”, The X International Conference on Surfaces, Materials and Vacuum, September 25 th -29 th , 2017, Ciudad Juarez, Chihuahua, México
23.	M. Meneghetti, T. N. L. Tran , L. Zur, T. T. Van Tran, A. Lukowiak, A. Chiappini, D. Zonta, G. C. Righini, M. Ferrari, “SnO ₂ - based glass ceramics for photonics”, Oral communication at International OSA Network of Students (IONS) Naples 2016 conference, July 6-8 th , Naples, Italy
24.	T. N. L. Tran , M. Meneghetti, I. Vasilchenko, L. Zur, A. Chiasera, S. Varas, C. Armellini, A. Carpentiero, A. Chiappini,

	G. Speranza, A. Vaccari, D. Zonta, D. Dorosz, A. Lukowiak, R. Ramponi, G. C. Righini, M. Ferrari, “Glasses and transparent glass-ceramics for photonics”, Invited talk at 6th International Conference on Excited States of Transitions Elements (ESTE), August 21 st -26 th , 2016, Polanica Zdrój, Poland
25.	L. Zur, T. N. L. Tran , Marcello, S. Varas, A. Carpentiero, A. Chiappini, C. Armellini, A. Chiasera, B. Boulard, D. Zonta, A. Lukowiak, Wojciech A. Pisarski, G. C. Righini, R. Ramponi, M. Ferrari, T. N. L. Tran, M. Meneghetti, L. Zur, T. T. V. Tran, A. Lukowiak, D. Zonta, G. C. Righini, M. Ferrari, “Glass-Ceramic Photonic Systems”, Oral communication at MATERIAL 2016, December 12 nd -16 th , Catania, Italy
26.	L. T. N. Tran , M. Meneghetti, L. Zur, A. Chiasera, C. Armellini, A. Chiappini, S. Varas, T. T. V. Tran, A. Vaccari, A. Lukowiak, D. Zonta, R. Ramponi, G. C. Righini, M. Ferrari, “Tin Dioxide based Photonic Systems: Heat-treatment strategy and energy transferring efficiency”, Oral communication at Fotonica 2017 19th Edition Convegno Italiano delle Tecnologie ottiche, May 3 rd -5 th , Padova, Italy



Except where otherwise noted, contents on this book are licensed under a Creative
Common Attribution - Non Commercial - No Derivatives
4.0 International License

ISBN (paper): ; ISBN (online):

University of Trento
Doctoral School in Civil, Environmental and Mechanical Engineering
<http://web.unitn.it/en/dricam>
Via Mesiano 77, I-38123 Trento
Tel. +39 0461 282670 / 2611 - *dicamphd@unitn.it*